THE OPTIMAL CONFIGURATION OF A MULTI-STACKED PERMANENT-MAGNET GENERATOR

A thesis presented for the degree of

DOCTOR OF PHILOSOPHY

of the

UNIVERSITY OF SOUTHAMPTON

in the

FACULTY OF ENGINEERING AND APPLIED SCIENCE

DEPARTMENT OF ELECTRICAL ENGINEERING

by

T. S. LOW

March 1982

UNIVERSITY OF SOUTHAMPTON

ABSTRACT

FACULTY OF ENGINEERING AND APPLIED SCIENCE

ELECTRICAL ENGINEERING

Doctor of Philosophy

THE OPTIMAL CONFIGURATION OF A MULTI-STACKED PERMANENT-MAGNET GENERATOR

by Teck Seng Low

The multi-stacked permanent magnet generator is studied in detail experimentally and its field analysed using two methods of computation. The first involves the discretisation of the magnetic circuit and obtaining a balance between the field of the magnet, the armature reaction of the stator and the reluctance of the discretised flux paths. This method is called the discrete-reluctance method. The second is a three-dimensional finite-element method using scalar potentials.

The accuracy of both methods of computation is discussed and their limitations assessed. The discrete-reluctance method is the less accurate of the two, but is much more efficient in computer processing time. The detailed analysis of the field using the finite-element method is used to refine the discrete-reluctance method by improving the accuracy of the representation of the flux paths of the magnetic circuit.

The analysis of the imbricated rotor using the finite-element program enables the three-dimensional field to be studied in a precise way. The leakage fluxes in the rotor are also quantified. The program is used to monitor the effect of changes in the geometry of the flux guides, in particular that of the pole profile, on the field of the rotor. From this analysis, conclusions are drawn about the optimal configuration of the flux guide.

The results of the field analysis using the finite-element program and the improved version of the discrete-reluctance method are used for the optimisation of designs and the study of the effect of scale and the influence of magnet characteristics on the optimal configuration of the multi-stacked permanent -magnet generator.

In addition, the behaviour of an anisotropic polymer-bonded rare-earth magnet under the influence of external crossfields at right-angles is studied. A tensor representation of the magnet is proposed from the analysis of the experimental data obtained. This representation is implemented in a finite-element program, and tested.

ACKNOWLEDGEMENTS

I would like to express my gratitude to my supervisor, Dr. K. J. Binns, for his close involvement and interest in the research, and without whose help and guidance this thesis would not have been possible.

My particular thanks go to Miss J. E. Sutton for typing most of this thesis, and to Miss S. Makin who typed the final two chapters.

I would also like to acknowledge the cooperation of Mr. J. Simkin on the work done with TOSCA, and the help and advice from the members of the Department of Electrical Engineering, Southampton University.

Finally, I would like to thank my family and friends, in particular Dr. M. A. Jabbar, for their support and encouragement during the research and the writing of this thesis.

CONTENTS

LIST OF SYMBOLS

Unless otherwise stated in the text, the symbols used in this thesis have the following meanings:

A	Area, vector potential
B, $\underline{B}$	Flux density vector
$B_m, B_1^I, B_2^I, B_{3j}^I$	Magnetic flux density
B_g	Air-gap flux density (fundamental)
B', $\underline{B}'$	Variable part of the flux density vector
B_r	Remanent flux density
b_1, B_1	The instantaneous flux density (fundamental)/ The amplitude of the flux density (fundamental)
(BH)	Energy product
C	Armature reaction constant
E, E_g, E_o	Machine e.m.f.
f_n	Frequency of the n^{th} harmonic
H, $\underline{H}$	Magnetic field intensity vector
H_c	Coercivity
$\underline{H}_c$	The field from current source
H_{3j}^I	Field intensity along the j^{th} path in iron region 3
$H_m, \underline{H}_m$	Positive value of the field intensity of the magnet/ The field from induced magnetisation
I, I_c	Electric current
I_q	Current linkage for the q^{th} branch
$\underline{J}$, J_m	Current density vector
K_n	Armature reaction mmf in the n^{th} air-gap path ($n = 1, 2, \ldots, 180$)

L	Length
L_1^A, L_2^A	Average length of flux path (air)
L_q^G, L_g	" " " " " (air-gap)
L_1^I, L_2^I, L_{3j}^I	" " " " " (iron)
M, $\underline{M}$	Magnetic polarisation vector
M_o	Initial magnetic polarisation
M', $\underline{M}'$	Variable part of the polarisation vector
M_q^G	Total potential in the air-gap
N	Number of turns per coil.
PF, PF_θ	Power factor
P	Power
$\underline{r}$, $\underline{r}'$	Vector of distance
R	Radius, Reluctance, Resistance
R_a	Armature phase resistance
R_L	Resistive Load
R_1^I, R_2^I	Reluctance of iron path 1/2
R_3^I	Equivalent reluctance of iron path 3
r_1^I, r_2^I	Ratio between path length and cross-sectional area (iron path 1/2)
S	Slots per pole per phase
S_1^A, S_2^A S_1^I, S_2^I, S_{3j}^I S_q^G, S_m	Path average cross-sectional area
s	Slot width
t	Time (seconds), tooth width
T	Time

V, V_o, V_s	Voltage
V_o, V_θ	
X_ℓ	Leakage reactance
α	Angle
β	Angle/Load angle
θ	Angle/Power factor angle
Λ_1, Λ_2	Permeance of leakage path 1/2
Λ_g	Permeance of air-gap path
μ	Permeability
μ_0	Permeability of free space
μ'	Apparent permeability
τ	Pole pitch
ϕ	Flux
ϕ_1^A, ϕ_2^A	Leakage flux 1/2
ϕ^G, ϕ_q^G	Total air-gap flux/Flux in the q^{th} air-gap path
ϕ_1^I, ϕ_2^I	Flux in iron path 1/2
ϕ_r, ϕ_{r1}	Total rotor leakage/Rotor leakage for one unit
ν	Reluctivity
ν', ν_m	Magnet apparent reluctivity
ν_1^I, ν_2^I	Reluctivity of iron in iron path 1/2
ν_{3j}^I	Reluctivity of iron in the j^{th} path of iron region 3 ($j = 1, 2, \ldots, 15$)
ψ, ψ_θ	Internal power factor angle (the angle between the centre of the phase belt carrying the maximum instantaneous current and the direct axis)
ψ_R	Reduced Scalar potential
ψ_T	Total Scalar potential

ω	Relaxation factor/Angular velocity (radians per second)
χ	Magnetic susceptibility
Δ	denotes charge
$\sum$	Summation
$\int$	Integral

Subscripts

A	Axial
R	Radial
T	Transverse
x	x-axis
y	y-axis
p	p-axis
q	q-axis
z	z-axis
θ	θ-axis
Ex	External
BN	Boundary number
SN	Slab number

LIST OF FIGURES

LIST OF TABLES

CHAPTER ONE

INTRODUCTION

CHAPTER ONE

INTRODUCTION

1.1 PROGRESS IN THE DEVELOPMENT OF PERMANENT-MAGNET GENERATORS

1.1.1 Introduction

After the early development work on permanent-magnet generators was almost completely abandoned, except for specialised applications such as pilot exciters, they were largely replaced by other forms of generator which made use of electromagnetic excitation. More recently permanent magnets have become increasingly used in applications up to 40 kW ratings and beyond. In some devices, the permanent magnet is a necessity in that wound excitation is not feasible. However, in most cases the reason for its use lies in the advantages that a permanent-magnet system possesses. In larger electromagnetic machines, such as a.c. generators, where large amounts of energy are involved, the permanent magnet has not been extensively used, though the permanent-magnet generator was one of the earliest forms of machine.

Much of the delay in exploiting permanent magnets for the field systems of generators can be attributed to the lack of understanding of the operation of the permanent magnet in producing excitation in electrical machines, and the limited choice of permanent-magnet materials. In a generator, permanent magnets are required to operate at a varying working point because of the demagnetising forces produced by the currents generated. If Alnico magnets are used, stabilisation of the permanent magnet is essential to avoid demagnetisation under load conditions. This arises because metallic magnets possess low coercivities and may operate on a minor loop. However, in the final analysis, for permanent magnets to become widely used in electrical machines, they must be competitive with or better than wound excitation.

There is evidence in recent years, with the progress in permanent-magnet technology, interest in permanent magnet-generators has been revived. Advances in all aspects of the permanent-magnet industry have been considerable over the past twenty-five years. New materials have been developed, and an improved knowledge of their properties has been achieved. The growth of this industry in the Fifties precipitated the development of a new generation of permanent-magnet generators which used Alnico alloys as the major source of their excitation[1,2,3]. In the Sixties, the trend was towards the more efficient anisotropic metallic magnets. These metallic magnets are expensive and prone to demagnetisation unless properly stabilised. In recent years, new materials have emerged such as the relatively cheap ceramic magnets, composed of either barium or strontium ferrite. In addition, materials of very high energy storage are available in the form of rare-earth magnets such as those made from samarium cobalt and misch-metal cobalt. A more recent development is the production of a magnet whose magnetic characteristics are better than the ferrites, though not comparable with the rare-earth magnets, but with no strategic materials in its composition and thus it has the potential to be inexpensive. This material is MnAlC, a manganese, alumium, carbon alloy. This selection of permanent-magnet materials offers a wide combination of magnetic and physical properties to meet the demands of designers. The availability of these magnets at commercially viable prices is an encouragement for the development of generators with permanent-magnet field systems.

1.1.2 Types of permanent-magnet rotors

Early designs of permanent-magnet generators made use of integrally cast magnets[5]. The material normally used, isotropic Alnico, has no directional properties, is magnetised to give poles of alternating

polarity on the rotor surface as shown in Figure 1.1. This one-piece construction for small multi-pole generators was manufactured up to diameters of 160 mm to 200 mm. An improvement to this design might be to die-cast the rotor into aluminium jackets. The aluminium acts as an extremely useful damping device. For bigger machines, block magnets were mounted on the rotor hub with the steel pole-shoes and the magnets supported by non-magnetic bolts[5] as shown in Figure 1.2. The direction of magnetisation of the magnets in this configuration is in the radial direction. The magnets alternate in their direction of polarisation, giving a heteropolar field on the rotor surface. Such a rotor design would be die-cast in aluminium as in Figure 1.3. A variation of this design[3] has laminated pole-shoes and inner-magnet ties locating the rectangular block magnets between annular discs of non-magnetic steel, and the whole configuration is cast centrifugally with an aluminium alloy. This is shown in Figure 1.4.

Another class of permanent-magnet generators use axially magnetised magnets. An early form of this type of rotor is called the Lundell or claw-type rotor[5,6], as shown in Figure 1.5. Alternate north and south poles are achieved by attaching fingers to the plates at the end of the magnet. Axially magnetised magnets have also been used in another type of rotor[7]. This rotor has a disc magnet with a central hole and a number of radially projecting parts on its periphery as seen in Figure 1.6. Pole-shoes are arranged on the projecting pole part and overlap the latter in the peripheral direction so that the polarity of the radial projections on the first is different from the second, therefore achieving alternating polarity. Another rotor[8] has a set of short bar magnets assembled to form a disc with axial polarity. Flux guides were used to guide the flux into the salient-poles.

The third class of permanent-magnet generators has rotors with tangentially magnetised magnets[9,10]. A twelve-pole version of this type of rotor is shown in Figure 1.7. Tangentially magnetised magnets are placed in radial slots so as to provide alternate polarities on the rotor poles lying between adjacent slots. Figure 1.8 shows an alternative form of construction where the poles and magnets are enclosed by annular rings. A form of generator with a rotor of this configuration had been produced by Siemens[9].

All the above three forms of permanent-magnet generator configuration, broadly classified with respect to the directions of their flux paths within their magnets (the three directions being radial, transverse and axial relative to the rotor's axis of rotation) have been employed by various designers for many years. Traditionally, metallic magnets have been used for the designs described[1,2,3,5,6,9]. These rotors with Alnico magnets are hardly optimal as the metallic magnets must work on a minor loop when stabilised under load conditions. However, in the past two decades, since the early Sixties, permanent-magnet materials offering desirable alternatives to Alnicos, such as ferrite magnets and rare-earth magnets, have been used by permanent-magnet generator designers for better performance. Their use has mainly been confined to the more popular radial and transverse magnet rotor configurations.

Designs involving the use of ferrites and rare-earth magnets radially magnetised for the type of rotor shown in Figure 1.3 have been studied by Peterson[11,12]. This configuration is simple to implement but has a disadvantage in that the air-gap flux density cannot exceed the flux density level in the magnet. The gap density can only exceed that in the magnet if the ratio of rotor surface area to the surface area of the poles of the magnets used is less than unity. This cannot be

achieved in the radial rotor configurations as a pole of each magnet represents a salient-pole of the rotor. The use of salient magnets inhibits the optimisation of the total flux from a given magnet volume.

The use of ferrite magnets, magnetised tangentially for the types of rotors described by Figures 1.7 and 1.8 had been discussed by Kelha and Sario[13]. The application of rare-earth magnets for this rotor configuration was studied by Richter and Bailey[10] as well as Peterson[12] and Knudson[14]. This configuration can produce flux densities in the air gap higher than the magnet flux density level if the magnets are deep enough. However, they are characterised by excessive end-leakage and interpolar-leakage. This could be reduced by a smaller pole-arc which would result in a lower leakage and thus lower voltage regulation. A reduction in pole arc would also reduce the total flux across the air gap and thus be undesirable[10]. This poses a problem in the design of rotor of this configuration. Another limitation of this configuration lies in its inefficient usage of both the iron and the magnet for rotors with less than 12 poles. In rotors with less than 12 poles, with the magnets set deeply to produce a high gap density, the pole would be almost wedge-like in shape. This would cause saturation at the tapered end and under-usage of the iron near the surface of the pole.

The axial rotor configuration has been neglected in the past due to the inherent difficulty in guiding the axial flux radially across the air gap. A possible form of generator using this rotor configuration has been described by Kumazawa[7]. More recently, Binns and Kurdali at Southampton University have designed a generator with a rotor using axially magnetised disc magnets[15,16]. This new rotor is suitable for use with ferrite magnets, rare-earth magnets, polymer bonded rare-earth magnets and MnAlC magnets[17]. This new multi-stacked permanent-magnet

rotor is described in detail in Chapter 2. An example of this rotor is shown in Figure 2.2. This new rotor forms the basis of research in this thesis.

1.2 THE ROLE OF PERMANENT-MAGNET GENERATORS

With the advent of cheap ceramic magnets and the high performance rare-earth magnets, permanent-magnet generators have commanded a lot of attention. Justification for research into the application of permanent-magnet field systems in generators lies in the advantages that a permanent-magnet field system can offer over electromagnetic excitation and its suitability for certain applications.

The merits of a permanent-magnet generator can be highlighted by a comparison with a conventional wound-rotor generator. The basic difference between a permanent-magnet field system and a wound field system lies in the absence of exciter field windings, slip rings and brushes in the former. The resultant comparison can be summarised as follows:

(a) A greater overall efficiency due to the elimination of all excitation losses.

(b) A higher reliability and ease in maintenance as the rotor has neither conductors nor insulators. The rotor is a solid mass of metal and magnet which makes it mechanically robust. The use of modern magnets like ferrites and rare-earth magnets, whose physical and magnetic properties are unaffected by ageing and mechanical vibration, renders the rotor its high reliability.

(c) Permanent-magnet generators have negligible heat generated in the rotor. If a machine is to be heavily loaded so as to secure the best power-to-weight ratio, one of the ultimate limits will be the dissipation of heat from the machine, and this will be facilitated if no heat is generated in the field system of the machine. For this reason the maximum capacity of a given unit is increased.

(d) Permanent-magnet generators in the past have been expensive[3,5] due to the use of expensive metallic magnets. The introduction of cheap ceramic magnets and the recently developed magnet composed of manganese, aluminium and carbon has reduced the cost of permanent-magnet rotors. The elimination of an exciter system saves winding cost. This makes the permanent-magnet field system even cheaper.

Permanent-magnet generators are also competitive with wound-rotor generators in terms of power density. Bell[18] and Parker[19] in their reports have concluded that for small machines, up to 1 kW, permanent-magnet field systems possess a higher power-to-weight and power-to-volume ratio[18]. Work by Richter and Bailey[10] and the research at Southampton University, have suggested that permanent-magnet machines are advantageous for ratings up to 10 kW or more if rare-earth magnets are used. The volume efficiency of a permanent magnet is proportional to its energy product. Rare-earth magnets have energy products of 3 to 6 times that of most other permanent-magnet materials. Their application to electrical machines allows permanent magnet field excitation to compare favourably with wound excitation in large machines. For very large generating units the wound rotor system is preferred. This is because the volumetric efficiency of electromagnetic machines improves with scale.

The inherent voltage regulation of the permanent-magnet generator is a disadvantage in that there is no simple means for controlling the field. With unity power factor loads the voltage regulation is good but for highly lagging power factor loads the regulation is poor. To improve the regulation capacitances can be used.

The choice between permanent-magnet and a conventional electromagnetic construction for a generator ultimately depends on the relative importance given to the various specific advantages of each type of excitation.

1.3 APPLICATIONS OF PERMANENT-MAGNET GENERATORS

Permanent-magnet generators are used widely in the form of small a.c. generators for military applications where environmental requirements are severe. They are highly suitable for mobile military applications such as guided missiles, rockets and aircrafts, where the absence of external excitation and moving contacts to cause radio interference make them ideal[6]. The use of permanent-magnet generators in aircrafts is indeed promising as shown in the report by Borger[20] of a permanent-magnet variable speed constant frequency power generator, generating 400 Hz aircraft power.

The independence and versatility of permanent-magnet generators make them ideal for isolated generating units like windmills, where regulation is of secondary importance. Work on windmills[21] has shown that a permanent-magnet generator is most suited.

The regulation characteristic can be used to advantage in the use of the permanent-magnet generator for welding purposes. A specific open-circuit voltage is required to strike the arc, subsequently only a fraction of this voltage is needed to sustain it whilst the higher current provides the power. This requirement is compatable to the drooping load characteristic of the permanent-magnet generator. The use of permanent-magnet generators for high speed applications is also very attractive. An example of this application is in satellite momentum wheels and another is the application in energy storage flywheel systems[22].

Many other applications could be listed, such as vehicle alternators, pilot exciters, emergency standby power generating units and auxilliary supplies in hydroelectric power stations, to name a few.

1.4 METHODS OF FIELD ANALYSIS FOR ELECTRICAL MACHINES

An accurate knowledge of the magnetic field distribution is of great importance in design optimisation for electrical machines. Analysis of the fields in electrical machines is never simple. An exact solution of the field is not possible due to the presence of non-linearities caused by iron saturation. In permanent-magnet machines, the problem is further complicated by the hysteresis effect of the magnet. Countless methods have been employed in the past for field analysis. Some of these methods were used by the authors in references 22-41.

There are two approaches in the solution of magnetic fields. They are the circuital approach and the field approach. A variety of techniques using both approaches for the solution of magnetostatic fields has been developed over the years.

1.4.1 The circuital approach

In engineering practice, it is generally required to find solutions to problems in a convenient form that are easy to interpret and visualise. This accounts for the wide usage of the circuit concept as distinct from field concept. Although all phenomena occur in space and time, and these are field phenomena, it is possible to approximate them by time relations only summarising the actual physical constants by parameters, preferably at constant value. The magnetic analogue to Ohm's Law was extensively used in both electromagnetic and permanent-magnet field calculations. This is not a very suitable method due to complexities of saturation, hysteresis and leakage in the magnetic circuits.

The application of Ampere's Circuit Law, in the summation of m.m.f.'s by $\oint H \cdot d\ell$ in a closed circuit is another formulation in the circuital approach. This, however, is a one-dimensional analysis. It can be extended for two-dimensional analysis[23] by dividing the

circuital path into finite strips along the circuit length and consider them as one-dimensional elements with a constant tube of flux in each of them. In similar manner it can be used for three-dimensional field analysis.

1.4.2 The field approach

Field theory as opposed to circuit theory is becoming increasingly important in many engineering problems. The field approach to a solution in electromagnetic field problems can be divided into four main groups: analytical (mathematical)[24,25], graphical[26], analogue[28] and numerical[29-41] methods. Mathematical difficulties occurring in the analysis of complicated geometries of electrical machines become insurmountable for finding explicit solutions. This led to the use of graphical methods such as curvilinear squares. Later experimental techniques using electrolytic tanks and resistance networks[28] were developed. In the analysis of permanent-magnet fields, the latter two had hardly been used. With the advent of digital computers, numerical methods have become most suitable.

The number of numerical methods used in the past to solve field problems is quite considerable. To discuss all these methods would be beyond the scope of this thesis. All of the methods in present-day use for analysing fields of electrical machines fall into three principal headings, namely: (i) Finite difference schemes, (ii) Integral equation techniques and (iii) Variational formulation.

The finite difference method[29,30,31] is a popular method. Full details of this method are given by Binns and Lawrenson[25] in their book.

The variational method leads to the solution of the partial differential equation of the field problem by means of finite element techniques. This method has been used successfully in solving two-

dimensional fields[32-35] and can be adopted for the solution of three-dimensional fields[36-38].

Another method for the solution of the partial differential equations, describing the field, uses Green's function to transfer the field equations into integral equations. This method is described in references 38 - 41.

1.5 SCOPE OF WORK

The work presented in this thesis concerns investigations into the designs of a permanent-magnet generator employing a multi-stacked imbricated rotor. It also includes the analysis of the three-dimensional field of this rotor. This form of generator is capable of producing air-gap fields higher than the flux density level at the working point of the magnet. It is also suited for use with a wide range of magnets.

In this study a discrete reluctance method program has been used to design and predict the performance of the permanent-magnet generator. It has also been used to investigate the factors affecting the design of the rotor and the prediction of its performance.

A three-dimensional finite element method using scalar potential is used for the analysis of the field of the rotor which is inherently three-dimensional. It is used to chart the direction of the flux paths to study the effect of changes in the geometry on the field distribution of the flux guide, leakage fields and air-gap flux waveform of the rotor. This analysis is then used to check the assumptions and the approximations for the flux paths in the discrete reluctance method. The finite element method is also employed to predict the performance of the generator as well as the waveform of its output.

The experimental work involves the determination of the terminal characteristics of the prototypes designed using the discrete reluctance method program and the extraction of the air-gap flux waveform by means

of search coils for analysis.

The air-gap flux waveforms from the prototypes and those predicted by the finite element method program are analysed to determine the presence and magnitude of the harmonic components.

The predictions from the discrete reluctance method program and those from the analysis using the three-dimensional finite element method are compared with the experimental results. This comparison, together with the investigation conducted on the rotor and its field distribution, are used to propose an optimal configuration for the multi-stacked imbricated rotor used in the permanent-magnet generator.

In addition to the work on permanent-magnet generators, this thesis also contains an investigation into the behaviour of a permanent-magnet material under the influence of external crossfields. In permanent magnets, particularly those which exhibit a high degree of anisotropy, the magnetic polarisation is aligned in certain preferred directions due to the phenomenon called magnetocrystalline anisotropy and manufacturing processes which encompass shape anisotropy and stress anisotropy. Permanent magnets have their B-H relationship in this preferred direction declared. However, in computational analysis of permanent-magnet fields, a vector representation of field variables is needed. Consequently, magnet characteristics in the directions other than the preferred direction of magnetisation have to be determined. The presence of the high degree of anisotropy in modern magnets results in B-H relationships in the non-preferred directions which are radically different from the normal demagnetisation curve. This problem is treated experimentally in a study conducted on a piece of polymer-bonded rare-earth permanent magnet. Its behaviour under the influence of fields perpendicular to its preferred direction of

magentisation is investigated. The study concludes with the proposal of a new model for the representation of permanent magnets for computational purposes. This new model is implemented in a two-dimensional finite-element field analysis program.

1.6 STRUCTURE OF THE THESIS

In Chapter 2, the design and configuration of the new imbricated rotor is described. This is followed by a description of the permanent-magnet materials, their properties both physical and magnetic and a discussion on how their properties affect the design and the use of this form of permanent-magnet generator. A brief review of the two methods of field analysis of the imbricated rotor is also given.

Chapter 3 is concerned with the experimental results obtained from the prototypes built. A comparison is done between the experimental results and the results computed using a discrete reluctance method. An analysis is also done on the air-gap flux waveform. A brief discussion on these results concludes this chapter.

In Chapter 4, the discrete reluctance method of field analysis, is described. Its implementation for the analysis of the imbricated rotor is also described. This is followed by a discussion in depth on its limitations as applied to this problem.

Chapter 5 is concerned with the analysis of the field of the imbricated rotor using a three-dimenisonal finite element technique. The formulation and discretisation of the problem are discussed, followed by a brief comment on the method.

The results obtained from the analysis of the field of the imbricated rotor using the method described in Chapter 5 are discussed in Chapter 6. These results include the flux distribution in the flux guide, the leakage fields and the air-gap fields. The effects of the changes in geometry of the flux guide on the field distribution, the

leakage fields and the air-gap field waveform of the rotor, are also discussed. The prediction of the generator terminal characteristic and its output waveform is also described.

In Chapter 7, a comparison is performed on the results computed by the discrete reluctance method program, the three-dimensional finite element program and the experimental results obtained from the prototypes. This comparison includes both the terminal characteristic and the harmonic content of the air-gap flux waveform. Following this comparison is a discussion of the merits of each method of field analysis.

In Chapter 8, the optimal configuration for the imbricated rotor of the multi-stacked permanent-magnet generator, based on the basic shape of the present flux guide, is proposed. The influence of the results of Chapters 3, 5 and 7 in the determination of this configuration is discussed. The effect of a change in magnet material used on the design is also described.

In Chapter 9 the experimental investigation of the behaviour of a polymer-bonded rare-earth magnet under excitation in two directions at right angles is described. The results from the experiments are analysed and a new model for the representation of this permanent magnet is proposed and implemented in a two-dimensional finite-element program.

Finally, in Chapter 10, the results of all the analyses and conclusions are drawn together, and suggestions made for future research.

1.7 REFERENCES

1. SAUNDERS, R. M. and WEAKLY, R. H. : 'Design of permanent-magnet generators', Trans. A.I.E.E., Vol. 70, Pt. II, pp. 1578-1581, 1951.

2. STRAUSS, F. : 'Synchronous machines with rotating permanent magnet fields', Trans. A.I.E.E., Vol. 71, Pt. III, 1952.

3. BRAINARD, M. W. : 'Synchronous machines with rotating permanent-magnet fields- Pt. I', Trans. A.I.E.E., Vol. 71, pp. 670-676, 1952.

4. McCAIG, M. : 'Present and future technological applications of permanent magnets', I.E.E.E., Trans., Vol. Mag.4, pp. 221-228, 1968.

5. MOLE, C. J. : 'Permanent-magnet generators', Electrical Times, Dec. 1956, pp. 893-898, 1956.

6. HARAHAN, H. R. and TOFFOLO, D. S. : 'Permanent-magnet generators - Pt. I : Theory', Trans. A.I.E.E., Vol. 76, pp 1098-1103, 1957.

7. KUMAZAWA, Y. : 'Improvements in or relating to permanent-magnet rotors for a.c. generators', U.K. Patent 1,204,844, May 1970.

8. GRATZMULLER, J, L. : 'Permanent magnet rotor for an electric machine', U.S.A. Patent 3,513,341, Sep. 1970.

9. SIEMENS : 'An electric machine having permanent magnets mounted in rotor between its pole segments', U.K. Patent 1,777,247, 1976.

10. BAILEY, L. J. and RICHTER, E. : 'Development report on a high-speed permanent-magnet generator of 200 kVA rating', Proc. of the 2nd Int. Workshop on Rare Earth Cobalt Magnets and their applications, Dayton, Ohio, 1976.

11. PETERSON, A. D. : 'The influence of magnet material selection on the configuration and performance of radial magnet permanent-magnet rotor', Proc. of the 3rd Int. Workshop on Rare Earth Cobalt Magnets and their applications, San Diego, Calif., 1978.

12. PETERSON, A. D. : 'Performance and producibility comparisons of the radial vs. transverse magnet $SmCo_5$ permanent-magnet generator configurations', Proc. of the 3rd Int. Workshop on Rare Earth Cobalt Magnets and their applications, San Diego, Calif., 1978.

13. KETHA, V. and SARIO, E. : 'On the construction of a generator magnetised by barium ferrite magnets', State Inst. Res. Rep. II (Finalnd), No. 24, pp. 1-24, 1968.

14. KNUDSON, L. I. : 'Design considerations for the optimisation of SmCo permanent magnet alternators', Proc. of the 2nd Int. Workshop on Rare-Earth Magnets and their applications', pp. 251-258, Dayton, Ohio, 1976.

15. BINNS, K. J. :'High-output stabilised permanent-magnet machine', U.K. Patent 1,437,348, 1976.

16. BINNS, K. J. and KURDALI, A. : 'Permanent-magnet a.c. generator', Proc. I.E.E., Vol. 126, No. 7, pp. 690-696, 1979.

17. BINNS, K. J. and LOW, T. S. : 'Multi-stacked permanent-magnet generators -the relationship between output and magnet characteristics', Second International Conference on Small and Special Electrical Machines, I.E.E., London, Sept. 1981.

18. BELL, D. A. : 'Permanent magnet versus electromagnet', Proc. I.E.E., Vol. 112, No. 9, pp. 1707-1712, 1965.

19. PARKER, R. J. : 'Rare-earth permanent magnets and large machines', Proc. of the 3rd Int. Workshop on Rare-Earth Magnets and their applications, San Diego, Calif., pp. 67-72, 1978.

20. BORGER, W. U. : 'Rare-earth magnets and 400 Hz aircraft power systems - an overview', Proc. of the 3rd Int. Workshop on Rare-earth Magnets and their applications, San Diego, Calif., pp. 88-109, 1978.

21. BOLTON, H. R. and NICODEMOU, V. C. : 'Operation of self excited generators for windmill operation', Proc. I.E.E., Vol. 126, No. 9, p. 815, 1979.

22. MILLNER, A. R. : 'A high-speed high-frequency permanent-magnet generator', Proc. of the 3rd Int. Workshop on Rare-Earth Cobalt Magnets and their applications, San Diego, Calif., 1978.

23. BINNS, K. J. and LLOYD, M. R. : 'A method of evaluating the starting characteristics of solid salient pole synchronous motors', Proc. I.E.E., E.P.A., Vol. 1, No. 4, 1978.

24. CARTER, F. W. : 'The magnetic field of a dynamo-electric machine', Journal of the I.E.E., Vol. 64, p. 1115, 1926.

25. BINNS, K. J. and LAWRENSON, P. J. : 'Analysis and computation of electric and magnetic field problems', Pergamon, Oxford, 1963.

26. STEVENSON, A. R. : 'Fundamental theory of flux plotting', Gen. Elect. Rev., Vol. 29, pp. 797-804, 1926.

27. HAGUE, B. : 'The principles of electromagnetism', Doror Publications, New York, 1962.

28. LIEBMANN, G. : 'Solution of partial differential equations with a resistance network analogue', British Journal of Applied Physics, Vol. 1, pp. 92-103, 1950.

29. WALSH, J. : 'Finite difference and finite element methods of approximation', Proc. Royal Soc. of London, Sr. A., Vol. 323, pp. 155-165, 1971.

30. AHAMED, S. V. and ERDELYI, E. A. : 'Flux distribution in d.c. machines on-load and overloads', I.E.E.E. Trans., Vol.PAS-85, No. 9, pp. 960-967, 1966.

31. ERDELYI, E. A. and FUCHS, E. F. : 'Non-linear magnetic field analysis of d.c. machines, Parts I, II, III', I.E.E.E. Trans., Vol. PAS-89, No. 7, pp. 1546-1572, 1970.

32. ZIENKIEWICZ, O. C. and CHEUNG, V. K. : 'Finite elements in the solution of field problems', The Engineer, Vol. 220, pp. 507-510, 1965.

33. ANDERSON, O. W. : 'Interactive solution of the finite element equation in magnetic field problems', presented at the I.E.E.E. (P.E.S.) Summer Meeting, San Francisco, Calif., July 1972.

34. SILVESTER, P. and CHARI, M. V. K. : 'Finite element solution of saturable magnetic field problems', I.E.E.E. Trans., Vol.PAS-99, No. 7, pp. 1642-1651, 1970.

35. SILVESTER, P., CABAYAN, H. S. and BROWNE, B. T. : 'Efficient techniques for finite element analysis of electric machines', I.E.E.E. Trans., Vol. PAS-92, pp. 1274-1281, 1973.

36. ARMOR, A. F. and CHARI, M. V. K. : 'Heat flow in the stator of large turbine generators by method of three-dimensional finite element - Parts I and II', I.E.E.E. Trans., Vol.PAS-85, No. 5, pp. 1648-1668, 1976.

37. SARMA, M. S. : 'Computer-aided analysis of three-dimensional electromagnetic field problems as applied to the design of electrical machinery', IE(I) Journal - EL, Vol. 54, 1974.

38. CARPENTER, C. J. : 'Comparison of alternative formulations of three-dimensional magnetic field and eddy-current problems at power frequencies', Proc. I.E.E., Vol. 124, No. 11, 1977.

39. SIMKIN, J. and TROWBRIDGE, C. W. : 'Magnetic field computed using an integral equation derived from Green's Theorems', RL-76-041, RAL, Oxon, 1976.

40. ZAKY, S. G. and ROBERTSON, S. D. T. : 'Integral equation formulation for the solution of magnetic field problems - Parts I and II', I.E.E.E. Trans., Vol. PAS-92, pp. 808-823, 1973.

41. KARMAKEV, H. C. and ROBERTSON, S. D. T. : 'An integral equation formulation for electromagnetic field analysis in electrical apparatus', I.E.E.E. Trans., Vol. PAS-92, No. 2, pp. 465-470, 1979.

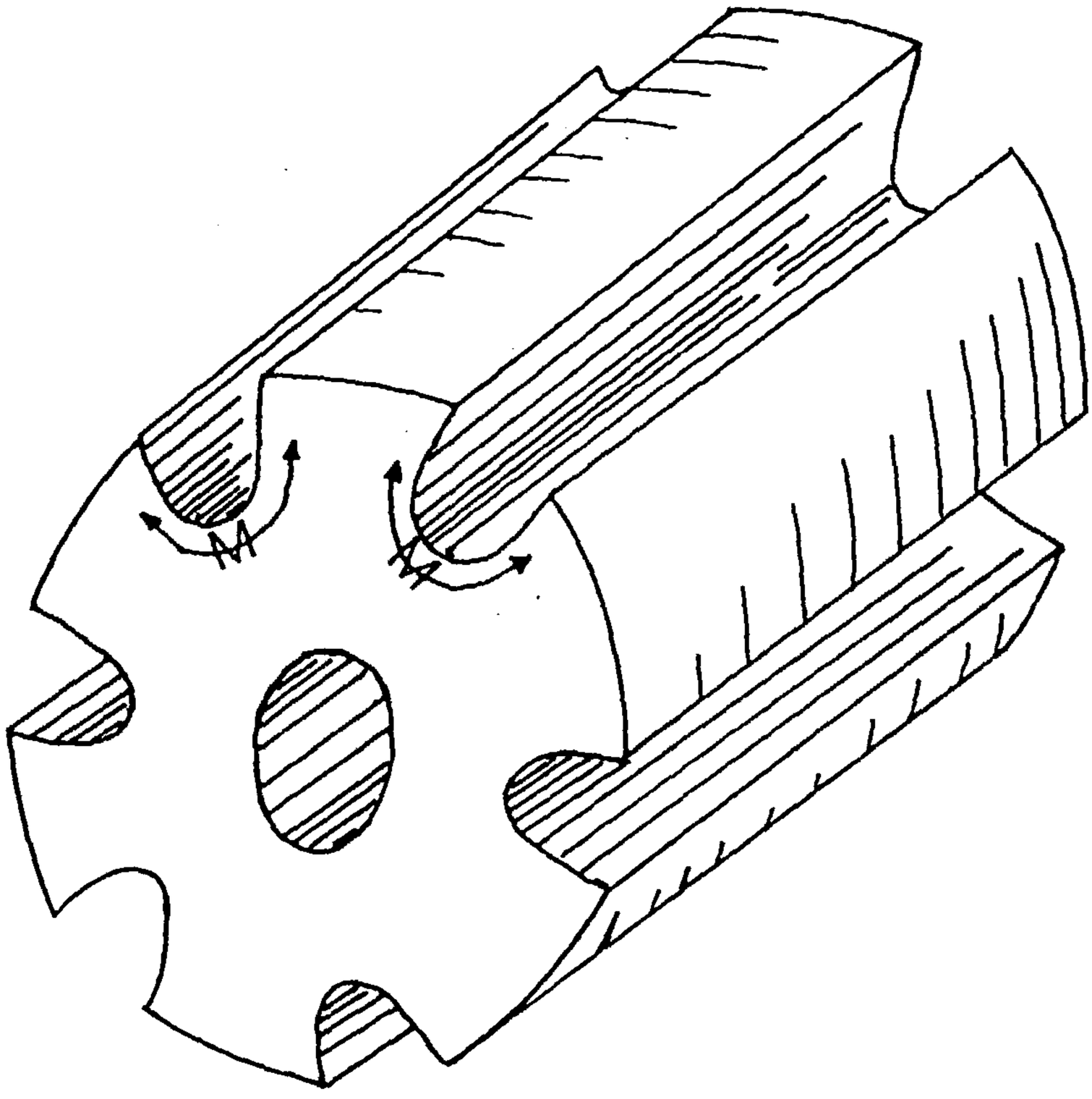

Fig. 1.1 Integrally cast magnet rotor

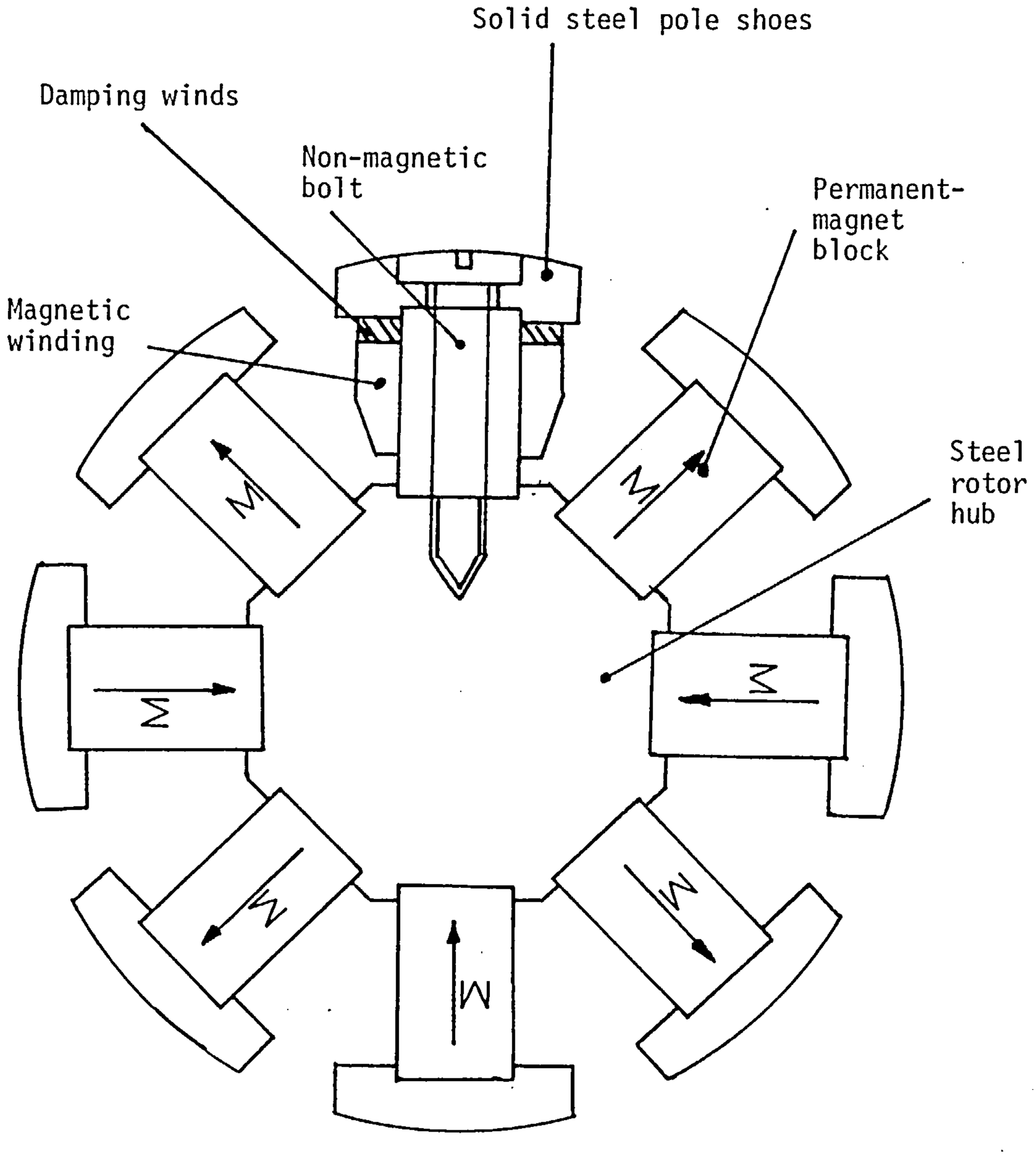

Fig. 1.2 Rotor using salient magnets and steel pole shoes.

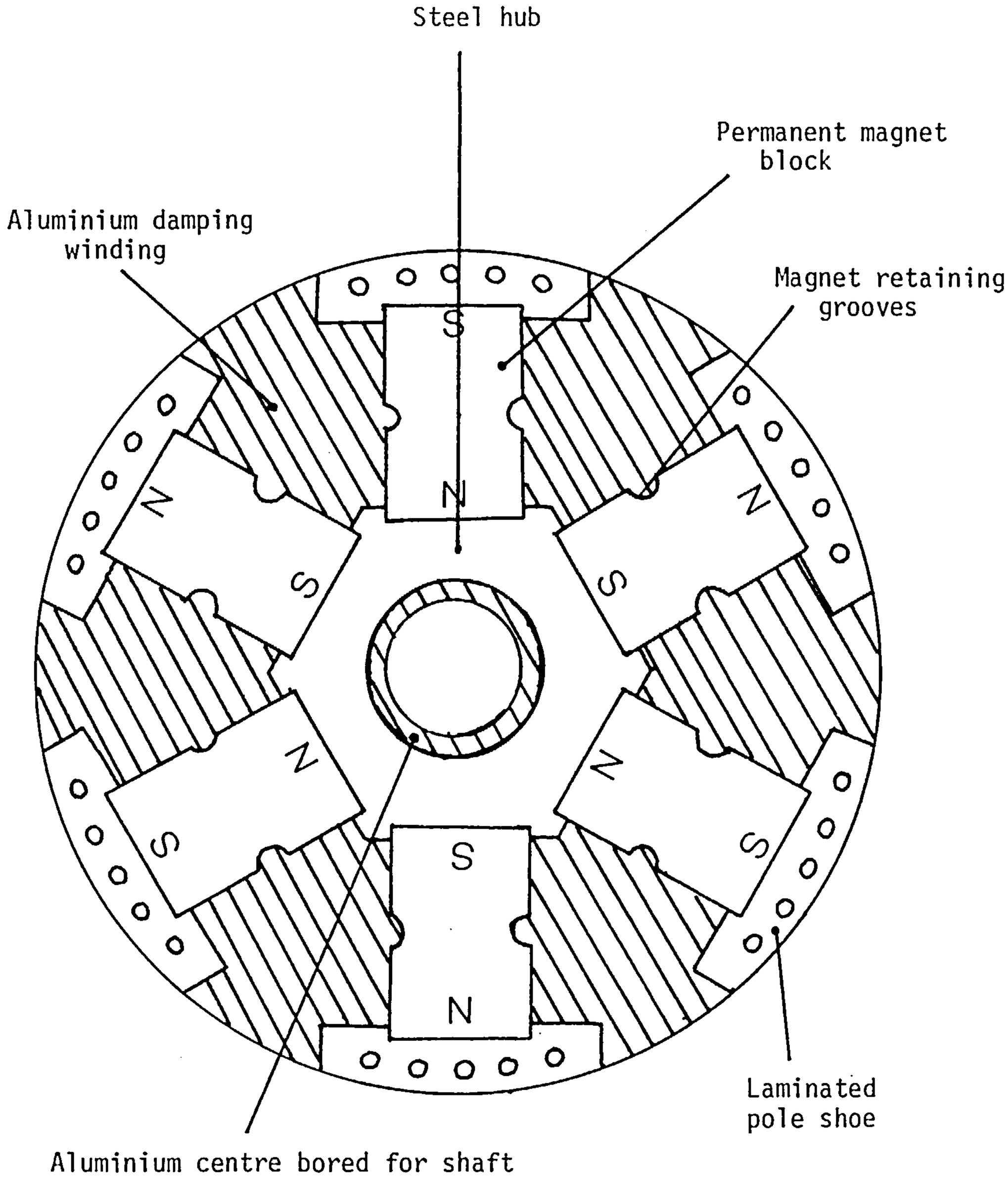

Fig. 1.3 Aluminium cast rotor

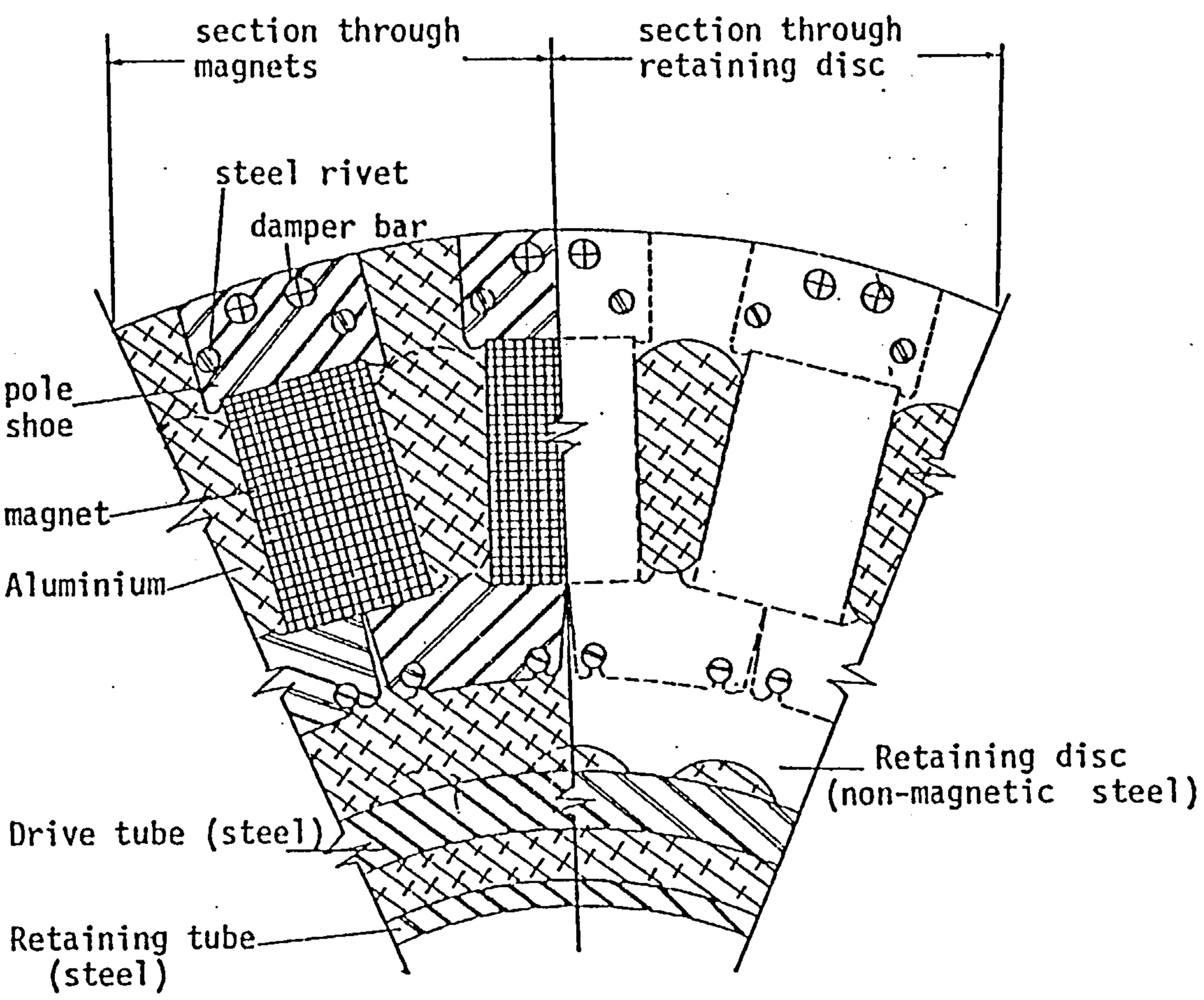

Fig. 1.4 Laminated pole shoe rotor

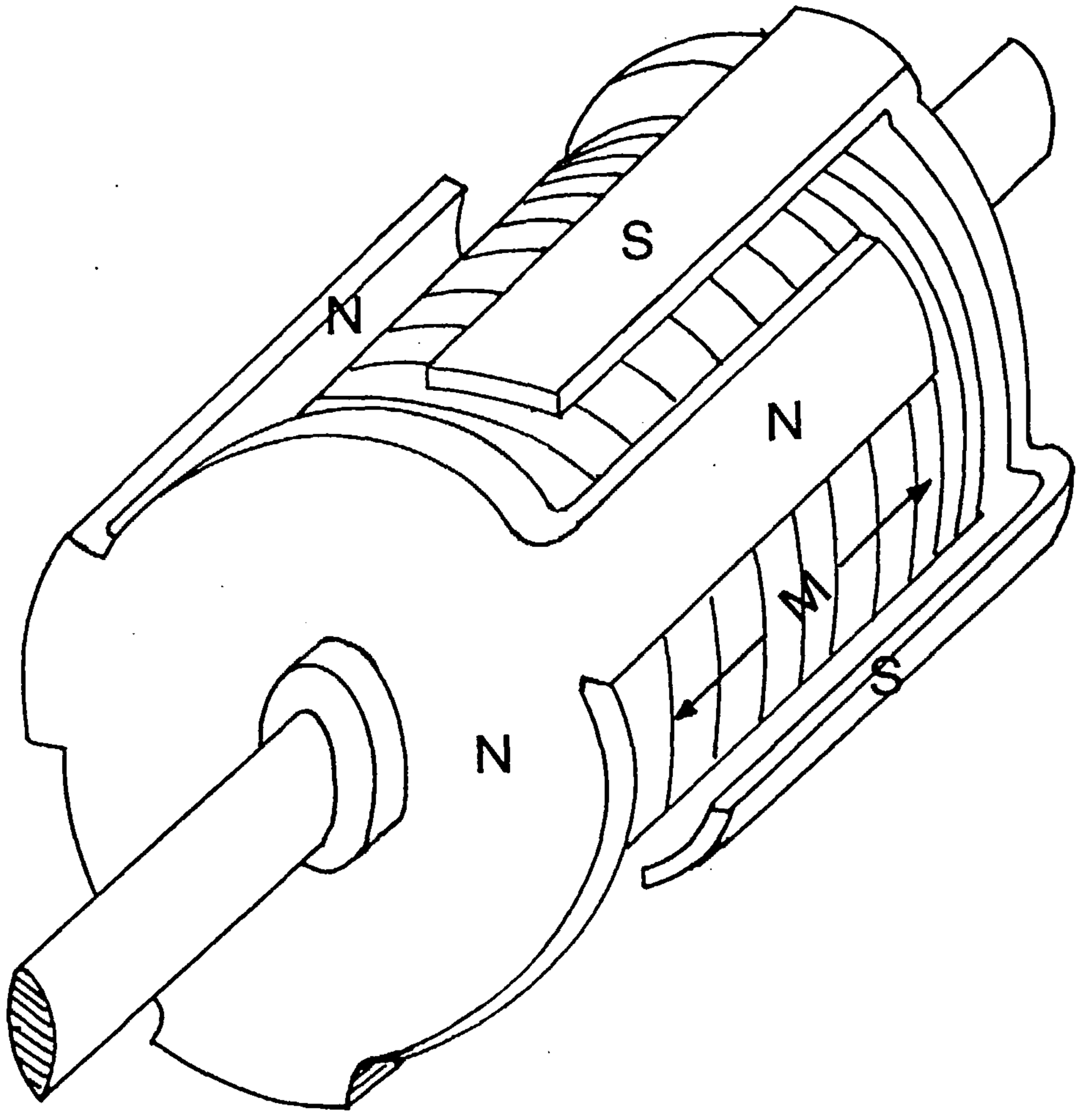

Fig. 1.5 Lundell rotor

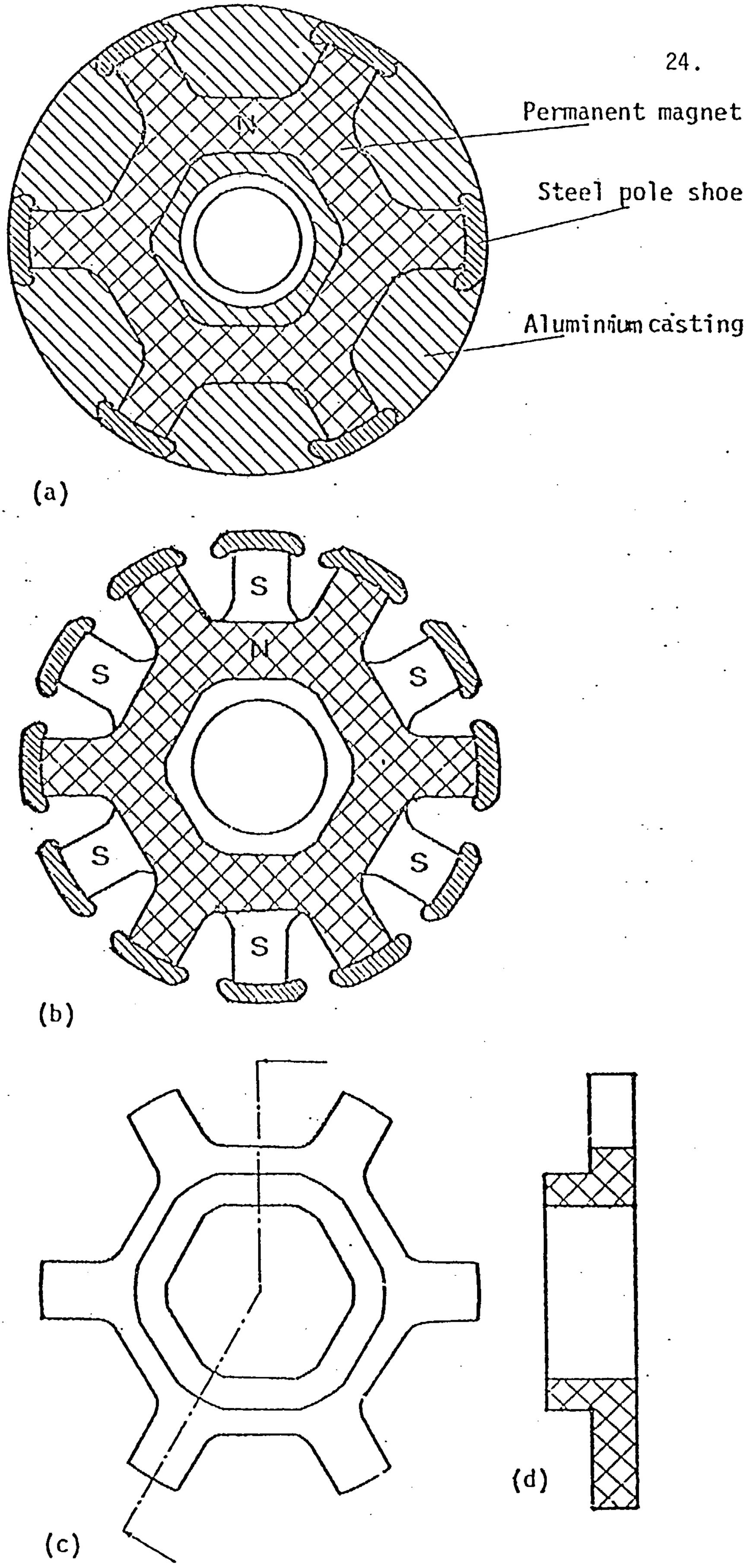

Fig. 1.6 Rotor using axially magnetised magnets

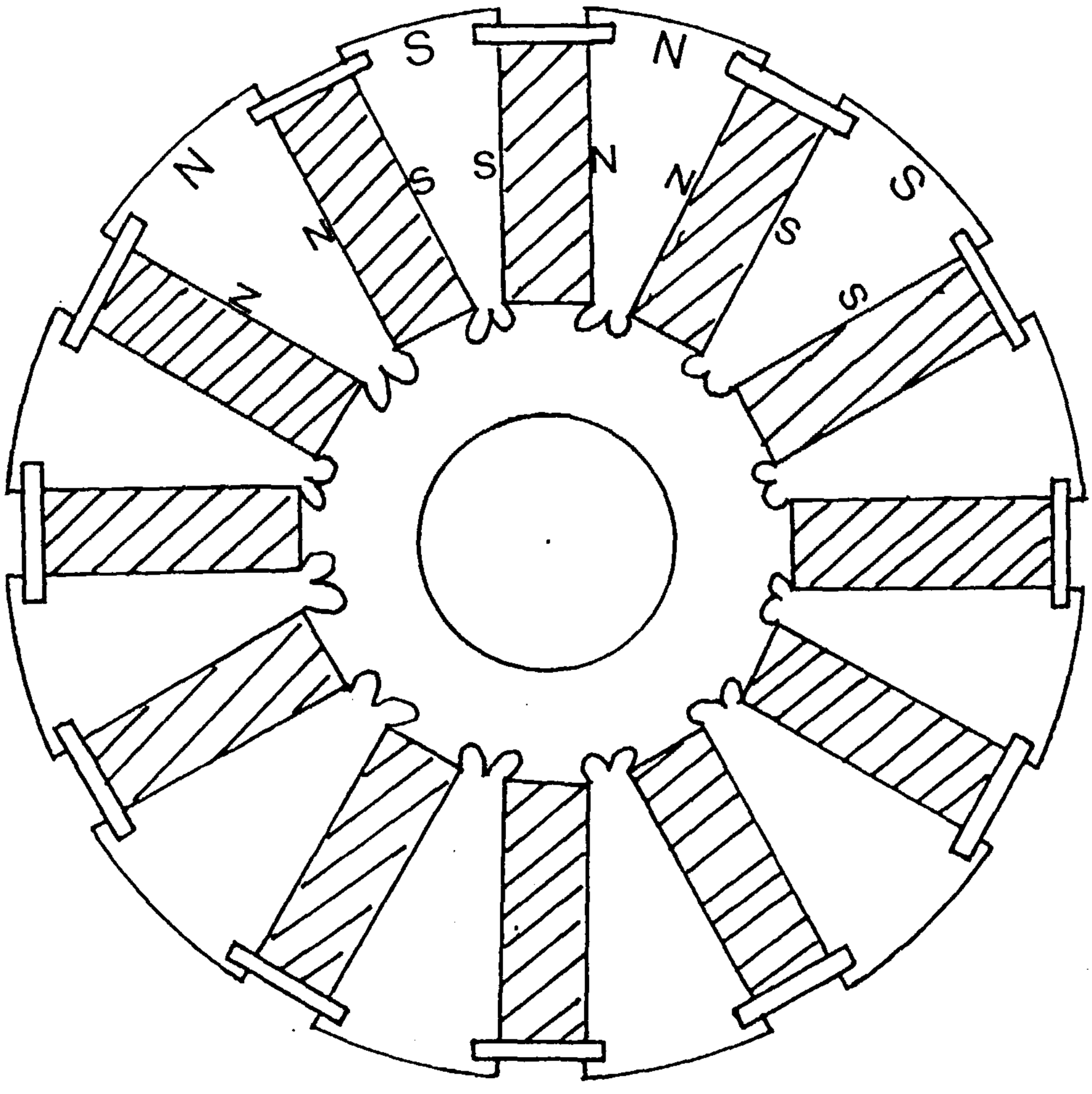

Fig. 1.7 A rotor with tangentially magnetised magnets

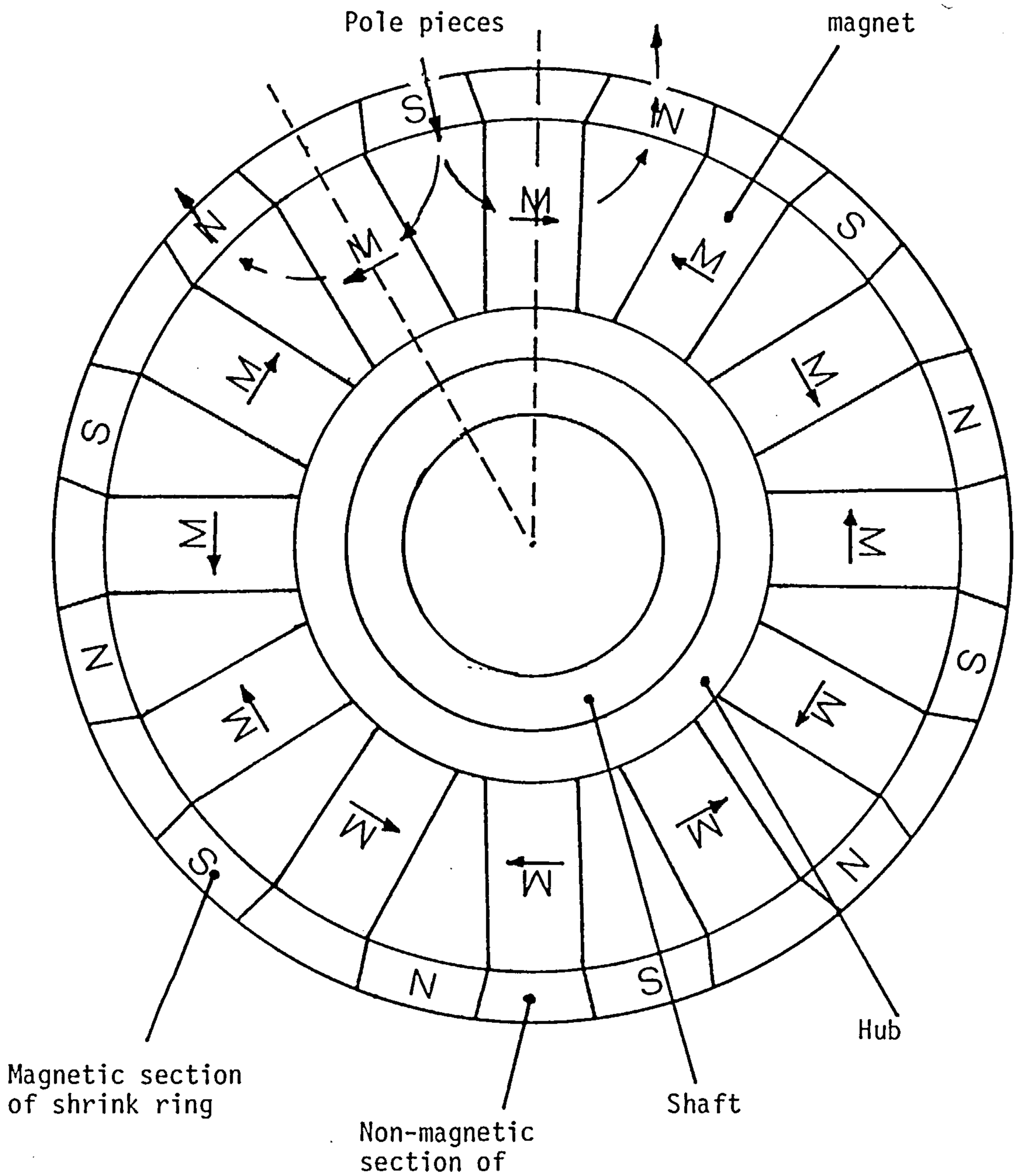

Fig. 1.8 Rotor configuration employing tangentially magnetised magnets

CHAPTER TWO

A NEW FORM OF PERMANENT-MAGNET GENERATOR

CHAPTER TWO

A NEW FORM OF PERMANENT-MAGNET GENERATOR

2.1 INTRODUCTION

The permanent-magnet generator developed at the University of Southampton[1,2,3] can use standard stators but has an unusual rotor. This rotor will be referred to in this thesis as the 'new rotor'. The new rotor uses axially magnetised magnets for excitation. This construction is ideally suited to the use of ceramic magnets and most other modern magnets, such as MnAlc and polymer-bonded rare-earth magnets, but pure rare-earth cobalt magnets can also be used to advantage. These magnet materials are characterised by high coercivity in contrast to that of anisotropic alnicos. The properties of these materials and their influence on the design of the new rotor and its applications are discussed later in section 2.4. The design of the new rotor is such that the flux density on the pole face is higher than on the magnet surface. It has been mentioned in Chapter 1 that this cannot be achieved with rotors having the radial magnet configuration but can be obtained with the tangential magnet configuration[4] if the magnets are wide enough. The imbricated rotor for this new form of generator using the axial magnet configuration is designed with the ratio of total surface area of the magnet to the rotor surface area exceeding unity and higher than any other traditional designs of permanent magnet generator. This produces a machine with a higher power density.

2.2 DESIGN AND CONFIGURATION OF THE NEW ROTOR

The new rotor derives its shape from the Lundell design. It is made up of a stack of rotor units. Each unit comprises two steel flux

guides, with an axially magnetised disc magnet sandwiched between them. Figure 2.1 shows a unit of the new machine. The three components are separated for clarity. The steel disc guides the flux radially to the poles. These poles are shaped like a trapezoid and extend like fingers from the plate which is attached to one pole face of the magnet. The trapezoidally-shaped poles are interlaced radially by the extensions from the plate attached to the other face of the magnet. This produces a unit with extensions of alternating polarity around its periphery. If these units are assembled with the direction of poalrisation of the magnet taking alternate directions up the shaft, like poles will be aligned, providing a heteropolar field at the rotor surface. Figure 2.2a shows an assembled rotor and Figure 2.2b shows an individual steel flux guide.

The final configuration of the new rotor is best determined by a search for the optimum design with the aid of a digital computer. A major part of the computer search is concerned with the shape of the rotor pole. The shape of the pole has a pronounced effect on the machine performance. It affects the amount of leakage between adjacent poles and between the poles and the steel discs of opposite polarity. The configuration of the poles also affects the shape of the flux density wave-form in the air gap. The optimum geometry has under-cutting on the poles to reduce leakage between the underside of the pole and the plate attached to the opposite face of the magnet, and side-cuttings to reduce interpolar leakage. Both these cuttings are illustrated in Figure 2.2b. It is important to note that the material removed in the under-cutting of the pole does not increase saturation because little flux is carried by the parts removed. Side-cuttings do not only reduce leakage, but also improve the air-gap flux wave-form. The thickness of the iron discs to which the poles are attached has to be optimised to

reduce excessive steel, and the steel joining the poles to discs is shaped to provide a smooth flow of flux. Figure 2.3a shows a plan view of a possible flux guide for an eight-pole generator. A cross-section of the same piece is shown in Figure 2.3b. By assembling a number of units together, a rotor is formed. The number of units and the width of each unit are other variables optimised to suit the application. Figure 2.3c shows a cross-section through the rotor axis of a four-unit machine.

The flux guides are made of mild steel whilst the rotor shaft on which the rotor units are assembled is made of non-magnetic material so as not to short-circuit the flux path through the shaft. The rotor units are located on the shaft by a key with a collar at one end of the shaft and a nut at the other end which would be threaded.

The finer points in the analysis and optimisation of this design are discussed in the following chapters.

2.3 THREE-DIMENSIONAL FIELD ANALYSIS OF THE NEW ROTOR

The design of the steel flux guide is a demanding problem in three-dimensional non-linear field analysis. The leakage flux has to be minimised for good output and the prediction of the working point of the magnet requires virtually a complete field solution for the whole machine. Non-linearities are also involved in the solution of the problem. These non-linearities are associated with iron saturation and magnet hysteresis. Thus a search is required to determine the working point of the magnet. The leakage field in the new rotor is also dependent on the magnet's working point as well as the geometry of the flux path. The geometry of this new rotor cannot be represented adequately in a two-dimensional model and can only be satisfactorily analysed with a three-dimensional model.

An analytical solution for the three-dimensional field of the new rotor is impossible due to the complicated geometry and the non-linearities involved. Instead an iterative numerical solution is required. The number of numerical methods for the solution of fields in electrical machines and those applicable for three-dimensional fields, has been reviewed in Chapter 1, section 1.4. Two methods have been successfully adopted to analyse the field of the new rotor. One uses the circuital approach and is called the discrete-reluctance method[2]. The other is a finite-element method based on field theory[5].

In the circuital method, the integral equation $\oint H \cdot d\ell = I$ is formed in many closed paths within the boundary of the problem. The integral can be formed for sufficient paths to get the required solution. The integral above is applicable to a flux tube which represents a one-dimensional field. However, for a three-dimensional field, it is possible to apply the integral to a finite number of paths, considering them as one-dimensional elements with a constant tube of flux in each. In this approach, the domain is assumed to have a discrete number of paths and thus described as the discrete-reluctance method. It is simple to implement and efficient as well as economical in computing time, which make it a useful design aid. The method and program based on it for the field analysis and performance prediction of the new rotor is described in detail in Chapter 4.

The three-dimensional finite-element method program is called TOSCA. In this method, the space occupied by the problem has got to be discretised. This method of analysis requires a large storage and considerable computing time. As a result, it is not practical and economical for this program to be used for design optimization. It is, however, more accurate. Its importance lies in its ability to monitor the changes in

field distribution due to a change in geometry, and is thus used to check the discrete-reluctance method program and to predict the harmonic content of the air-gap flux wave-form of the generator as well as for the analysis of the effect of a change in geometry on the output and the air-gap flux wave-form. The implementation and use of the three-dimensional finite-element technique for the field analysis of the new rotor is discussed in Chapter 5 and 6.

2.4 PERMANENT-MAGNET MATERIALS FOR USE IN THE NEW ROTOR

The variety of permanent-magnet materials available today for industrial applications is considerable, but only a few are suitable for incorporation in permanent-magnet machines. Figure 2.4 shows the B-H characteristics of a selection of permanent-magnet materials widely used in electrical machines. The figure also shows the curves of the B-H product of the materials. This selection includes the alnicos, the ferrites, the polymer-bonded rare-earth magnets, pure rare-earth magnets and the compound MnAlC. The first four types are used extensively in permanent-magnet machines but MnAlC is still a relatively new material. The magnetic and physical properties of an example of each class of material are listed in Table 1.

Alnicos were the traditional metallic magnets used in most permanent-magnet appliances in the'Fifties, 'Sixties and early 'Seventies. They could be isotropic or anisotropic and the latter could be divided into random grained materials and the columnar materials. They are characterised by high flux densities and low coercivities. The low coercivities of these metallic magnets demand stabilisation and keepers may be required when the rotor is outside the stator. Furthermore, if a rotor employing metallic magnets is stabilised for short-circuit conditions,

it will inevitably operate on a minor loop. For this reason, these materials are not used for this rotor. Alnicos are hard, brittle materials and are also very heavy. Their temperature stability is the best in this selection of permanent-magnet materials with a temperature coefficient of 0.005%. This is perhaps its only strong point.

Ferrites are marketed under various trade names. They are either barium or strontium ferrite. These materials are characterised by much lower flux densities, but possess higher coercivities than the metallic magnets. There are again subdivisions covering isotropic and anisotropic ferrites. These magnets, also known as ceramic magnets, possess a high specific resistance (10-100 ohm cm) and are thus unaffected by alternating fields. They are, however, highly unstable in fluctating temperature with temperature coefficients in the region of -0.2% per degree Centigrade. They are very light and are cheap. An example is Ceramic-8.

Rare-earths are the new generation of permanent-magnets. An example is Samarium Cobalt. Rare-earth magnets offer the possibility of producing stronger fields whilst possessing a very high coercive force. They are marketed under various trade names and differ in their quality according to the constituents of the composition. The maximum energy product of these magnets are very much higher than those possessed by the other materials. Samarium Cobalt has a maximum energy product of 200 KJ/m^3. They are very brittle and difficult to machine.

The replacement of part of the samarium in pure samarium cobalt magnets with lighter rare-earths called Mischmetal, which is very much less expensive, would reduce cost and if this mixture is polymer-bonded, it would render the material less brittle and consequently machineable. This process is achieved at the expense of the quality in terms of magnetic properties. An example is HERA which has a maximum energy product

of 55 KJ/m^3. This material is lighter due to the presence of the lighter rare earth with a density of 5.2 gm/c.c. It has a poor temperature coefficient, though better than the ferrites. Its use is, however, limited to low temperature applications as the polymer breaks down at temperatures exceeding 80^{o}C.

MnAlC is a relatively new development. It is a manganese, aluminium, carbon alloy. It has comparable magnetic properties with polymer-bonded rare-earth magnets, but with lower coercivity. It is a light material, but poor in temperature stability like the ferrites. It could be a very cheap material due to the mass availability of its constituents.

The design and output performance of the rotors employing the different materials in Table 1 can be expected to be different. The influence of the material can be divided into that attributed to the difference in physical properties and that due to the varied magnetic properties.

In the design of the new rotor, the magnet is sandwiched between the two flux guides; it is therefore essential for the surfaces of the magnets to be parallel and smooth. The types of material would thus affect the technique in cutting and grinding and thus the producibility. In this respect, ferrite and polymer-bonded rare-earth magnets are more desirable. The difference in densities of the materials would offset the output-to-weight ratio. However, heavier materials like the rare-earths are compensated for by higher energy stores. The temperature stability property would have to be considered critically in the light of the environment the generator is supposed to work in. It would also influence the design of the cooling system of the machine and the choice of stator laminations, as stator losses would be an important

factor with the rotor losses minimised due to the absence of excitation losses. Reversible air-gap flux losses with temperature in a permanent magnet rotor is due to the decrease in magnetisation intensity which occurs in all ferromagnetic materials, including magnets, with increasing temperature. The average reversible temperature coefficients for alnicos, ferrite and rare earths are: - 0.005, - 0.20, - 0.04 % per degree Centigrade respectively. The reversible range for these three classes of material is between -65^{o}C to 200^{o}C. Polymer-bonded rare-earth magnets have an added disadvantage in that the binding polymer disintegrates at temperatures above 80^{o}C.

The magnetic properties of the materials have a direct bearing on the terminal characteristics of the generator. The permanent-magnet is the source of excitation and as such determines the output. The power output would be directly related to the energy product of the magnet at its working point and volume of the magnet material. The flow of load current in the generator produces a demagnetising m.m.f. The very high coercivity of the rare-earth magnets permitsthem to be used without concern over demagnetisation. Ceramic magnets possess a knee which occurs at a sufficiently low permeance slope for them to be employed without stabilisation. The effects of the magnetic properties on the design and output of the new rotor is considered in detail in Chapter 8.

2.5 REFERENCES

1. BINNS, K. J. : 'High output stabilised permanent magnet machine', British Patent 1437348, November 1976.

2. KURDALI, A. : 'Analysis and the performance of a permanent-magnet alternator with disc magnets', Ph.D. Thesis, Southampton University, 1979.

3. BINNS, K. J. and KURDALI, A. : 'Permanent-magnet A.C. generator', Proc. I.E.E., Vol. 126, No. 7, p. 690, 1979.

4. RICHTER, E. : 'Rare-earth cobalt permanent magnet for electric machines of medium to large power rating', Goldschmidt, 2/79, p. 50, 1979.

5. SIMKIN, J. and TROWBRIDGE, C. W. : 'On the use of total scalar potential in the numerical solution of field problems in electromagnets', Int. Journal for Numerical Methods in Engineering, Vol. 14, pp. 423-440, 1979.

6. BOHLMANN, M. A., KOO, J. C. and WISE, J. H. : 'Mn.Al.C. for permanent magnets', Journal of Applied Physics, Vol. 52(3), March 1981.

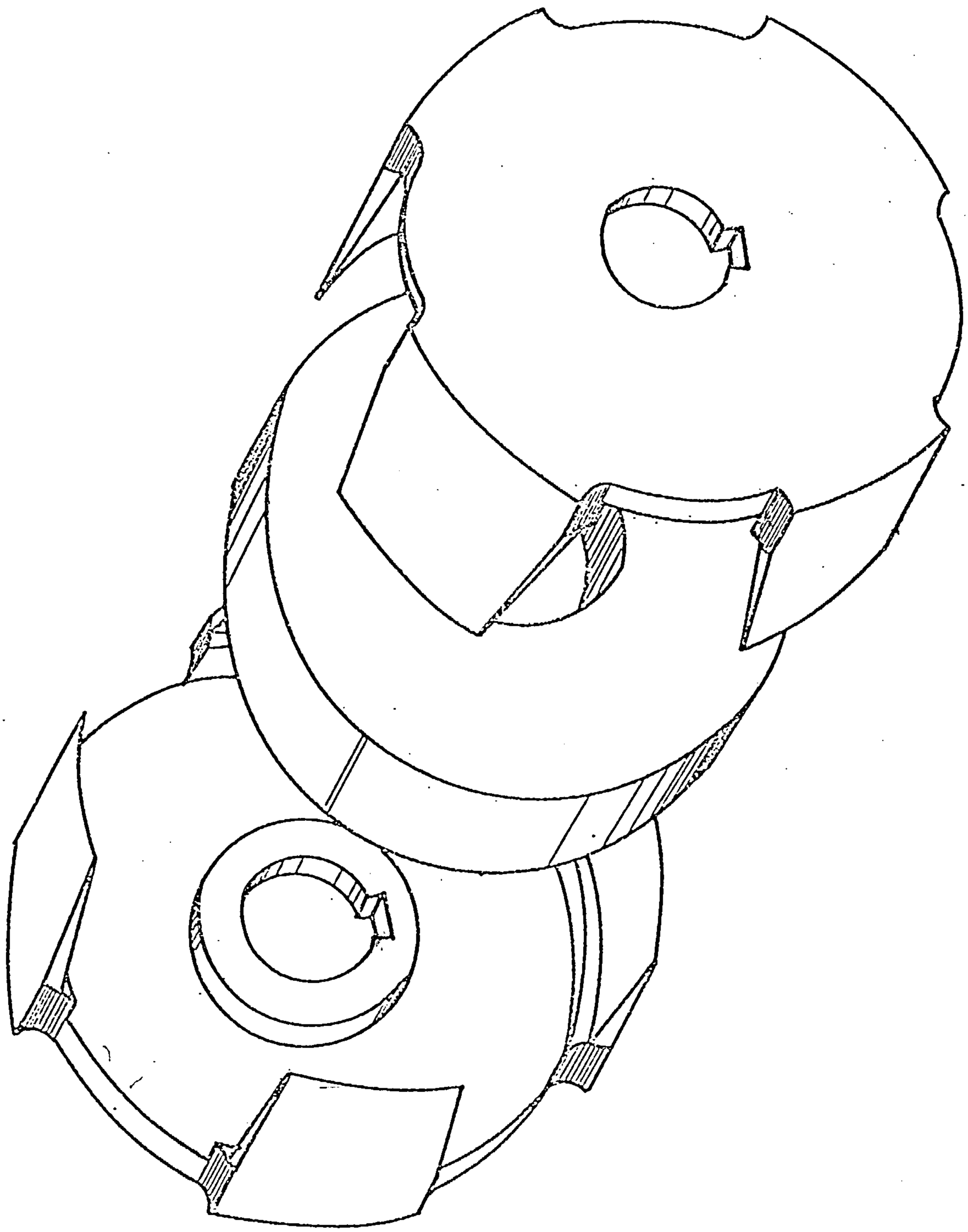

Fig. 2.1 A rotor unit

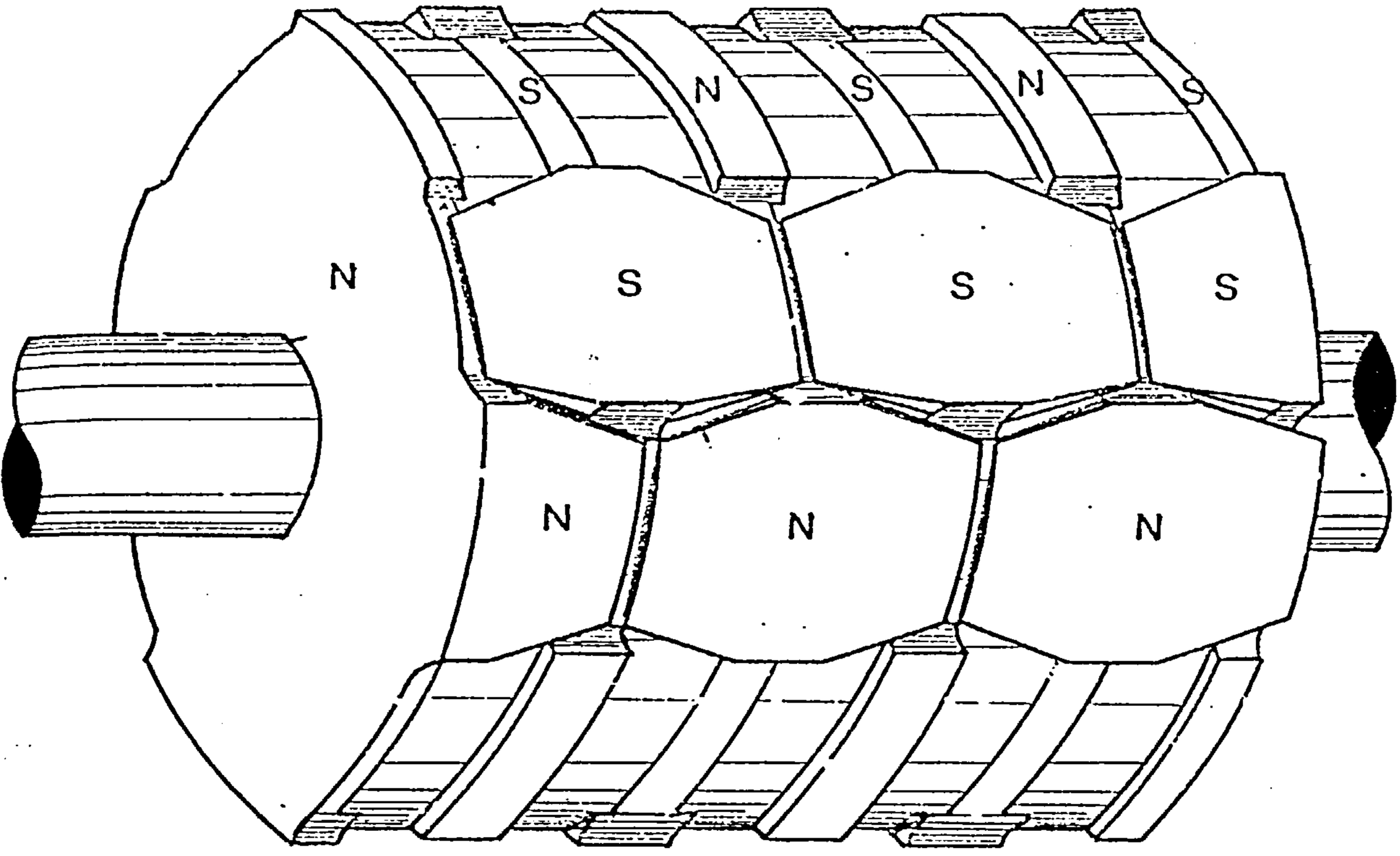

(a)

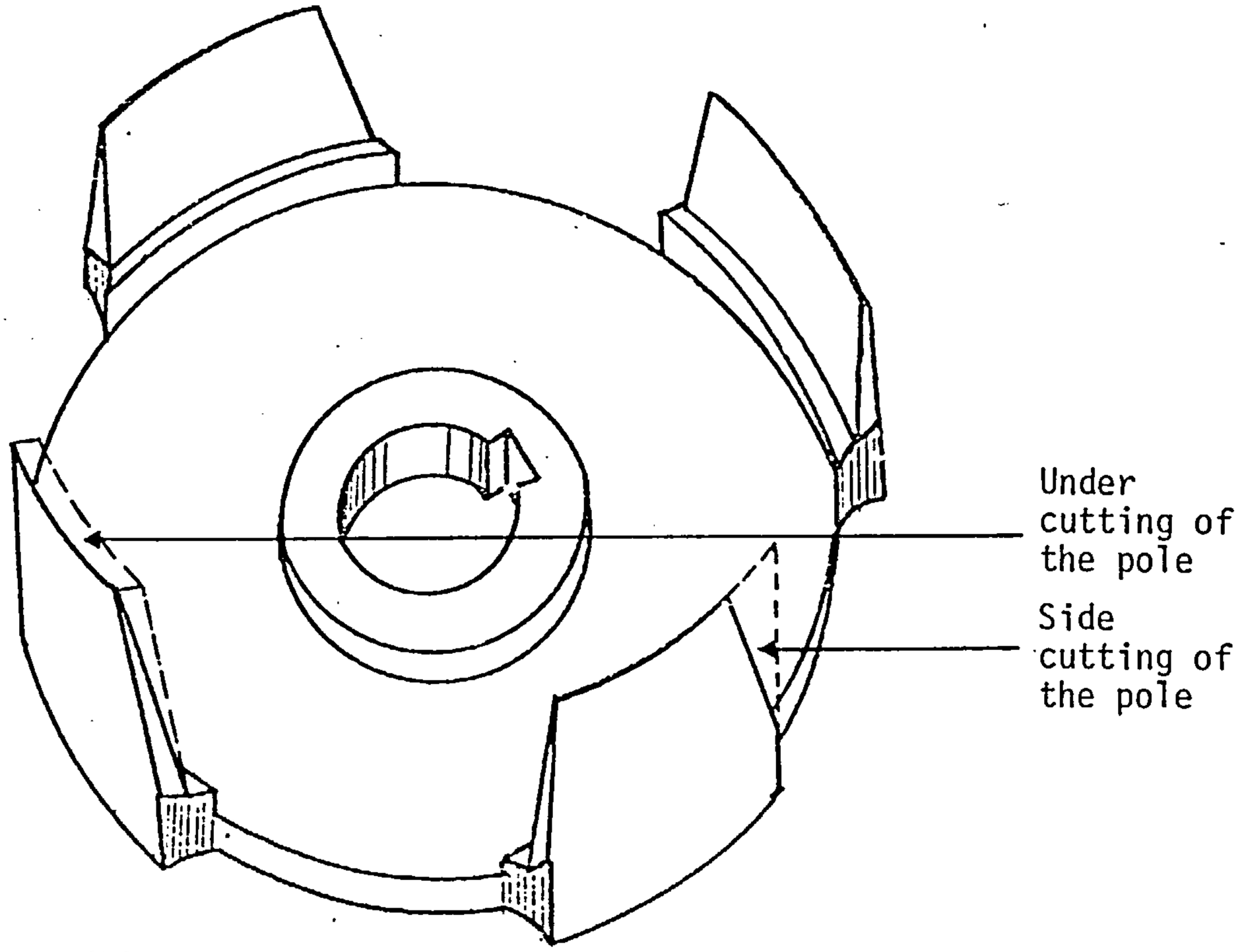

(b)

Fig. 2.2 Basic construction of the multistacked rotor

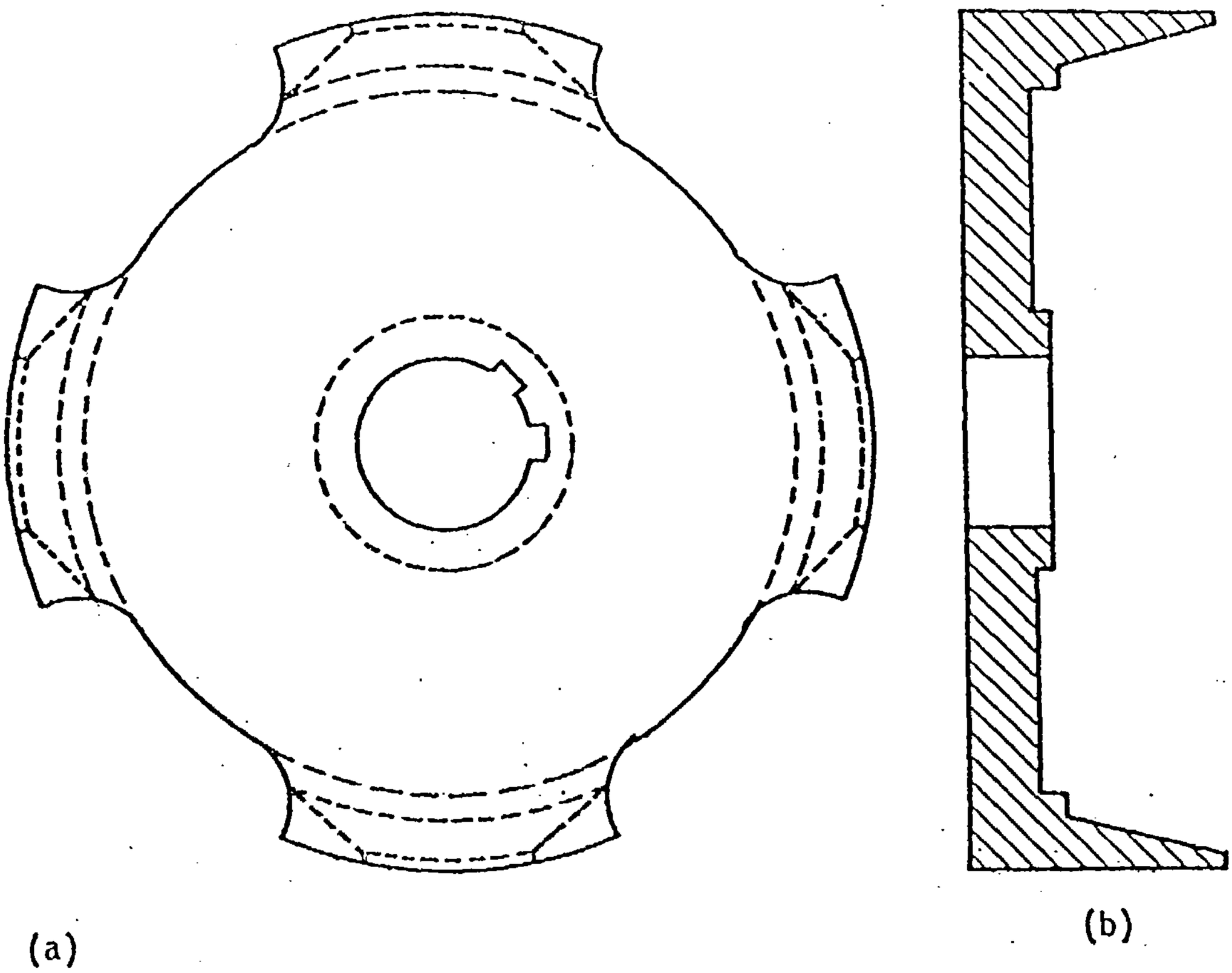

(a)

(b)

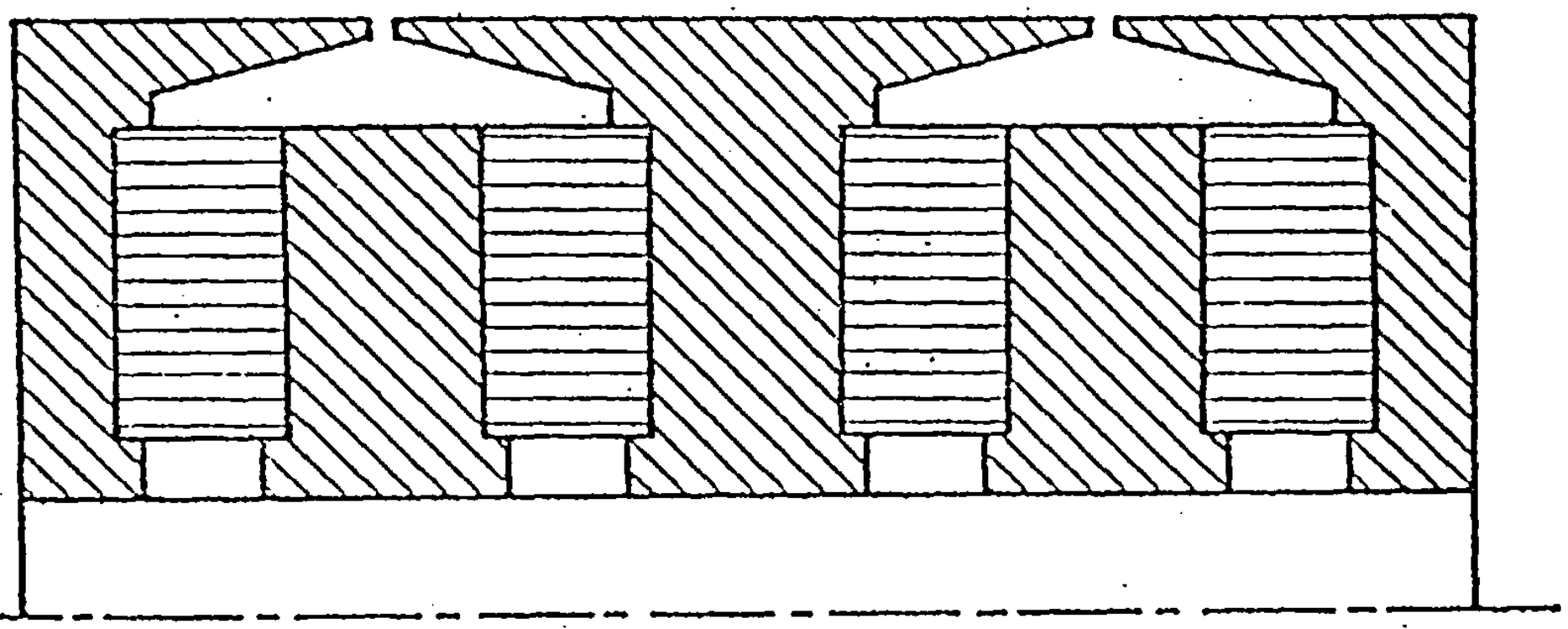

(c)

permanent magnet material

steel

Fig. 2.3

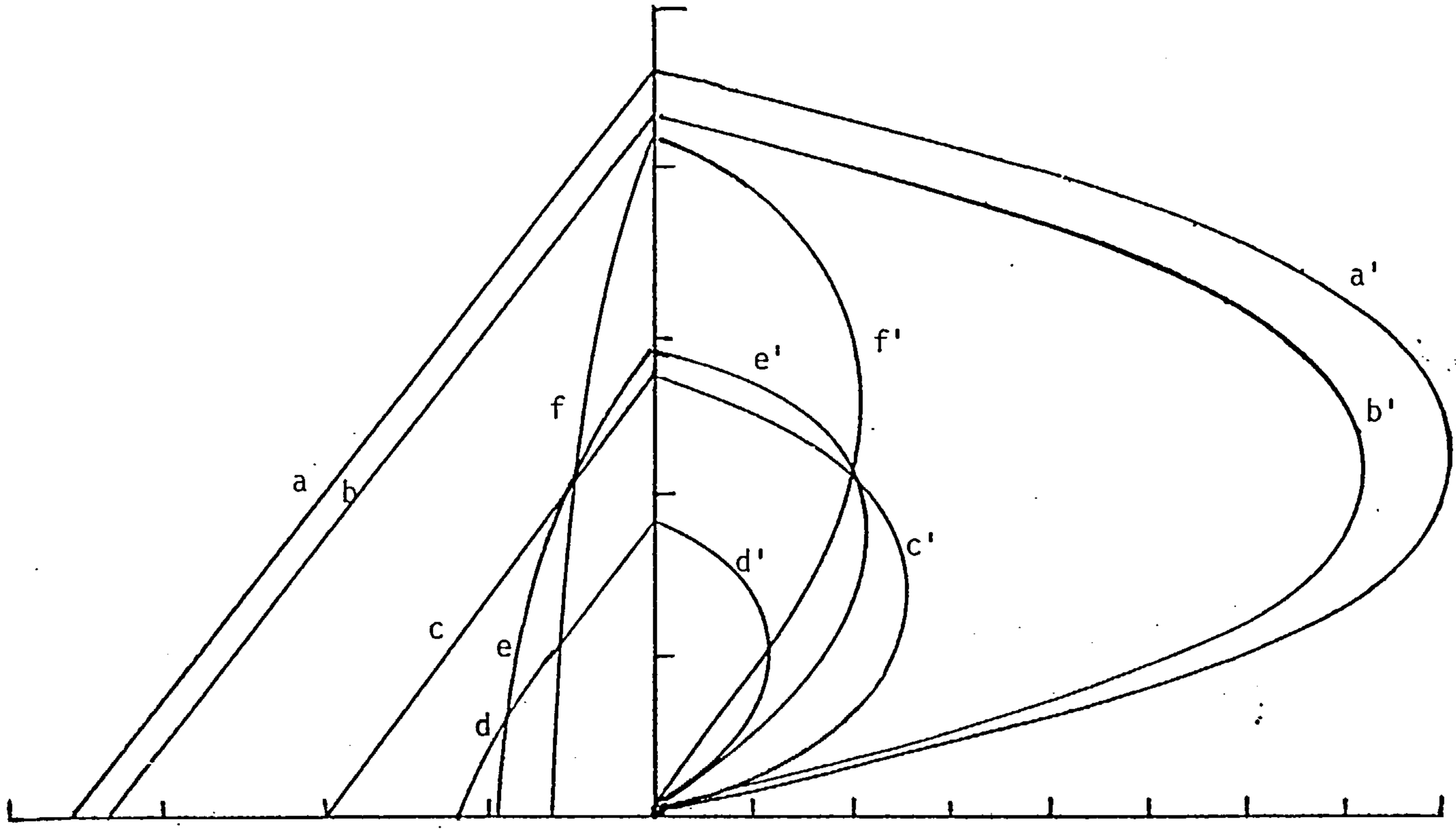

a = H22-A (rare earths)

b = H18-B

c = HERA (Polymer bonded rare earth)

d = Ceramic-8 (Barium Ferrite)

e = MnAlC

f = Alnico-8

Fig. 2.4 The B-H characteristics and (B-H) curves of for some permanent magnets

Magnet Material	Abbrev. for Material	B_R (T)	H_C (kA/m)	$(BH)_{max}$ (kJ/m^3)	Density (kg/m^3) x10^3	Max. Operating Temp. ^oC	Temp. Coeff. % per ^oC	Curie Temp. ^oC
Rare Earth H22-A	R1	0.92	705	167	8.30	250	-0.040	710
Rare Earth H18-B	R2	0.87	666	143	8.30	250	-0.040	710
Polymer-bonded Rare Earth	HE	0.55	400	55	5.20	80	-0.100	*
Ceramic-8	CE	0.37	238	26	4.90	250	-0.200	450
AlNiCo-8	AL	0.85	120	43	7.30	550	-0.005	850
MnAlC	MN	0.58	190	45	5.00	300	-0.140	350

*This material disintegrates structurally at temperatures higher than 80^{o}C as a result of the breakdown of the polymer.

Table 2.1

CHAPTER THREE

EXPERIMENTAL RESULTS

CHAPTER THREE

EXPERIMENTAL RESULTS

3.1 INTRODUCTION

Several machines were built with the aid of the discrete reluctance method described in Chapter 4 of this thesis. A computer program based on the method was used for the optimisation of the designs. Six of the prototypes built are listed in Appendix I as generators A, B, C, D, E and F. The table gives the dimensions of these machines. They vary in size and in their output characteristics since each was designed for a specific purpose and/or to suit a particular stator. Generators C, E and F were designed for specialised applications whilst generators A, B and D were optimised within the constraints imposed by the stators with which they were paired.

Generator A : This is a 1.7 Kilowatt machine designed to fit a standard stator. The nominal speed is 1500 r.p.m. The rotor has eight poles thus producing a 100 Hz output. The standard stator used and the required air gap predetermine the length of the rotor and its maximum diameter. The optimisation is thus confined to the shape of the flux guide, the shape of the pole and the number of units. The rotor for this generator has 4 units.

Generator B : This generator is a bigger version of generator A, producing 3 Kilowatts. The constraints imposed on the optimisation of this machine is exactly the same as in generator A. This generator has a rotor with 5 units.

Generator C : This is a generator designed for a particular application. It is designed to work as a welding generator. The open

circuit voltage is low, 67 volts, but sufficient to strike up the arc, and the short circuit current is high. Its requirements are such that the load characteristic of the generator drops sharply at voltages near the short circuit condition giving an operating range of voltages with the current output remaining stable. Generator C is designed to be driven by a motor at 3,000 r.p.m.

Generator D : This is a design which makes use of a standard induction machine stator. It is particularly long and is rated at 7 Kilowatts. It has 4 poles and a nominal speed of 1,500 r.p.m.

Generator E : This is another generator designed for a specific purpose. It has sixteen poles to enable the production of a reasonable output frequency when it is run at low speeds. It would produce 50 Hz at 350 r.p.m. This generator is suitable for use with windmills.

Generator F : This is a generator designed for use as a vehicle alternator, in particular heavy duty vehicles where there are many electrically motorised mechanisms, such as buses.

All these generators are designed for use with barium/strontium-ferrite magnets, sometimes known as ceramic-8 magnets.

3.2 THE TERMINAL CHARACTERISTICS OF THE GENERATOR

Experiments were conducted with the generators built to obtain their terminal characteristics for comparison with computed values and for analysis. The measurements obtained experimentally include the output voltage and current, the output power and the input power. The input power is calculated from the measurement of torque by the torque transducer, which couples the generator and the motor, and the speed.

Figure 3.1 shows the output characteristics of machine B and the efficiency curve obtained experimentally. The shape of these curves are typical of these permanent-magnet generators. The open circuit voltage is 240 volts and the maximum power output is 2.75 Kilowatts. The regulation at the peak power point is 30%. The output voltage drops fairly sharply at high loading due to the demagnetisation effects of the generated current. This pushes the working point of the magnet further down and therefore producing a lower air-gap flux density. The curve representing efficiency can be seen to be flat over a wide range of current. It is in excess of 80%. This is a desirable feature for many applications.

Experiments were also conducted for the rest of the generators in similar fashion at unity load power factor and at various load power factors. The influence of series and parallel capacitors was also studied.

3.3 COMPARISON OF PERFORMANCE PREDICTED BY THE DISCRETE RELUCTANCE METHOD PROGRAM WITH EXPERIMENTAL RESULTS

It is vital to compare the results of the predictions by the computer program with the performance of an actual machine in order to assess the reliability of the program as a design aid. This was done for machines A, B, C, D and F. Work in this respect has been done by Kurdali[1] with the generator under different load conditions as well as the effect of capacitors. A more critical comparison is discussed in this thesis for machines subjected to unity power factor loads, and the influence of capacitors is studied in more detail. The effects of load power factor is also briefly discussed. A comparison is also done for the output-speed relationship.

For the purpose of computation, only the fundamental voltages and currents are used and the contribution from the harmonics are ignored. The experimental results are values measured with moving iron instruments which take into account all the harmonic components. In the comparison both the computed and the experimental results are expressed as r.m.s. values. This introduces an inherent error in the comparison as the harmonics are neglected in the computation.

3.3.1 Comparison of results at unity power factor

Figures 3.2 and 3.6 show the comparison of the curves of output phase voltage and power output against load current for values measured, with the curves predicted by the program. The broken lines represent the experimental results. The comparisons shown in these figures are for the machines subjected to unity power factor loads. It is clear from the figures that the accuracy of the prediction differs from one machine to another. This is due to the difference in certain critical features of the designs such as the air gap which varies from 0.386 mm in generator A to 0.737 mm in generator D. The dimensions of their flux paths are also different due to the difference in the dimensions of the flux guide and the pole shape. These effects are discussed in greater detail in Chapter 4 where the limitations of the discrete reluctance method are discussed.

From these comparisons, two notable features are observed. In the region between open circuit and the point where the power output is at its maximum, the correlation is close and acceptable. However, on further loading the correlation between the computed values and those from experiments deteriorates. In this region the program is unreliable. It may be argued that most generators work within the first region described and thus would be within the region where the

predicted performance is valid, but there are applications in which the machine is required to work near to its short circuit point as in machine D or as in a car alternator, in such circumstances reliance on the program cannot be justified.

In the comparison of the power output curves, it is noted that the prediction of the maximum power output is never more than 7% in error when compared with the experimental results for the range of generators considered.

The correlation between the predicted voltage against load current characteristic and that obtained experimentally for machine A is shown in Figure 3.7. It is a graph of the difference between computed and measured voltages (V_{ex} - V_c), V_{ex} being the experimental value and V_c is the value computed, plotted against load current. This graph shows the deterioration of correlation at high loads very clearly. The variation of (V_{ex} - V_c) with load can be seen to be highly non-linear. This can be attributed to several factors whose effects vary non-linearly with the load current. These factors include those which are independent of the computational method used for the prediction of the machine's performance and those due to the program. These factors are discussed in section 4.8 of the following chapter.

Figure 3.8 is a comparison of the experimental open circuit output voltage and speed relationship with that predicted by the computer program, for generator A. On open circuit iron losses predominate. These losses are not accounted for in the prediction which shows a linear relationship. The experimental curve shows the increase in losses as speed goes up. This increase is due to a rise in friction losses with speed to a small extent but is largely due to iron losses which increase almost as a square of the frequency. The error in prediction at 1,500 r.p.m. with

the generator producing an output of 100 Hz is 0% and the error at 200 Hz is 6%.

3.4 THE EFFECT OF LOAD POWER FACTOR

The output characteristics of generators with this new rotor are clearly affected by changes in the load power factor since the armature reaction field changes its position in space relative to the rotor depending on the load power factor. This effect requires consideration in permanent magnet generators as the rotor field which is acted on by the armature reaction is uncontrollable except by complicated means. Figure 3.9 shows the terminal characteristics of machine B obtained experimentally at different load power factors. Curves a, b, c, d and e represent the terminal voltage and output for load power factors varying from 0.8 lagging to 0.8 leading. It shows that the maximum output can be increased significantly by changing the load power factor from lagging to leading. The output at 0.8 leading is about seven times that at 0.8 lagging. Another important effect is the change in regulation. The votlage drop on load varies from a relatively small value for unity power factor to poor regulation for highly lagging loads. A slightly leading power factor gives negligible voltage change over a significant range. A highly leading power factor load will result in negative regulation. Therefore, to achieve a reasonable output at an acceptable regulation, it may be necessary to compensate for load lagging power factors. A means of doing this is the incorporation of capacitors in the output circuit of the generator.

3.5 THE EFFECT OF CAPACITORS

An improvement in the output characteristics can be achieved by the use of capacitors. They can be connected in series with the load

or in parallel, see Figures 3.10.a and 3.10.b. Series capacitors improve the terminal characteristics of the permanent-magnet generator by improving the load power factor. This effect is described in the previous section. This mechanism is shown in Figure 3.11.a. Figure 3.12 shows the effects of series capacitors on generator A. The results are measured experimentally with capacitors of 100 μF and 175 μF. The broken lines in the graph represent the load characteristics with series capacitors and the full line represents the load characteristics without any capacitors in the circuit. It can be seen that the 100 μF capacitors have negligible effect on the output of the generator, however, with the capacitors valued at 175 μF a significant improvement can be noticed. The need for such large capacitors to achieve an improvement is impractical and uneconomical.

Parallel capacitors improve the output by supplying capacitance currents which assist the rotor field. This process is described by the circuit in Figure 3.10.b and the phasor diagram in 3.11.b. The improvements in the output characteristics of generator A with the use of parallel capacitors are shown in Figures 3.13 and 3.14. In Figure 3.13 the generator line voltage as a function of load current with parallel capacitors of 8 μF, 20 μF and 30 μF are compared with the curve for the generator loaded with pure resistive loads. Figure 3.14 is a comparison of the output power curves of the generator with and without parallel capacitors. The comparisons show that with parallel capacitors of 8 μF, 20 μF and 30 μF the increase in maximum output power is 11%, 35% and 54% respectively. The regulation improves at low currents but increases at high currents. This effect is more pronounced with an increase in the value of capacitance. The capacitance current produced by the capacitors is proportional to the

terminal voltage and not the load current. This is shown by the circuit in Figure 3.11.b and the phasor diagram in Figure 3.11.b. This capacitive current produces a field almost in phase with the rotor field of the permanent magnet generator resulting in an improvement in output. As the effect is voltage dependent, the improvement fades at high loads. This voltage dependency thus causes the use of parallel capacitors to be ineffective for generators C and F whose open circuit voltages are 67 volts and 33 volts respectively. Experimental work has shown this to be true. However, parallel capacitors remain an effective means of controlling the output and the regulation of permanent-magnet generators using the new rotor, if its terminal voltage is significantly high.

3.6 THE HARMONIC ANALYSIS OF THE AIR-GAP FLUX WAVEFORM

3.6.1 The harmonic components in the air-gap flux waveform

The air-gap flux density waveform in the permanent-magnet generator is a non-sinusoid. Its flux distribution consists of space harmonics which are attributable to the construction of the machine. Their magnitude and harmonic order depend on the stator structure, the winding configuration and the rotor geometry. The most important space harmonic components of the flux are,

(i) the fundamental or the main flux,

(ii) the phase belt harmonic components due to the winding being distributed in phase belts,

(iii) the rotor harmonics which are due to the rotor field, and

(iv) slot harmonics which are due to the windings being distributed in discrete slots.

The mmf harmonics produced by the stator windings are a result of the flow of load currents. This family of harmonics should not contain

even or triplen harmonics. The absence of even harmonics is due to the symmetry of the armature mmf wave over a double pole pitch. Triplen harmonics cannot exist if a three phase machine is considered as their 120^{o} symmetry prohibits such order. Therefore, in a three phase generator the harmonic components contributed by the stator windings are of the order m where m is 5, 7, 11, 13, 17, 19, ...

The first order slot harmonics are of the order $(2S \pm 1)$ where S is the number of slots per pole. This pair of harmonics has winding factors equal to those of the fundamental wave. They are considerable in magnitude as they nearly fit the steps in the mmf which occur at each slot.

The rotor field waveform is dictated by the configuration of the pole face of the rotor flux guides. Figure 3.15 shows an example of a flux waveform due to the rotor only. The departure from the desired sinusoidal waveform results in the preponderance of rotor harmonics in the air-gap flux wave. In this waveform all even harmonics are absent due to symmetry and only the odd harmonics are present.

3.6.2 Harmonic effects

The presence of harmonics in the air-gap flux wave has two adverse effects. The first is the production of a distorted voltage waveform and secondly, the increase in losses in the machines which reduces the efficiency.

The voltage waveform of the output produced may be important in certain applications. In such circumstances, a distorted waveform would be undesirable. Rectification of the a.c. output would eliminate the problem.

Losses due to harmonics are usually termed as stray losses. A component of these stray losses is pole face losses due to the stator

mmf harmonics. This is caused by the relative motion of the stator mmf harmonics and the rotor surface. Slot harmonics have the same effect. Another component of stray losses is the short circuit iron losses. On short circuit the percentage of harmonic content is large as certain harmonics produced by the rotor are not produced by the stator. This effect is most prominent in salient pole machines, like the permanent-magnet generator, where saliency leads to a large third harmonic. The harmonics also give rise to open circuit stator core losses. These losses could be reduced by improving the quality of the core laminations and by segmental core construction. Further reduction can be achieved by avoiding flux harmonics.

Harmonic effects cannot be neglected. A knowledge of the extent of harmonic distortion of the air-gap flux waveform and its relation to the design of the rotor is important. The harmonic analysis of the flux waveform of the permanent magnet generator employing the new rotor had been briefly discussed by Binns and Kurdali[2]. Their results show a significant presence of harmonics in the flux waveforms of these generators. The third and the fifth harmonics were most prominent.

3.6.3 Further investigation on the air-gap flux harmonics of the permanent magnet generator

A comprehensive analysis is done on the flux waveform of generator A obtained experimentally. This would compliment the analysis of the air-gap field using a three-diemnsional finite element technique to investigate the relationship between the production of the flux harmonics and the rotor design which is described in Chapter 6. The analysis is performed on the signals obtained from the terminals. The expression for the emf induced in a coil is

$E = -\frac{d\phi}{dt} N$, where N is the number of turns in the coil. The

voltage waveform and the flux waveform are therefore identical in shape but shifted by 90^{o}. Analysis of the output voltage would therefore yield information about the air-gap flux waveform. The output voltage waveforms are obtained with generator A loaded with a pure resistive load at intervals from open circuit to short circuit. Figure.3.16 shows a block diagram of the scheme of the experiment. The generated voltage waveforms of the generator is first reduced to an acceptable level with a potentiometer and tape recorded. The signals are then filtered to eliminate any high frequency noise. The waveforms in the form of analogue signals are acquired by a data analysis computer to be analysed. At each step an oscilloscope is used to monitor the signals.

The computer used for the analysis of the signals recorded is a PDP 11/75. The routines used to perform the Fourier Analysis, the modulus and phase analysis and the power-spectrum analysis are available with the computer.

3.6.4 The modulus and phase analysis of the voltage waveform

This analysis is performed with program A which is listed in Appendix II. The signal is first processed with a fast-Fourier transform algorithm. The modulus and phase is then computed from the output. This analysis gives the spectrum of the voltage waveform. The harmonics present are revealed together with their magnitudes. The harmonics extracted are calculated as a percentage of the fundamental and plotted against the load current.

Figure 3.17.a shows the signal from generator A on no load and Figure 3.18.a is one on load. Figures 3.17.b and 3.18.b are their respective spectra. They show the presence of all the odd harmonics. The third harmonic is the dominant harmonic, however, the fifth, seventh and the ninth are also measurable. Higher order harmonics can be neglected as their magnitudes are small. Curve (a) from

Figure 3.19 shows the influence of load on the percentage content of the third harmonic in the generated output. The percentage drops with increasing load very gradually from 20% on open circuit condition to 17.5% with a load current of 2 amps. Beyond this point the percentage content of the third harmonic rises very sharply. At the peak power point with the generator supplying 6 amps, the percentage content of the third harmonic is in excess of 50%. This characteristic occurs because at small loads the load angle is small which leads to the armature mmf being almost cross magnetising. As such, it has very little effect on the rotor fundamental. When load increases, the phase of the stator fundamental shifts, due to the increase in the load angle, to oppose that of the rotor. This gives the regulation characteristic of the generator. The third harmonic produced by the rotor has no counterpart produced by the stator windings to oppose it. However, third harmonics could be produced by uneven loading of the three phases. This could explain the slight drop in the percentage harmonic of third harmonic in the flux wave at loads between 0 amps and 2 amps. This third harmonic opposing the rotor third harmonic is small, as such when the load increases causing the fundamental to drop steeply, the third harmonic drops gradually resulting in a fast rising percentage of the third harmonic component. The occurence of saturation in the iron regions of the magnetic circuit produces third harmonic components which increases the percentage of the third harmonic component. further. These effects account for the shape of curve (a) in Figure 3.19.

The 5th, 7th and the 9th harmonics behave in similar fashion. However, there is a difference in the case of the 5th and the 7th harmonics as they are both produced by the stator windings. This

results in a moderation in the rise of the percentage content of these two harmonics as the generator is loaded. At small loads the harmonics from the rotor dominates while at high loads the stator mmf harmonics take over. The ninth harmonic is a triplen harmonic like the third harmonic. It is not produced by the stator field but associated with the rotor field and the saturation of the rotor iron. As the magnitude of 9th harmonic is small, the absence of the opposing stator harmonic is insignificant. The behaviour of the 5th harmonic is shown in curve (b) in Figure 3.19 and the characteristics of the 7th and the 9th harmonics as a percentage of the fundamental are shown in Figure 3.20.

3.6.5 The power-spectrum analysis of the voltage waveform

Program B in Appendix II is a power-spectrum analysis program. It is used to investigate harmonic power losses. The power density spectrum can be expressed in the following manner:

$$S_{xx}(f) = \lim_{t \to \infty} E\left[\frac{|X_{(f)}|^2}{T}\right] \qquad (3.1)$$

where E is the averaging function, T is the time and $X_{(f)}$ the signal. The signal is the voltage waveform V(t), therefore,

$$S_{xx} \alpha V(t)^2 \qquad (3.2)$$

In general the total harmonic losses can be expressed as

$$P_L = \sum_n V_{pn} I_{pn} \cos\phi_n \qquad (3.3)$$

and for a resistive load,

$$P_L = \sum_n V_{pn} I_{pn} = \sum_n \frac{V_{pn}^2}{R_L} \qquad (3.4)$$

where R_L is the resistive load.

The power density spectrum and the losses are both proportional to the square of the voltage. The spectrum would therefore give the relative power dissipated by each harmonic. Figure 3.21 shows a typical power spectrum of a voltage waveform generated by the generator A. The value of the peaks of the spectrum gives the average power associated with a bandwidth of 1 Hz centred at that frequency. Figure 3.22 shows the variation of $(V_3)^2$ as a percentage of $(V_1)^2$ as the load changes. The percentage of 3^{rd} harmonic power losses from circuit condition to a loading of 6 amp, which is the peak power condition, is 5% or less, but beyond this load the percentage rises very rapidly.

3.7 DISCUSSION

The discrete reluctance method program as shown by the experimental results and the comparison of these results with the corresponding computed values, is not entirely satisfactory. Its limitations are such that for certain conditions its prediction is unreliable. However, it is a simple and efficient program and would serve as a fair guide for design purposes.

One of the limitations of the program lies in the inefficiency in handling harmonics. It is not a practicable computational method for considering harmonic effects. The effects of harmonics have therefore been omitted from the program. In this respect, the computer program can be improved by incorporating a mechanism which would take the harmonics into consideration. However, it is not feasible for the program, even after the improvement to optimise a design which would generate voltages with minimal harmonic distortion nor would it be able to predict the harmonic content.

The harmonic distortion of the air-gap field is due predominantly to the pole profile. To optimise a design for the pole face is a

demanding problem in three-dimensional field analysis. In changing the configuration of the pole face, the leakage flux paths would change accordingly and their effects must be monitored. Research in this area is facilitated by the use of the finite-element method for field analysis. This is discussed in Chapters 5 and 6.

3.8 REFERENCES

1. KURDALI, A. : 'Analysis and the performance of a permanent-magnet alternator with disc magnets', Ph.D. Thesis, Southampton University, 1979.

2. BINNS, K. J. and KURDALI, A. : 'Permanent magnet a.c. generator', Proc. I.E.E., Vol. 126, No. 7, p. 690, July 1979.

3. I.S.V.R., Southampton University : 'Description of available programs in the PDP 11/75 - Sections 1, 2, 3 and 4.' Data Analysis Centre, I.S.V.R., Southampton University.

4. CHALMERS, B. J. : 'Electromagnetic problems of A.C. machines', Chapman and Hall, 1965.

(a) voltage
(b) power output
(c) efficiency

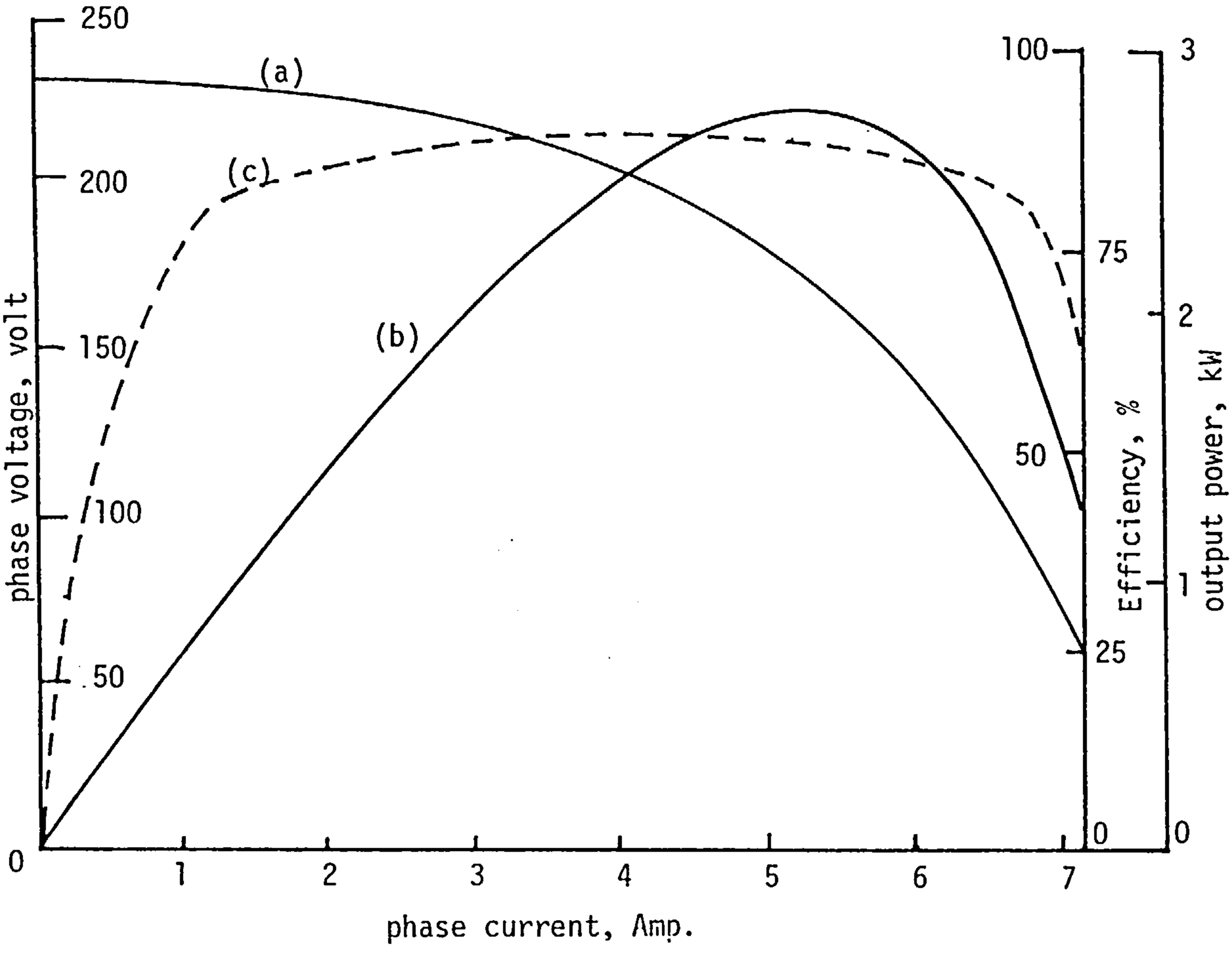

Fig. 3.1 The output characteristic of generator B found experimentally.

——————— predicted results {(a) for voltage and (b) for power output}

– – – –o– – – – measured voltage

– – –· x – – – – measured power output

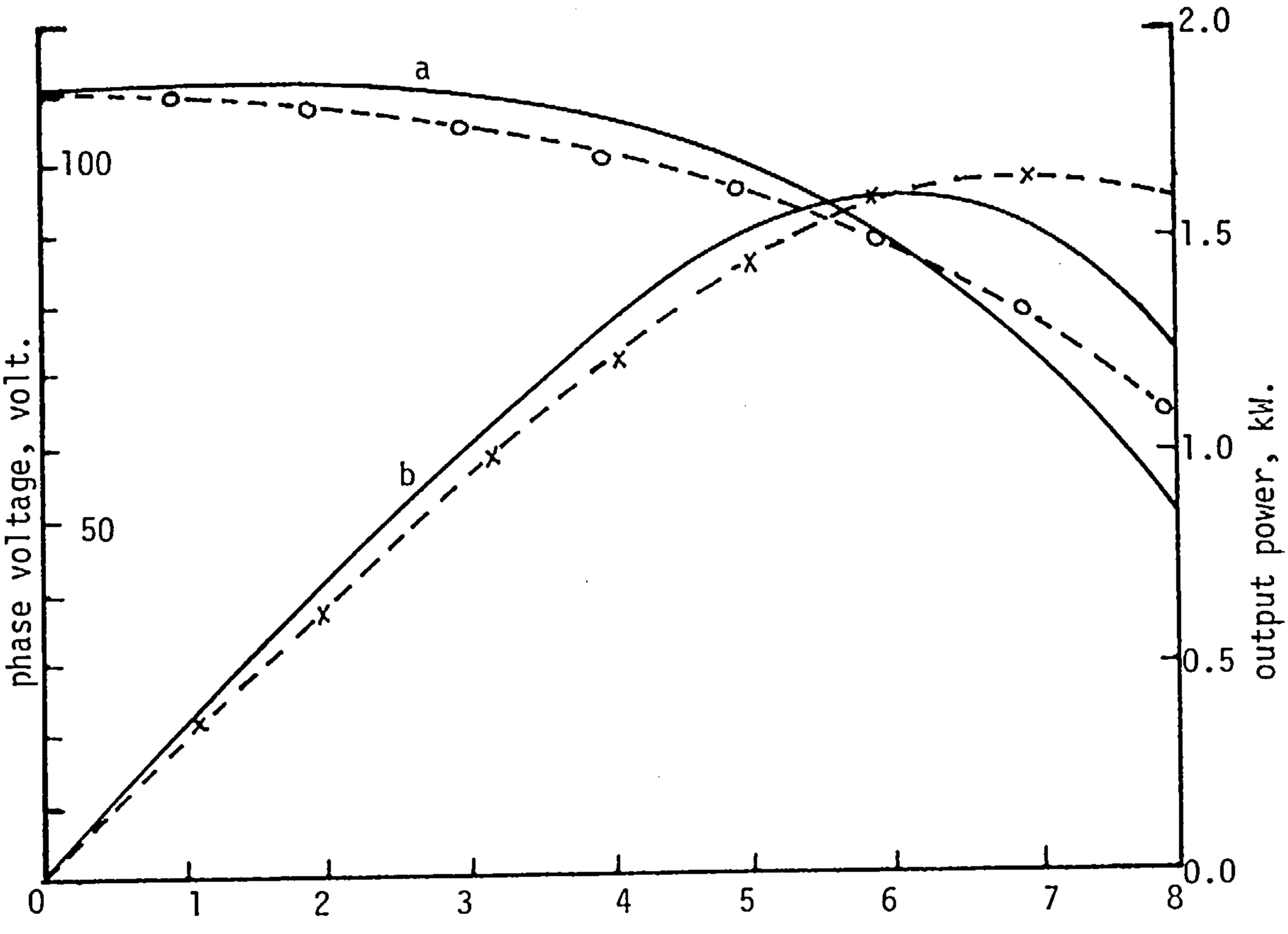

Fig. 3.2 The terminal characteristic of generator A at unity power factor.

——————— predicted results {(a) for voltage and (b)for power output}

– – – –o– – – – measured voltage

– – –·x– – – ·· measured power output

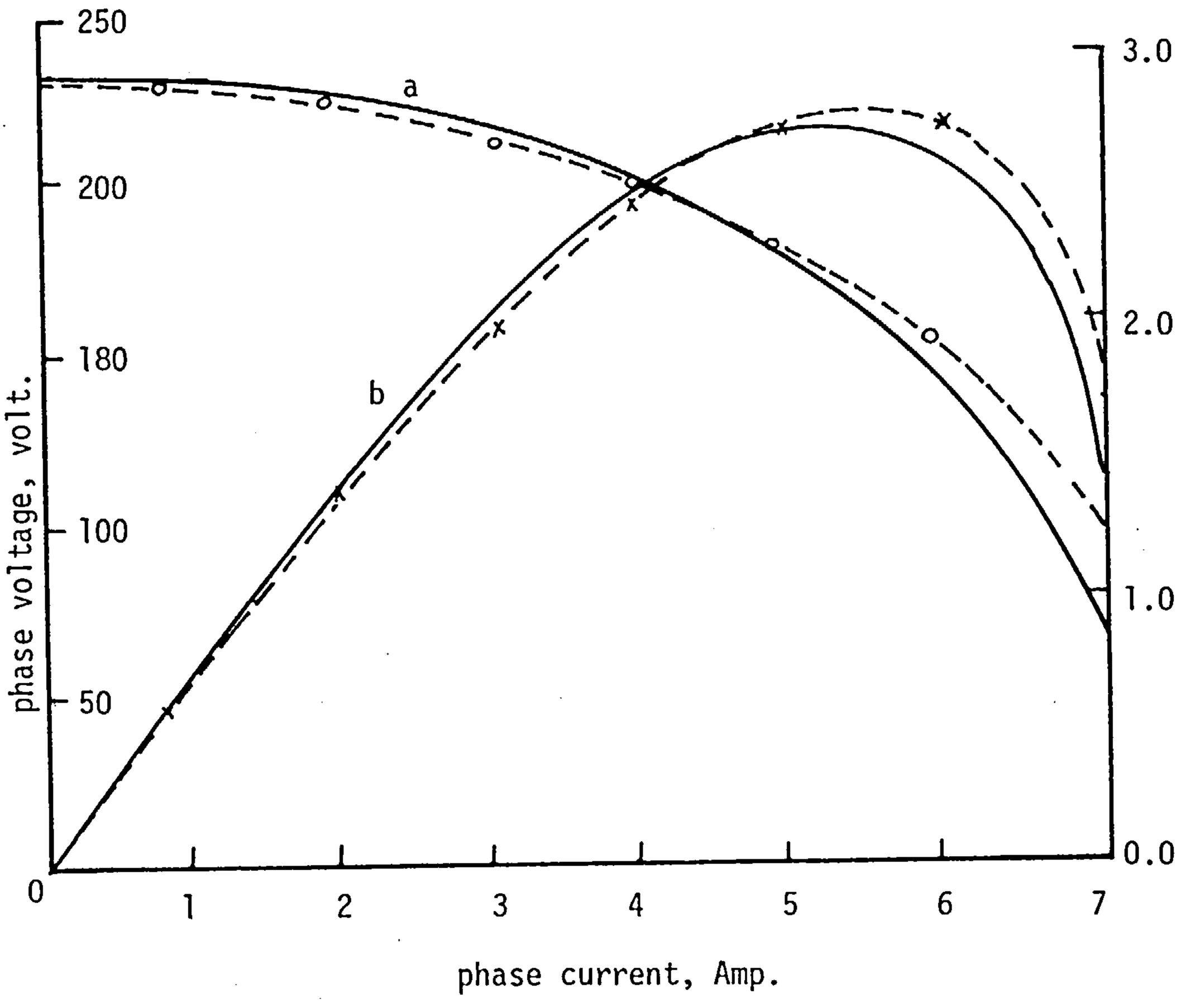

Fig. 3.3 The terminal characteristic of generator B at unity power factor.

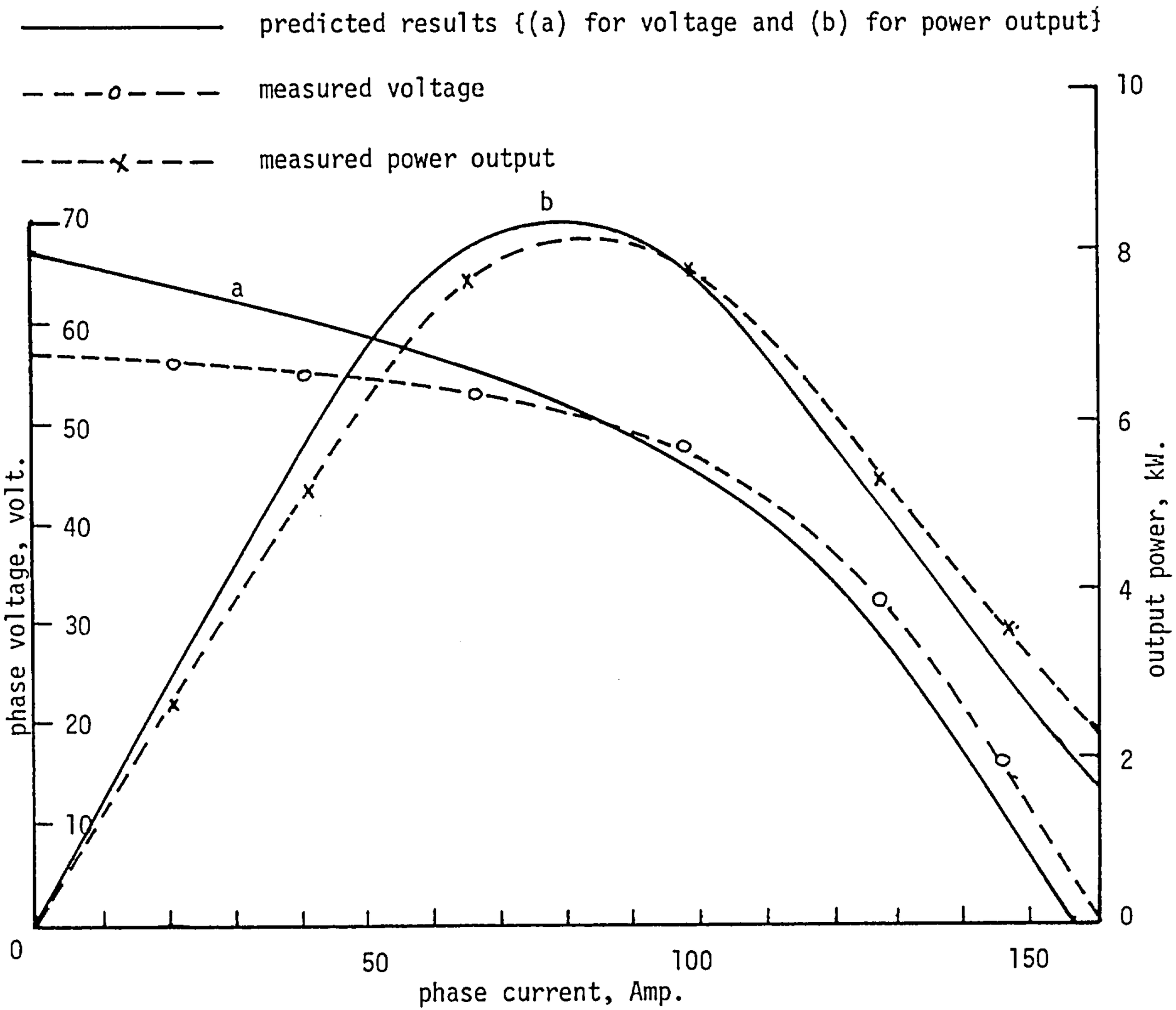

Fig. 3.4 The terminal characteristic of generator C at unity power factor.

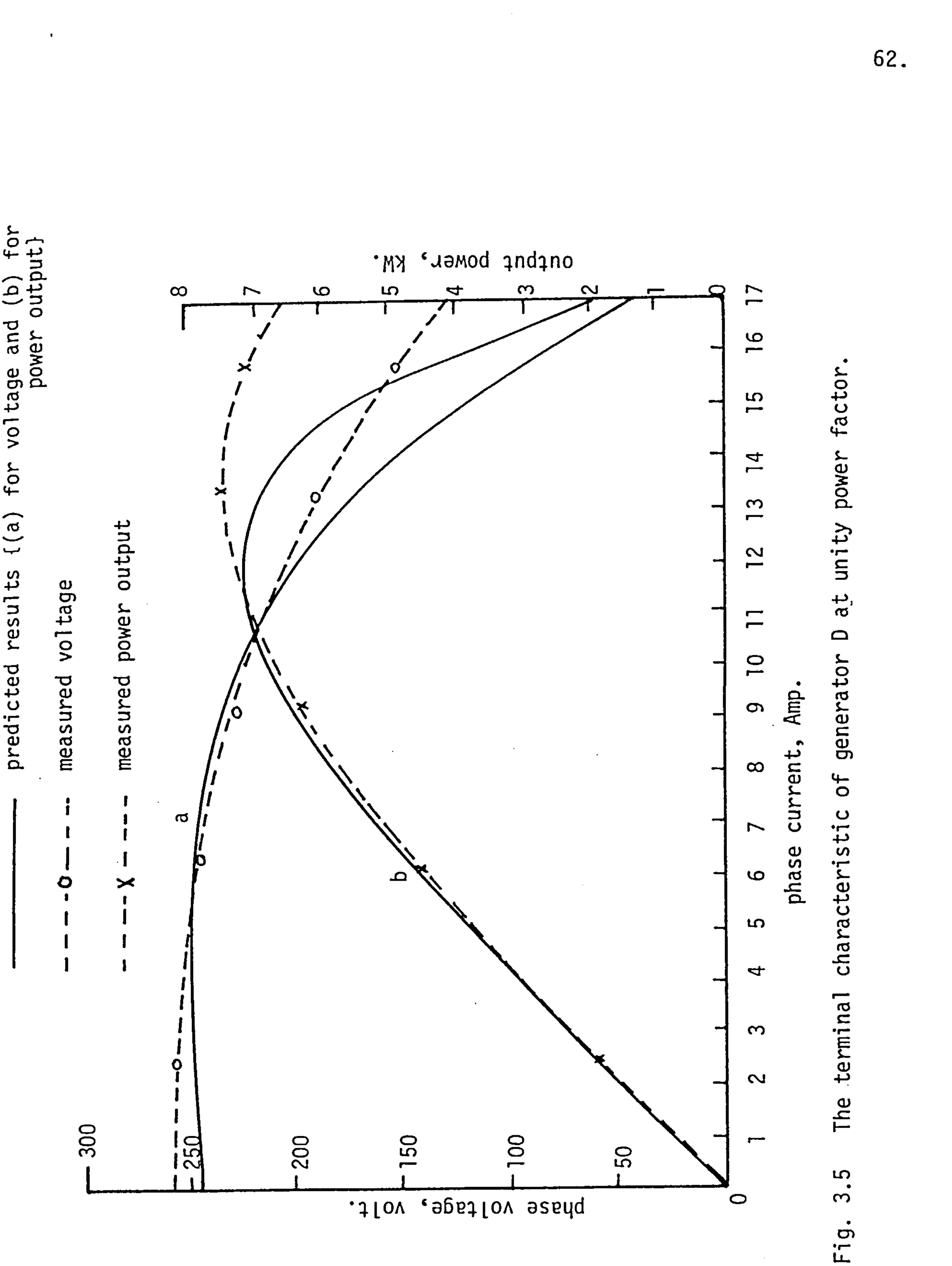

Fig. 3.5 The terminal characteristic of generator D at unity power factor.

——————— predicted results {(a) for voltage and (b) for power output}

– – – o – – · measured voltage

– – – x – – – measured power output

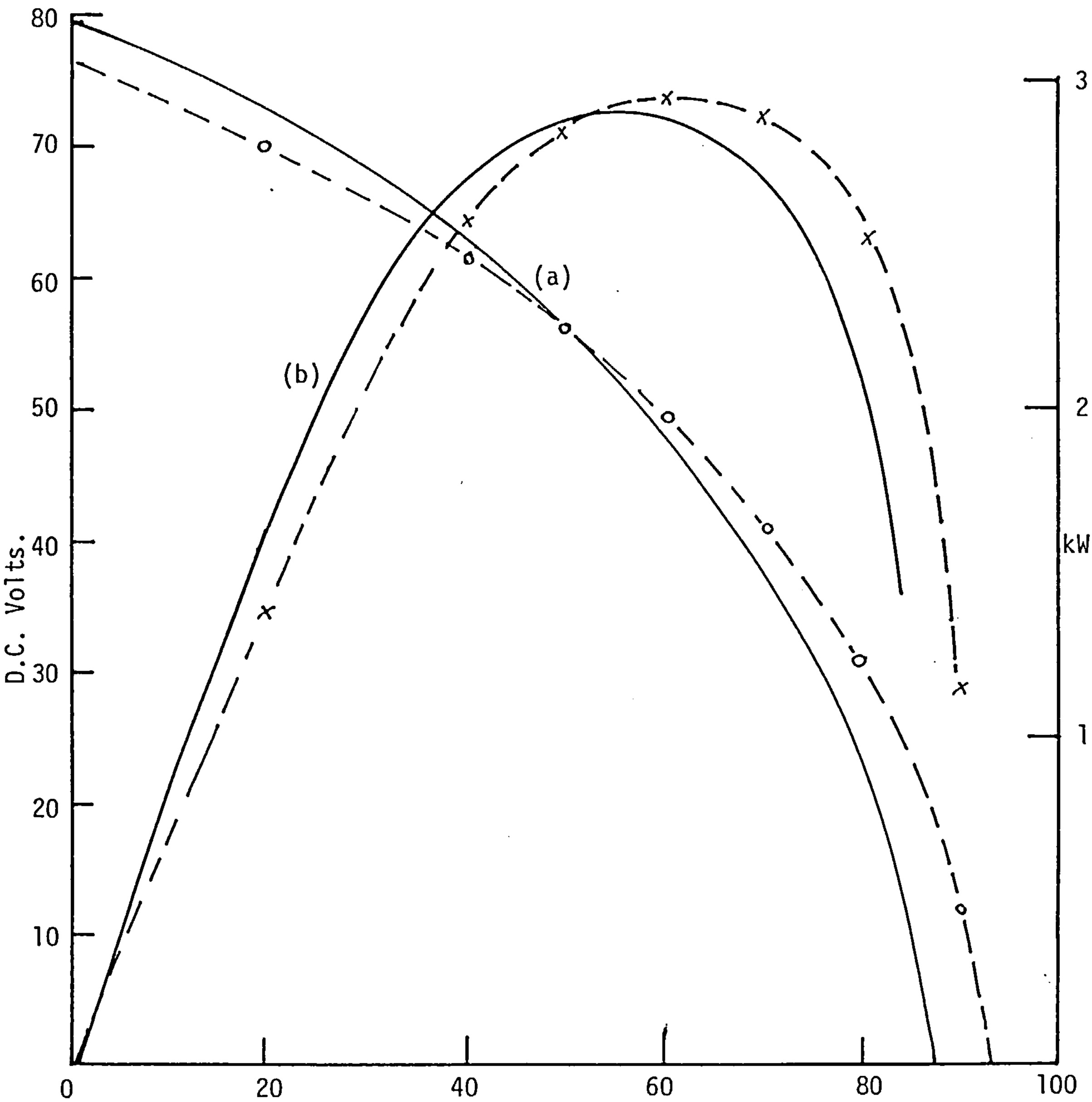

Fig. 3.6 The terminal characteristic of generator F at unity power factor.

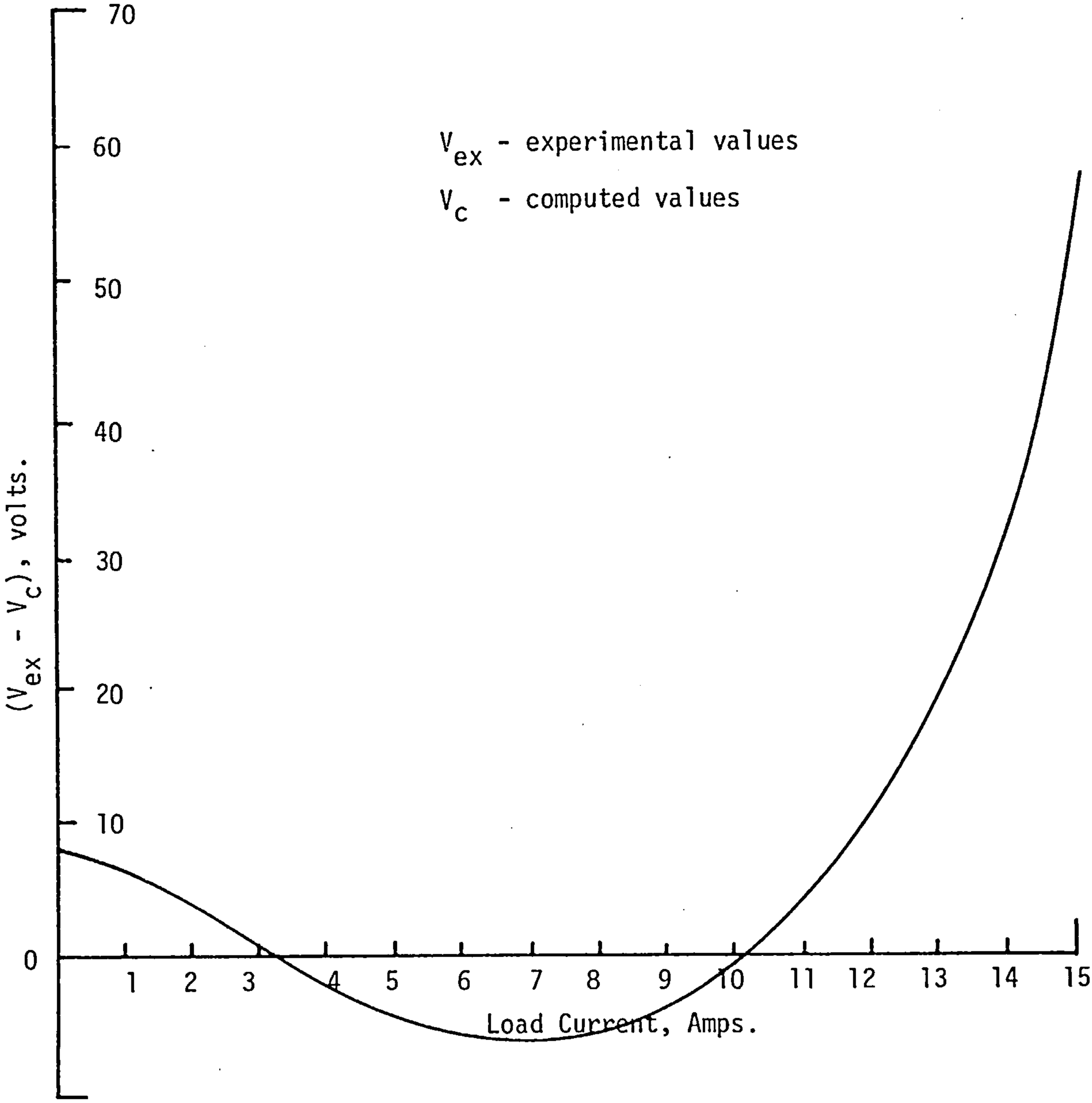

Fig. 3.7 The corretlation between experimental and predicted values.

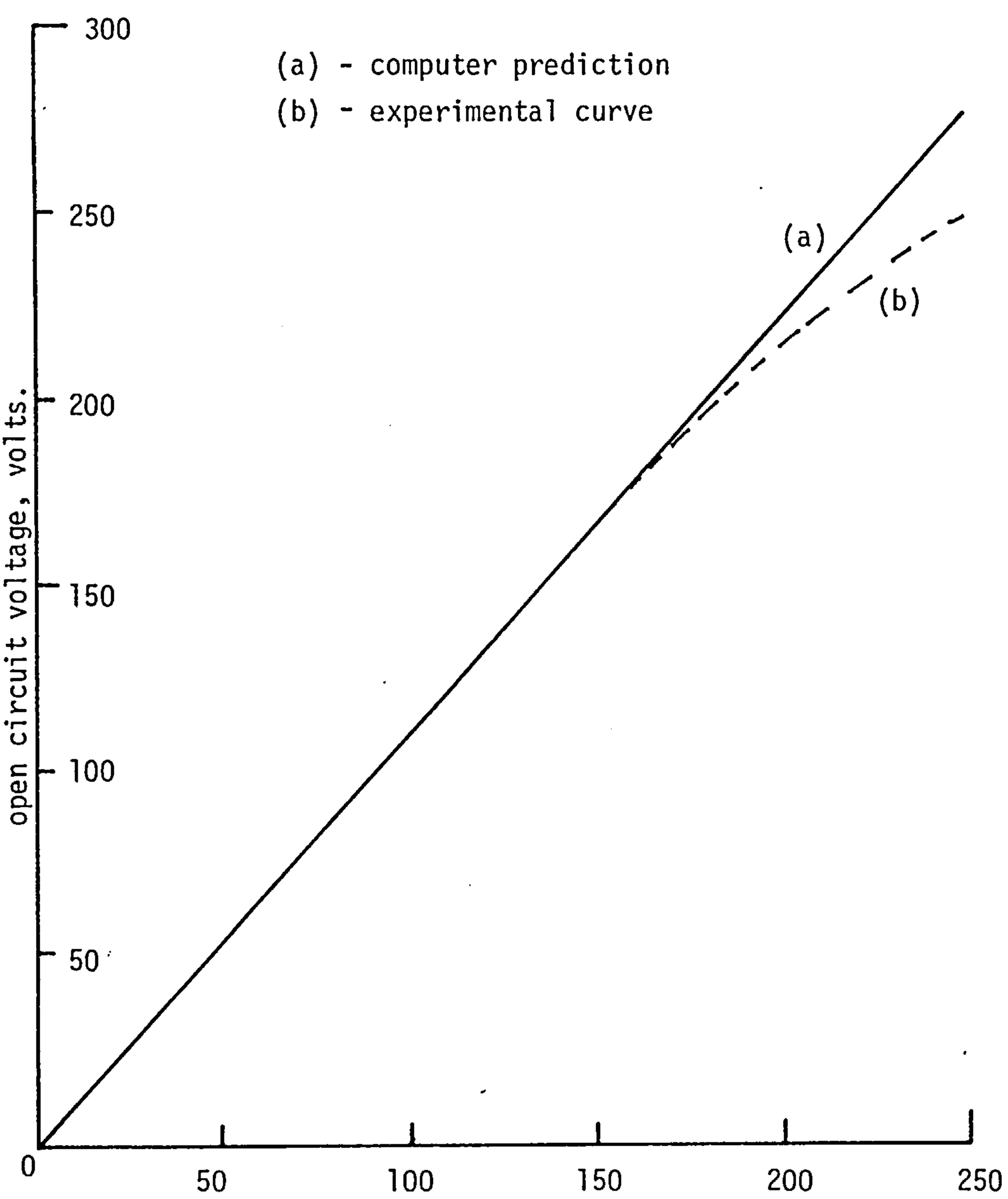

Fig. 3.8 The terminal open circuit voltage-speed relationship for generator A.

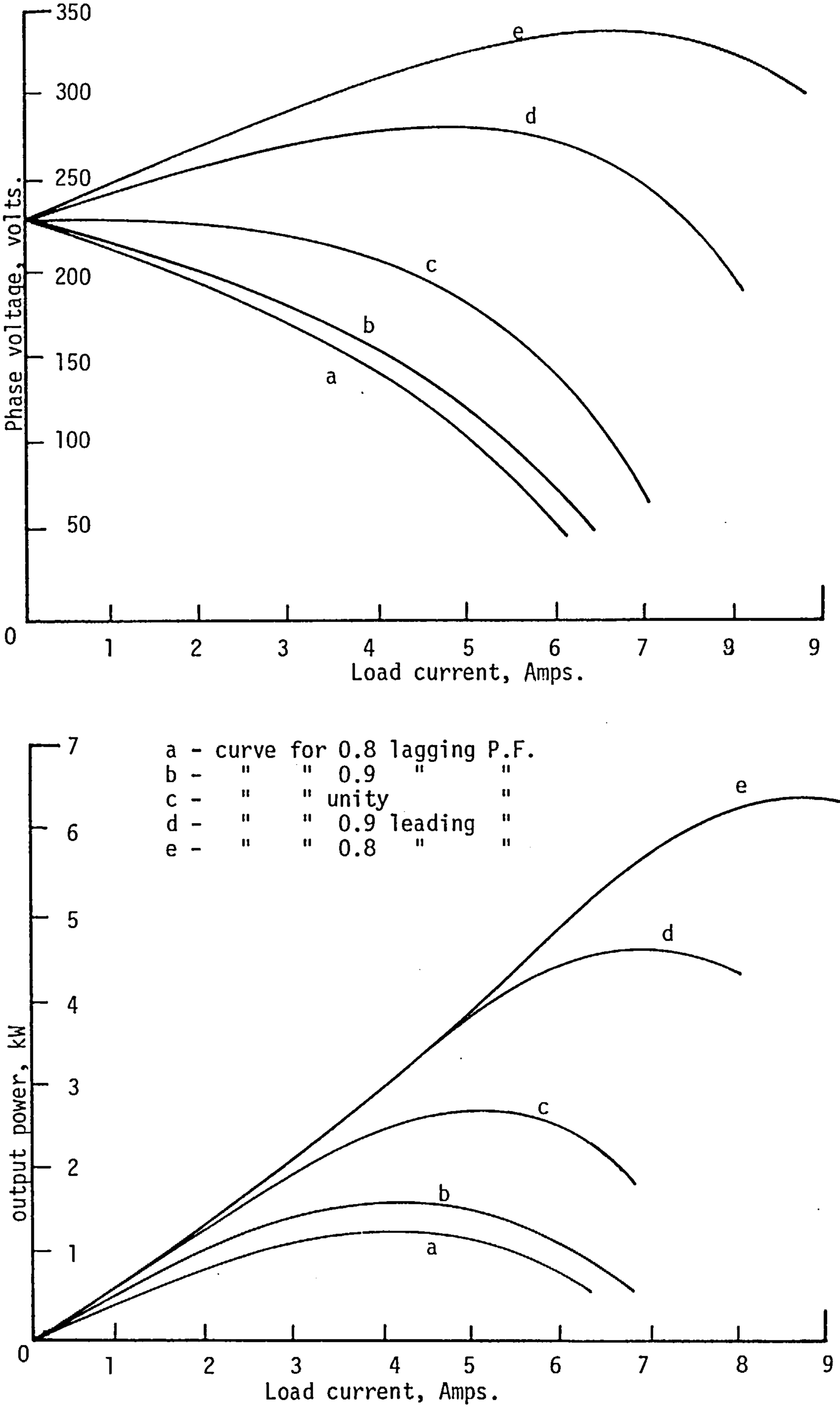

(b) Output curves for varying power factor

Fig. 3.9 Effect of load power factor on generator B.

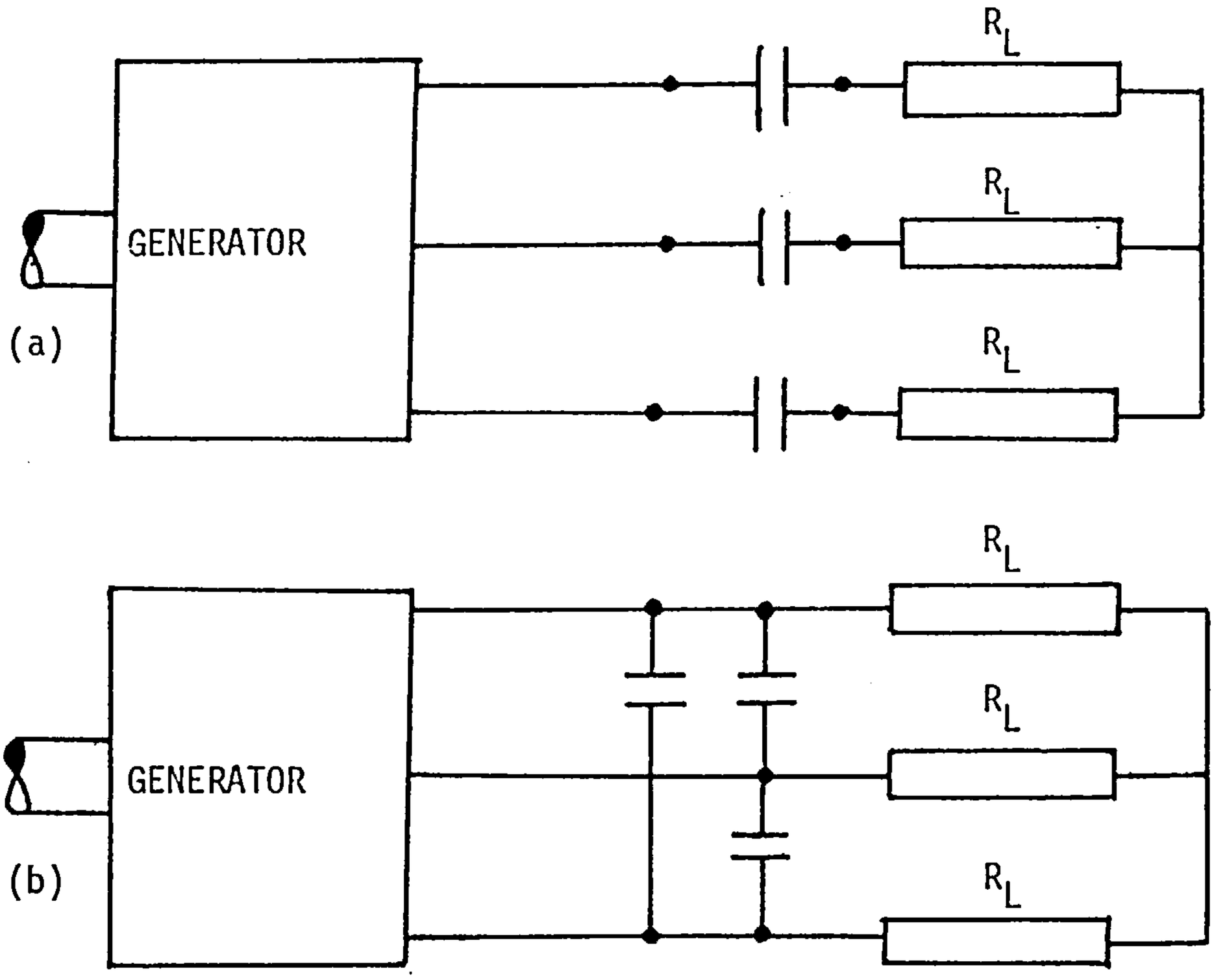

Fig. 3.10 The use of capacitors to change the output of the generator magnet generator.

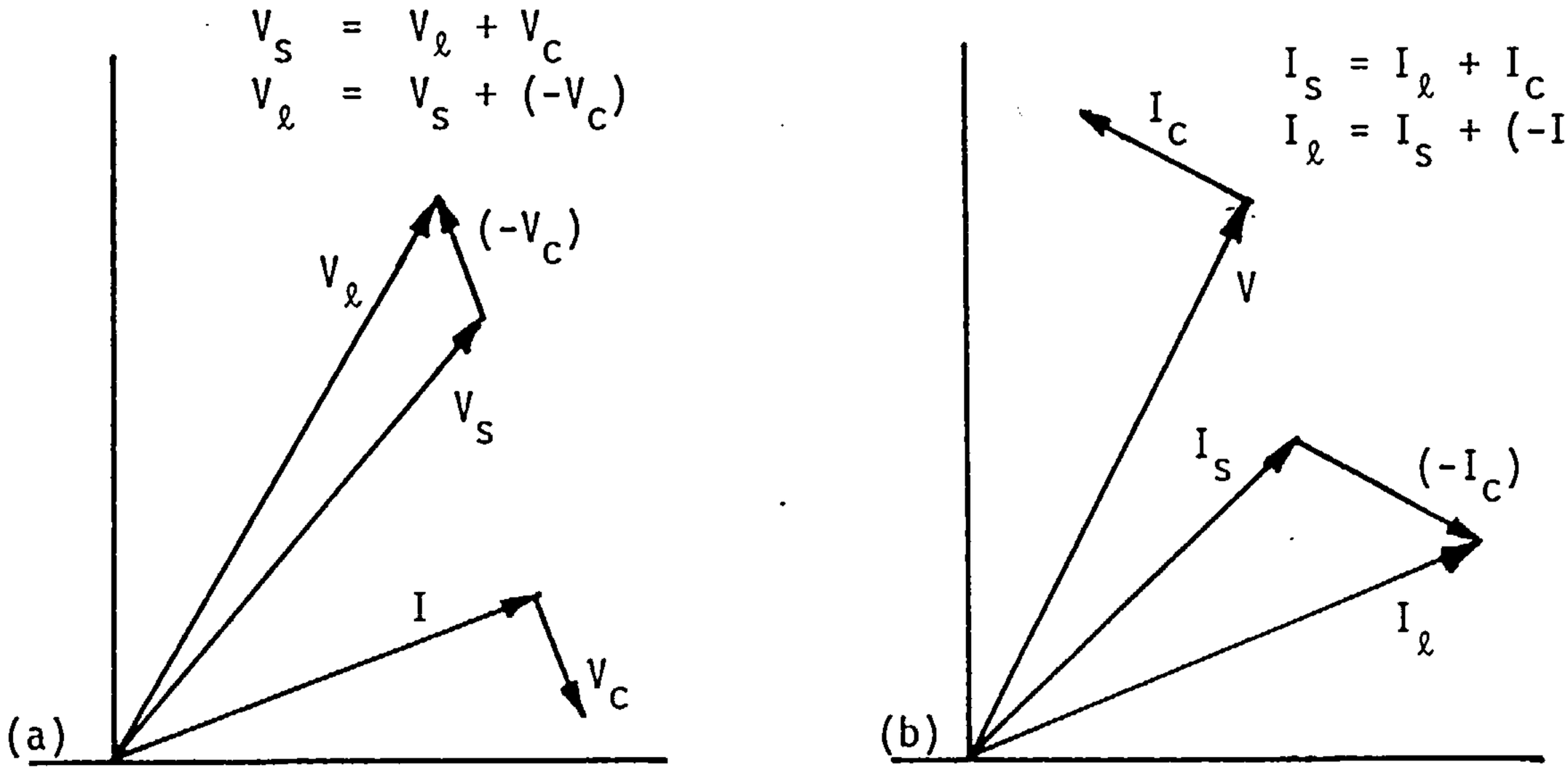

Fig. 3.11 Phasor diagrams for generators with capacitors in their output circuit.

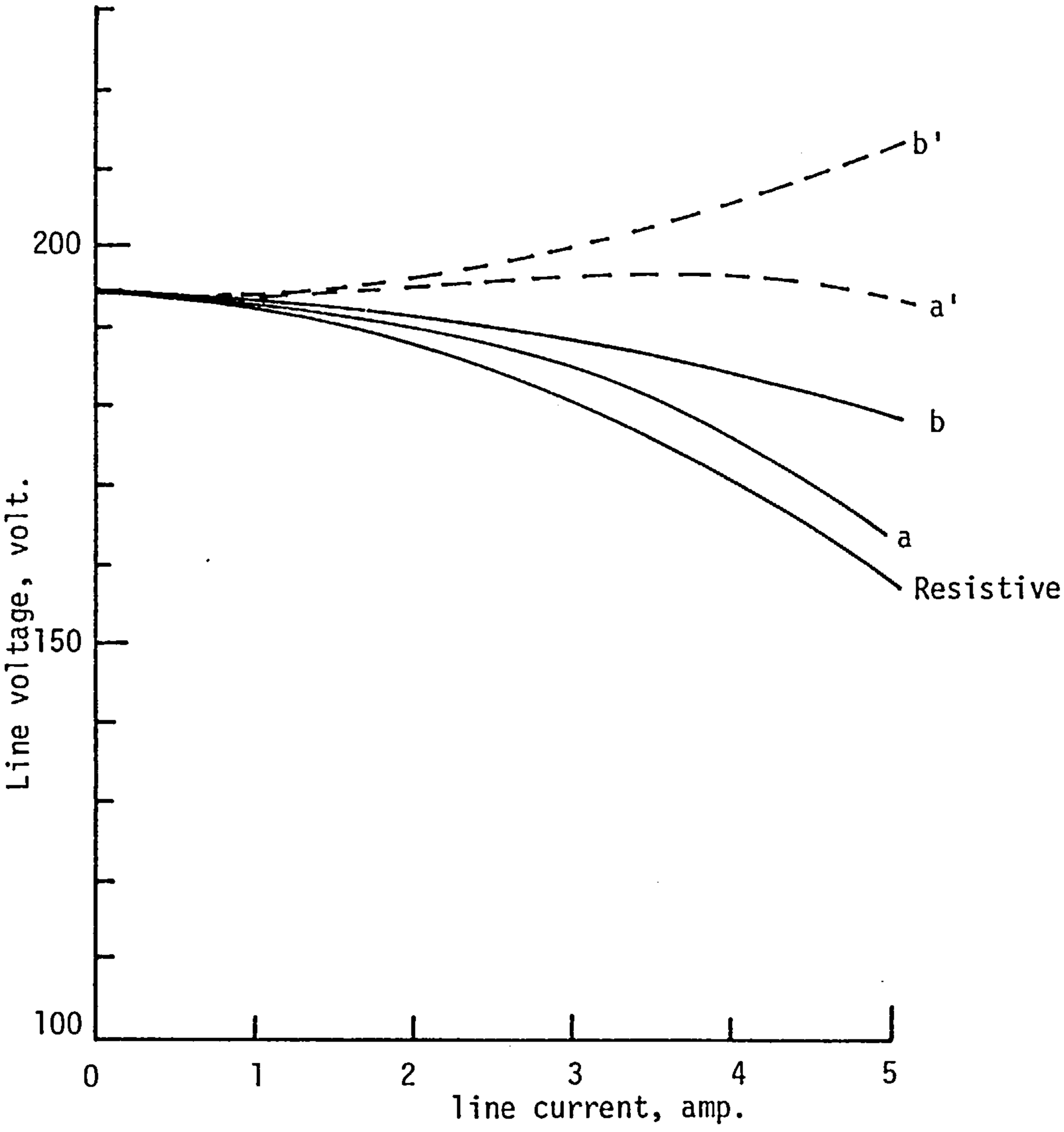

--- stator line voltage with capacitor.

—— load line voltage

a 100 μF

b 175 μF

Fig. 3.12 The effect of series capacitors.

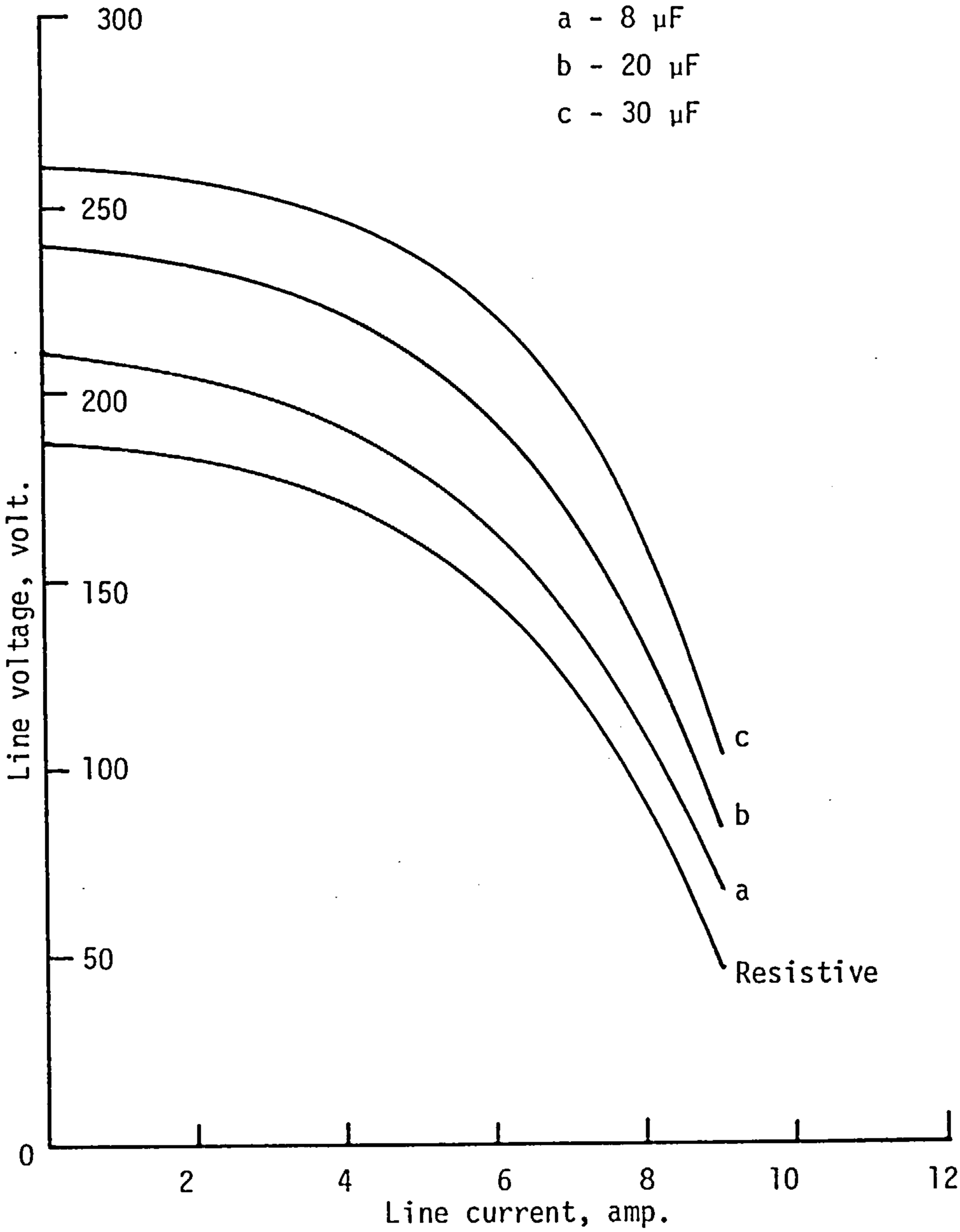

Fig. 3.13 The effect of parallel capacitors on the output voltages.

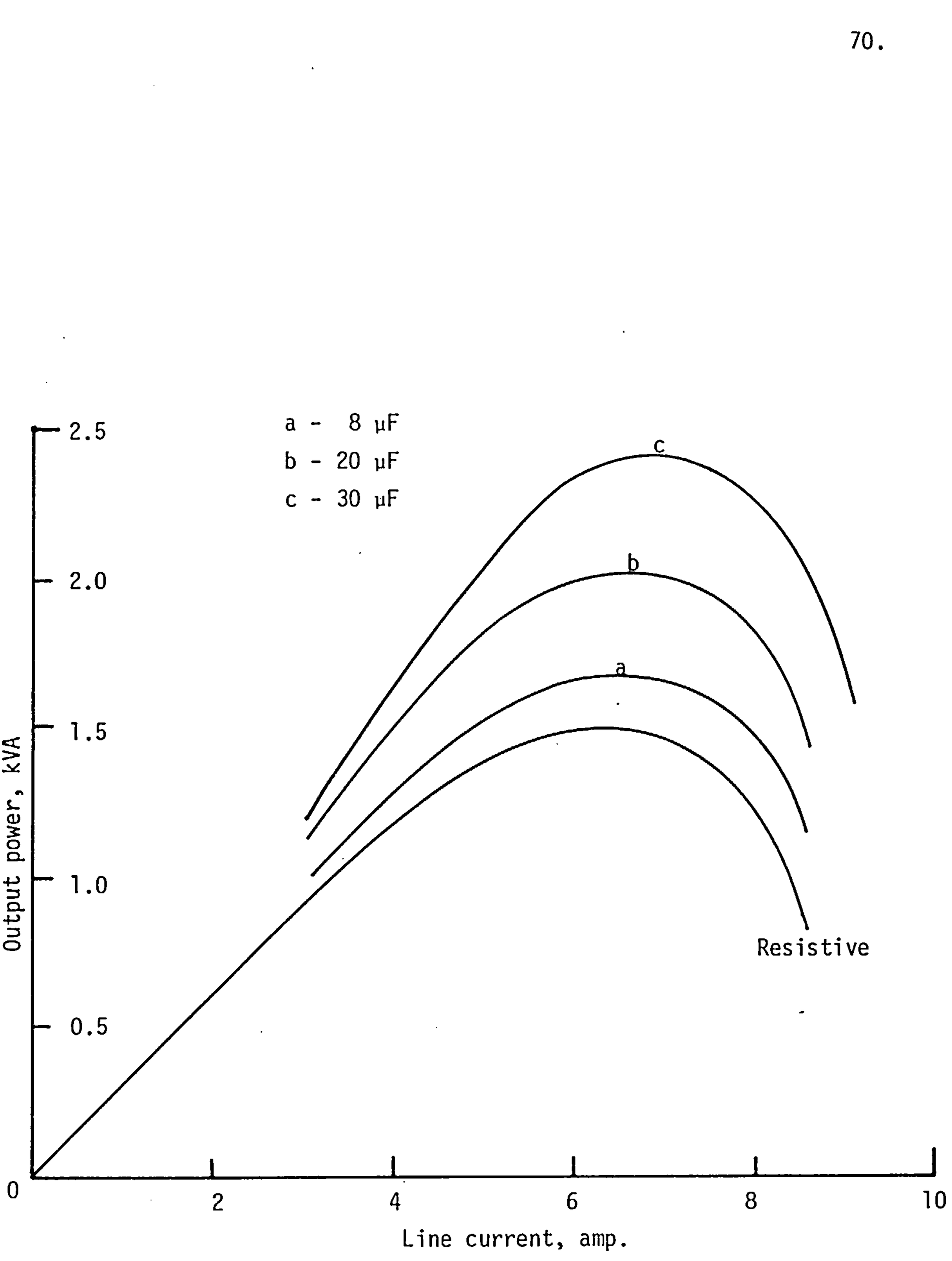

Fig. 3.14 The effect of parallel capacitors on output power.

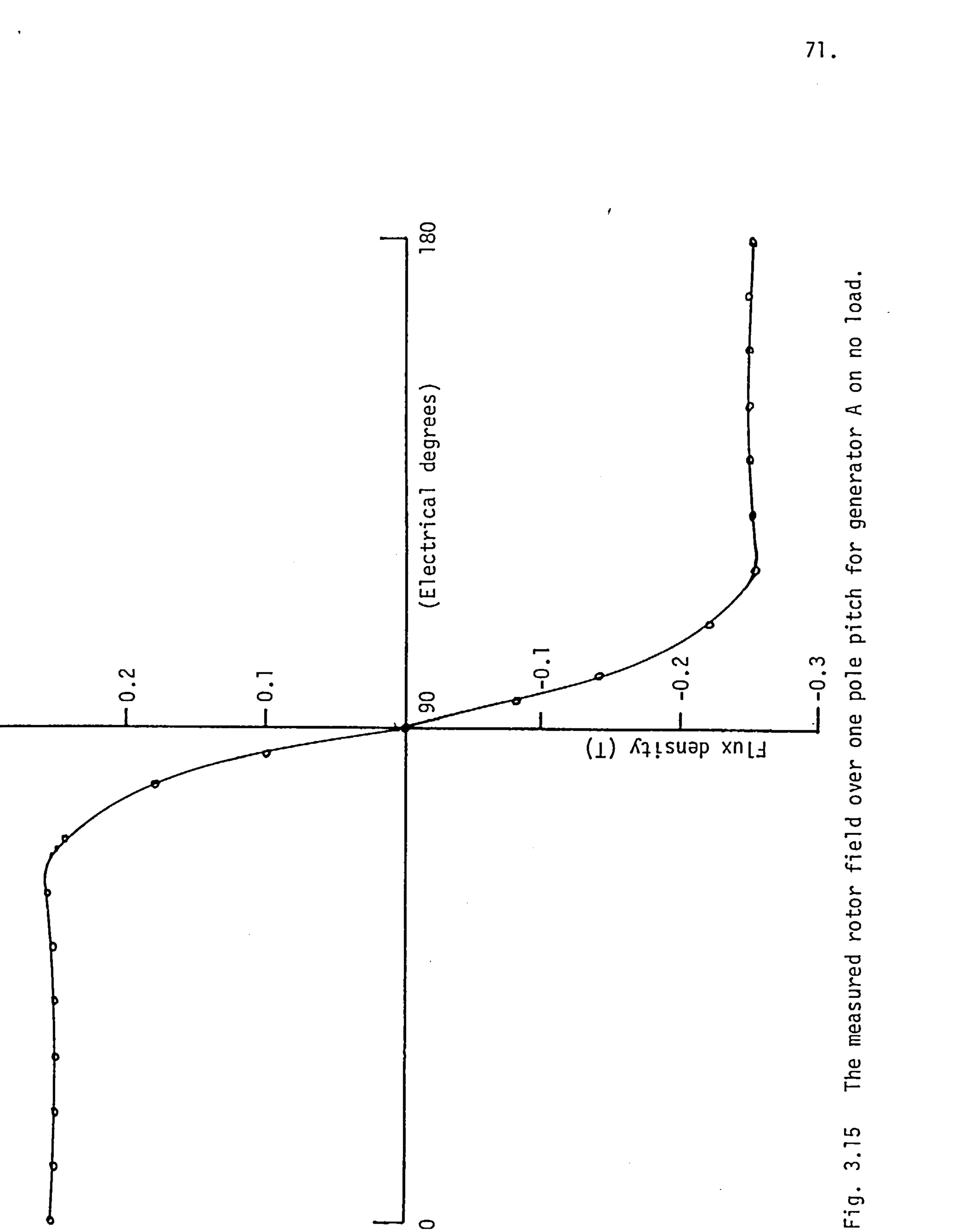

Fig. 3.15 The measured rotor field over one pole pitch for generator A on no load.

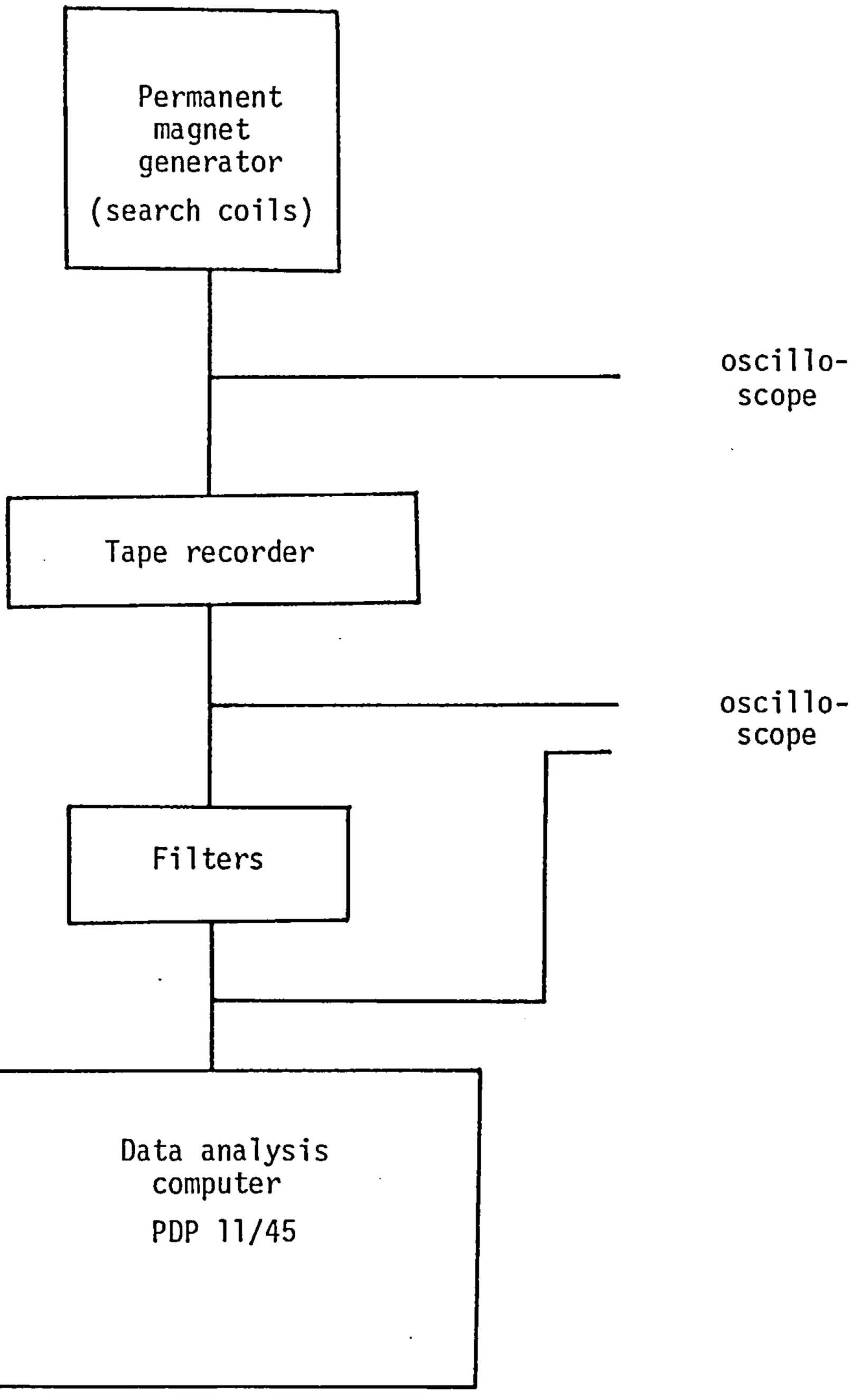

Fig. 3.16 Block diagram showsing the scheme for the harmonic analysis experiment.

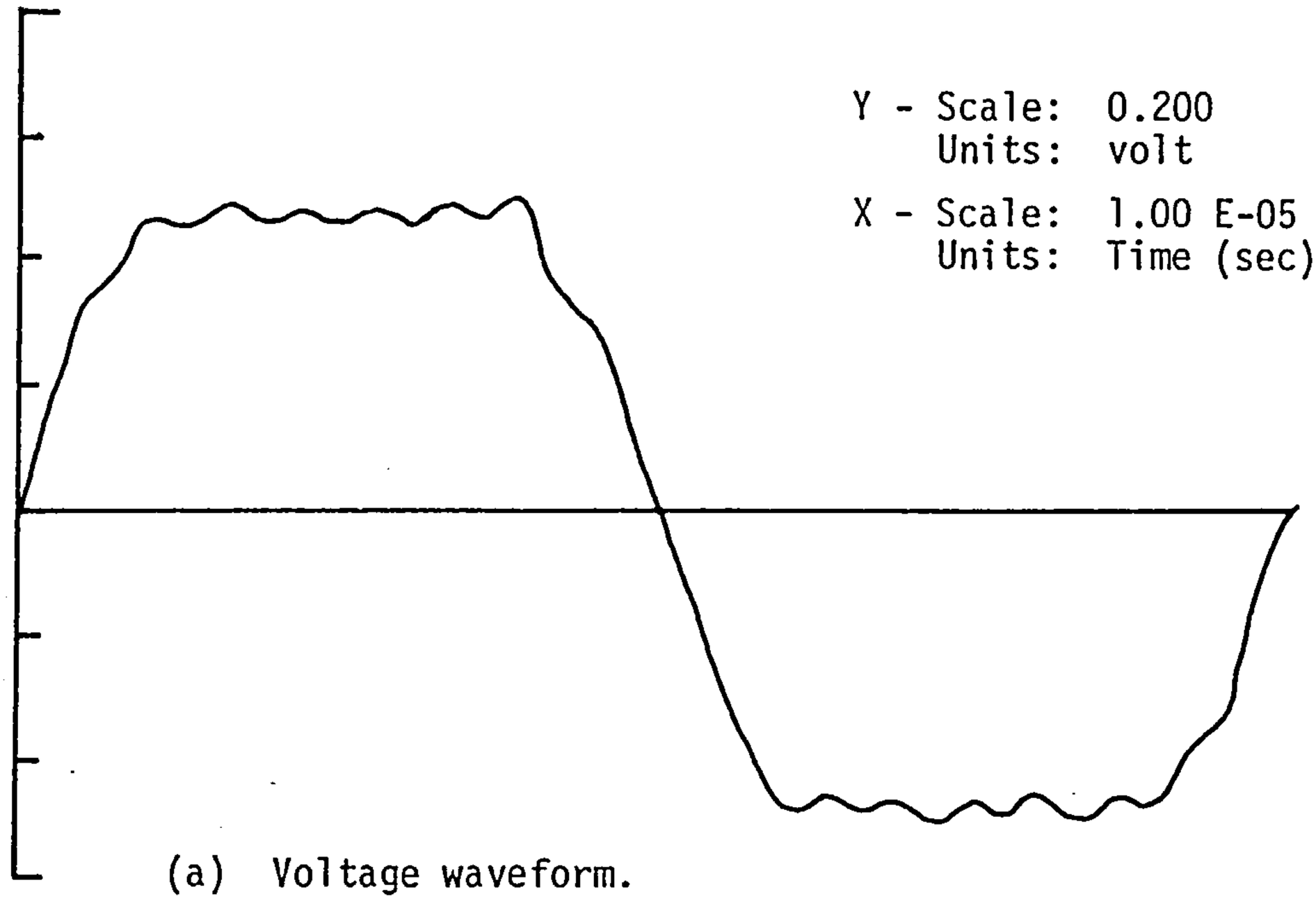

(a) Voltage waveform.

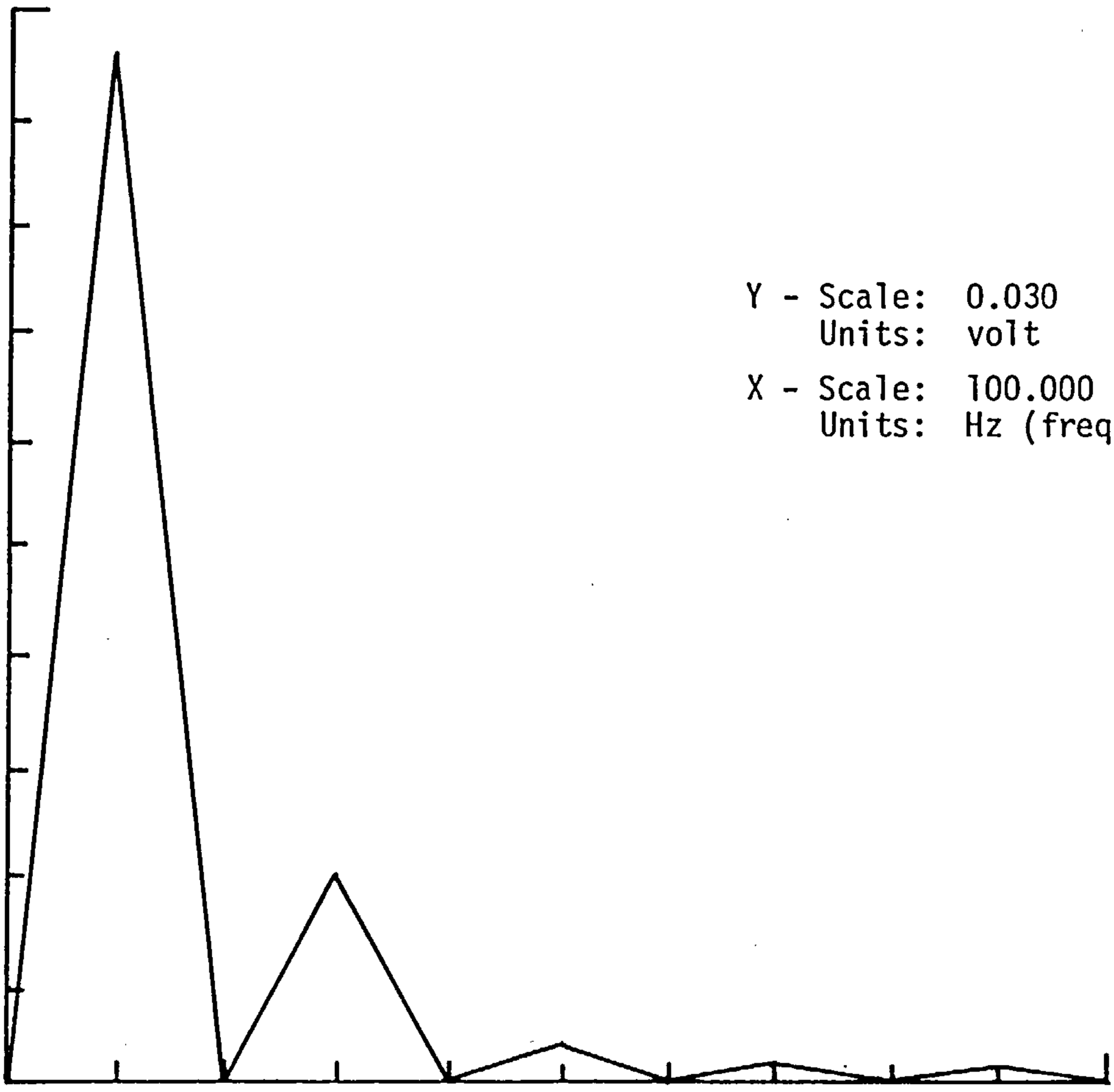

(b) Spectrum of stator voltage waveform.

Fig. 3.17 Voltage Harmonics on no load.

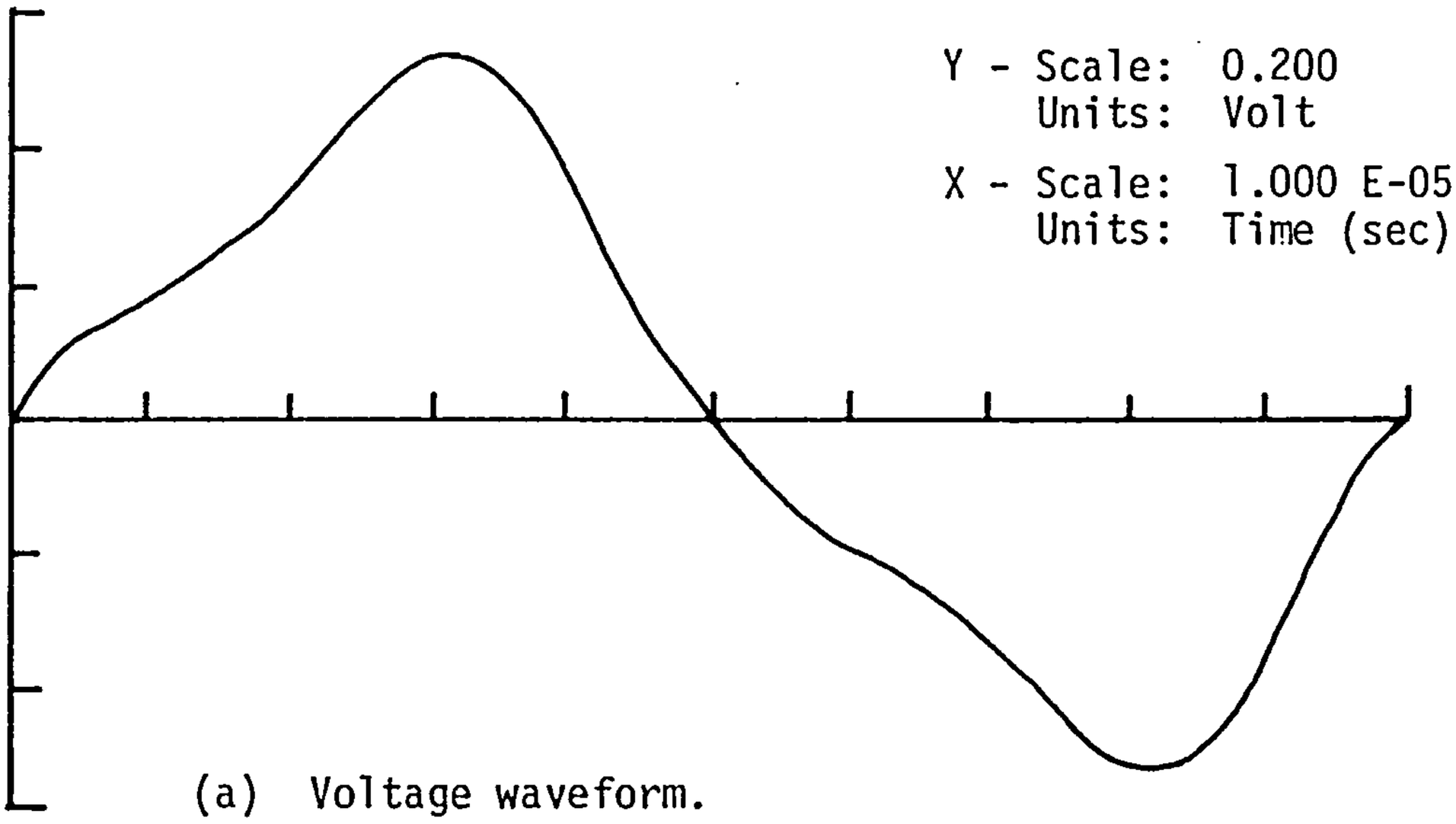

(a) Voltage waveform.

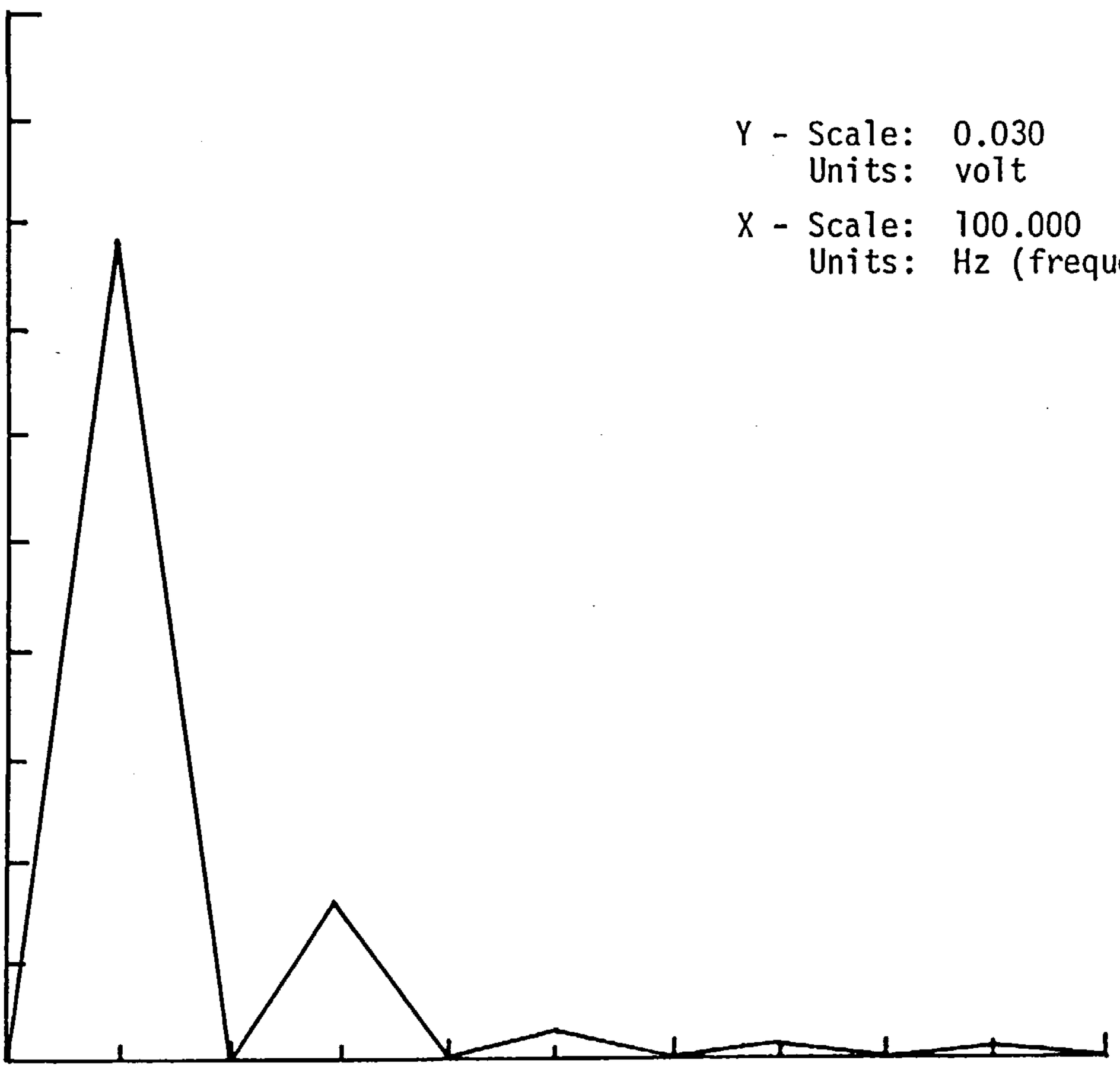

(b) Spectrum of the stator voltage waveform.

Fig. 3.18 Voltage harmonics on-load.

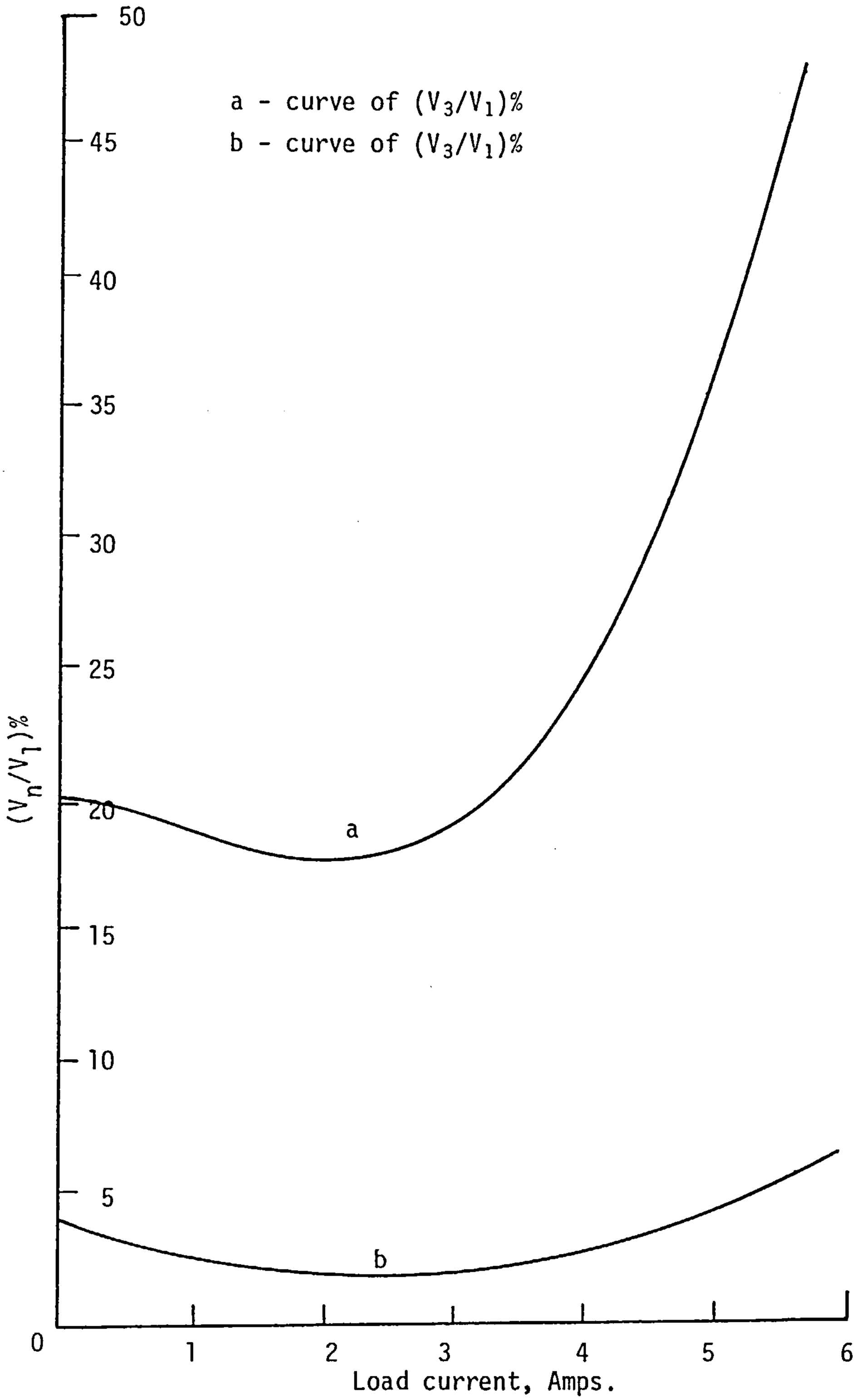

Fig. 3.19 The 3rd and 5th harmonics as a percentage of the fundamental of the voltage waveform.

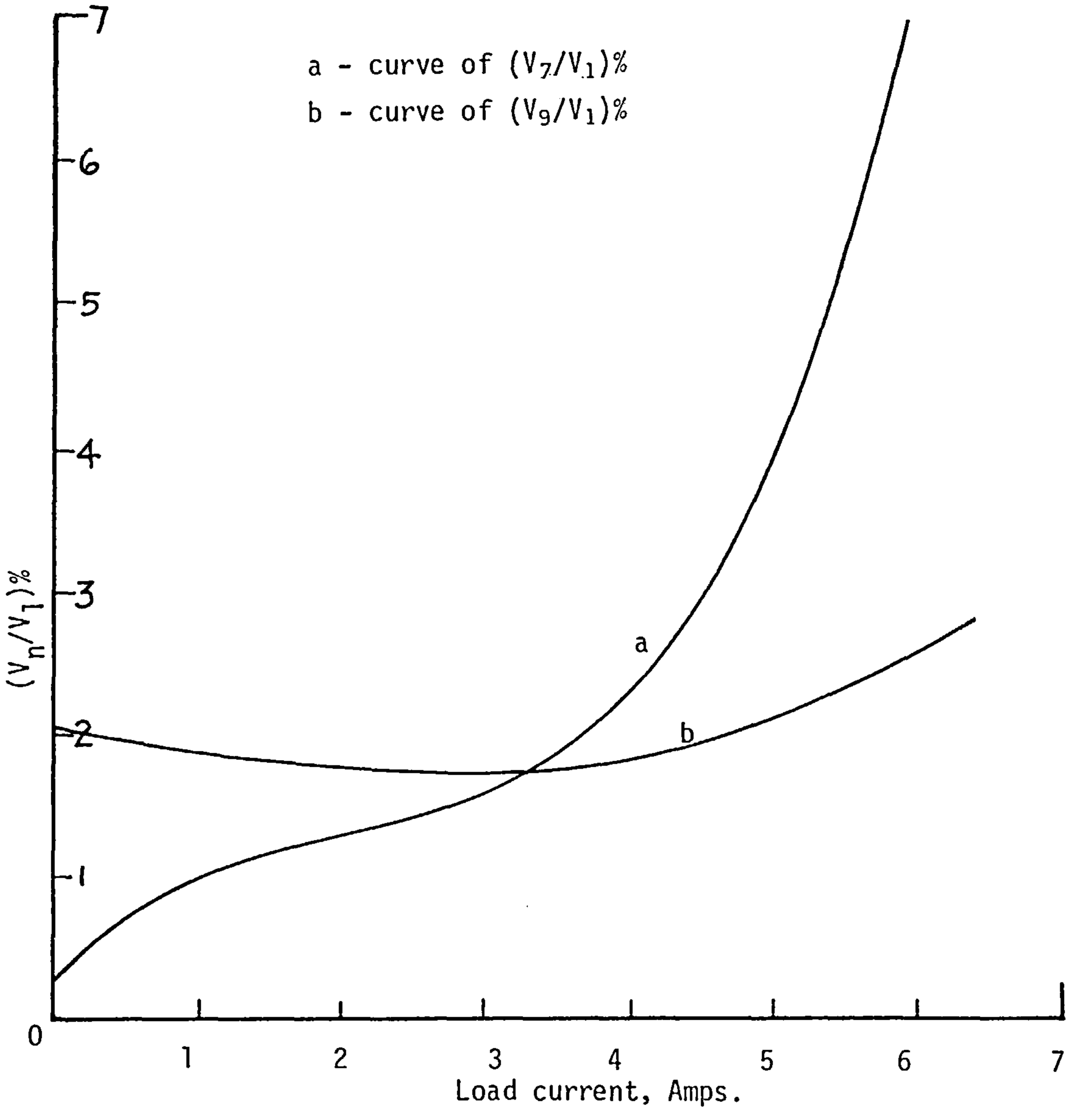

Fig. 3.20 The 7th and the 9th harmonics as a percentage of the fundamental of the voltage waveform.

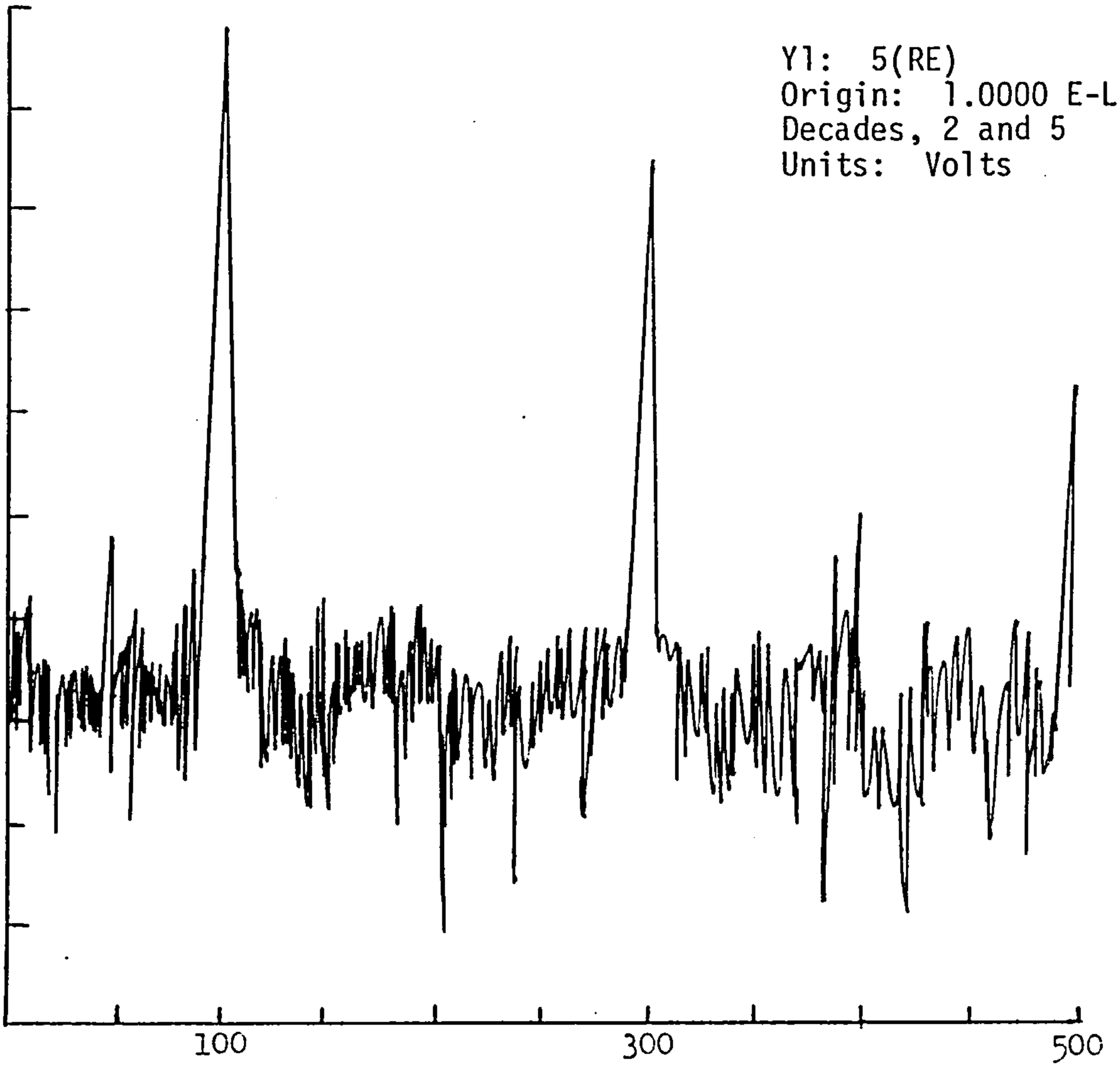

Fig.21 The power density spectra of the voltage waveform of generator A with a load current of 5.85 amps.

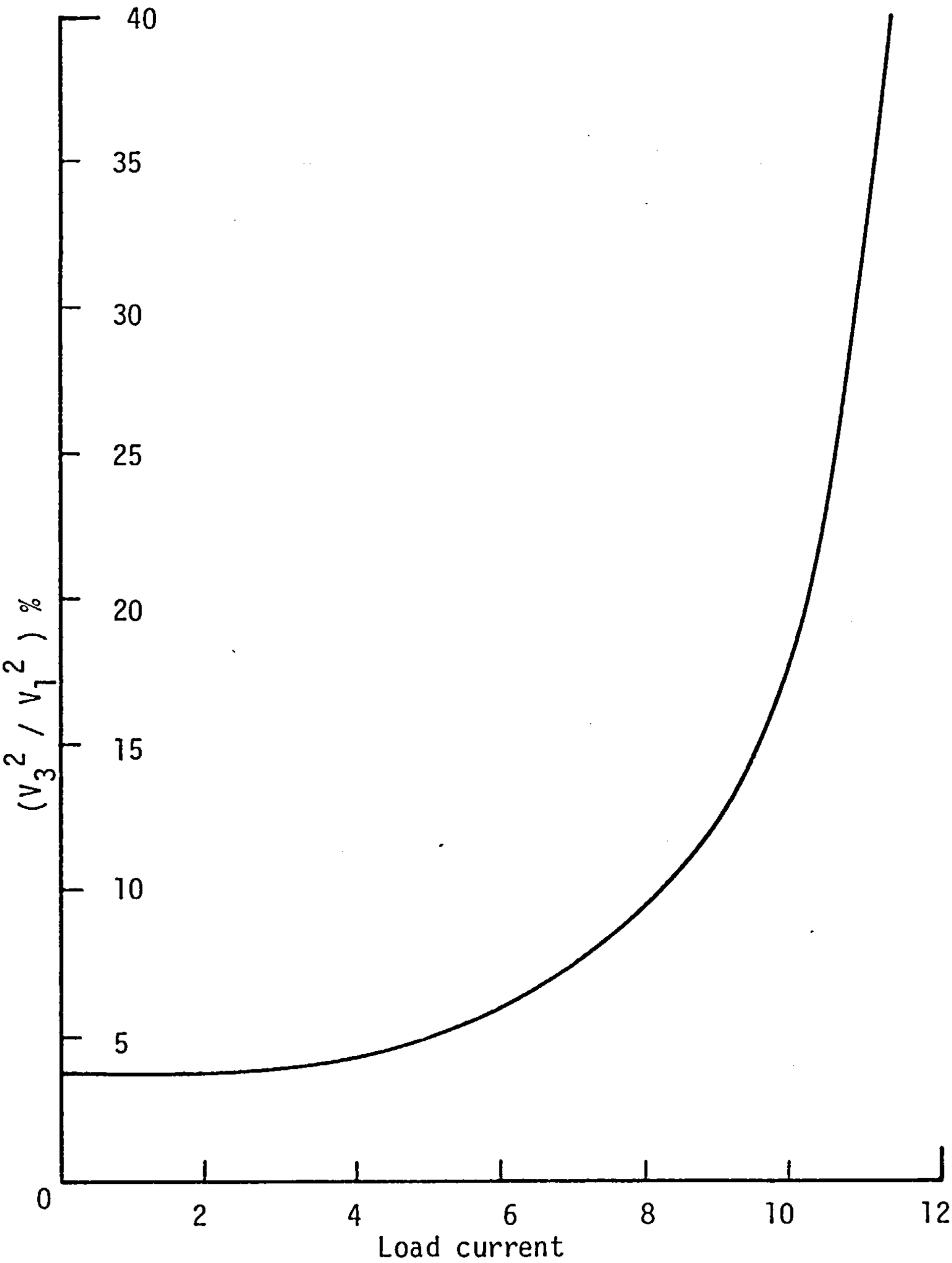

Fig. 3.22 The percentage of 3rd harmonic power at various load currents.

CHAPTER FOUR

THE DISCRETE-RELUCTANCE METHOD

CHAPTER FOUR

THE DISCRETE-RELUCTANCE METHOD

4.1 INTRODUCTION

The design of the new rotor involves the solution of a three-dimensional field problem. A method based on the integral equation $I = \oint H \, d\ell$, for closed paths within the boundary, has been used successfully[1]. The choice of the paths of integration in this method of computation is equivalent to the construction of the mesh in other discretisation methods such as the finite-element method and the finite-difference method. The field equations of the flux tubes are solved numerically because no explicit solution can be found due to the non-linearity of the magnetic circuit and the dependence of the working point of the magnet on the field. This method is different from the circuital approach used in the past[2,3] where linearity of the magnetic circuit is assumed and the working point of the magnet fixed by the assumption of fixed iron reluctivity. A load line based on these linear assumptions is then used to adjust the working point of the magnet. Thus in references 2 and 3 the problem is reduced to the solution of a set of algebraic equations with lumped parameters. In the discrete-reluctance method, the non-linearity of the circuit is preserved and the working point of the magnet is a flux-dependent quantity, and the solution is obtained by means of an iterative process.

4.2 THE DISCRETE-RELUCTANCE METHOD - THE PRINCIPLE OF THE METHOD

The essence of this method of computation is that for a given flux density distribution in the air gap the reluctance of the rotor can be determined in the presence of leakage flux owing to the polarisation of the magnet which provides the source of magnetisation. If a magnetic

circuit is assumed to consist of a discrete number of branches, a set of simultaneous equations relate the magnetic potential differences throughout the parts of each branch. If the reluctance of the stator core is not included, the set of equations becomes:

$$\left(\int H\, d\ell\right)_q^m - \left(\int H\, d\ell\right)_q^I - \left(\int H\, d\ell\right)_q^G - I_q = 0 \qquad (4.1)$$

for branch q,

where $\left(\int H\, d\ell\right)_q^m$ is the integral in the magnet region.

$\left(\int H\, d\ell\right)_q^I$ is the integral in the iron region.

$\left(\int H\, d\ell\right)_q^G$ is the integral in the air-gap region

and I_q is the stator current enclosed.

These equations cannot be solved explicitly because the working point of the magnet and the reluctivities of the materials in the rotor are not fixed but are flux dependent. Therefore, an interative procedure is used in which an initial value is given to the flux in the various parts of the magnetic circuit. The various reluctivities are then calculated from the B-H characteristics of the materials and the working point of the magnet found from its demagnetisation curve. These are substituted into the field equations and solved for the flux. The value of the flux is then used to calculate the reluctivities and to locate the working point of the magnet. This process is repeated many times until a stable solution is found. An under-relaxation factor is applied to dampen fluctuations between iterations.

4.3 ASSUMPTIONS MADE

Simple assumptions are necessary and reasonable in numerical methods to obtain a solution without undue complications. The assumptions made in the discrete reluctance method program are listed below:

(i) The stator iron is infinitely permeable.

(ii) The fringing at the end region is neglected and is treated as a flux barrier. With this assumption, the analysis of a multi-stacked rotor can be reduced to the analysis of a single rotor unit comprising one magnet and two flux guides.

(iii) The stator bore is considered to have a smooth surface. The effect of slotting is accounted for by extending the air gap. The formulae governing the extension of the air gap is found in references 4, 5 and 6.

(iv) The magnet has a stabilised demagnetisation curve and a single valued relationship. This assumption is reasonable for materials such as the rare-earths and polymer-bonded rare-earths as they possess linear B-H curves. It is also reasonable for use with ceramic magnets if the working point is not pushed down below the knee (See Figure 2.4).

(v) The B-H characteristic of iron is to be single valued.

Hysteresis in iron is neglected.

(vi) Eddy current losses are neglected.

4.4 THE MATHEMATICAL MODEL OF THE MAGNETIC CIRCUIT

The mathematical solution of the field problem posed by the new rotor is based on the magnetic circuit model in Figure 4.1. The rotor iron is divided into three paths represented by R_1^I, R_2^I and R_3^I. R_1^A and R_2^A are the leakage flux paths. The upper branches represent the air-gap flux path which includes the effect of armature current, I_q. Some of these paths are sub-divided into a finite number of parallel flux carrying tubes. This process is equivalent to multiplying the total number of closed paths by n when one part is sub-divided into n tubes and hence the application of equation (4.1) n time.

The iron paths are shown in Figure 4.2. The boundary between each of these regions is an equipotential surface. Iron path 1 lies in the region between the magnets and is a disc. The flux path in this region is considered to have a reluctance in the radial direction. The reluctance in the axial direction is assumed to be negligible. Iron path 2 is bounded by cylindrical surfaces, one being the surface of flux exit of iron path 1 and the other, the surface of flux entry into the pole. This path has a relatively short length and the flux density in it is assumed to be uniform. Iron path 3 lies in the rotor pole shoes. The direction of the flux is both radial and axial. This region has to be divided into a number of sections and each one has a different cross-section which is dependent on the machine geometry. Flux pass through the pole along these elemental paths. It is assumed that the normal flux density entering the pole surface does not vary axially, but there is of course an accumulation of flux giving rise to an axially varying flux density in the iron pole shoes.

The leakage flux paths inside the rotor include the interpolar leakage which is termed as leakage flux path 1, and leakage between the underside of the poles and the steel disc attached to the opposite pole of the magnet which is called leakage path 2. These paths are shown in Figures 4.3 and 4.4. The significance of these two leakages are appreciable as would be shown later in this chapter.

The air-gap is represented by $R^{(G)}$. The flux crossing the air gap is assumed to be radial with a negligible axial and tangential component.

This mathematical model forms the basis of the discrete-reluctance method program used for the analysis of the field of the new rotor and the design of the generators listed in Chapter 3.

4.5 THE REPRESENTATION OF THE PERMANENT MAGNET

The flux density in the magnet is assumed to be constant, by an initially known value. This assumption is reasonable if the steel flux guides are adequate for directing the flux out. The value H_m is found by a direct reference to the B-H curve. It is reasonable to take this assumption since a magnet of such properties, dimensions and initial polarisation is chosen so as to operate on its major B-H loop. To simplify convergence a method described by Binns, Jabbar and Barnard is adopted. In this method, the basic formula of magnetisation

$$B = \mu H$$

is replaced in the magnet region by

$$B = \mu_o H + M$$

where M is the magnetisation vector. M can be expressed as the sum of two values, a constant M_o, and a variable quantity M' which is a function of the field H. This representation results in

$$B = \mu_o H + M' + M_o$$

If the constant M_o is expressed as

$$M_o = B_r$$

where B_r is the remanence of the magnet, the field equation becomes

$$B = \mu_o H + M' + B_r$$

The term $\mu_o H + M'$ represents any assumed material having the same field intensity H and a flux density B'

$$B' = \mu_o H + M'$$
$$= \mu' H$$

μ' is called the 'apparent permeability'.

The field equation can now be written as

$$B = \mu' H + B_r$$

or $$-H = (B_r - B) / \mu'$$

This can be rewritten as

$$H_m = -H = (B_r - B)\ \nu' \qquad (4.2)$$

where ν' is the apparent reluctivity.

By putting

$$\left(\int H\ d\ell\right)_a^M = H_m\ L_m$$

in (4.1), and

$$\nu' = \nu_m$$

in (4.2), and solving (4.1) and (4.2) the following equation results:

$$(B_r - B)\ \nu_m\ L_m = \sum \left(\int H\ d\ell\right)_q^I + \left(\int H\ d\ell\right)_q^G + I_q \qquad (4.3)$$

Equation (4.3) replaces (4.1) for any possible closed path since the integral of $Hd\ell$ in the magnet region is independent of the path.

Magnet representation is discussed further in Chapter 9 of this thesis.

4.6 THE ARMATURE REACTION EFFECT

The air-gap flux is significantly affected by the armature mmf set up by the load current. The armature current is represented by discrete currents distributed around the periphery of the stator bore. The mmf resulting from these currents will be involved in the field calculations. The air-gap flux wave is influenced by both the armature reaction and the configuration of the pole face. To consider these two effects the air-gap flux path is divided into many sections as shown in Figure 4.5.c. Figures 4.5.a and 4.5.b show an arbitrary armature reaction pattern and the effect of pole face configuration on the air-gap path's reluctance respectively. The armature mmf could change in its spatial position relative to the rotor poles depending on the load. The mmf pattern is related to an effective armature current of 1 amp. The effect of a load current is obtained by multiplying the related

value in Figure 4.5.a by the value of the stator phase current. The total potential across the air-gap including the effect of stator current is referred to as M_q^G which is equal to

$$\left(\int H \, d\ell \right)_q^G + I_q \quad \text{in equation (4.3)}$$

4.7 PROBLEM FORMULATION AND SOLUTION

The equations for the flux quantities required for the solution of the problem are based on the model in Figure 4.1. The derivation of these equations is described in Appendix III.

The aim of the field solution is to find the air-gap flux density distribution for a given load. Equation (A3.8) in Appendix III gives this distribution by supplying the values of the total flux in the different air-gap paths. To achieve this, M_q, which is a function of ϕ must be found, hence the need to solve for ϕ.

ϕ is a function of the non-linear reluctivities ν_1^I, ν_2^I, ν_{3j}^I ($j = 1, 2, 3, \ldots n$) and ν_m. These reluctivities are non-linear functions of ϕ itself. ϕ is also a function of C, the armature current parameter which itself is a function of the internal power factor angle, ψ. The problem is thus reduced to the solution of a set of non-linear equations with independent ψ with an iterative process. The terminal voltage is computed together with the load power factor related to the load current and angle θ once a stabilised solution is found.

The flow chart for the program based on the discrete-reluctance method is described in Appendix IV.

4.8 LIMITATIONS OF THE DISCRETE RELUCTANCE METHOD PROGRAM

The comparison of terminal characteristics predicted by the program for a range of generators with the new rotor, with the results obtained experimentally, in the last chapter indicates the limitations of this

method and the program. The discrepancy between the predicted values and the experimental results has been shown in Figure 3.7 to be considerable on high loads. This feature can be attributed to the cumulative effect of several factors. These factors fall into two categories: those which are independent of the computational method and those which are due to the program and the computational method.

4.8.1 Limitations due to factors independent of the computational method

This class of factors encompass all the input data fed to the program. Each set of data includes the B-H characteristics of the iron and the magnet used for the construction of the rotor. The accuracy of the data describing these two curves is critical. A change in the iron characteristic would alter the level of saturation and a change in the characteristic of the magnet would alter the level of excitation. Figure 4.6 shows the effect of changing the B-H curve for the rotor iron. The effect of this change can be seen to be amplified as the load increases. This is due to the iron working in the non-linear regime of the B-H curve on high loads. This illustrates the importance of the accuracy of the B-H curves. The curves used for computation in this thesis are supplied by the manufacturers of the material and are assumed to be correct though the curves for iron is liable to be erroneous to a certain degree due to the different types of steel used.

The values of the armature resistance and the slot leakage reactance are also very important. The investigation into the effects of inaccuracies in the calculation of these values on the predicted terminal characteristics of machine C is presented in Figure 4.7. It shows a family of curves of different terminal characteristics predicted with different values of armature resistance and slot leakage reactance.

It can be seen that any inaccuracies in these two values would be magnified with load. This is because armature losses increase as the square of the armature current. In high frequency machines, the accuracy in the value of slot leakage reactance is essential as any inaccuracy would result in an exaggerated loss on load in the prediction.

4.8.2 Limitations due to the factors related to the program and the computational method

The accuracy of the program depends primarily on the accurate calculation of the reluctances involved. The geometry of the rotor is such that exact calculations of these values are impossible. Approximations and assumptions are used to facilitate the calculation of these reluctances. As a result of these approximations and assumptions, errors can arise in the calculation of the reluctance of the various flux paths in the iron and the magnet as well as that of the leakage flux paths.

Figures 4.8 and 4.9 show the flow of flux in iron path 1, iron path 2 and iron path 3 respectively. The program assumes that the axial reluctance in iron path 1 is negligible and is considered to have reluctance in the radial direction only. It also assumes that the reluctance is uniform over the whole region. It is clear from the direction of the flow of flux that these assumptions are not absolutely correct. The flux lines are not all radial throughout that iron path as can be seen in Figure 4.8. This introduces an approximation into the caluclation and thus a source of inaccuracy. Iron path 1 which is a disc-like sturcture, is used to guide the flux to the pole shoes. The flux density would vary radially, axially and tangentially. It would be denser as the radius increases due to the accumulation of flux from the magnet, and in the segmentswhere poles are attached due to the chanelling of flux to these poles. Thus the assumption that the

reluctance is uniform over the whole of this region is another source of inaccuracy. Iron path 3 is another region where the flux is not entirely radial; the division of this path into a number of separate paths as shown in Figure 4.10 for computation helps to improve the accuracy in the estimation of the length and area of leakage path 3.

Figures 4.3 and 4.4 show the leakage flux paths 1 and 2 in the new rotor. The paths are complicated as the geometry is irregular. An accurate value of the reluctance of each of these two paths cannot be calculated from the basic dimensions of the rotor. This is becuase the reluctance is a direct result of the length and area of the flux path, and these two leakages are three-dimensional. Arbitrary constants are used in the approximation of the reluctances of these two leakage flux paths. These constants are chosen by a trial and error procedure from the comparison of the experimental and the computational results of a particular machine. They may, therefore, be suitable for a particular machine but they are not universal. Figure 4.11 shows two families of curves, a and b, superimposed on Figure 3.7, which is the graph showing the correlation between predicted and measured values. These curves represent the effects of changing the reluctances approximated for the two leakage paths. The constants for calculating the reluctances vary between 67%and150% for leakage path 2 and between 50% and 200% for leakage path 1. The curves are plots of the difference between the results obtained with the new reluctances and the original values against load current. a_1, a_2, a_3 and a_4 are curves representing the results of changes of 150%, 130%, 77% and 67% in the value of the reluctance of leakage path 2 respectively. b_1, b_2, b_3 and b_4 show the effects of a change in the value of leakage path 1 of 200%, 150%, 67% and 50% respectively. These results relate to generator D. The figure shows the relative importance of leakage path 2. It is obvious that by

adjusting the constants used for the calculation of the reluctances of the two leakage paths, the correlation curve in Figure 3.7 can be smothered giving an increased accuracy in the predicted characteristic. The two leakages are very sensitive to the geometry of the new rotor. The introduction of arbitrary constants for their calculation is thus a source of error.

4.8.3 Shaft leakage

The importance of leakage flux in the new rotor has been discussed. It is therefore essential that any other sources of leakage be identified and taken into consideration in the field solution of the rotor. A conspicuous omission in the program is the leakage which occurs between the inner parts of adjacent flux guides. This is the only other major source of leakage and is shown in Figures 4.3 and 4.4. This leakage is referred to as leakage path 3. The GFUND[8,9] program was used to compute the leakage in this region. It was found to be 7.7% of useful flux per pole. Leakage of this order of magnitude is not negligible. To improve the existing program this leakage is taken into account. The circuital model in Figure 4.1 is modified to accommodate this improvement. The flux equations are charged accordingly. The equations in Appendix IIIhave incorporated the effect of shaft leakage. To account for this leakage, the reluctance of this path has to be determined. It can be found by using geometrical approximations or by the method of conformal transformation.

A comprehensive discussion of the conformal transformation method is described in a book by Binns and Lawrenson[10].

In the method employing conformal transformation, the boundaries of the region are represented on the Z-plane as in Figure 4.12a. By

symmetry, only half of it is required for the solution. Since impermeable surfaces are present, two transformations are required, a transformation into the t-plane, shown in Figure 4.12b, and finally into the p-plane, described in Figure 4.12c. The resulting field equation[10] is

$$W = \frac{1}{2\pi} \log \frac{(p-b)}{(p+b)}$$

where $p = 2\sqrt{t}$

Therefore the field equation in the t-plane is,

$$W = \frac{1}{2\pi} \log \frac{(2\sqrt{t}-b)}{(2\sqrt{t}+b)} \qquad (4.4)$$

where $$\frac{dz}{dt} = \frac{S\sqrt{(t^2-a^2)}}{\sqrt{(t^2-1)(t^2-b^2)}}$$

The solution of this Schwarz-Christoffel equation is shown in reference 10 (page 209).

$$W = If(t) \qquad (4.5)$$

$$\phi = \mu_o \mu_r W \qquad (4.6)$$

$$\phi = I\Lambda \qquad (4.7)$$

Equating equation (4.6) and (4.7)

$$\mu_o \mu_r f(t) = \Lambda \qquad (4.8)$$

but $$\Lambda = \mu_o \mu_r S/L \qquad (4.9)$$

where S is the cross-sectional area and L the length of the flux path.

Equating equations (4.8) and (4.9)

$$S/L = (f(t))$$

gives the reluctivity of the flux path.

The reluctance of leakage path 3 can also be found by geometrical approximations. The field equation for the leakage flux path in the shaft region is

$$\int H \, d\ell = \phi_3 (\Lambda_s) + \Phi_3 (\Lambda_m) + \phi_3 (\Lambda_s) \qquad (4.10)$$

Therefore $$\phi_3 (\Lambda_{L3}) = \phi_3 (2\Lambda_s + \Lambda_m) \qquad (4.11)$$

$$\Lambda_{L3} = \frac{2L_s}{S_s} + \frac{L_m}{S_m} \qquad (4.12)$$

where L_s, L_m, S_s, S_m are lengths and surface areas indicated in Figure 4.3.

The calculation of the reluctance of leakage path 3 using geometrical approximation is easier to incorporate into the existing program. This method was therefore adopted and implemented. The improvement of the predicted characteristics for machine D is shown in Figure 4.13.

4.8.4 Harmonics

A severe limitation of the discrete-reluctance mthod program is its inability to cope with harmonics. The calculation of the harmonics in the air-gap field with this method is inaccurate and unreliable. However, computational techniques can be used with this method to take the more prominent harmonics into consideration. This would be an improvement to the original program which utilises only the fundamental of the air-gap field for the calculation of the terminal characteristics. A scheme which could be incorporated into the discrete-reluctance method program to account for the third harmonic in the computation is shown in Figure 4.14. The scheme is as follows:

Step 1 : Using the rms of the load current, I_{rms}, and the armature reaction constant, ACN, the armature mmf distribution is set up.

Step 2 : The air-gap flux waveform is then computed.

Step 3 : The waveform is Fourier analysed and the fundamental and the third harmonic are used to calculate V_1 and V_3 (1, 3 denotes the harmonic number).

Step 4 : V_1 and V_3 are tested for convergence to a stable value by comparing them with their previous values.

Step 5 : I_1 and I_3 are calculated from the voltages extracted and the load resistance, R_L.

Step 6 : I_1 and I_3 are fed back to Step 1 to set up a new armature mmf distribution.

The whole process is repeated until stable values of V_1 and V_3 are found.

4.8.5 Eddy Currents

The discrete-reluctance method program ignores the effects of eddy currents. This introduces an error to the prediction of the output characteristics of the generators as eddy current losses are not accounted for. These losses are frequency dependent and would increase in importance in high-speed machines. The assumption neglecting this effect is implemented despite the possible error it could introduce, to simplify the computation. The influence of eddy current losses on the load characteristics of permanent magnet generators can be assessed experimentally by running it over a range of speeds. This experiment is described in Chapter 3. The results show that eddy current losses in these machines are negligible at 50 Hz.

4.9 CONCLUDING REMARKS

The discrete-reluctance method, despite its limitations, is simple and easy to implement. The program based on this method of analysis is cheap and fast in computer terms. The limitation of this program and the method has been discussed and certain improvements have been introduced where applicable. The program is still far from accurate at high loads and is therefore still not entirely satisfactory. It is, however, a useful design aid. Its low running cost and high speed are attractive features as a design aid especially when an interactive computing facility is employed.

Research using a 3-dimensional finite-element technique for the field analysis of the new rotor is described in the following chapters. They provide a more accurate analysis of the new permanent-magnet generator. It is also used to improve the discrete-reluctance program by checking the assumptions used for the estimation and approximation of the flux paths in the iron, and the leakage fields in the new rotor.

4.10 REFERENCES

1. KURDALI, A. : 'Analysis of and the performance of a permanent-magnet alternator with disc magnets', Ph.D. Thesis, Southampton University, 1979.

2. SAUNDERS, R. H. and WEAKLY, H. : 'Design of permanent magnet alternators', Trans. A.I.E.E., Vol.70, Part II, pp. 1578-1581, 1951.

3. STRAUSS, F. : 'Synchronous machines with rotating permanent magnet fields, Part II : Magnetic and electrical designs considerations', Trans. A.I.E.E., Vol. 71, Part III, pp. 887-893, 1952.

4. CARTER, F. W. : 'Note on air-gap and interpolar induction', Journal of the I.E.E., Vol. 29, p. 925, 1900.

5. CARTER, F. W. : 'The magnetic field of the dynamo-electric machine', Journal of the I.E.E., Vol. 64, p. 1,115, 1926.

6. JABBAR, M. A. : 'Analysis of the performance of a permanent-magnet A.C. machine', Ph.D. Thesis, Southampton University, 1977.

7. BINNS, K. J., JABBAR, M. A. and BARNARD, W. R. : 'Computation of the magnetic field of permanent magnets in iron cores', Proc. I.E.E., Vol. 122, No. 12, pp. 1377-1381, 1975.

8. SIMKIN, J. and TROWBRIDGE, C. W. : 'Magnetic fields computed using an integral equation derived from Green's Theorems', RL-76-041, Rutherford Laboratory, 1976.

9. TROWBRIDGE, C. W., ARMSTRONG, A. G., COLLIE, C. J., DISERENS, N. J. NEWMAN, M. J. and SIMKIN, J. : 'New development in the magnet design program GFUN', RL-75-066, Rutherford Laboratory, 1975.

10. BINNS, K. J. and LAWRENSON, P. J. :'Analysis and Computation of electric and magnetic field problems', Pergamon, Oxford, 1963.

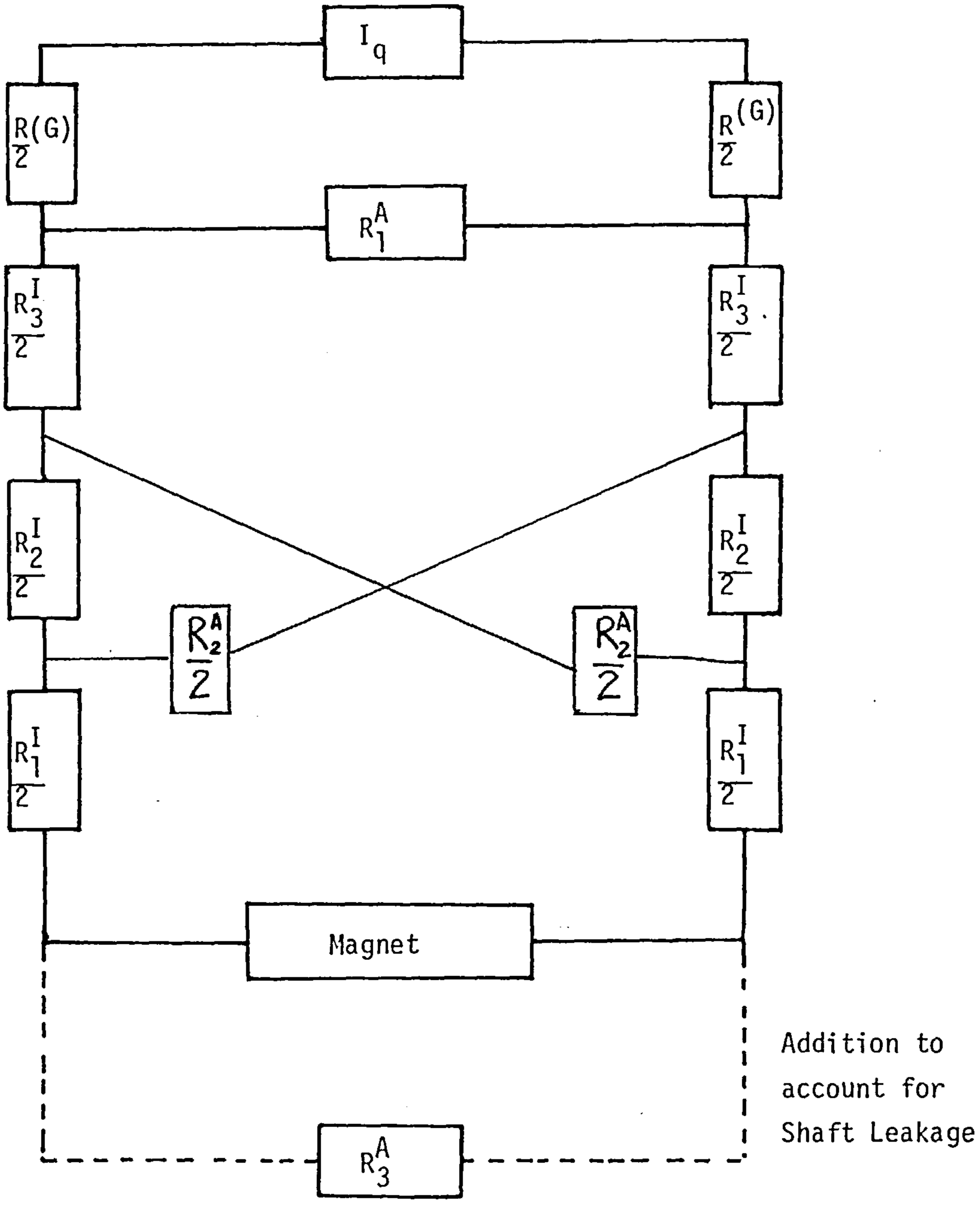

Fig. 4.1 Circuit for branch q.

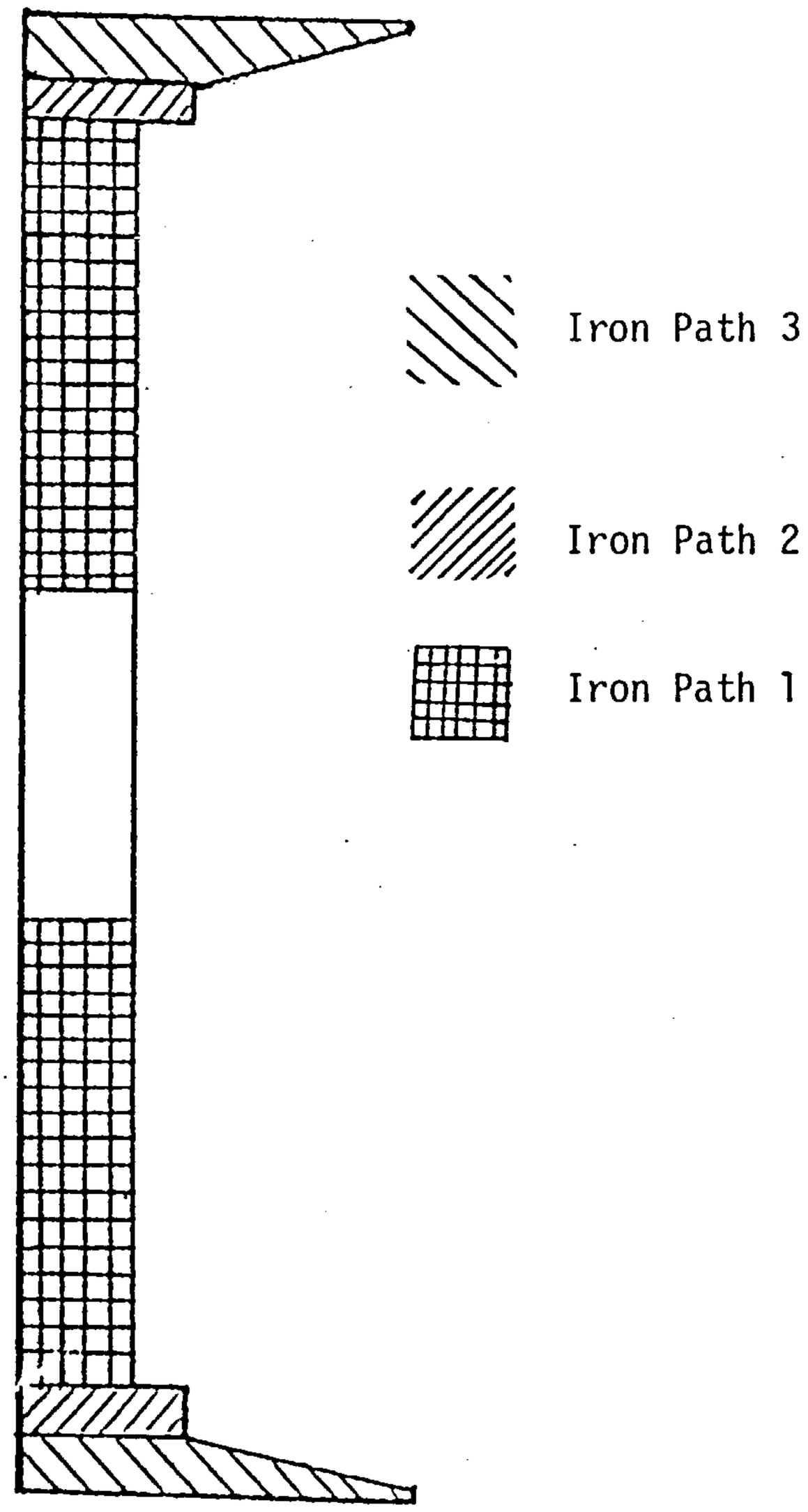

Fig. 4.2 A cross-section of the steel flux guide showing the three iron paths.

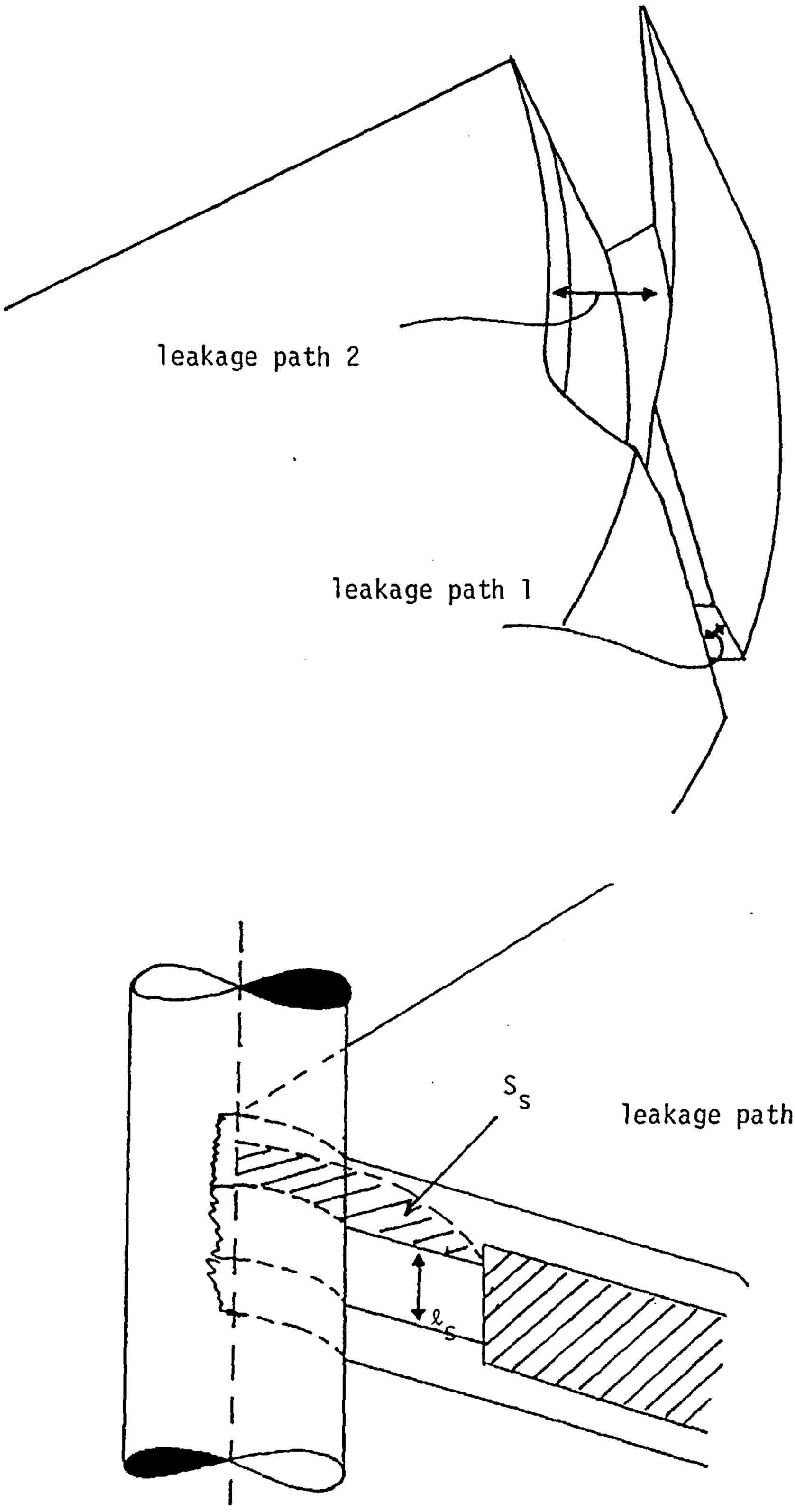

Fig. 4.3 A 3-dimensional view of the leakage paths.

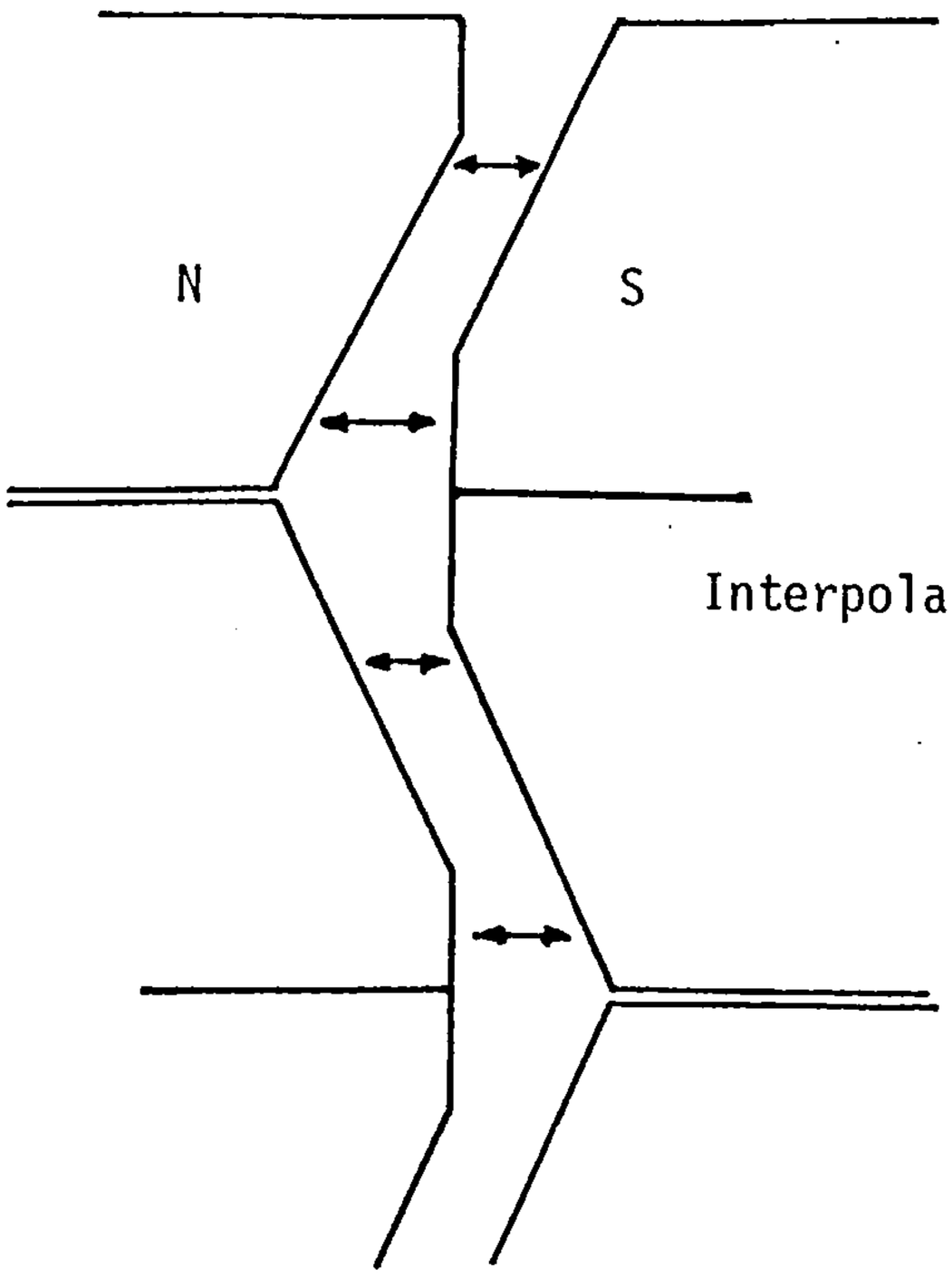

Interpolar leakage

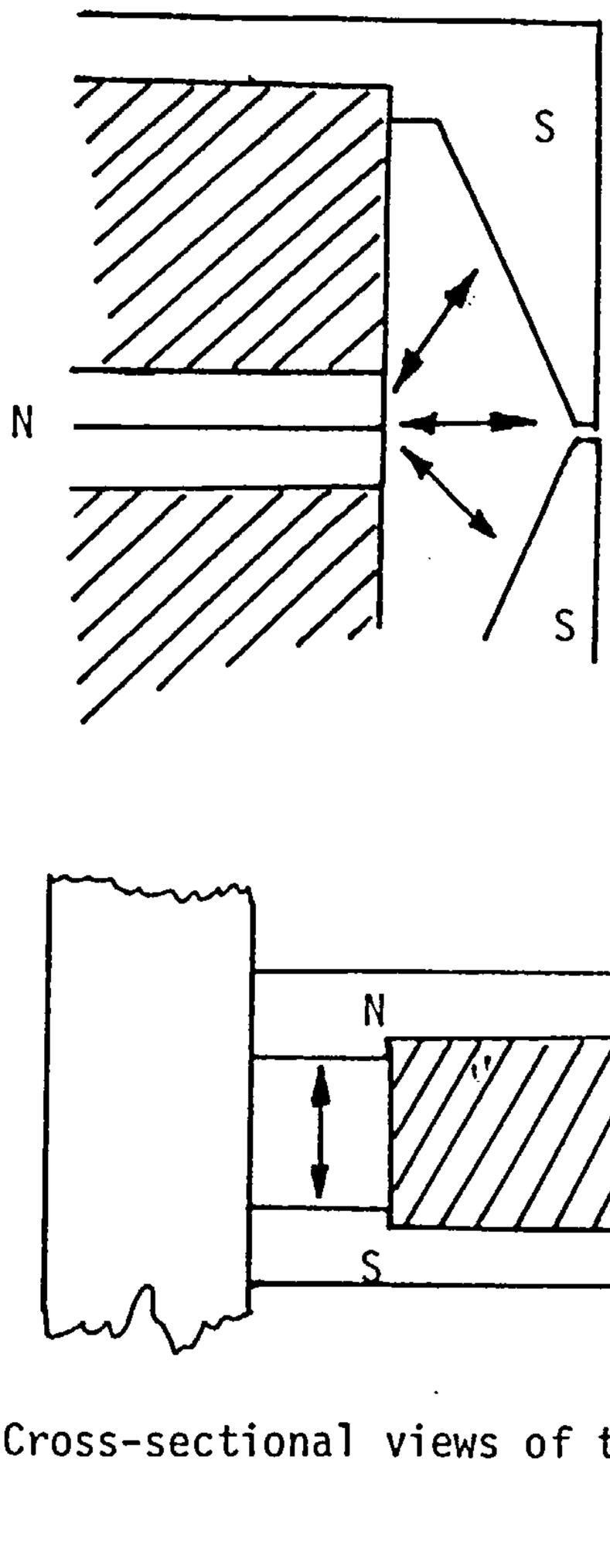

Leakage between the underside of the pole and the steel discs

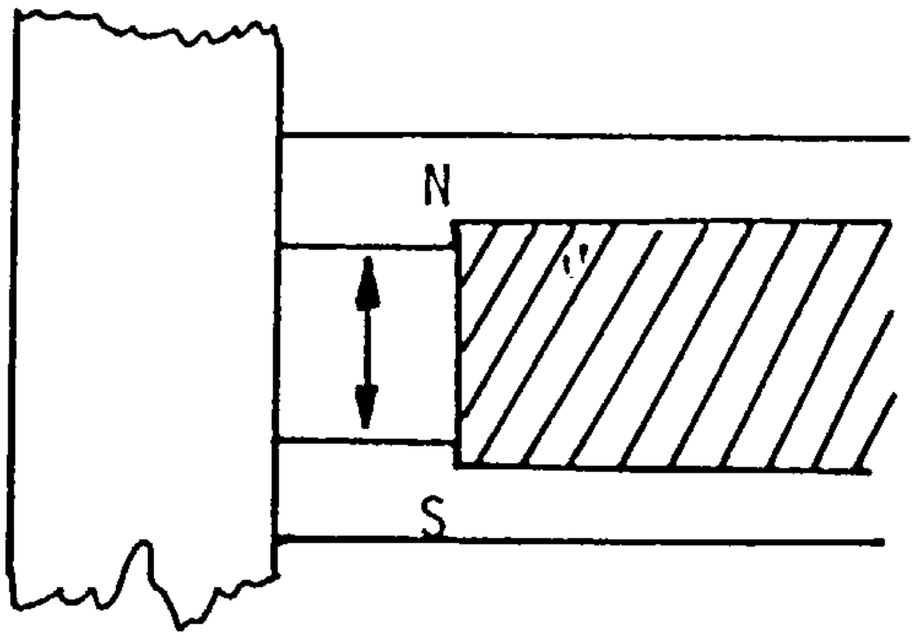

shaft leakage

Fig. 4.4 Cross-sectional views of the leakage paths.

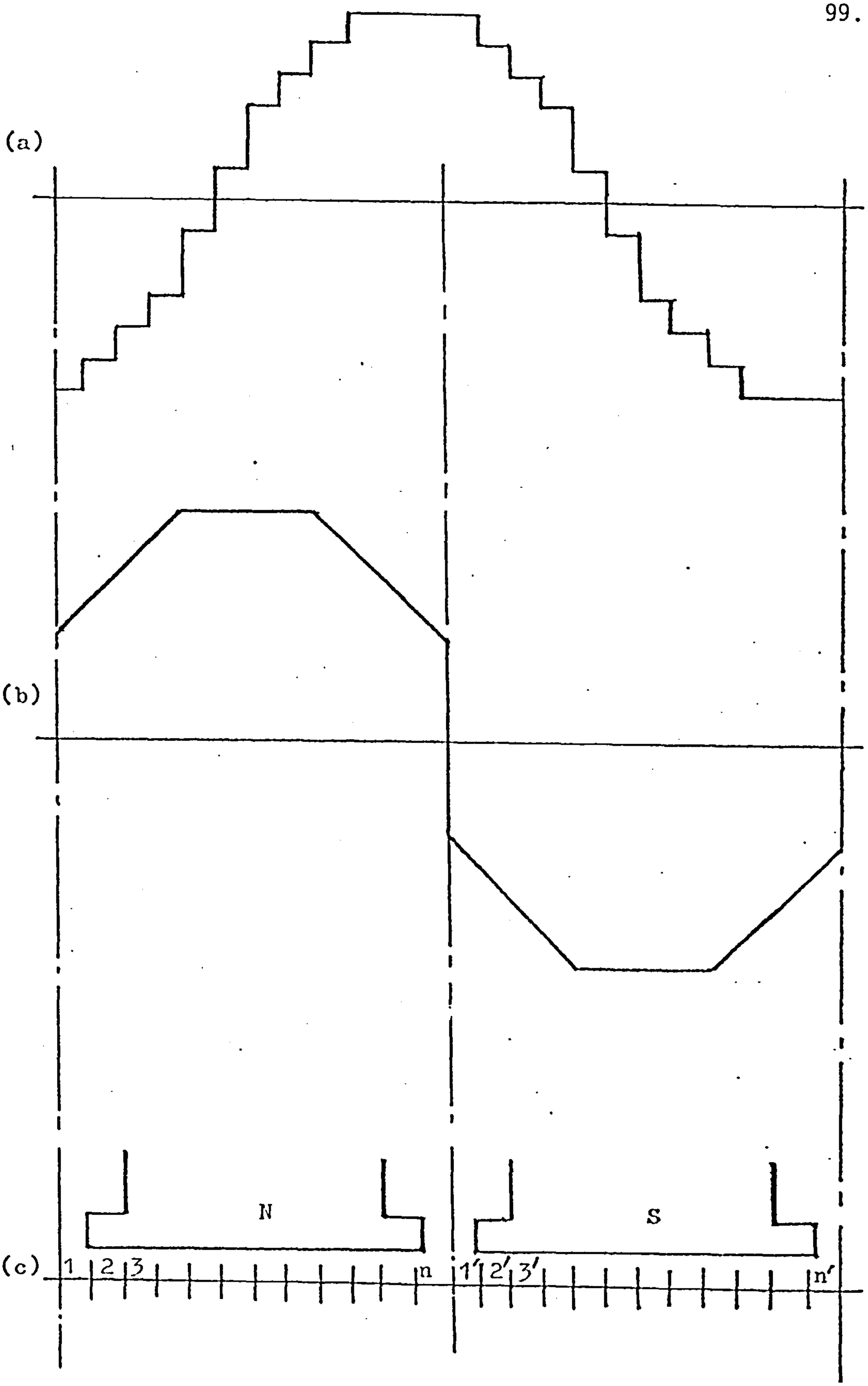

Fig. 4.5 Surface pole sections and m.m.f. distribution.
(a) a typical armature mmf pattern.
(b) the effect of pole shaping on the air-gap permeances.
(c) The air-gap region divided into flux paths.

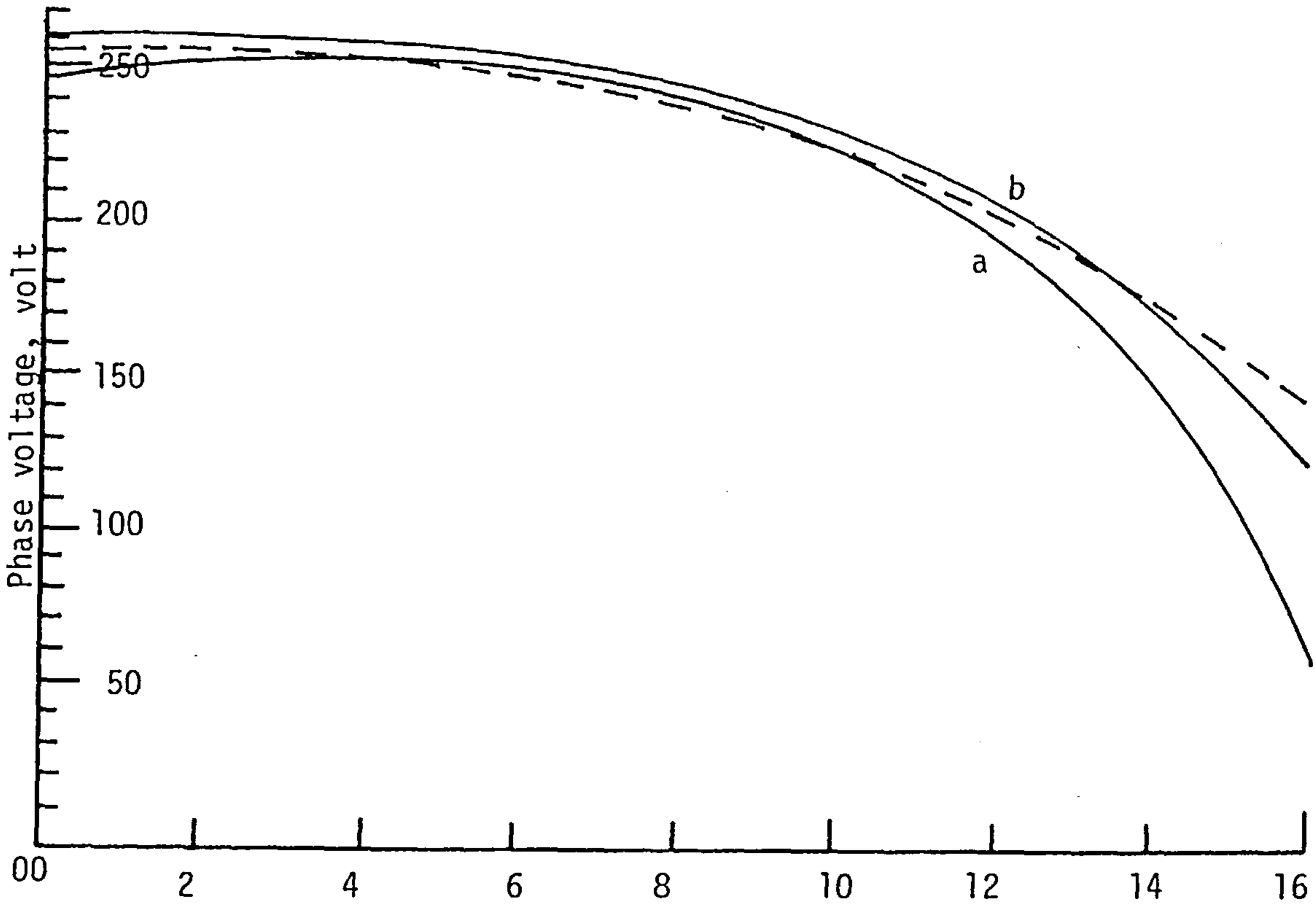

– – – – – measured phase voltage

a
——— predicted phase voltage with original B-H curve

b
——— predicted phase voltage with H values increased by 1%

Fig. 4.6 The effect of a change in B-H characteristics on the prediction.

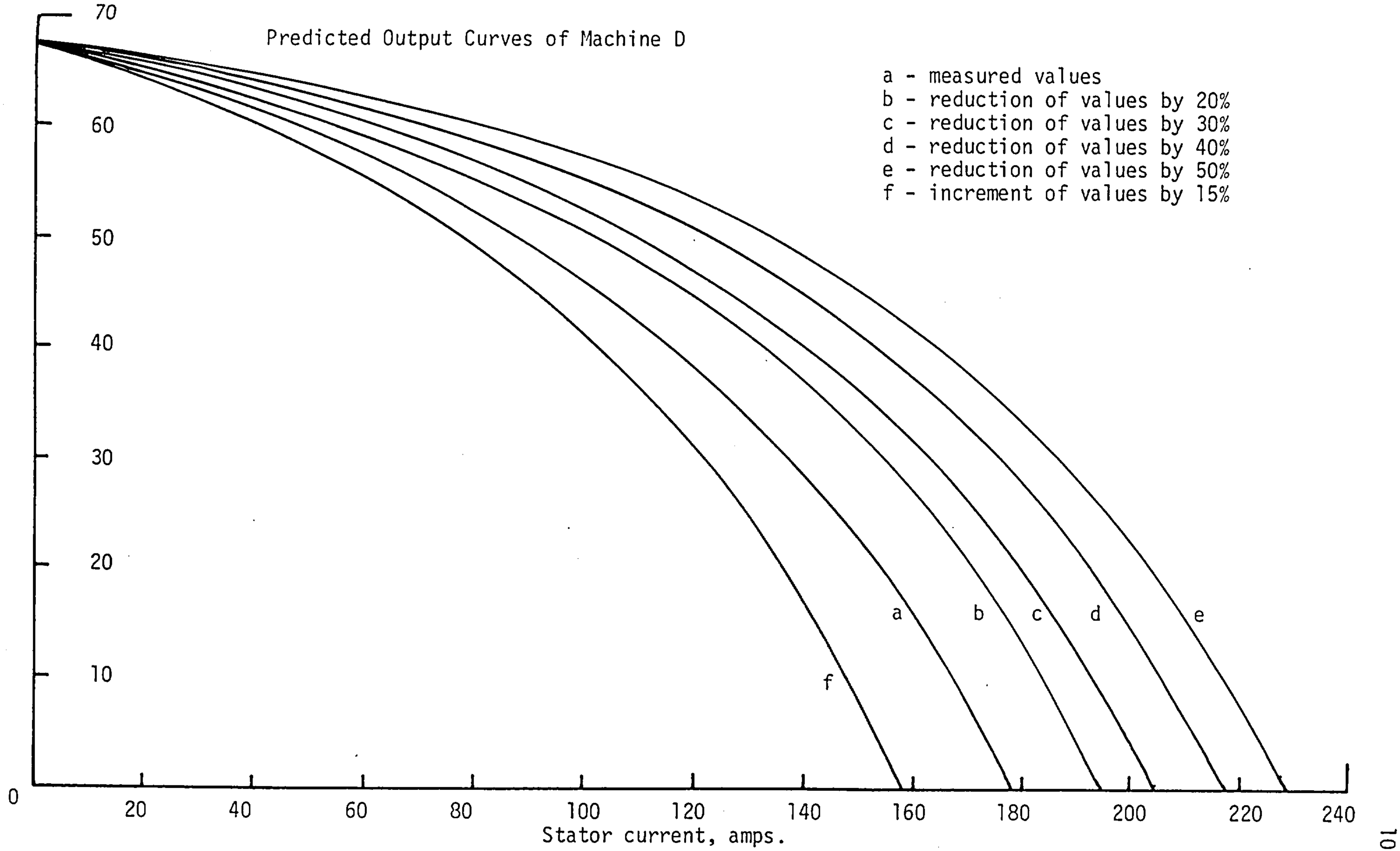

Fig. 4.7 The effect of changes in armature resistance and reactance on predicted terminal characteristics.

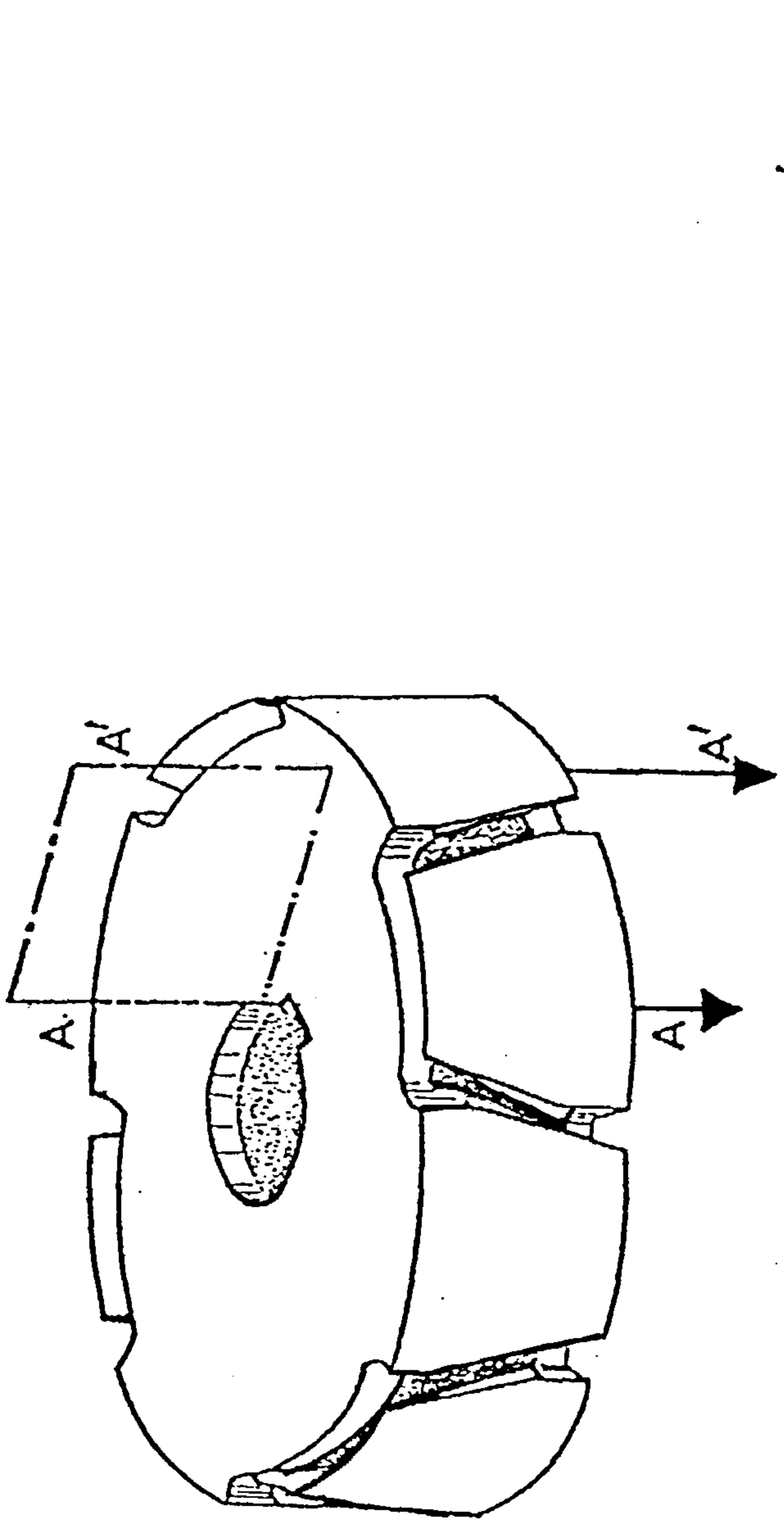

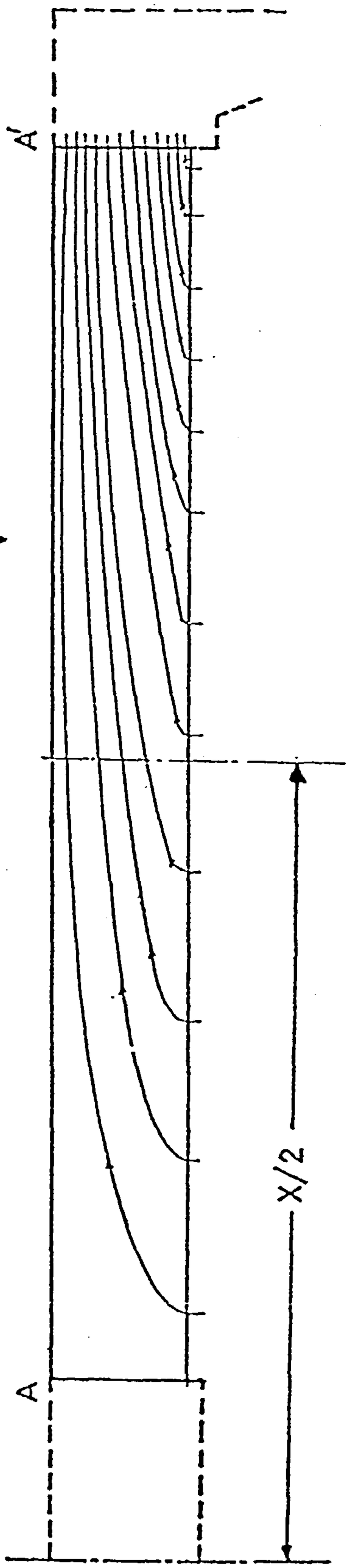

Fig. 4.8 A cross-section in iron path 1.

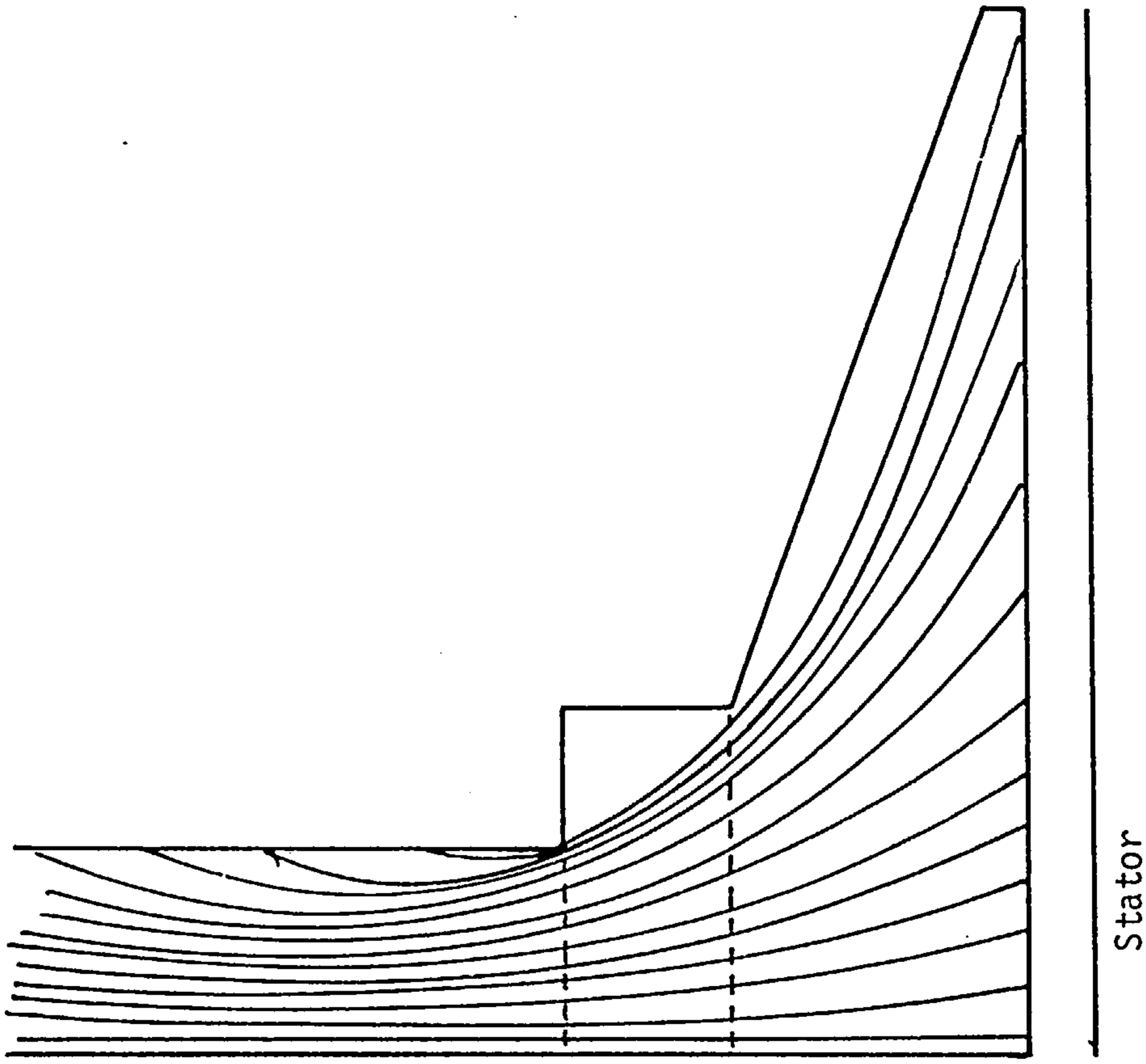

Fig. 4.9 Cross section of the flux guide showing the flow of flux in iron paths 2 and 3.

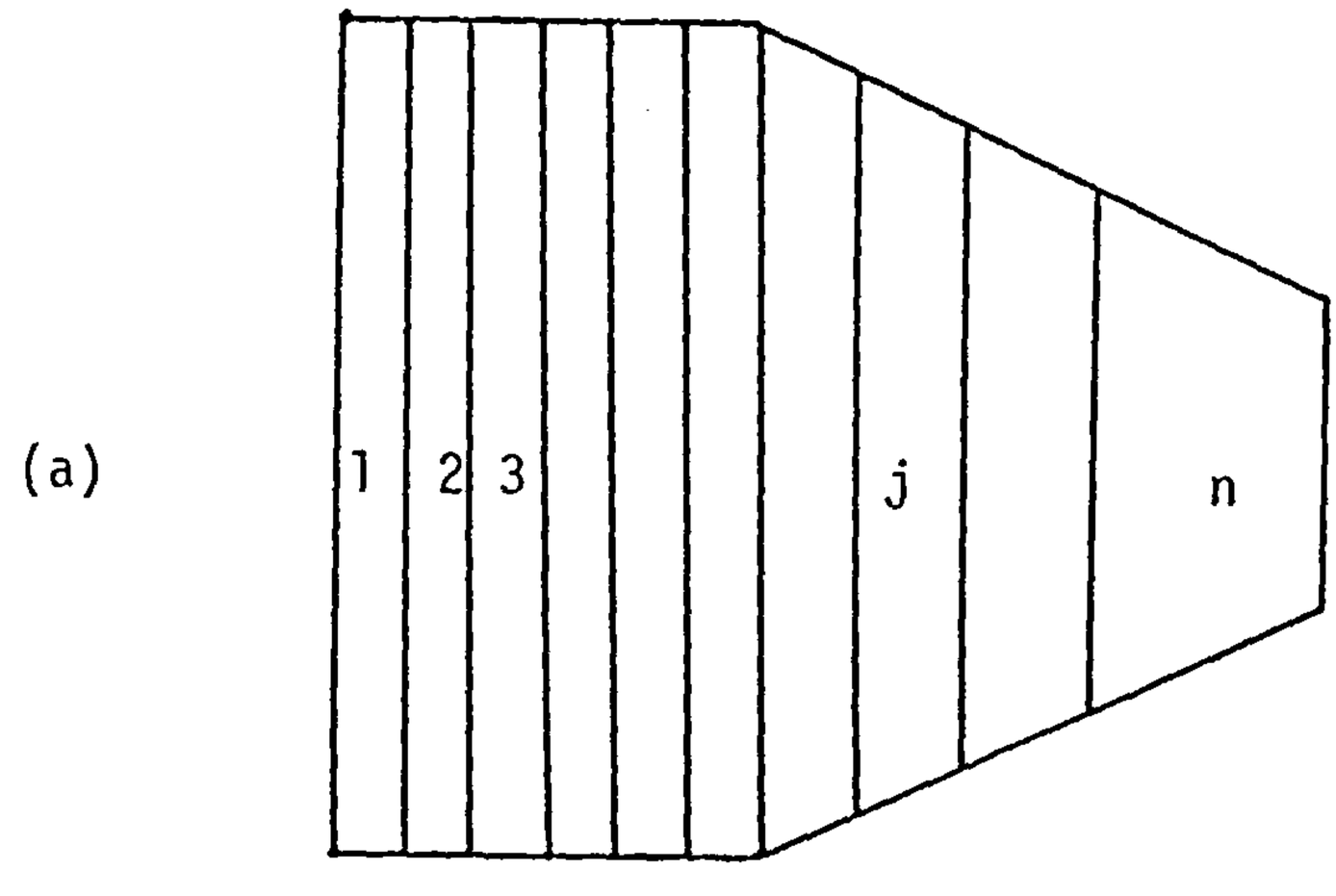

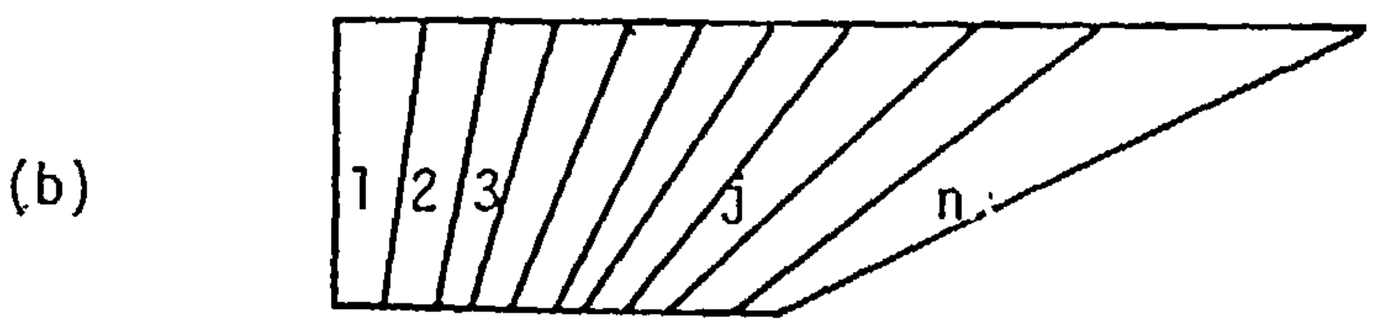

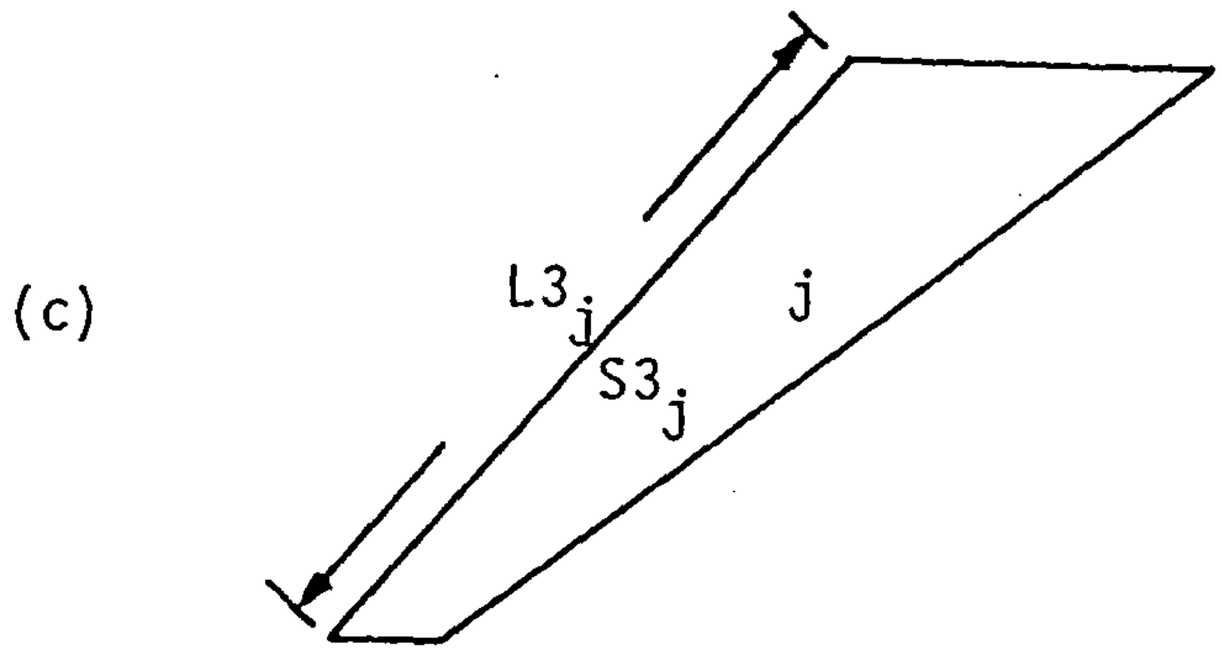

Fig. 4.10 The division of iron path 3.

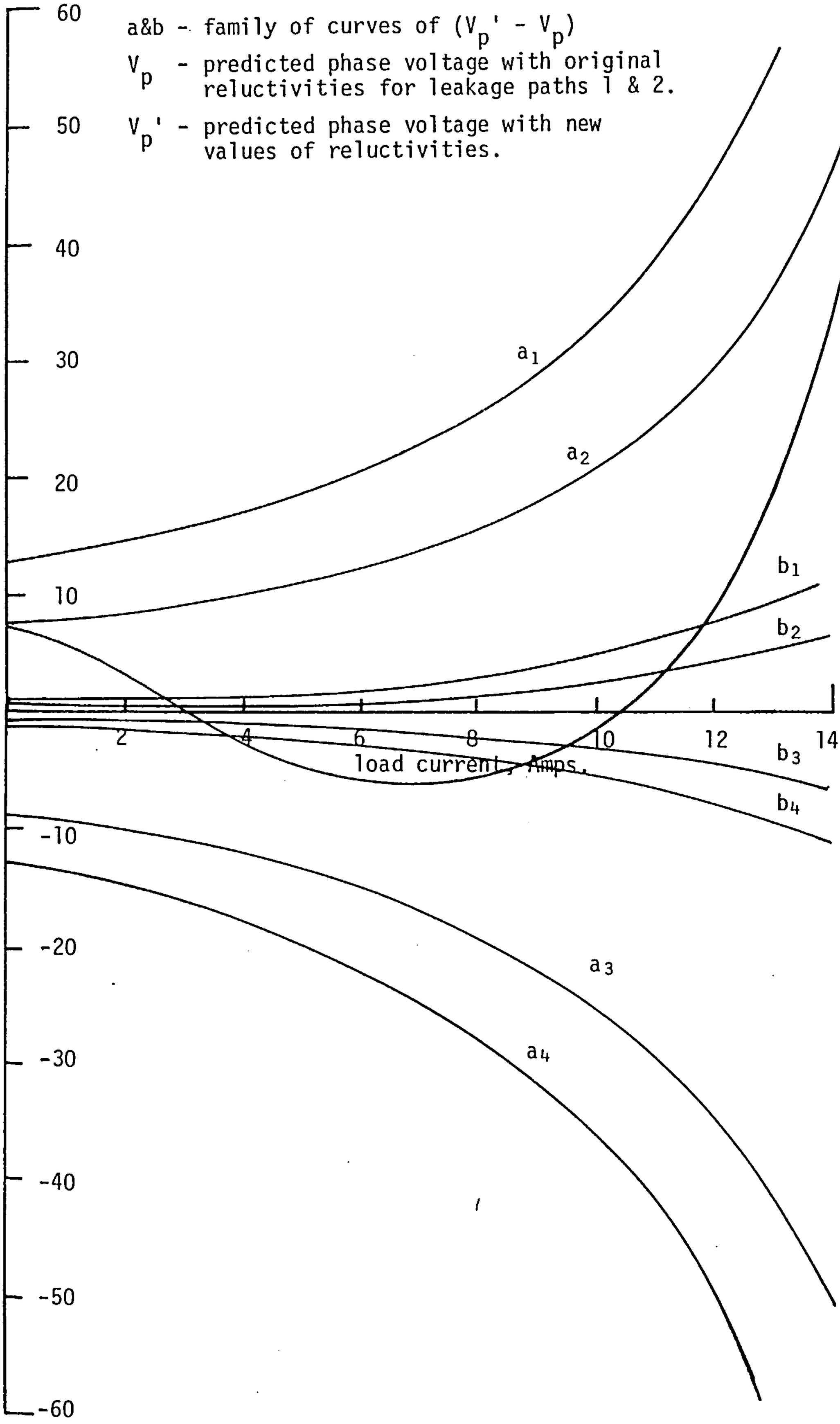

Fig. 4.11 Effect of changes in the leakage flux reluctivities on the predicted output.

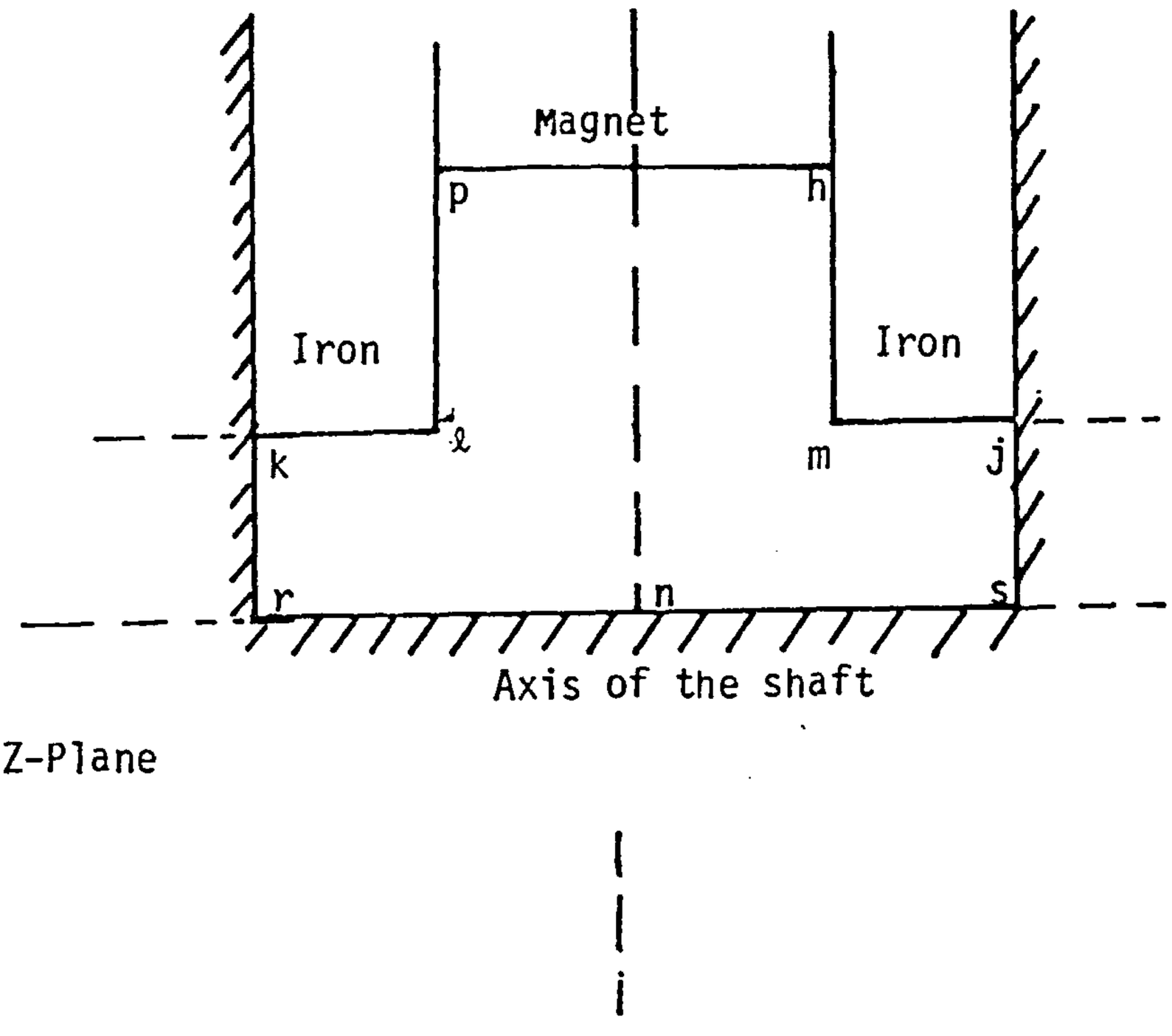

Note: ////// are impermeable surfaces.

Fig. 4.12 The transformations of the boundary of the shaft leakage.

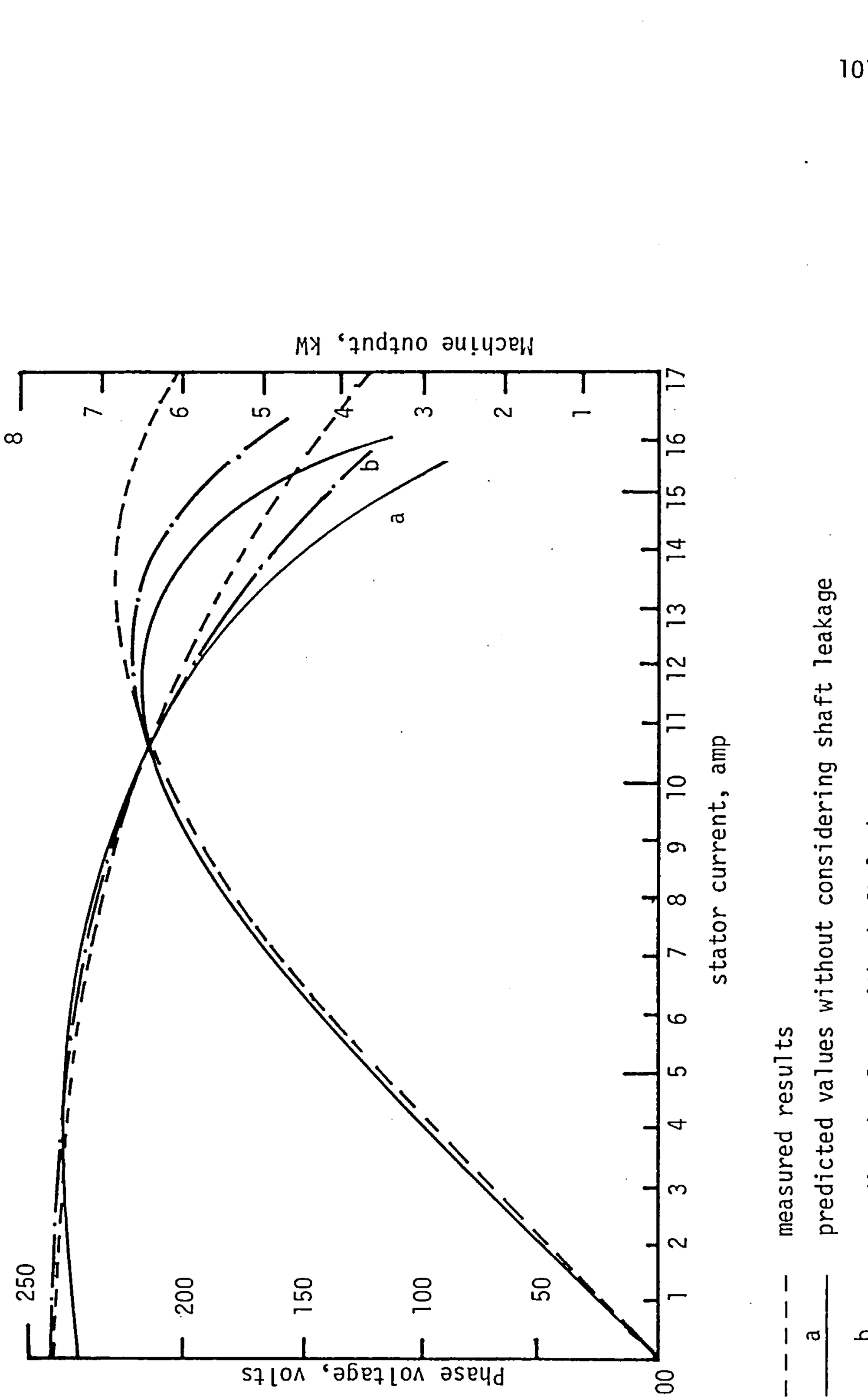

Fig. 4.13 The improvement in prediction with the inclusion of shaft leakage.

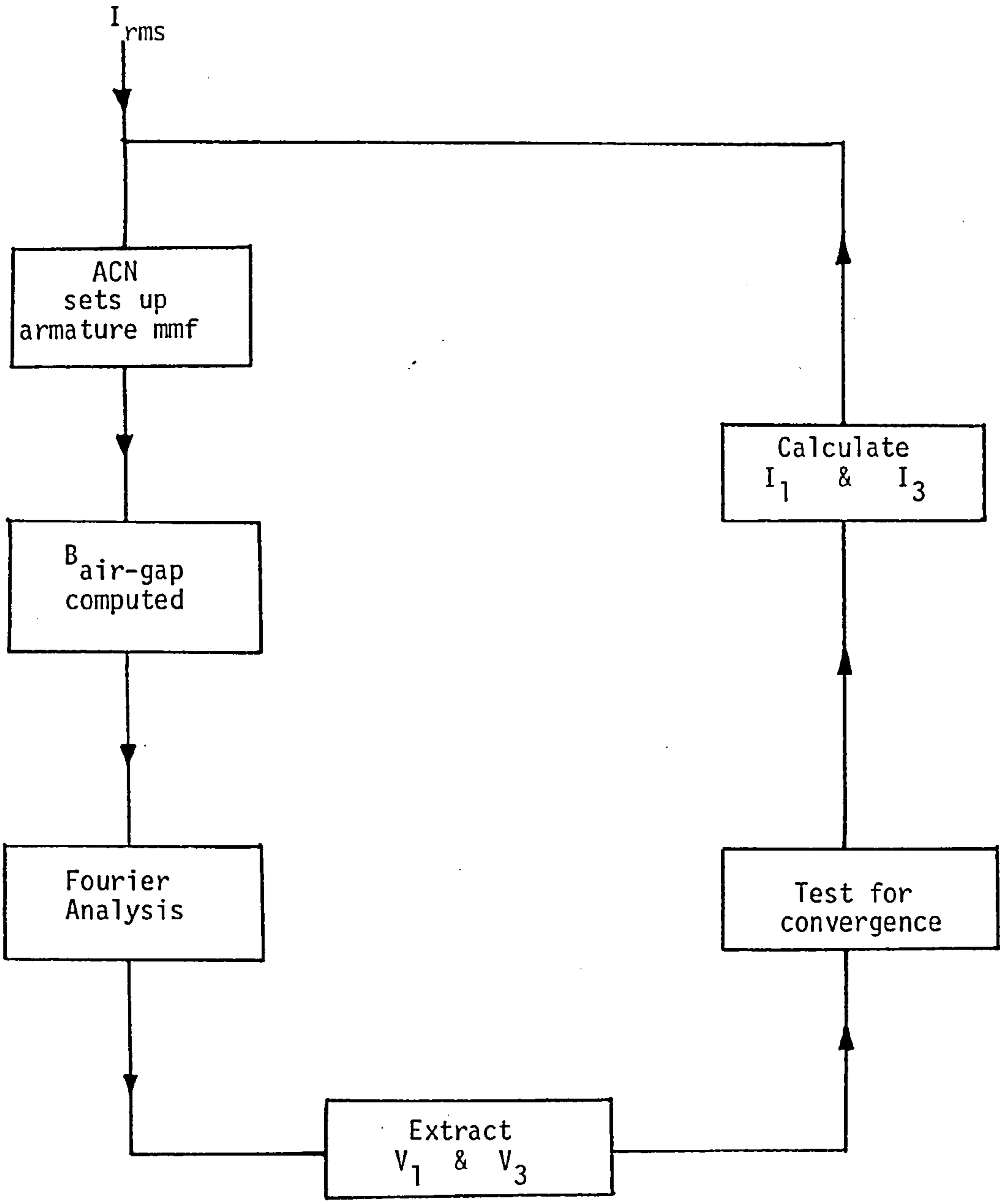

Fig. 4.14 Scheme for the inclusion of the third harmonic in the prediction of terminal characteristic.

CHAPTER FIVE

THREE DIMENSIONAL FINITE ELEMENT FIELD ANALYSIS OF THE IMBRICATED ROTOR

CHAPTER FIVE

THREE-DIMENSIONAL FINITE ELEMENT FIELD ANALYSIS OF THE IMBRICATED ROTOR

5.1 INTRODUCTION

There are many methods suitable for use in the solution of the three-dimensional field of the new rotor. Methods already used to solve this complicated field include an integral equation method[1,2]. The GFUN3D program is based on an integral equation method and employs Green's function to transfer the field equations into integral equations. The formulation of the problem leads to integral equations in terms of the unknown magnetisation vector, M. The use of this method for solution requires discretisation in the iron and magnet regions only and the need for false boundaries is eliminated. This method is not satisfactory as it requires excessive storage and computing time[3]. Another method used is the discrete-reluctance method which has been discussed in the last chapter.

An alternative to these two methods is one which uses scalar potentials for the solution of magnetostatic fields[4,5]. The three-dimensional problem is formulated using a combination of two scalar potentials. The advantage in the use of scalar potentials for three-dimensional field analysis lies in the fact that there is only one unknown quantity to solve for each mesh point. Formulation of the problem is based on total scalar potential in current-free regions and reduced scalar potential elsewhere. This procedure has been used to solve two-dimensional and three-dimensional magnetostatic problems with success, using differential finite-element formulation[4,5]. A program based on this procedure is called TOSCA.

5.2 TOSCA

TOSCA is a three-dimensional differential operator finite-element program. It solves the non-linear Laplace equation with particular emphasis on magnetostatic fields[4,5].

5.2.1 Field Equations and the Choice of Potentials

In order to be able to use scalar potential and have current, the total field has to be divided into two parts: the field from conductors carrying currents ($\bar{H}_s$) and the remainder of the field ($\bar{H}_m$) which can be represented as the gradient of a scalar potential ($-\nabla\psi_R$). This division results in the calcellation of the two components of the total field intensity where permeability is large. Consequently, accuracy is poor. To overcome this problem, a potential (ψ_T) whose gradient is the total field, is used. This is only possible on the condition that the region is current free.

Hence, to solve a magnetostatic problem which has current-carrying conductors, the space must be divided into regions, those which include current donductors and those that do not. In the former, the reduced scalar potnetial (ψ_R) is used and in the other, the total scalar potential (ψ_T) is used.

The total field H is the sum of,

$\underline{H}_s$ - the field of the sources, and

$\underline{H}_m$ - the field from the induced magnetisation (supplied by the permanent magnets)

$$\underline{H} = \underline{H}_m + \underline{H}_s \tag{5.1}$$

$\underline{H}_s$ is known from $\underline{J}$, the current density.

$$\underline{H}_s = \frac{1}{4\pi} \int_{\Omega_J} \underline{J} \times \left(\frac{1}{R} \right) d\Omega \tag{5.2}$$

where Ω_J is the space occupied by the region containing current-carrying conductors, and $R = |\underline{r}' - \underline{r}|$ is the distance between the source point $\underline{r}'$

and the field point $\underline{r}$,

or $\nabla X \underline{H}_s = \underline{J}$

this implies that $\nabla X \underline{H}_m = 0$

Therefore $\underline{H}_m$ can be expressed as the gradient of a scalar potential (ψ_R)

$$H_m = -\nabla\psi_R \tag{5.3}$$

with $\phi = \frac{1}{4\pi}\int_{\Omega_I} \underline{M} \cdot \nabla\left(\frac{1}{R}\right) d\Omega$

Ω_I is the space occupied by regions which are current free.

The fundamental magnetic quantities $\underline{B}$, $\underline{H}$, and $\underline{M}$ are related by,

$$\underline{B} = \mu(|\underline{H}|)\, H$$

$$= \mu_o\,(\underline{H} + \underline{M}) \tag{5.4}$$

$$\underline{M} = \chi\,(|\underline{H}|)\,\underline{H}$$

$$\text{with } \nabla.\underline{B} = 0 \tag{5.5}$$

from equations (5.1), (5.3) and (5.4)

$$B = \mu(\underline{H}_s - \nabla\psi_R)$$

if $\underline{H}_s$ is large compared with $\underline{H}$, it is preferable to solve for $\underline{H}$ directly instead of ψ_R. For current-free regions, this can be done by solving for the total scalar potential.

$$\underline{H} = -\nabla\psi_T \text{ (valid when } \nabla X \underline{H} = 0) \tag{5.6}$$

This results (by equation (5.5)) to

$$\nabla \cdot (-\mu\nabla\psi_T) = 0 \quad \text{(when valid)} \tag{5.7}$$

$$\text{and} \quad \nabla \cdot (-\mu\nabla\psi_R + \mu\underline{H}_s) = 0 \quad \text{(elsewhere)} \tag{5.8}$$

These are non-linear partial differential equations of the Laplace and Poisson type respectively.

In addition to the external boundary conditions such as, $\psi_R = 0$ at infinity for example, there are interface conditions between a ψ_T region (subscript 1) and a ψ_R region (subscript 2).

$$-\mu_1 \frac{\partial \psi_T}{\partial n} = \mu_2 \left(-\frac{\partial \psi_R}{\partial n} + \underline{H}_{s_n}\right) \tag{5.9}$$

$$-\frac{\partial \psi_T}{\partial t} = -\frac{\partial \psi_R}{\partial t} + \underline{H}_{s_t} \tag{5.10}$$

where n and t denote the normal and tangention components respectively. The integration of equation (4.10) gives the contribution of ψ_s to the total potential

$$\psi_s = \psi_T - \psi_R = -\int \underline{H}_{s_t}\, dt \tag{5.11}$$

Hence, the knowledge of $\underline{H}_s$ on the interface is sufficient to determine the problem. Thus equation (5.11) is more important than equation (5.10). The arbitrary constant in equation (5.11) is removed by equating ψ_T and ψ_R at an interface point.

5.2.2 Differential Formulation

The partial differential equations (5.7) and (5.8) are to be solved simultaneously by dividing the space into finite elements and applying a weighted residual technique. In region 1, which contains the non-linear iron, the residual equation is:

$$R_1 = \int_{\Omega_1} W\nabla \cdot (-\mu\nabla\psi_T)\, d\Omega \tag{5.12}$$

and in region 2, which is free space with conductors, the residual equation is

$$R_2 = \int_{\Omega_2} W\nabla \cdot (-\nabla\psi_R)\, d\Omega \tag{5.13}$$

(since $\nabla \cdot \underline{H}_s = 0$)

for any suitably chosen weighting function W.

These two equations are transformed by Green's theorem to

$$R_1 = \int_{\Omega_1} \mu\nabla W \cdot \nabla\psi_T\, d\Omega - \int_{S_1} \mu W\nabla\psi_T \cdot d\underline{s} \tag{5.14}$$

$$R_2 = \int_{\Omega_2} \nabla W \cdot \nabla\psi_R\, d\Omega - \int_{S_2} W\nabla\psi_R \cdot d\underline{s} \tag{5.15}$$

This requires W to be continuous across the interface and differentiable within regions Ω_1 and Ω_2. This is a reasonable assumption[5]. By setting $R_1 + R_2 = 0$,

$$\int_{\Omega_1} \mu \nabla W \cdot \nabla \psi_T \, d\Omega + \int_{\Omega_2} \nabla W \cdot \nabla \psi_R \, d\Omega = \int_{S_1} W \left(\mu \frac{\partial \psi_T}{\partial n} - \frac{\partial \psi_R}{\partial n} \right) ds$$

$$= \int_{S_1} W \underline{H}_{s_n} \, ds \qquad (5.16)$$

A set of basic functions N(x, y, z) is chosen so that in each of the elements

$$U = N_1 U_1 + N_2 U_2 + N_3 U_3 + \ldots$$

where U is ψ_T or ψ_R. U_i is the value of U at the element node I, and N_i is 1 at node i and 0 everywhere else. The Galerkin procedure is used to choose a weight function for each node. Equation (5.16) then yields one equation for each node i:

$$\sum \left\{ \left(\psi_R \int \mu \nabla N_i \cdot \nabla N_j \, d\Omega + \psi_{Rj} \int \nabla N_i \cdot \nabla N_j \, d\Omega \right) - \int_{S_1} - N_i \underline{H}_{s_n} \, ds \right\} = 0 \qquad (5.17)$$

The result of equation (5.17) is a set of n linear equations for the U_i of the form

$$K_{ij} U_j = Q_i \qquad (5.18)$$

in which K_{ij} is a banded symmetric matrix with elements which are sums of term like:

$$K_{ij} = \int \mu \nabla N_i \cdot \nabla N_j \, d\Omega \qquad (5.19)$$

and Q_i are mostly zero, except for terms of the forms

$\sum \int N_i \underline{H}_{s_n} \, ds$ and $K_{ij} \int^{t_j} \underline{H}_{s_t} \, dt$.

5.3 THE ANALYTICAL MODEL OF THE ROTOR

The use of the three-dimensional finite-element program, TOSCA, for the field analysis of the new rotor, requires the representation of the rotor in a manner acceptable to the program. The choice of a model would have to take into consideration the accuracy desired, computer storage in relation to the number of elements available and the ease in discretisation.

In representing the rotor a balance between accuracy and the reduction of the number of mesh elements has to be achieved. The geometrical and field symmetry are exploited to reduce the number of mesh elements, thus decreasing computer storage demand, without a deterioration in the accuracy of the computed result. In all other circumstances, the decrease in the number of mesh elements would be at the expense of accuracy in the computed results. A basic unit of the new rotor comprises two flux guides and a disc magnet as shown in Figure 2.1. This unit does not need to be represented fully. By invoking geometrical and field symmetry a segment which spans 180 electrical degrees, from mid-North pole to mid-South pole would be sufficient for analysis. Figure 5.1 shows the segment used for analysis by the three-dimensional finite-element program. This representation is applicable for the no-load (open-circuit) condition. In the load case, a span of 360 electrical degrees or 2 pole pitches is required to cover the symmetry of the armature mmf due to the armature current. However, if repeatability boundary conditions are imposed, a segment spanning 1 pole pitch would be sufficient.

5.4 STATOR REPRESENTATION

The stator is assumed to be smooth. This assumption is justified as the primary concern is the design of the rotor. The effects of

slotting on the air-gap field is, however, given due consideration and is taken into account using a method described by Carter[6,7], which employs a coefficient now known as Carter's coefficient (σ). σ can be defined as the loss of peripheral section per slot width.

$$\sigma = \frac{2}{\pi} \tan^{-1} \left(\frac{X}{2} \right) - \left\{ \frac{\log \left(1 + \left(\frac{X}{2} \right)^2 \right.}{X} \right\}$$

where $X = \frac{S}{g}$ and S is the slot width and g is the air-gap clearance. Using the coefficient above a gap extension factor is determined using

$$G_m = \frac{1}{1 - \frac{s\sigma}{s+t}}$$

where t is the tooth width.

Armature slotting also causes a reduction in the permeable material in the stator and thus increases the magnetostatic potential difference across a tooth due to saturation. In fact tooth saturation demands more mmf in this region and reduces the available ampere turns in the air-gap, thus the overall air-gap flux is also reduced. To account for this effect, a material of different permeability μ_t can be used for the slotted region where

$$\mu_t = \mu \frac{t}{s+t} + \mu_o \frac{s}{s+t} .$$

5.5 THE DISCRETISATION OF THE MODEL

TOSCA requires discretisation throughout the space occupied by the problem. To discretise the model described above into an acceptable mesh for the 3-dimensional finite-element program to work on, the TOSCA pre-processor[8] is used. The mesh can have any connectivity (topology) in a plane but it must always have the same connectivity in all the other logical planes in the third dimension. The mesh structure needs to be planned. The maximum mesh complexity needed for the model has to be

defined in the base plane. On the completion of the node definition in the base plane, the quadrilateral blocks are defined by specifying the connection between the nodes, forming the topology of the base plane. The subdivisions can then be specified in the blocks to determine the mesh intensity of each block.

Mesh extensions in the third dimension, normally the z-direction, are implemented after the definition of the base plane. The global z-coordinate of the next mesh plane is specified. Individual node coordinates can then be changed in this mesh plane. By joining the nodes of each mesh plane with the corresponding nodes of the plane immediately above it, hexahedral bricks are formed. In this manner, layers of three-dimensional blocks, which are subdivided into elements, are formed. Once the entire space occupied by the problem is discretised, the material and potential types of the blocks are defined. The potential types are either total or reduced as had been discussed. In the new rotor, all the blocks are total potential types with the exception of the air-gap region which has current-carrying conductors. The material types present in the new rotor are: the stator iron, the rotor iron, the magnet and air.

The final phase of the data preparation is the definition of the boundary. The choice of the boundary conditions is very important and is discussed in detail in sub-section 5.5.2.

5.5.1 The Basic Blocks and Choice of Subdivisions for the New Rotor

Polar coordinates, radius (R), angle (θ) and thickness (z) are used in the data preparation and the field computation of the new rotor using TOSCA. Figure 5.2 shows a typical flux guide of the new rotor. It is for an eight-pole generator. The dimensions in Figure 5.2 are those of Generator A. The segment required for discretisation to represent a rotor unit employing this flux guide would be 45^{o}. The base plane of

this unit is shown in Figure 5.3. This topology is the simplest possible whilst maintaining the required connectivity and the differentiation of material types and potential types. There are three basic divisions in θ which are due to the two overlapping poles and the inter-polar gap. The divisions along the radial direction are determined by the different radii shown in Figure 5.2(b), defining the boundary of the iron paths, the air-gap and the stator.

The extensions in the third dimension which is the z-direction is governed by the geometry of the flux guide. The basic layers of this new rotor is shown in Figure 5.4. It shows the five layers and how the layers relate to the geometry of the flux guide.

The blocks that are formed by the extension can be sub-divided in all three dimensions to form elements of the required mesh intensity. The choice of subdivisions depends on the required accuracy, the level of saturation and the uniformity of flux flow. The subdivisions were initially chosen based on the flow of flux shown in Figures 4.8 and 4.9, and on the expected region of saturation at the neck between the poles and the iron disc. From the computation with these subdivisions, a more accurate knowledge of the field structure is obtained and used via an iterative process to achieve the eventual subdivisions. The final subdivisions for the model of a unit from generator A are denoted by the numbers beside their respective edges in Figures 5.3 and 5.4. These subdivisions give an accurate field solution with 5896 nodes, and takes twelve minutes of CPU time on the IBM 360/195 Computer in the Rutherford Laboratories when no conductor data is specified, and twenty-two minutes of CPU time if there are current-carrying conductors. The mesh with 5896 nodes is not as fine as one would wish, for a very accurate field solution, and as such errors and discrepancies are present which become

obvious when the results from computation using this discretisation are compared with experimental results, and results from the discrete reluctance method in a later Chapter. However, this discretisation is a fair compromise between accuracy and computer time, and the storage required for computation.

The discretised model is shown in Figures 5.5 to 5.10. Figure 5.5 shows the basic block discretisation of the model without the subdivisions.

Figure 5.6 shows the block discretisation of the rotor iron.

Figure 5.7 shows the block discretisation of the magnet.

Figure 5.8 shows the block discretisation of the stator iron.

Figure 5.9 shows the block discretisation of the air regions.

Figure 5.10 shows the elements of the rotor iron.

5.5.2 The Boundary Conditions imposed on the Model

The natural boundary condition is $\partial\psi R/dn = 0$. This is a flux line boundary condition where no flux flows out in the direction normal to this boundary. The other boundary conditions available are, the potential boundary condition where the boundary is at a specific potential and the symmetry or repeatability boundary condition. The symmetry boundary condition can also be defined to be an inverse symmetry boundary condition.

To enable the use of 1 pole pitch for analysis for both the no-load and load condition, the inverse symmetry boundary condition is applied to the two radial planes of the segment. The inner arc which is the boundary of the shaft and the rotor unit has the natural boundary condition as the shaft is made of non-magnetic material (See Figure 5.12). The outer arc, which is the surface of the stator, also has the natural boundary condition imposed on it (See Figure 5.12). The final two faces of the segments are the base plane and the last plane. If both

have the natural boundary condition imposed on them (see Figure 5.12), the unit would represent a middle unit of a very long machine which has infinite reflections on both sides. In this case, end effects cannot be studied. However, if one face possesses the natural boundary condition and the other defined to be an interface with air, with the boundary at a fair distance from the plane of the segment defined to have a potential 0, it would be treated as an end unity of a very long machine. In the analysis of Generator A, computations are done on a middle unit. The end effects can be neglected as measurements with a Hall probe suggest that end leakage from the rotor is negligible.

5.6 DISCUSSION

The machine discretised for computation using the three-dimensional finite element is Generator A. All the analyses and studies of the flux distribution, leakage fields and air-gap fields done with computations on Generator A are discussed in Chapter 6. These results are compared with the experimental results and the results computed using the discrete-reluctance method, in Chapter 7.

5.7 REFERENCES

1. Simkin, J. and Trowbridge, C. W. : 'Magnetic field computed using an integral equation derived from Green's Theorems', RL-76-041, Rutherford Laboratories, 1976.

2. Trowbridge, C. W., Armstrong, A. G., Collie, C. J., Diserens, N. J., Newman, M. J. and Simkin, J. : 'GFUN3D User Guide', RL-76-029/A Rutherford Laboratories, 1976.

3. Kurdali, A. : 'Analysis and the performance of a permanent magnet alternator with disc magnets', Ph.D. Thesis, Southampton University, 1979.

4. Simkin, J. and Trowbridge, C. W. : 'On the use of total scalar potential in the numerical solution of field problems in electromagnets', Int. Journal for Numerical Methods in Engineering, Vol. 14, pp 423-440, 1979.

5. Armstrong, A. G., Collie, C. J., Simkin, J. and Trowbridge, C. W. : 'The solution of 3-dimensional magnetostatic problems using scalar potentials', RL-78-088, Rutherford Laboratories, 1978.

6. Carter, F. W. : 'Note on air-gap and interpolar induction', Journal of the IEE, Vol. 29, pp. 925-933.

7. Carter, F. W. : 'The magnetic field of dynamo-electric machine', Journal of the IEE, Vol. 64, pp. 1115-1138, 1926.

8. Simkin, J. : 'TOSCA Pre-Processor', Rutherford Laboratories, CAG/80-13, 1980.

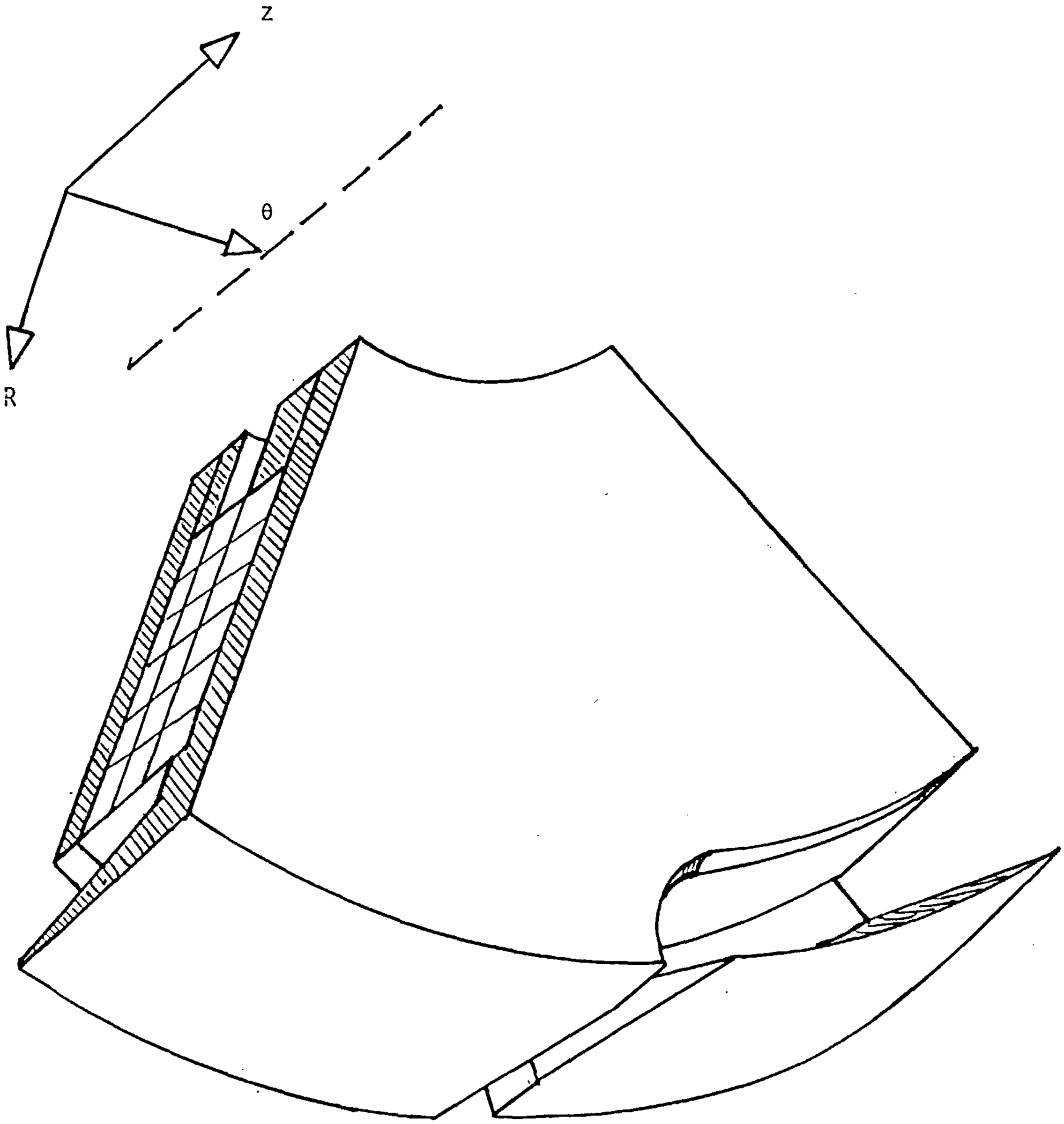

Figure 5.1 The segment chosen to represent the rotor.

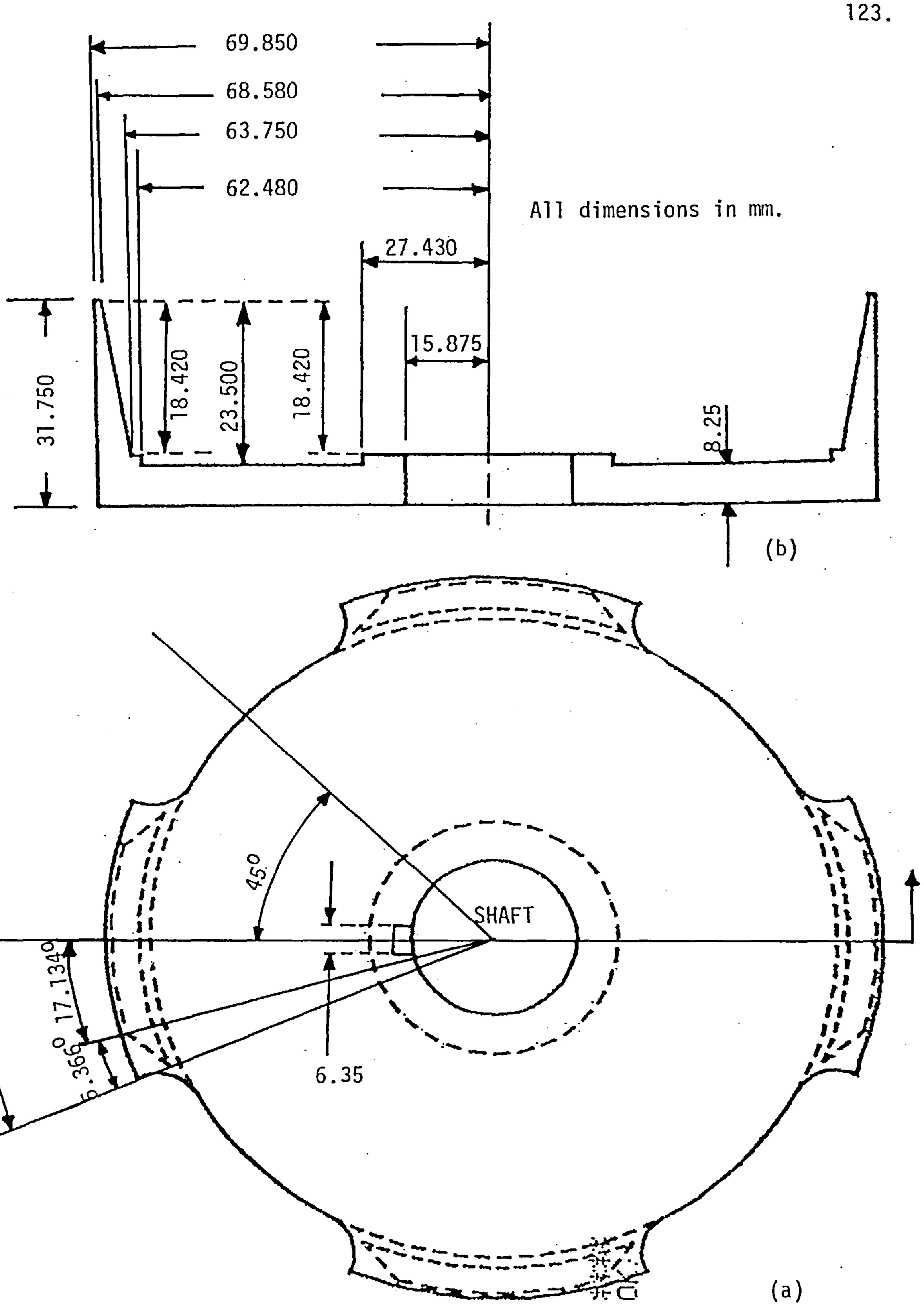

Fig. 5.2 The flux guide of generator A.

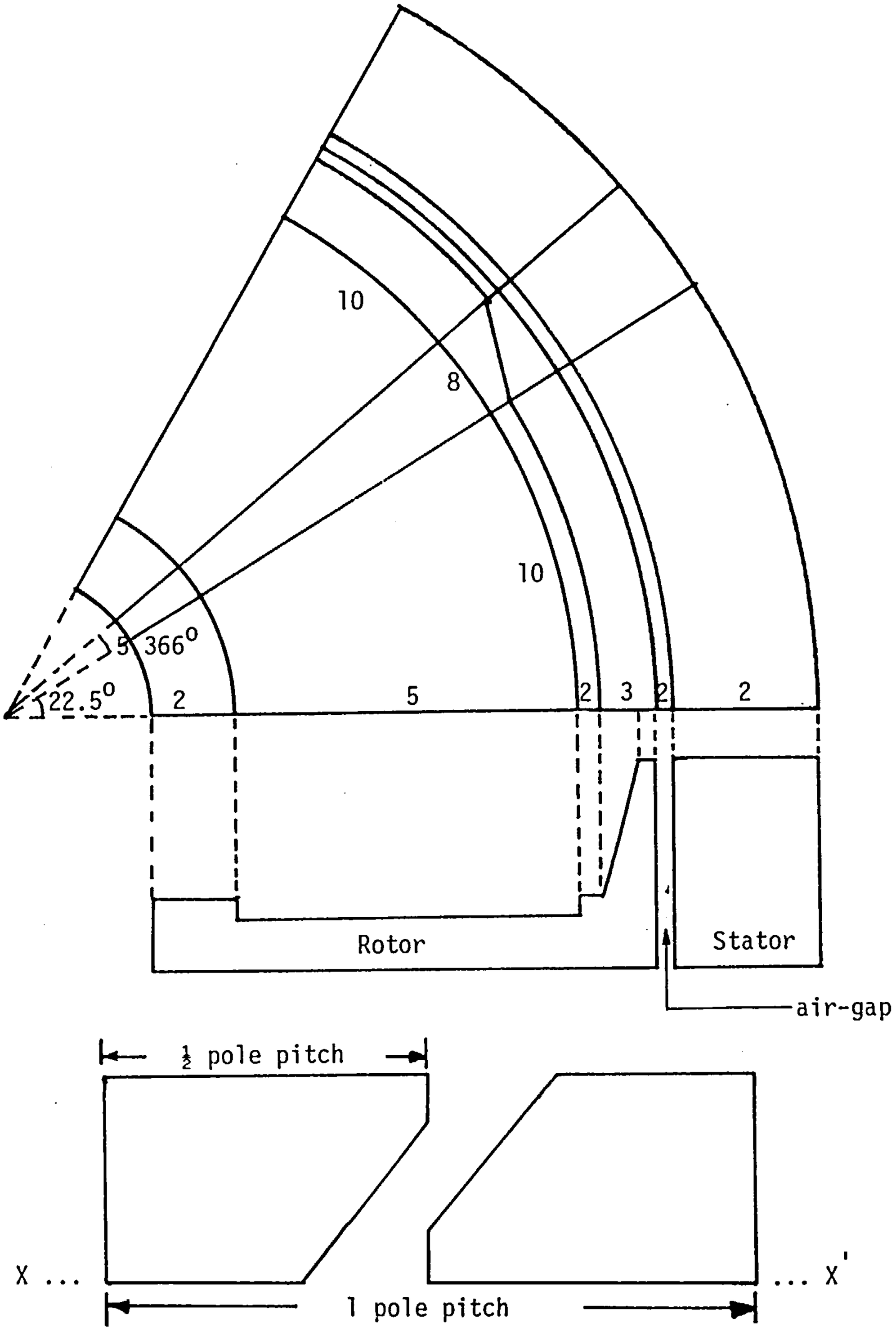

Fig. 5.3 The topology of the base plane.

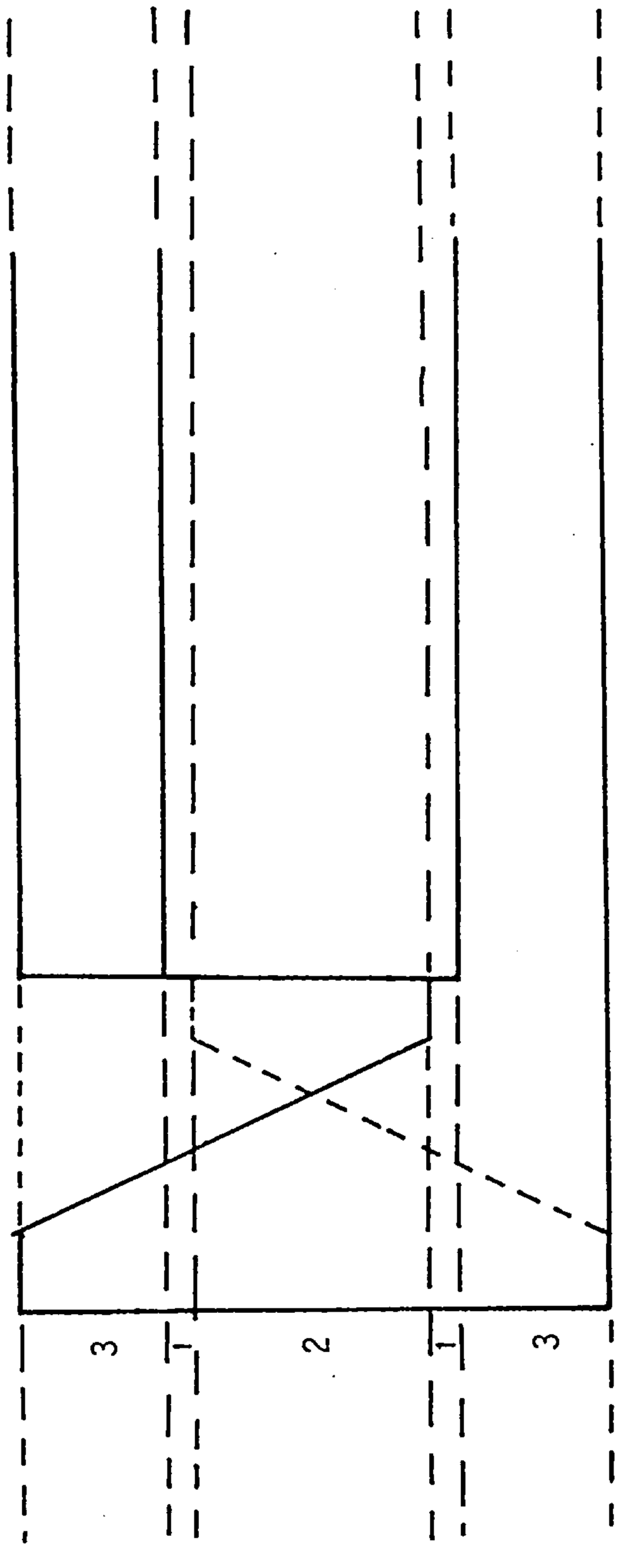

Fig. 5.4 The basic elemental layers in the model.

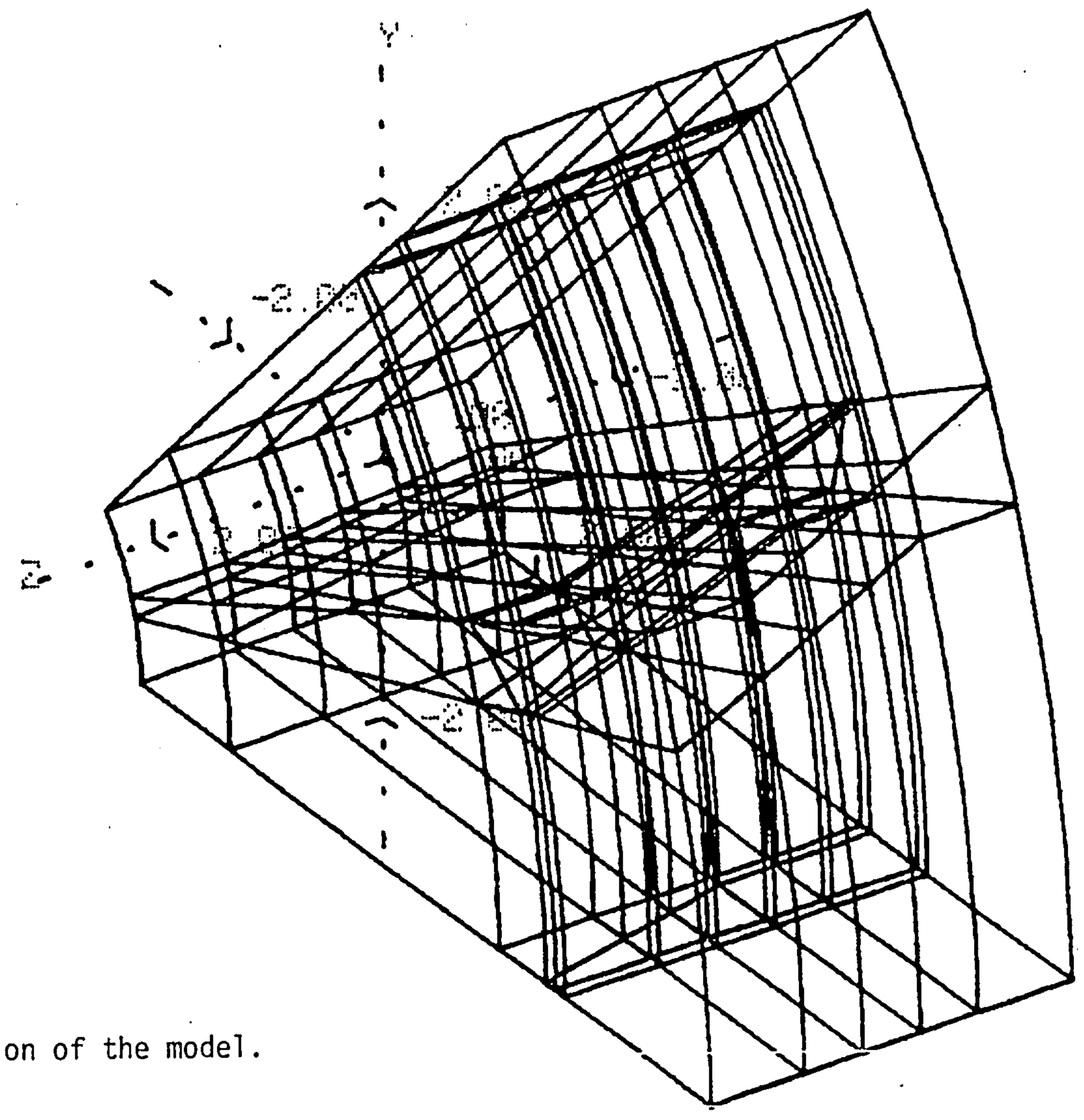

Fig. 5.5 Block discretisation of the model.

LSE
02/10/81 10:20: 7
OK
.

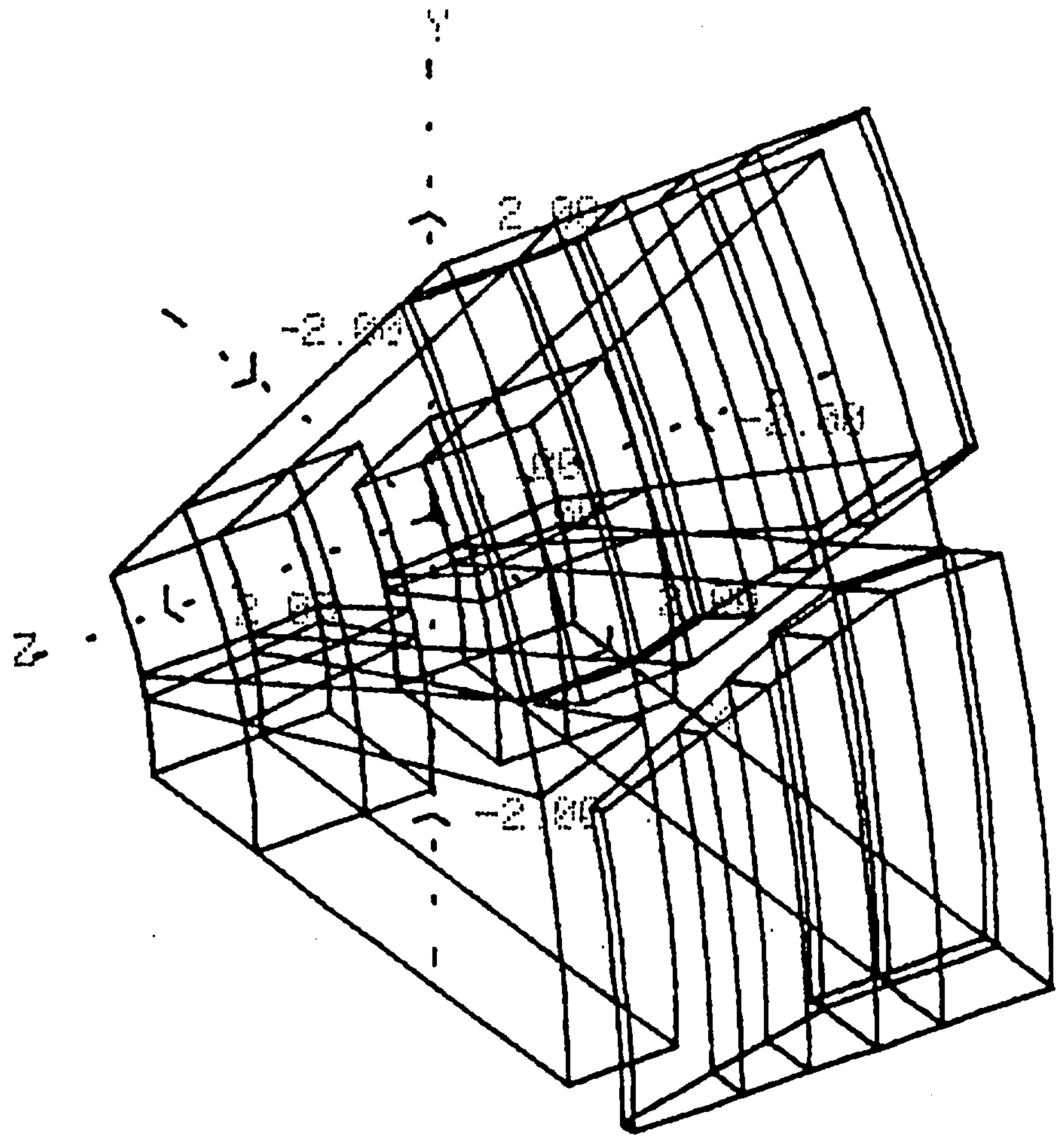

Fig. 5.6 The block discretisation of the rotor iron.

LSE
02/10/81 10:23:53
OK
.

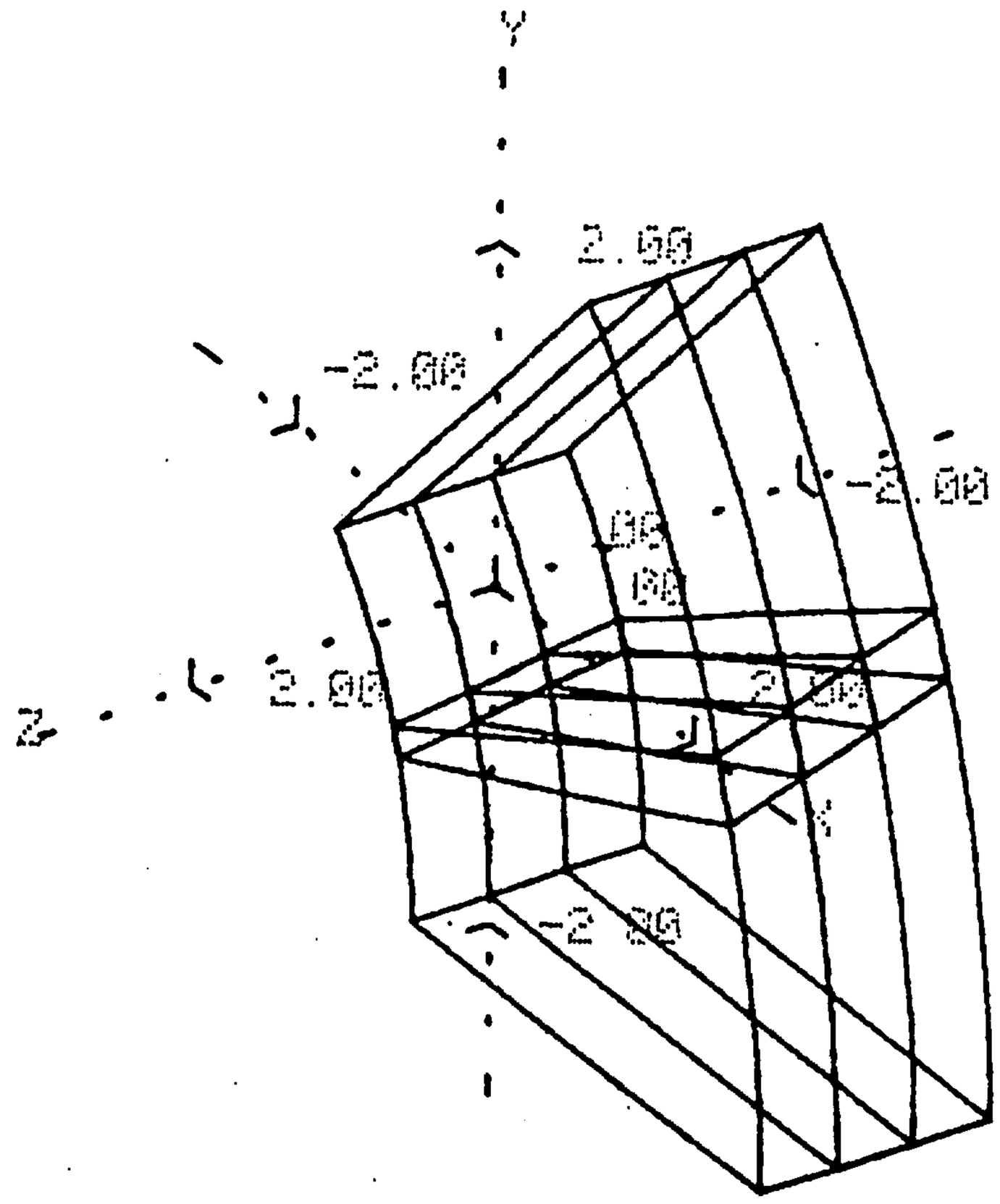

Fig. 5.7 The block discretisation of the magnet.

LSK
02/10/81 10:32:43
OK
.

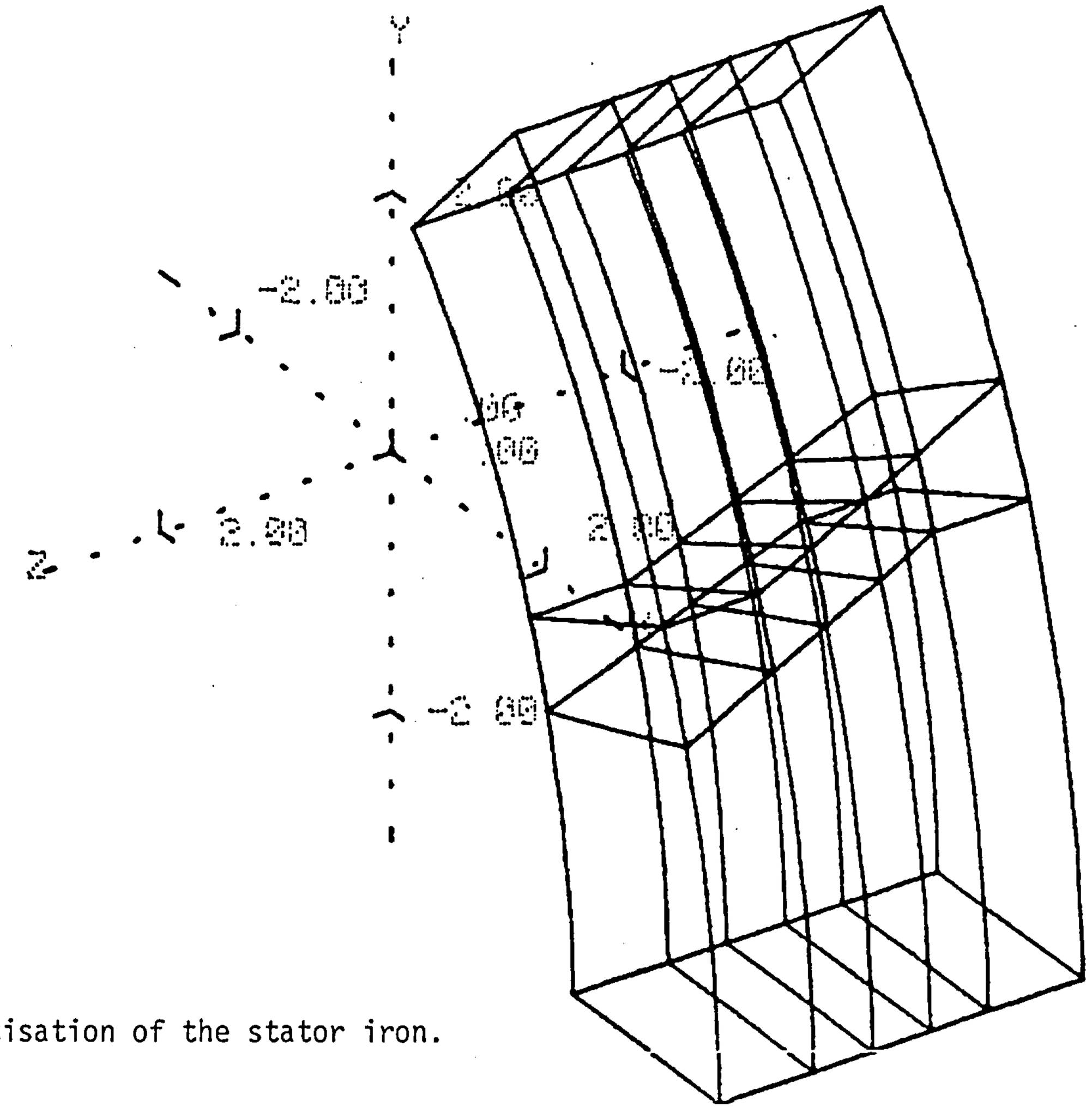

Fig. 5.8 The block discretisation of the stator iron.

LSE
92/10/21 10:25: 5
DK

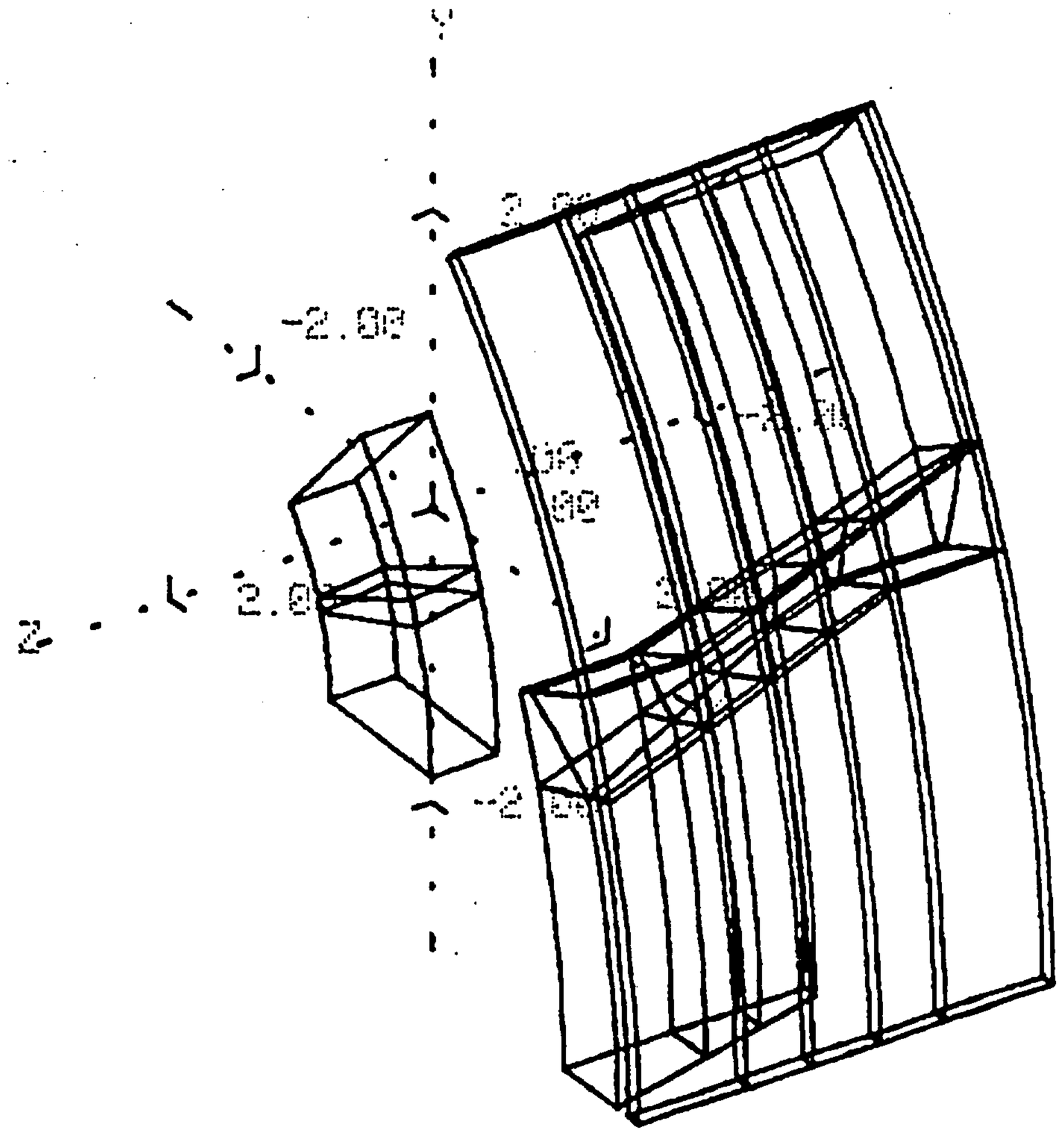

Fig. 5.9 The block discretisation of the air regions.

LGE
02/18/81 10:54:23
OK

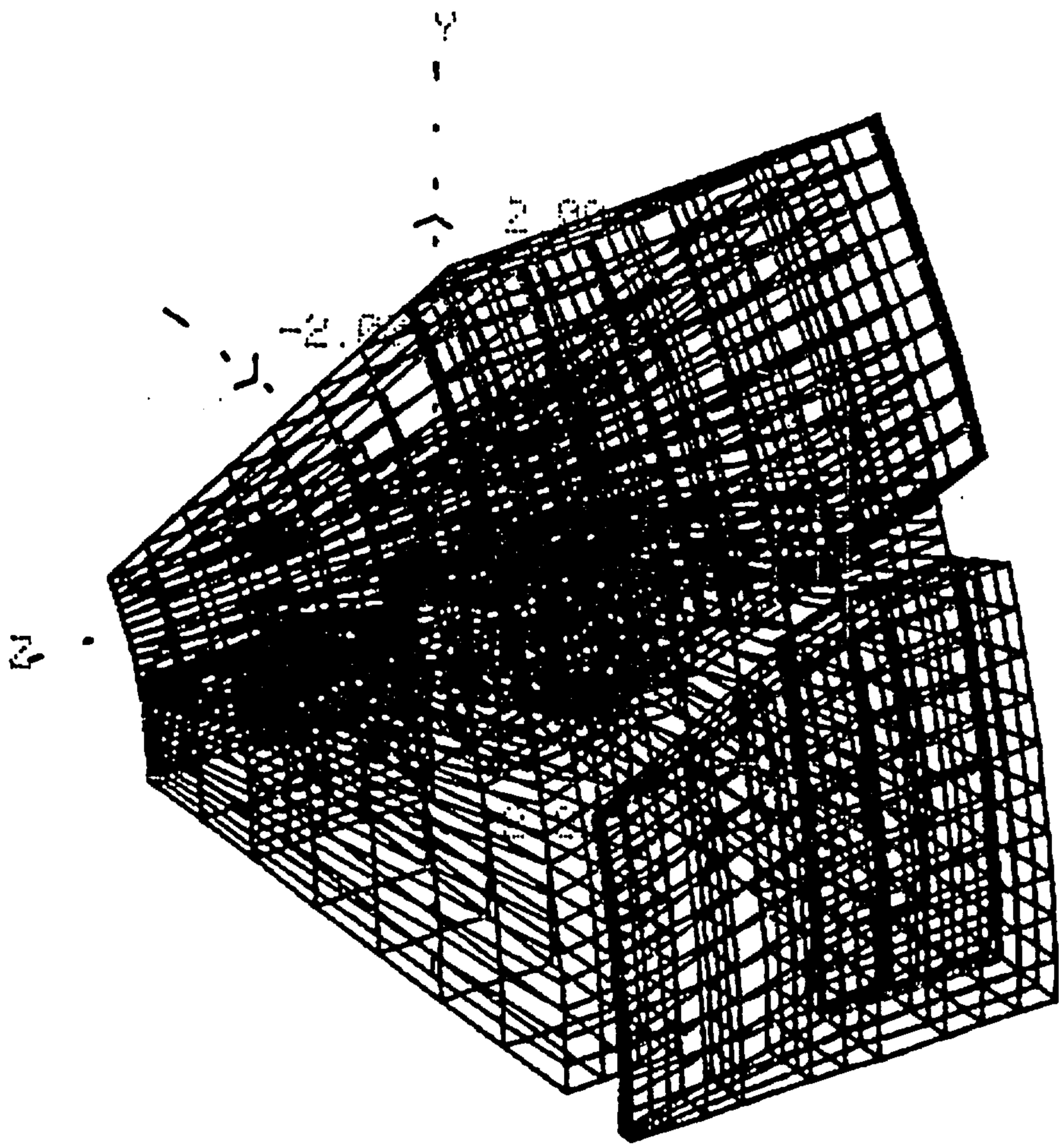

Fig. 5.10 The elements of the rotor iron.

LSE
02/10/31 10:35:31
OK
.

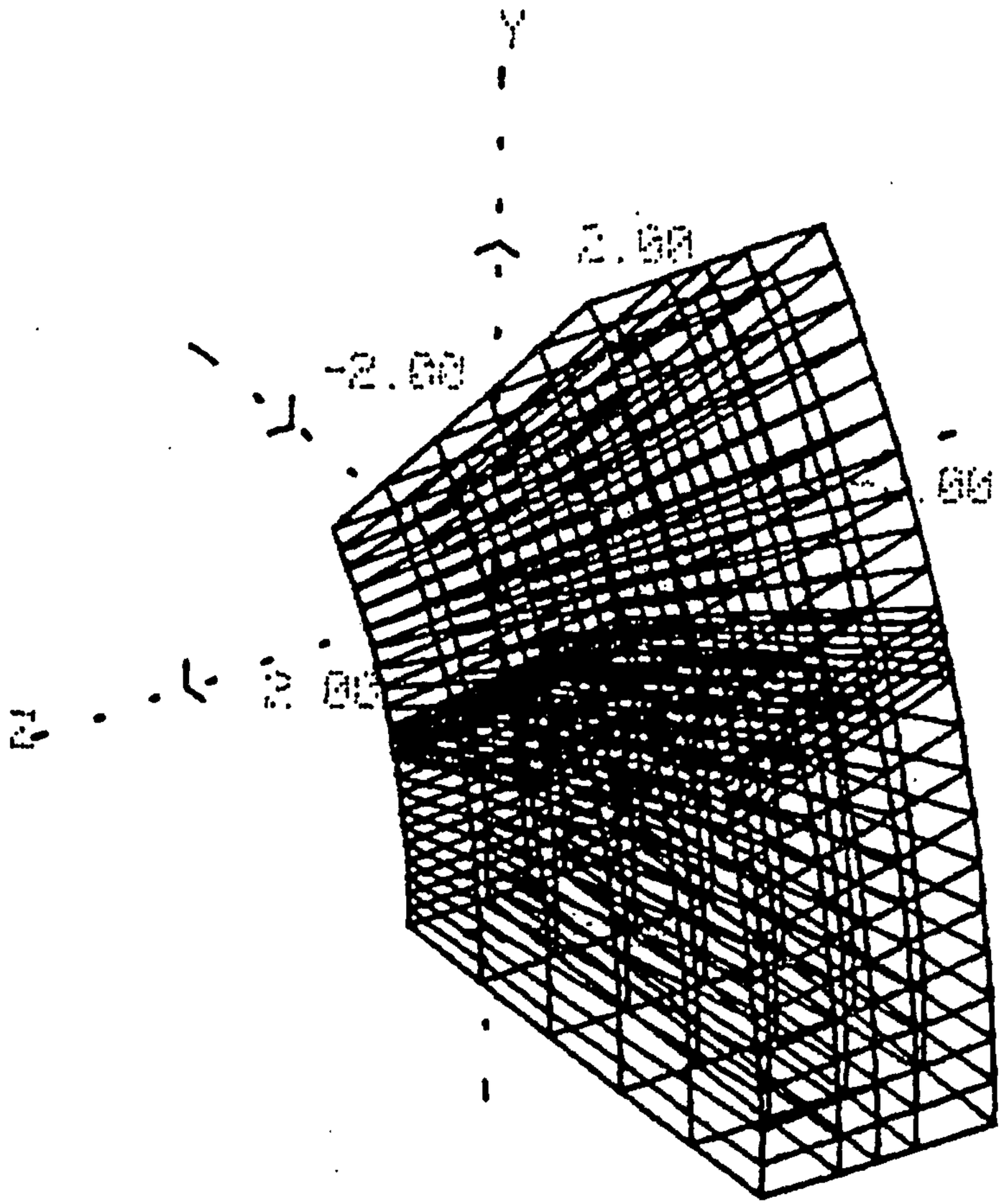

Fig. 5.11 The magnet elements.

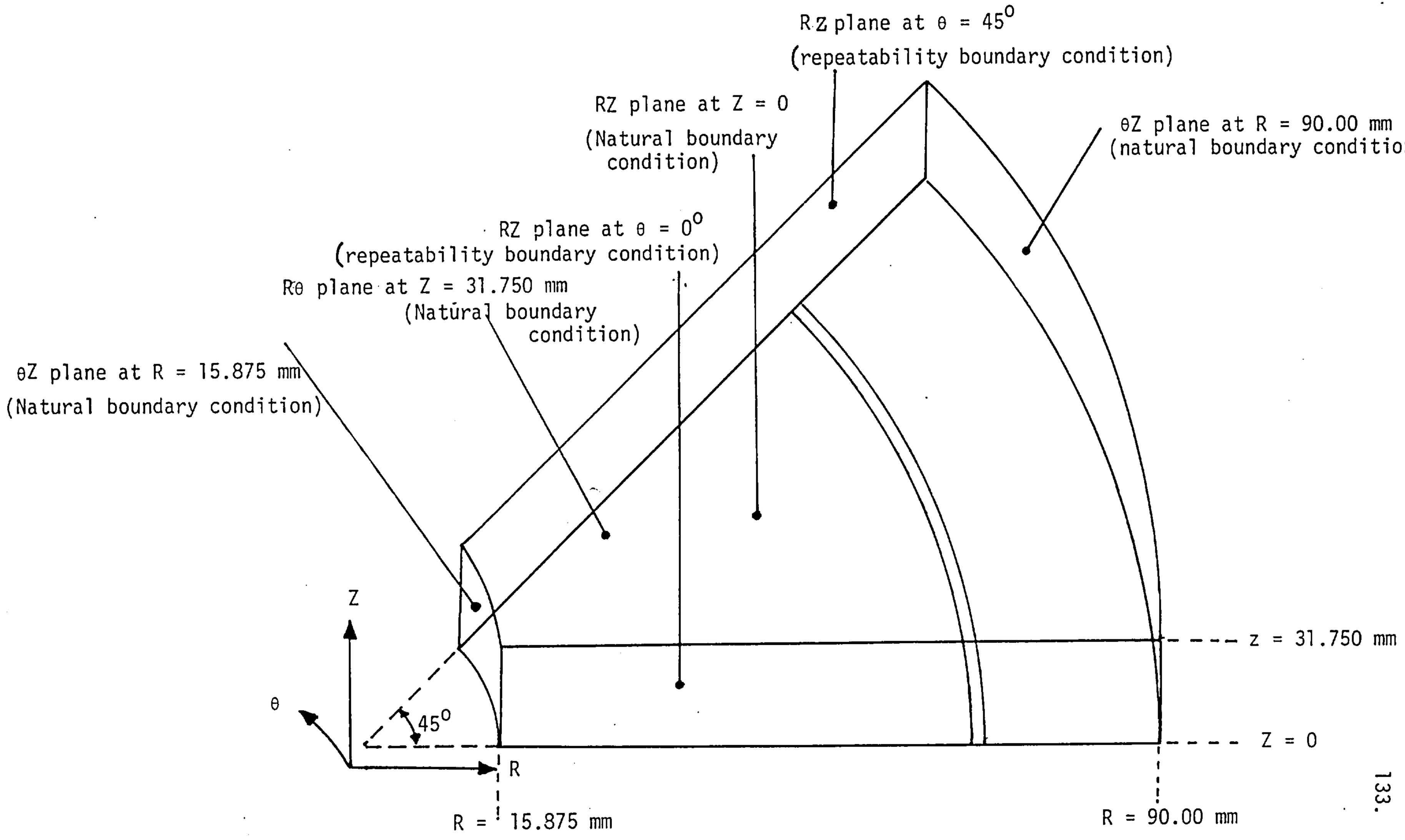

Fig. 5.12 Diagram showing the different planes of the model of Generator A and the boundary conditions associated with each face.

CHAPTER SIX

ANALYSIS OF THE RESULTS FROM FIELD COMPUTATION USING A THREE-DIMENSIONAL FINITE-ELEMENT PROGRAM

CHAPTER SIX

ANALYSIS OF THE RESULTS FROM FIELD COMPUTATION USING A THREE-DIMENSIONAL FINITE-ELEMENT PROGRAM

6.1 INTRODUCTION

The model used for computation of the field of the new rotor is described in the previous chapter. The dimensions of the model used in this analysis are those of a rotor designed for generator A (see Appendix I) and this is an eight-pole rotor which fits a standard stator frame.

The analysis of the results from computations of the field in the imbricated rotor is carried out with data having the following characteristics.

(i) In the first case, the model has the dimensions shown in Figure 5.2. The boundary conditions imposed define it to be a middle unit of a long machine. The radial planes of the model are defined using inverse symmetrical boundaries. This case applies to the no-load condition as it does not have conductors in the air gap. The computation using this set of data is used as the basis for comparison with results obtained for changes in the geometry of the rotor. This set of data is named BASE.

(ii) The sets of data in this case have all the conditions specified in Case i with a single exception. The difference is the change in the pole shape due to a change in the angle of taper of the pole. The original taper of the pole, shown in Figure 5.2, is such that the section spans an angle α where $\alpha = 5.366^{o}$. This angle is changed to 10^{o}, 15^{o} and 20^{o} for data P10, P15 and P20 respectively. This change in pole geometry is shown in Figure 6.1a.

(iii) In Case 3, the data P10 is used but a change is made in 'a', the width of the collar between the pole and the disc. This changes the width of iron path 2 as well as the pole profile. The changes in 'a' are shown in Figure 6.1b. These two sets of data are named P10-R65 and P10-R66.

(iv) This set of data has all the conditions described in Case 1 but with a change in the geometry involving the removal of the collar on the disc by the shaft, shown in Figure 6.1c. This changes the path of leakage 3 and this set of data is labelled XL3.

(v) Case 5 is the computation of the load case. The specification of Case 1 is applicable but conductors are placed in the air gap. The conductors are defined as solid bars positioned in the extended area of the air gap. The number of conductors is dictated by the number of slots per pole per phase. In the case of generator A, there are nine conductors over a pole pitch. The current density in the bar is determined by the number of conductors per slot and the load current. The mmf pattern produced by these conductors can be shifted to account for a change in load angle. These sets of data are labelled CCI-JK, where I is the current per conductor in the slot, that is the load current, and JK indicates the angle between the axis of the rotor field and the axis of the stator mmf waveform. On no-load the angle between the two axes is 90^{o}. This angle increases on load to 180^{o} on short circuit. Therefore, the data for a current loading of 3 amperes with the angle fixed at 130^{o} would be labelled as CC3-40.

In all the cases above, the stator iron and the rotor iron are assumed to be of the same material. The permanent magnet material used for the excitation is ceramic 8.

6.2 THE USE OF THE FIELD SOLUTIONS TO GIVE THE USEFUL AND LEAKAGE FLUXES

The solution from TOSCA, the three-dimensional finite-element program, is stored in datasets. The calculation of the field in a particular region is effected by defining a mesh of field points in the region of interest and processing the solution[1]. Solutions from this program are in terms of H, the field intensity; therefore if B, the flux density, is required, the relationship between B and H governed by the magnetisation curve of the material must be used for conversion. However, if the region of interest does not contain any magnetic material, B and H are simply related by the equation $B = \mu_o H$. Therefore, from the field solutions, the flux density at any point in the model can be found. The flux density obtained is resolved into components B_R, B_θ and B_Z.

Line and surface integrals are used to calculate the average flux density over a line or a surface area and the amount of flus passing through that surface[1]. The field and flux values calculated by taking the integrals are presented as individual components in the three principal directions R, θ and Z.

The results obtained from the field solutions can be processed further to provide more information. The air-gap flux waveform can be constructed and analysed to provide the harmonic content. The load characteristic of the model can also be calculated from the air-gap flux waveform having a known winding design and the speed of rotation.

The following sub-sections describe the analysis of the results extracted from the field solutions computed using the program, TOSCA.

6.3 THE ANALYSIS OF THE FLUX DISTRIBUTION IN THE FLUX GUIDE

The detailed analysis of the flux distribution in a flux guide of the imbricated rotor is obtained from the results of the computation using the data described in Case 1 in section 6.1, called BASE. Three meshes of field points are used to study the distribution of flux in the steel flux guide. These three meshes effectively divide the analysis of the flux distribution into three parts. The first is the iron disc which has been defined earlier as iron path 1; iron path 2 is the collar joining the iron disc to the pole piece and the third is the pole which has been described as iron path 3, see Figure 4.2.

The results obtained using these three meshes of field points give the flux density of each of the three components at the field point from which the flux density level, the modulus of the three components is calculated. The direction of the resultant flux density vector at each point is also calculated. As a result of these calculations, a picture of the flux distribution in the steel flux guide can be constructed.

6.3.1 The Flux Distribution in the Iron Disc (Iron Path 1)

Iron path 1 is the disc which is in contact with one of the poles of the disc magnet. Flux crosses the magnet into the iron disc axially and is guided to the poles radially. The flux is thus angled in the Rθ plane and the RZ plane. These angles can be calculated from the values of B_R and Bθ, and, B_R and B_Z respectively. The argument of the flux density B_{RZ} over the RZ plane at $\theta = 9^o$, 18^o, 27^o and 36^o is shown in Figure 6.2. It should be noted that the length of the arrows do not indicate the magnitude of the modulus. The flux distribution is also highly non-uniform in the Rθ plane due to the channelling of the flux to the poles. This effect is shown by Figure 6.3 which charts the argument of $B_{R\theta}$ over the Rθ plane at Z = 2 mm and Z = 6 mm from the base plane.

It shows the flux being directed to the poles. This results in a very uneven distribution of flux density in the iron disc. By resolving the flux density into three components B_R, B_θ and B_Z and plotting them over the Rθ plane in Figures 6.4, 6.5 and 6.6 respectively, the characteristic of each component can be observed. The B_R component increases steadily from the centre where it has a value of 0.0 T to the sector where the pole is attached, in the radial direction, and from the sector where there is no pole attachment to the sector where the pole is attached, in the θ direction. B_R is maximum at the boundary between the disc and the collar which links it to the pole. The distribution of B_θ shows the accumulation of flux directed from the sector without the pole to where the pole is attached. The behviour of B_Z is quite different. It remains almost at a constant level over the Rθ plane due to the change in the axial direction of the flux as it passes from the magnet into the iron, to the radial direction as it flows out to the poles. The distribution of the modulus of these three components is shown in Figure 6.7.

The three-dimensional nature of the field can be visualised from the diagrams in Figures 6.1 to 6.7. It can also be observed from Figures 6.2 and 6.3 that the iron flux guide is attached to the south pole of the magnet and as such the flux enters the magnet from the iron. These two figures also show that the output flux from the magnet resolves into two components flowing in opposite directions. One component contributes to leakage 3, the leakage by the shaft, while the other flows out to the poles as the useful flux, the interpolar leakage and the leakage between the underside of the poles and the steel discs of opposite polarity. The dotted line in Figure 6.3b divides the area which contributes flux to leakage 3 and the area which contributes to the flux that flows to the poles. Using geometrical approximations the surface area of the magnet

whose flux is lost at leakage 3 is found to be 10% of the total magnet surface area.

Due to the non-uniformity of the flux distribution in the iron disc shown by the plot of B_{mod} over the Rθ plane in Figure 6.7, there are areas where the iron is underused. These regions are marked in Figure 6.8. The flux density is highest in the region adjacent to iron path 2. Figure 6.7a shows that the peak is at $\theta = 23^{o}$ with $B_{mod} = 1.3$ T.

6.3.2 The Flux Distribution in Iron Path 2

Iron path 2 is the part which links the pole to the iron disc. Its radial width is denoted by 'a' and its axial length by 'aℓ'. The reasons for the incorporation of this structure in the design are: to hold the magnet in place and to provide a smoother path for flux passing through to the poles.

The picture of the flux distribution and the behaviour of each of the three components are obtained in the same way as for the iron disc. These are shown in Figures 6.9a, 6.9b and 6.10. They show the flux diverging as it passes from the iron disc into iron path 2. It is also angled into the middle of the pole as shown in Figure 6.9b. This direction of flux into the middle of the pole is due to the tapering of the pole which results in an increased reluctance at the edges of the poles. The surface flux plot in Figure 6.10 also shows this effect resulting in a high level of B_{θ} at the edge of the pole and a high B_{R} at the centre of the pole.

The flux density in iron path 2 is high. This is shown by Figure 6.11 which is a plot of the average flux density along the line R = 63 mm, calculated from the line integrals taken in the Z-direction for θ from 0^{o} to 22.5^{o}.

6.3.3 The Flux Distribution in the Pole (Iron Path 3)

Iron path 3 is the trapezoidally shaped pole. As flux passes from iron path 2 into the pole it diverges as the cross-sectional area increases from the narrow boundary between the pole and iron path 2, to the wide pole face. The flux is directed into the middle of the pole due to the taper on the sides which creates a differential between the reluctance at the edge of the pole and the reluctance in the middle. This is shown in Figures 6.12 and 6.13. Due to the increase in surface area, the flux density level in the pole is much lower than in iron path 2.

6.3.4 Conclusions

This analysis gives a comprehensive picture of the three-dimensional field in the flux guide. It also charts the direction of the flux in the three iron paths of the flux guide. From these results and the analysis, several conclusions can be drawn which would aid in the design of an optimum flux guide.

(i) The usage of the iron in the flux guide is highly uneven and is therefore somewhat inefficient. This is shown in Figure 6.8. The disc of the flux guide can be remodelled to make use of the iron more efficiently. This remodelling is described in Chapter 8.

(ii) It is clear from the analysis that the limiting factor in the passage of flux produced by the magnet from the surface of the magnet to the poles is the surface area of the boundary between the iron disc and iron structure linking the disc with the pole. The cross-sectional area of this surface is $I_{th} \times \pi R$ (where I_{th} is the iron thickness, and R is the outer radius of the magnet. Therefore, the flux density over this surface is $(B_m \pi R^2)/I_{th} \pi R$, where B_m is the flux density level at the working point of the magnet. Since some of the flux from the magnet is lost at leakage 3, the flux density

over the surface of the boundary is $(B_m\ F\ \pi R^2)/I_{th}\ \pi R$, where F is the percentage of total flux from the magnet passing through this boundary into the pole.

(iii) The distribution of flux in the pole depends on the shape of the pole. The tapering of the pole results in the variation of reluctance between the edge of the pole and the middle of the pole. Thus, tapered ends of the poles have very high flux density levels which contributes to leakage between the poles. Due to the direction of the flux in the pole because of the pole shape, the air-gap flux waveform also changes with the pole profile. This is studied in detail in a later section.

(iv) The values of 'a' and 'aℓ', the dimensions of the structure linking the pole and the iron disc, are not significant as regards the carriage of flux but are important as they have a significant influence on the reluctance of the leakage path 2. This is considered in the following section.

(v) Only a proportion of the flux produced by the magnet passes out ot the poles. The remainder manifests itself as leakage 3. Leakage path 3 forms an alternative route for the flux, thus any changes in the pole profile or in the geometry of the flux guide which changes the reluctance of the flux paths would affect leakage 3. In the model analysed, 10% of the flux produced is lost in the form termed as leakage 3. The behaviour of this leakage with changes in the pole profile is discussed later in this Chapter.

6.4 THE ANALYSIS OF THE LEAKAGE FIELDS IN THE ROTOR

The three leakage paths in the new rotor have been discussed in Chapter 4. They are leakage 1, the interpolar leakage, leakage 2, the leakage between the underside of the pole and the disc of opposing

polarity, and leakage 3, the leakage by the shaft region. It is important that the magnitudes of these leakages are computed and the effects of the changes in the geometry of the flux guide on these leakages studied. This would enable the modelling of optimum flux guide as regards minimum leakage.

The results from computation using the data BASE forms the basis for comparison with the results from computation using the other sets of data. The pole shape can be changed by altering the taper and the value of 'a' (see Figure 6.1). These changes in the geometry of the pole cause the dimensions and thus the reluctivity of leakage paths 1 and 2 to change. Their effects on leakage 3 is also studied. The influence of the collar by the shaft on the flux guide on the field of the rotor is also studied using the results from the computation with data, XL3.

6.4.1 Interpolar Leakage - Leakage 1

Interpolar leakage occurs in all salient pole machines. In the imbricated rotor it is reduced considerably by tapering the pole, thus increasing the reluctivity of the path. This leakage is computed by defining a mesh of field points in the RZ plane, at $\theta = 22.5^{o}$, in the air region between the poles. This mesh is shown in Figure 6.14. The two leakage components are B_{θ} and B_{Z}. The B_{R} component is negligible. The magnitude calculated for the data, BASE, is 2.729×10^{-5} Wb. This is 6.51% of the flux per pole. As the model represents a pole pitch, this leakage is thus 6.51% of the total useful flux of the rotor. The change in the taper as in data P10, P15 and P20 would change the magnitude of this leakage and is computed to be

1.775×10^{-5} Wb for P10
1.511×10^{-5} Wb for P15
and 1.311×10^{-5} Wb for P20.

The other factor which affects the reluctance of the flux path of leakage 1 is the dimension 'a'. This is shown by the value of this leakage computed using the data,

P10-65 which has interpolar leakage of 1.760×10^{-5} Wb,

and P10-66 which has interpolar leakage of 1.762×10^{-5} Wb.

The results show that interpolar leakage is very sensitive to the tapering of the pole. A doubling of the angle of taper reduced the interpolar leakage by 35%. A further increase in the taper is not matched by a proportional reduction in this leakage. This trend is shown by the graph in Figure 6.15.

The changing of the pole profile by altering the dimension 'a' has no pronounced effect on leakage 1.

6.4.2 Leakage from the Underside of the Pole (Leakage 2)

To compute leakage 2 in the model, two meshes of field points are defined, one each for the underside of the two half poles. This is shown in Figure 6.14. Any flux passing through these surfaces is leakage. The magnitude of the leakage is calculated by taking the surface integral of the flux density over the surfaces defined for the field points. The computed value of leakage using the data BASE is 5.430×10^{-5} Wb over a pole pitch and is 12.95% of the flux per pole.

This leakage path is changed if the taper of the pole changes. If the taper is increased, the cross-sectional area of this leakage flux path is reduced, consequently the reluctance increases thus reducing the magnitude of the leakage. This is shown by the calculation for leakage 2 from the computations using the data,

P10 which has leakage 2 of $5.3.2 \times 10^{-5}$ Wb
P15 which has leakage 2 of 5.016×10^{-5} Wb
P20 which has leakage 2 of 4.726×10^{-5} Wb

They represent a reduction of 2, 8 and 13 per cent respectively. This influence of taper on leakage under the poles is shown graphically in Figure 6.16 which is a plot of the flux density of leakage path 2 from 0^{o} to 22.5^{o}. The shape of this distribution curve follows the shape of the pole profile. This graph only represents half a pole, the other half is similar in every respect except for its direction due to the change in polarity.

The other factor which changes the reluctance of leakage path 2 is the dimension of 'a' as it determines the length of the flux path. The effect of charging 'a' is shown by the computations with data P10-65 and P10-66, whose underpole leakages were calculated to be

P10-65 - 5.040×10^{-5} Wb

and P10-66 - 4.750×10^{-5} Wb.

These two figures represent a reduction of 5% and 10% in the magnitude of leakage in this region. This reduction in leakage by altering the path length for a fixed taper in pole profile is shown in Figure 6.17.

These results show that leakage two is sensitive to both changes in the taper and changes in the value of 'a'. Leakage in this region has been reduced significantly by the undercutting of the pole. It can, however, be further reduced by optimising the pole shape as regards the taper and the dimension of 'a'.

6.4.2 The Leakage by the Shaft Region - Leakage 3

This leakage is computed by taking the surface integral over the mesh of field points defined in the air region by the shaft. This mesh is shown in Figure 6.14. This leakage path forms an alternative path for the flux from the magnet which, ideally, should all be directed outwards to the poles. It is therefore affected by any changes in the geometry of the flux guide and the pole profile. The magnitude of this leakage

in the model, computed with the data, BASE, is 3.034×10^{-5} Wb over a pole pitch. This is 7.24% of the useful flux per pole. This leakage is considerable as the reluctance of this path is very low, having a large cross-sectional area and a short length. This leakage can be reduced if the reluctance of this path is increased. This is achieved by the elimination of the collar by the shaft (see Figure 6.1). This increases the length of the leakage path by 150%. The leakage computed for this case using the data, XL3, is 1.109×10^{-5} Wb. This represents a reduction of leakage 3 by 58%. This reduction is matched by increases in leakage 1, leakage 2 and the output of flux from the poles of 1.570×10^{-5} Wb, 3.920×10^{-5} Wb and 1.225×10^{-5} Wb respectively.

The change in the taper and the change in 'a', used to reduce the interpolar leakage and the underpole leakage, do affect leakage by the shaft. These changes in geometry of the pole change the reluctance of of the iron pole. An increase in the reluctance of this pole structure encourages flux to use the alternative path provided by leakage path 3. The magnitude of this leakage, computed with the following sets of data, show the influence of changes in pole profile on leakage 3.

P10 - 3.221×10^{-5} Wb

P15 - 3.432×10^{-5} Wb

P20 - 3.800×10^{-5} Wb

P10-R65 - 3.519×10^{-5} Wb

P10-R66 - 3.402×10^{-5} Wb

All the above cases show an increase in leakage 3. The change in the geometry of the pole by changing the taper as in the data P10, P15 and P20 increases the air-gap reluctance. The increase in the value of 'a' increases the reluctance of iron path 2. These increases in reluctance encourage the flux to use the alternative path by the shaft to complete

the magnetic circuit. This is reflected in the magnitudes of leakage 3 computed for the various sets of data with changes in the pole shape.

6.4.4 The Effect of Load on Leakage

The three leakage paths play an important role in the design and output of these generators. They have to be minimised to reduce the wastage of the potential of the magnet. However, at short circuit, when almost all the flux produced by the magnet flows through the three leakage paths, it must be of a magnitude which will work the magnet at a point which will not result in the demagnetisation of the magnet material.

The effect of load on leakage is shown in Figure 6.18. The load produces a stator mmf which opposes the rotor field. All three leakages increase with load. The rise is gradual and consistent. The rate of increase in leakage by the shaft and interpolar leakage are nearly equal at 3.87% per Amp and the rate of increase in leakage 2 is 3.69% per Amp. At short circuit, the total leakage is 1.7×10^{-4} Wb with the magnet working at a flux density level of 0.12 T. This working point is above the knee in the demagnetisation characteristic of ceramic-8 and is therefore not susceptible to demagnetisation and operation on a minor loop.

6.4.5 Conclusions

The knowledge of the leakage in the imbricated rotor is essential for the design of an efficient flux guide with minimum wastage of the flux produced by the magnet. These leakages in the imbricated rotor are three-dimensional in nature and thus a three-dimensional field analysis technique was used to analyse it. From the study of these leakages using TOSCA, some valuable conclusions can be drawn regarding the characteristics and behaviour of the three leakages.

i) The interpolar leakage in the model is 7% of the total air-gap flux. This is reduced by 35% if the taper of the pole is double. Subsequent increase in the taper is not matched by a proportional reduction in leakage. The change in the pole profile by charging 'a' has negligible effect on it.

ii) The underpole leakage is computed to be 12.95% of the useful flux crossing the air gap. This is the biggest of the three leakages studied. This leakage is sensitive to both the taper of the pole and the value of 'a'. It can be reduced by 12% if the taper is double and the value of 'a' is increased by three times the value in the model.

iii) The changes in the pole profile changes the reluctance of the air gap and the reluctances of the iron paths. These changes have a pronounced influence on the leakage by the shaft. The increase in taper and in 'a' results in reduction of leakages 1 and 2 but increases leakage 3.

iv) Leakage by the shaft is 7% of the useful flux in the model. This is reduced drastically if the collar by the shaft is eliminated. A reduction of 58% is achieved. This reduction in leakage 3 is matched by an increase in the leakages between the poles and in the output flux by the poles.

v) All three leakages increase with load. At short circuit the total leakage over a pole pitch is 1.7×10^{-4} Wb. Under this condition the magnet works at a flux density level of 0.12 T which is above the knee on the demagnetisation characteristics of ceramic-8, and therefore works on the major loop.

Therefore, by choosing the right pole profile and eliminating the collar, the performance of the flux guide can be more efficient. However,

another factor needs to be considered; this is the influence of the pole profile on the shape and magnitude of the air-gap flux waveform. This is discussed in the following section.

6.5 THE ANALYSIS OF THE AIR-GAP FIELD

The results of the computed field of the generator can be used to compute the performance of the machine. From the known air-gap field, the machine terminal voltage can be calculated. Using the computed values of the air-gap radial induction, it is a simple matter to compute the generated emf in the armature conductors. In a particular conductor this emf will be

$$e = B(\theta)\, LV$$

where L is the length of the conductor and V is the velocity of rotation of the rotor. With the machine at constant speed, the conductor voltage will follow the variation of $B(\theta)$, where $\theta = \omega t$. If $B(\theta)$ is Fourier analysed the generated emf in the conductor will be,

$$e = LV \sum_{r=1}^{\infty} B_r \sin(r\omega t) + B_r$$

where r = harmonic order.

If the coil is not fully pitch, e is multiplied by the pitch factor K_p. A complete phase of the winding normally consists of several coils in series displaced in space by a slot pitch. In this case the phase voltage can be computed by multiplying coil voltage by the number of coils in series. For a distributed winding the phase voltage is multiplied by a distribution factor K_d. Thus the emf per phase is[2]

$$E = e\ T\ C\ K_p\ K_d$$

where T = turns per coil

C = coils per phase.

The air-gap field of the model is extracted from the field solution by defining field points in a mesh in the air gap. By taking the line integral in the axial direction, the average flux density along that line is calculated. From these calculations the air-gap flux waveform is obtained. The surface integral of the flux density over the area of the mesh from 0^{o} to 22.5^{o} would give the amount of flux from half a pole.

6.5.1 The Shape of the Air-Gap Flux Waveform

The flux density in the air gap varies in both the θ and the Z direction. These variations are due to the pole shaping of the air-gap permeance. Figures 6.19 and 6.20 show two plots of the flux distribution in the RZ plane. Figure 6.19 is a plot from the results computed with the data BASE and Figure 6.20 is a plot from the results of computation using the data P20. Both the plots show the flux density level in the air gap bearing a close relationship with the pole shape. Therefore, by changing the taper of the pole, the air-gap flux waveform can be shaped.

A one-dimensional view of the air-gap flux waveform can be obtained by taking the line integrals in the Z-direction. Figure 6.21 shows the air-gap flux waveforms calculated in this manner from the results of computations with BASE, P10, P15 and P20. It shows the influence of the taper of the pole on the output waveform of the rotor. Improvements to the pole shape is achieved by increasing the taper of the poles. This will become obvious when a harmonic analysis is performed on these waveforms. This is discussed in the following section.

Figure 6.22 is a comparison of the air-gap flux waveform with that measured experimentally using a search coil. The comparison shows the absence of ripples in the computed results. This is due to the

representation of the stator as a smooth surface[3]. Inaccuracies are also introduced by the discretisation of the model. This error is more pronounced in the regions of taper of the poles and between the poles, where the change in flux density results in a high non-uniformity of the field. The error is accentuated by the limited number of discretisation of the air-gap in the θ-direction. The 45^{o} span of the model is divided into 28 sections in the θ-direction. The error, calculated by taking the integrals of the two waveforms, is 8%. This error is reflected in the calculation of the output voltage on the open circuit condition.

6.5.2 The Harmonic Analysis of the Computed Air-Gap Flux Waveform

The air-gap flux waveform computed is Fourier analysed to determine the extent of harmonic distortion. The third harmonic which has been found to be predominant from the experimental results is chosen for analysis. Its magnitude is calculated as a percentage of the fundamental and are as follows:

BASE	-	30%
P10	-	23%
P15	-	14%
P20	-	7.5%
P10-R65	-	24%
P10-R66	-	25%
XL3	-	30%

The results show that the effect of the taper in the pole shaping the air-gap flux results in a more desirable waveform with a much lower proportion of harmonics. In data P20, the pole face profile is nearly a triangle, instead of a trapezoid, and this gives a near sinusoidal waveform with a third harmonic component which is only 7.5% of the fundamental. However, the improvement of the waveform is not the only

consideration. The optimal solution of the air-gap flux waveform is not necessarily a sinusoid. The excessive tapering of the pole could result in the saturation at the pole tips and inhibit output of flux from the poles.

The influence of 'a' on the waveform is small. The elimination of the collar by the shaft, implemented to reduce leakage 3, does not improve the waveform and thus the same level of harmonic distoriton is maintained.

6.5.3 The Magnitude of the Output Flux per Pole and the Calculation of Terminal Voltage

The magnitude of the flux per pole is double the surface ingegral taken over the half of the pole represented in the model. This value is the amount of useful flux produced in each geometry over a pole pitch. The results computed are as follows:

BASE	-	4.1918×10^{-4} Wb
P10	-	4.2178×10^{-4} Wb
P15	-	4.1602×10^{-4} Wb
P20	-	3.9322×10^{-4} Wb
P10-R65	-	4.3124×10^{-4} Wb
P10-R66	-	4.2862×10^{-4} Wb
XL3	-	4.4268×10^{-4} Wb

The amount of output flux is affected by the change in pole geometry due to a change in the tapering of the pole and a change in 'a' or both. It is also affected by the change in the geometry of the flux guide due to the elimination of the collar by the shaft.

The increase in α which changes the taper of the pole reduces leakage and improves the air-gap flux waveform. This does not necessarily lead to an increase in the output of flux per pole due to the decrease

in surface area of the pole. It also increases the reluctance of the flux path through the pole. There is, however, an optimum which is seen in the graph in Figure 6.23. The graph is a plot of the amount of output flux per pole against α, the extend of taper of the pole. The peak occurs at a taper with $\alpha = 8.5^{o}$.

The effect of a change in 'a' is more complex. Iron path 2 has a very high flux density level and thus any change in the geometry of this path has a pronounced effect on the reluctance of this path. This, in turn, would affect the flux distribution in the whole flux guide. An increase in 'a' reduces leakage 2 but this also causes an increase in the reluctance of iron path 2. The results of the calculation of the flux per pole show these two opposing effects. When 'a' is small, the reluctance of iron path 2 is low but leakage 2 is large and when 'a' is large, the leakage is reduced but the reluctance in increased. The optimum is a balance between the two and in the model, this optimum occurs with the value a = 2.95 mm.

The most effective improvement is caused by the elimination of the collar by the shaft, due to the subsequent reduction of leakage 3. The magnitude of the output flux per pole is not the only factor which affects the load characteristics of the generator. The shape of the waveform must be considered.

A comparison of the induced voltage per phase on no load for each set of data, with a stator winding of 11 Tuns/coil and 12 coils/phase, show the influence of harmonics on the output of the machine.

BASE - 119.95 Volts

P10 - 122.70 Volts

P15 - 122.80 Volts

P20 - 117.30 Volts

A plot of the above results in Figure 6.24 shows that the peak is at $\alpha = 12^{o}$ which is higher than the optimum for the maximum flux per pole which is at a taper with $\alpha = 8.5^{o}$.

6.5.4 The Analysis of the Air-Gap Field On Load

For the analysis of the air-gap field on load, the conditions specified in case (v) in section 1 are used. The load levels studied are between 1 Ampere per conductor to 11 Amperes per conductor with the armature mmf pattern displaced between 90^{o} and 180^{o} from the rotor mmf thus covering the entire range of load angles. The load angle of the resultant of the air-gap flux waveform, with the armature mmf pattern at a fixed displacement, can be determined by doing an analysis of the waveform using the MOPH (modulus and phase) program[4] available with the data analysis computer at the I.S.V.R., University of Southampton. From this analysis the load characteristics of the generator represented by the model analysed, at different load angles, is calculated and is shown in Figure 6.25. The load angle at the different load levels can be obtained experimentally. Waveforms at the different loads are recorded as described in Chapter 3. A search coil is used to determine the position from which the cycle to be analysed starts. The load angle will be simply the shift of the fundamental from the position on no-load to that position on-load. The load angle is plotted against load current in Figure 6.26. Using Figure 6.25 and Figure 6.26, the load characteristic of generator A computed by the three-dimensional finite-element method is drawn. This is shown by the full line in Figure 6.27. The dotted line in the same figure is the characteristic determined experimentally. In the comparison of these two curves, it must be borne in mind the characteristic computed by the finite-element method considers only the declared values of armature resistance and reactance of the generator.

The correlation between the computed curve and the experimental curve is close. The error is never in excess of 6%.

The harmonic components of the voltage at the different loads are obtained from their respective waveforms and plotted in Figure 6.28. It shows the third and the fifth harmonics as a percentage of the fundamental, as load varies. These two curves are compared with the experimental results, discussed in Chapter 3, represented in Figure 6.28 as dotted lines. The correlation is close but the computed value is consistently higher than the experimental result. This can be attributed to the crude discretisation of the air-gap resulting in the error in the computation of the shape of the air-gap flux waveform. These results also reflect the omission of eddy currents in the computation.

6.5.5 The Effect of a Change in the Pole Face Profile on the Maximum Power Output

The peak power point of generator A, obtained experimentally, is at a load current of 6 amps. This matches the results obtained by both the discrete reluctance method and the three-dimensional finite-element program. The latter technique is used to change the pole geometry by changing the taper of the pole. The peak power output computed with the different values of α are plotted in Figure 6.29. The optimum is at $\alpha = 10^{o}$. This point occurs at a value of α between the optimum for maximum flux per pole and the optimum for output voltage (see Figures 6.23 and 6.24).

6.5.6 Conclusions

The following conclusions can be drawn from the analysis of the air-gap field of the imbricated rotor.

i) The shape of the air-gap flux waveform is dependent on the pole face profile. By changing the taper of the pole, a better wave-

form can be achieved. The increase in taper of the pole results in a waveform closer to that of the desired sinusoid.

ii) The air-gap flux waveform computed differs from the experimental value by 8%. This is reflected in the output voltage calculated.

iii) The effect of the taper on the waveform results in a decrease in harmonic distrotion. An increase of the taper α from approximately 1/9 of a pole pitch ($\alpha = 5.366^{o}$) to 4/9 of a pole pitch ($\alpha = 20^{o}$) reduces the third harmonic content from 30% to 7.5%.

iv) The shape of the waveform is only influenced by the profile of the pole face.

v) The magnitude of the output flux per pole depends on the whole geometry of the flux guide. It is sensitive to both the taper and 'a'. The optimum taper as regards maximum flux output is at $\alpha = 8.5^{o}$. This increases the flux output from the model analysed by 1%. The optimum value of 'a' is 0.295 mm. This results in an improvement of 1.9%. The combined effect is an improvement of 3.0%.

vi) The elimination of the collar adjacent to the shaft results in an increase of flux output by 5.6%.

vii) By optimising for 'a' and α and eliminating the collar, the flux output can be increased by 8.6%.

viii) The calculation of the voltage from the air-gap field considers both its magnitude and its shape. It is found that the optimum taper for maximum output voltage is at $\alpha = 12^{o}$.

ix) The output characteristic of generator A computed using the three-dimensional finite-element method has a close correlation with the experimental results. The error is never in excess of 6%.

x) The harmonic content computed at the various loads compares

favourably with the results obtained experimentally. It is consistently higher than the experimental results.

xi) The maximum power output occurs at a taper with $\alpha = 10^{o}$.

6.6 THE WORKING POINT OF THE MAGNET

The working point of the magnet is charted from the computation of the field of the model on-load. As the load increases, the opposing mmf due to the armature currents, pushes the working point of the magnet down its demagnetisation curve. This results in the regulation characteristics of permanent-magnet generators. As the model is optimised for maximum output, the working point of the magnet at that point should be working at the $(BH)_{max}$ point. This is confirmed by the computation using using TOSCA.

6.7 GENERAL CONCLUSIONS

i) This three-dimensional analysis of the field of the imbricated rotor has shown the influence of various parameters on the flux distribution and leakage fields in the rotor.

ii) The pole geometry is the single most important factor in the design of the flux guide. The taper and the parameter 'a' affect the flux distribution and the leakages as well as the shape of the air-gap flux waveform.

iii) There is a critical balance between the magnet surface area and the thickness of the iron discs (iron path 1).

iv) The collar by the shaft is redundant and contributes to leakage and should be eliminated in the design of the flux guide.

v) The iron disc which carries the flux from the surface area of the magnet to the poles is inefficient. (This is discussed in Chapter 8).

vi) The air-gap flux wave form can be optimised for maximum output or minimum distortion.

vii) Optimising the geometry of the pole and the elimination of the collar by the shaft result in a substantial increase in the output of the generator.

viii) The characteristic of the generator A computed using the three-dimensional finite-element method is accurate. It, however, requires an excessive amount of computer time and is expensive. Thus, it is not the most efficient use of limited resources.

6.8 REFERENCES

1. Simkin, J. : 'TOSCA User Guide', Rutherford Laboratories, Didcot, Oxon, 1981.

2. Langsdorf, A. S. : 'Theory of a.c. machinery', McGraw Hill Book Company, New York, N.Y., 1955.

3. Jabbar, M. A. : 'Analysis of the performance of a permanent magnet alternating current machine', Ph.D. Thesis, Southampton University, 1977.

4. I.S.V.R. Southampton: 'Description of available programs on the DAC-PDP11/75, Sections 1, 2, 3 and 4', University of Southampton.

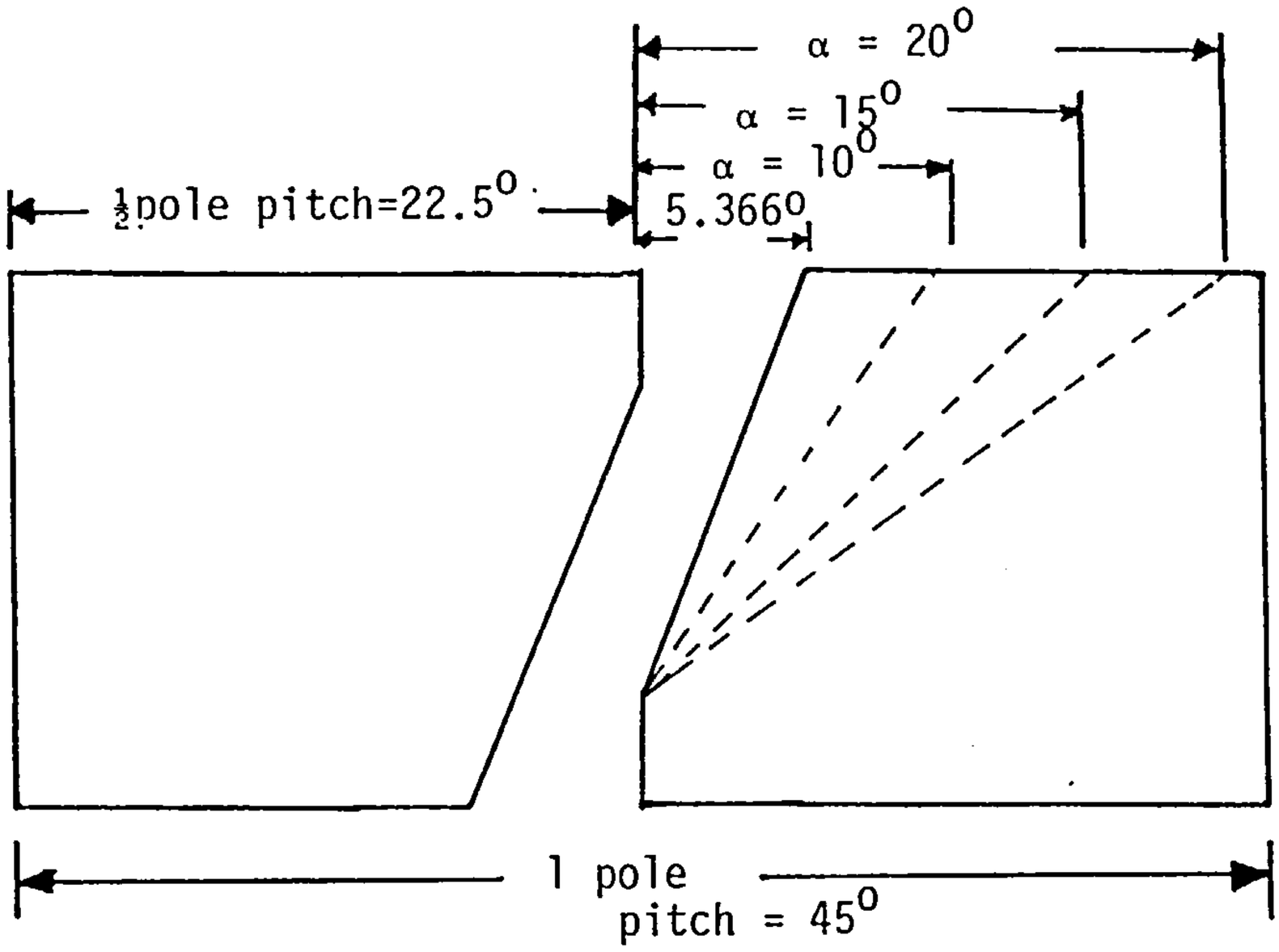

(a) Change in α

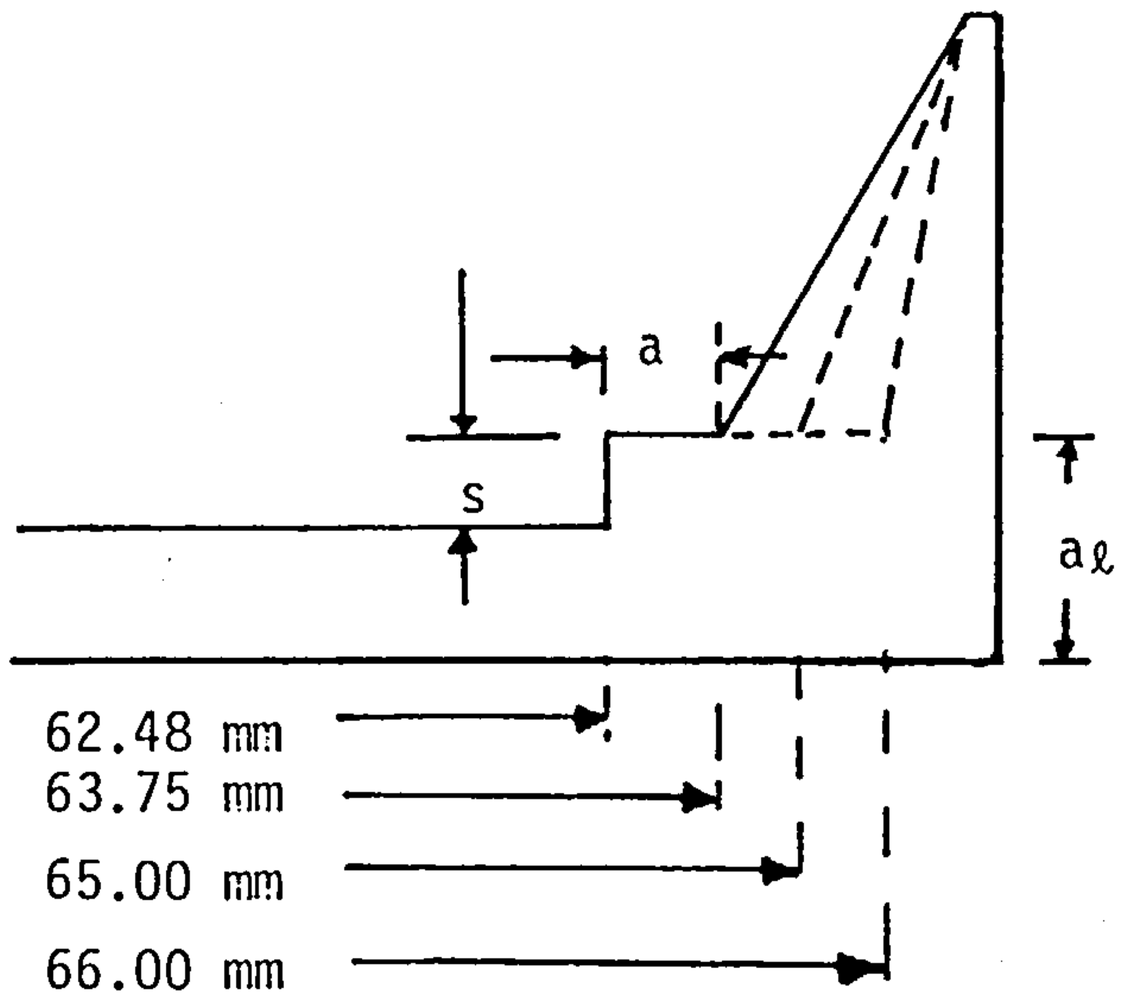

(b) Change in 'a'

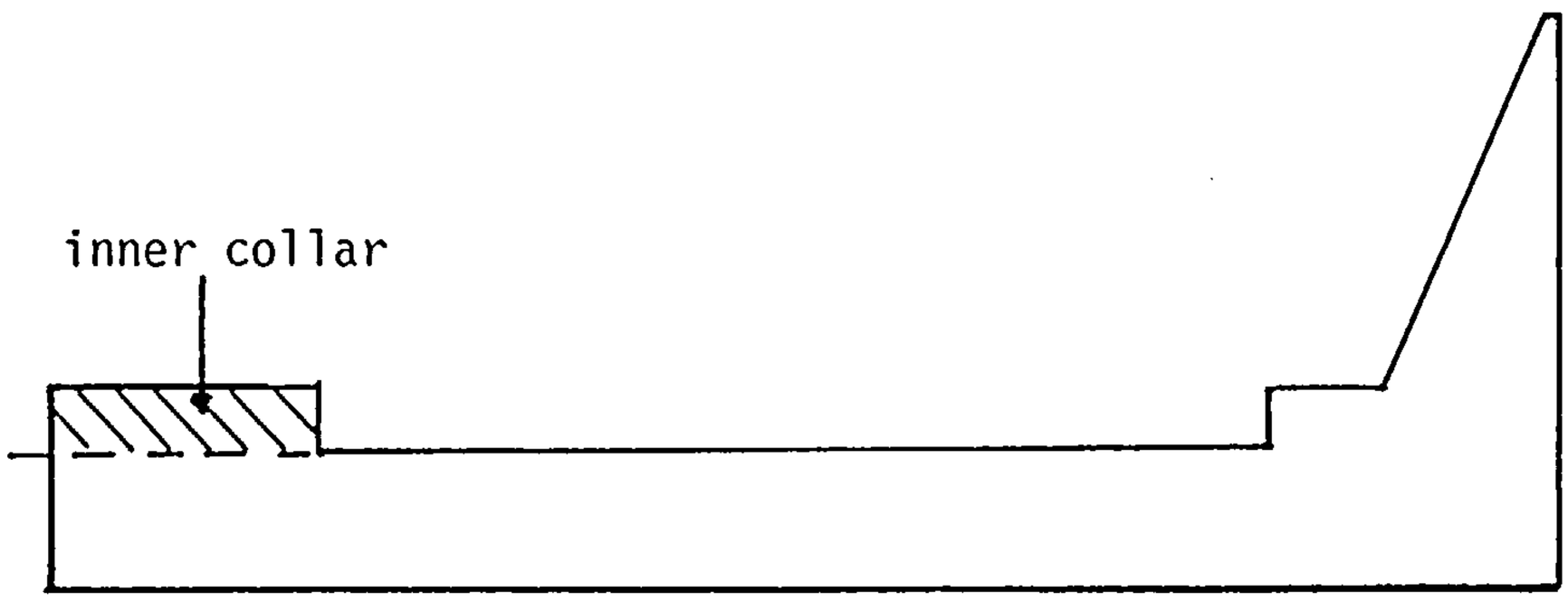

(c) Geometry with the inner collar removed

Fig. 6.1 Diagrams showing the changes in geometry of the flux guide

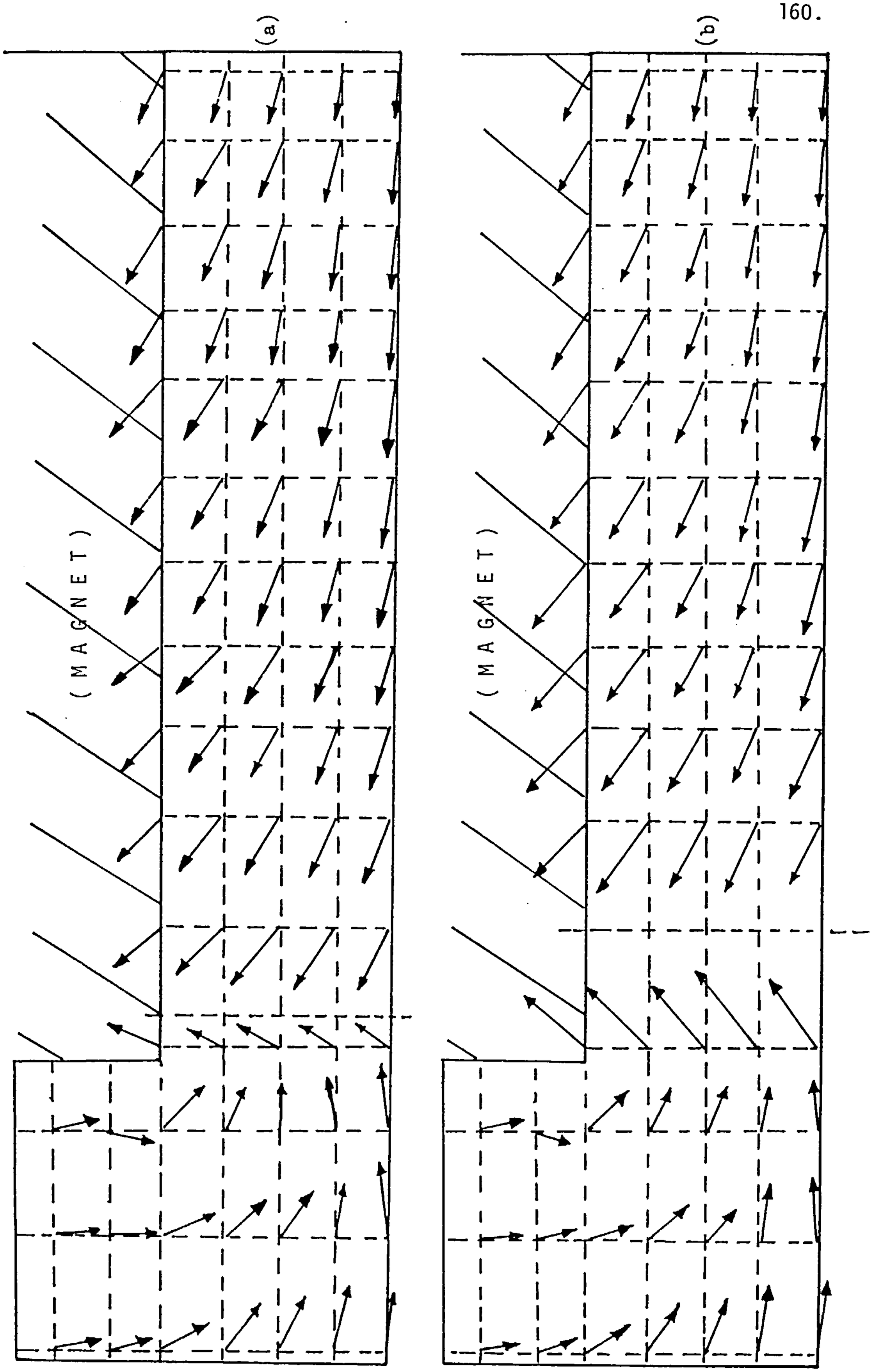

Fig. 6.2 (a, b) The direction of flux in the flux guide on the RZ plane at $\theta = 9^{o}$ and $\theta = 18^{o}$

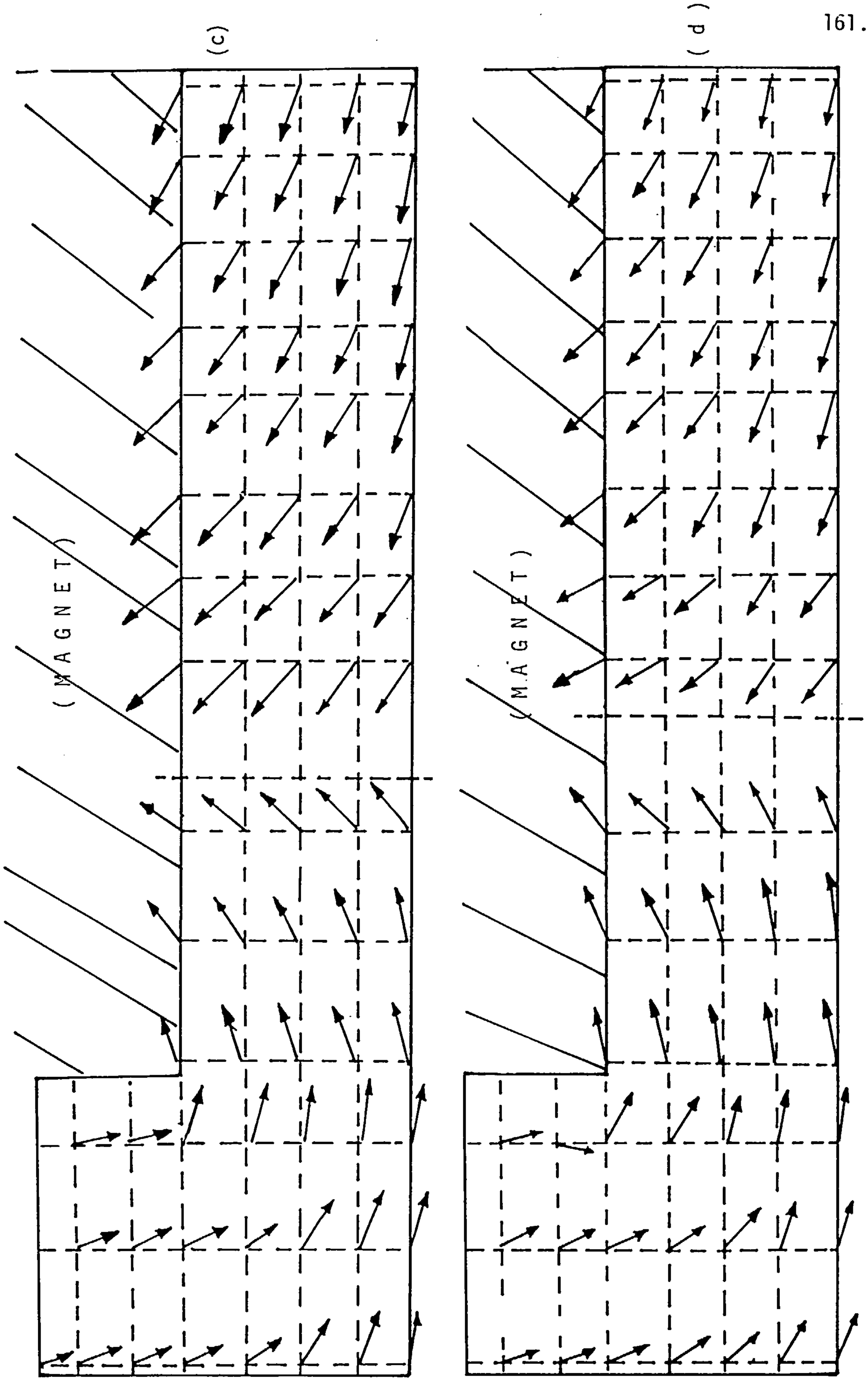

Fig. 6.2 (c, d) The direction of flux in the flux guide on the RZ plane at $\theta = 27^{o}$ and $\theta = 36^{o}$

Scale = 1 : 2

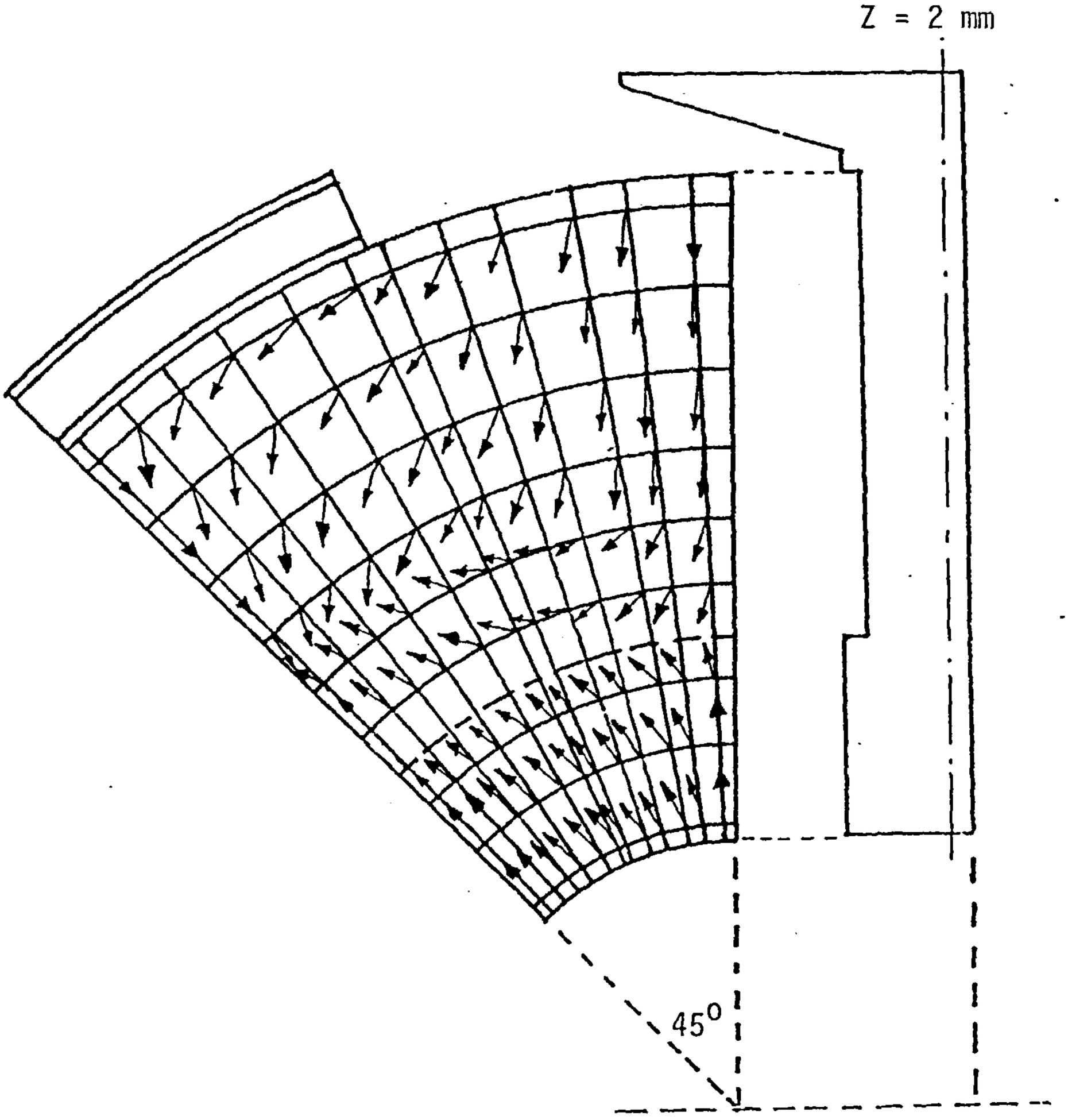

Fig. 6.3(a) The direction of the flux in the Rθ plane at Z = 2 mm from the basic plane.

Scale = 1 : 2

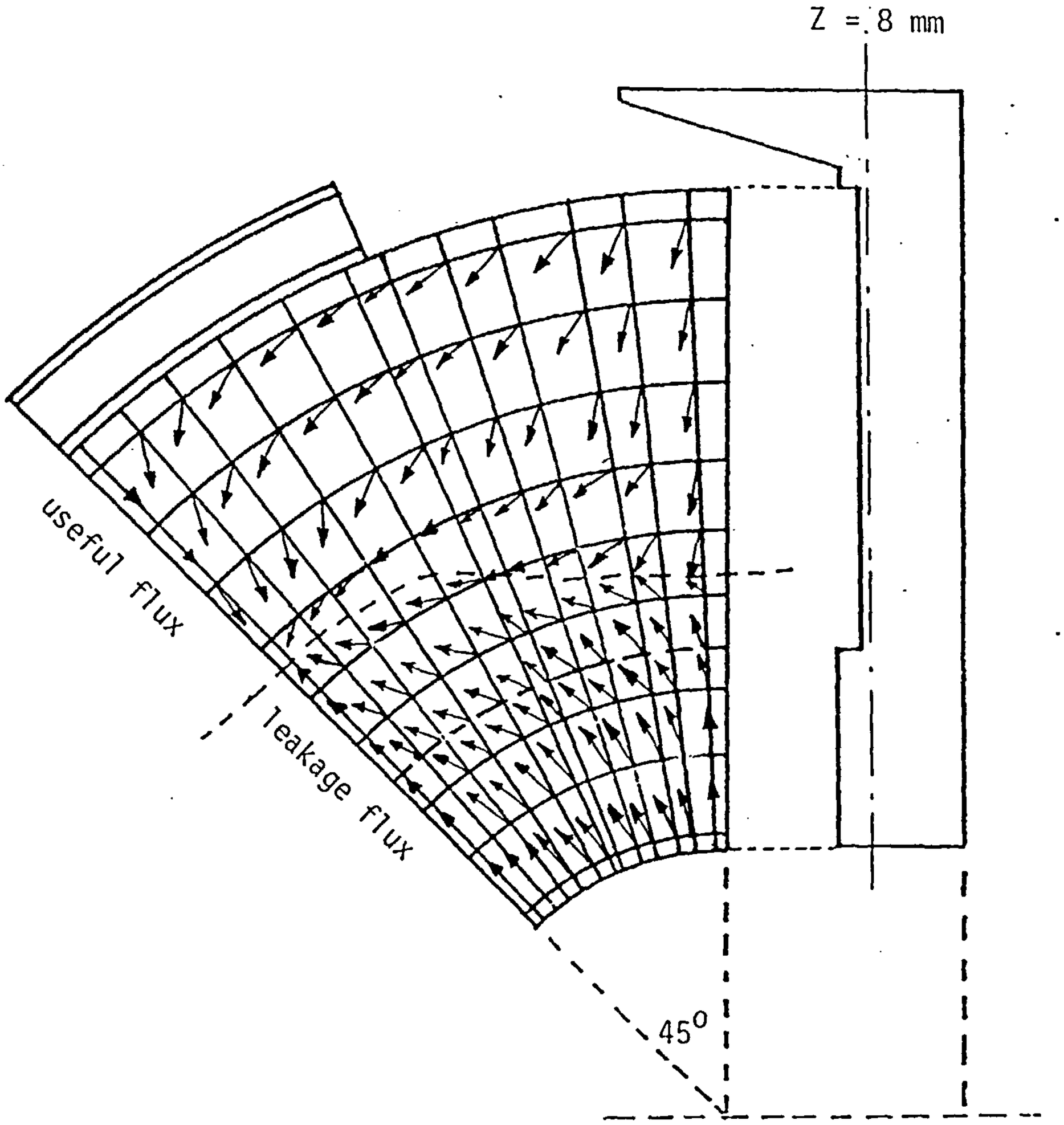

Fig. 6.3(b) The direction of the flux in the Rθ plane at Z = 8 mm from the base plane.

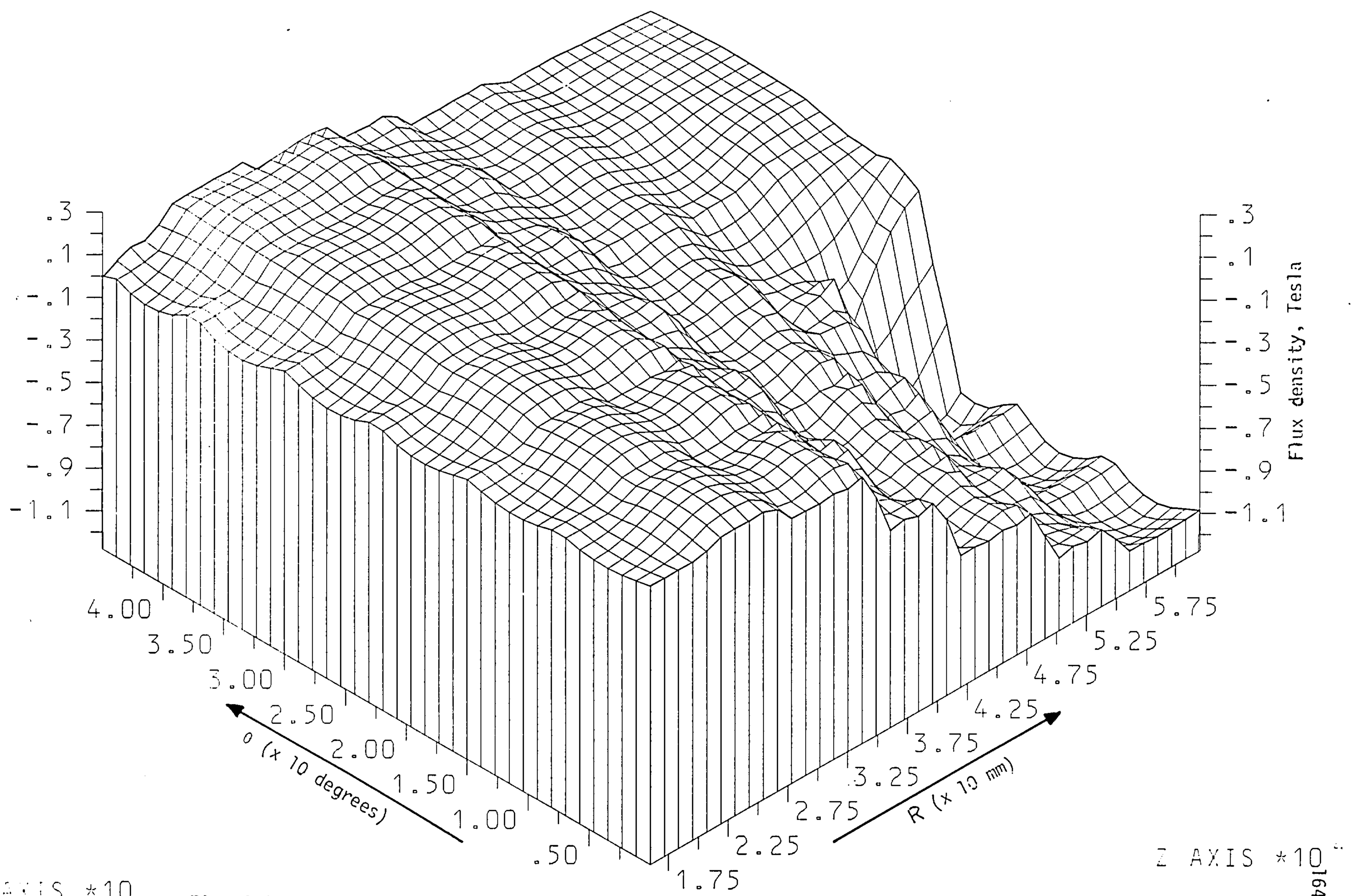

Fig. 6.4 The distribution of B_R over the Rθ plane in iron path 1 Z =

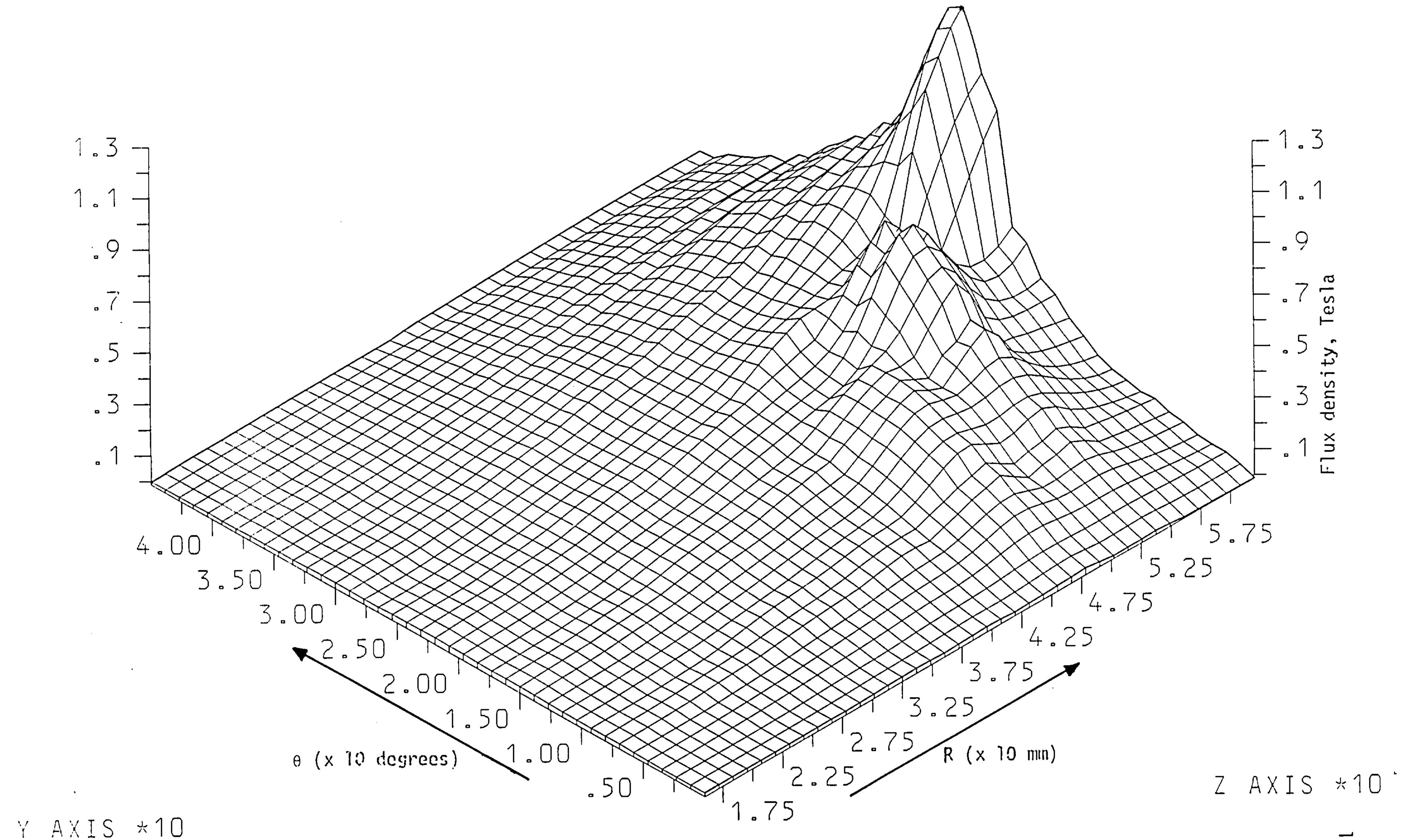

Fig. 6.5 The distribution of B_θ over the Rθ plane in iron path 1 Z = 4 mm

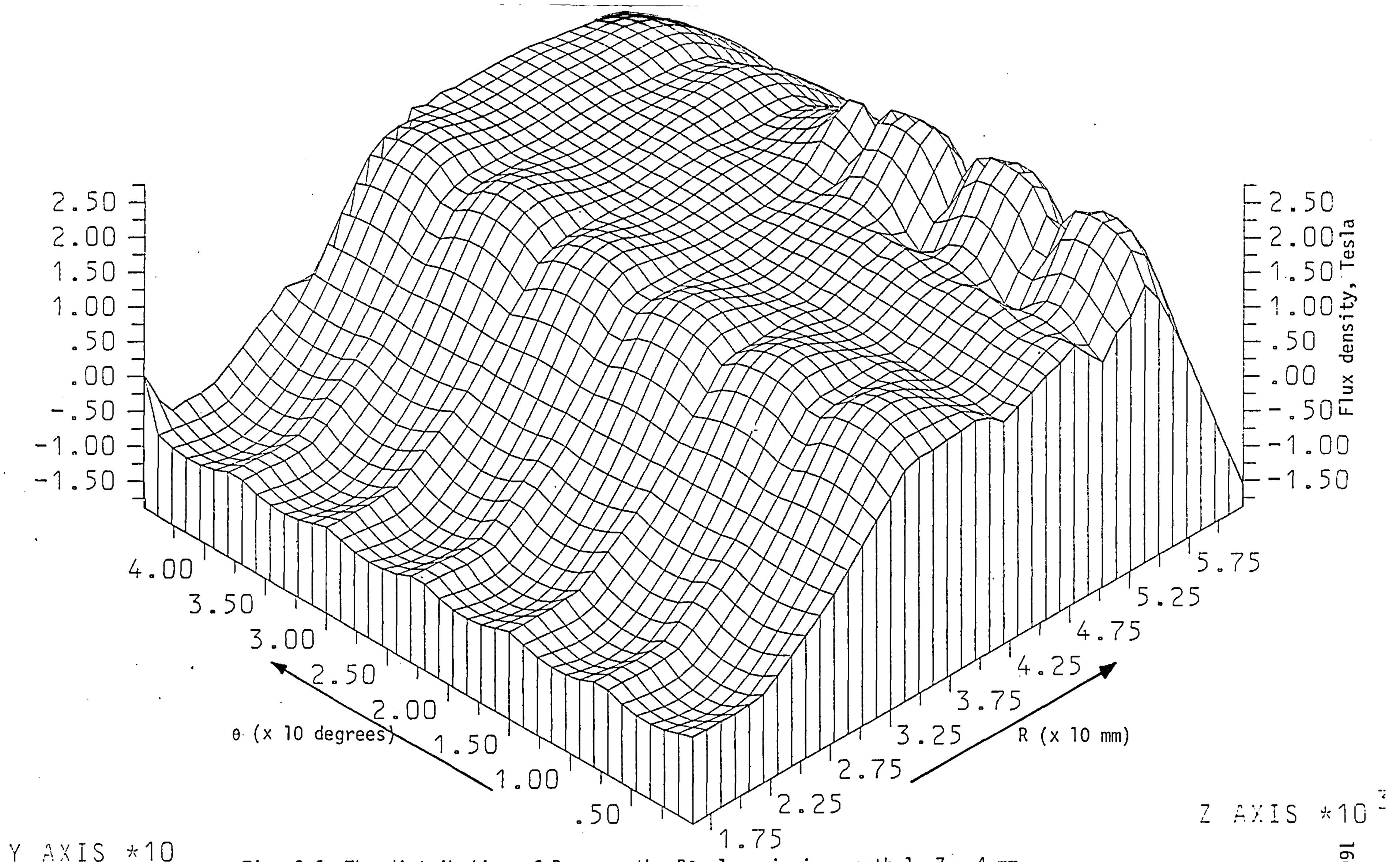

Fig. 6.6 The distribution of B_Z over the Rθ plane in iron path 1 Z = 4 mm

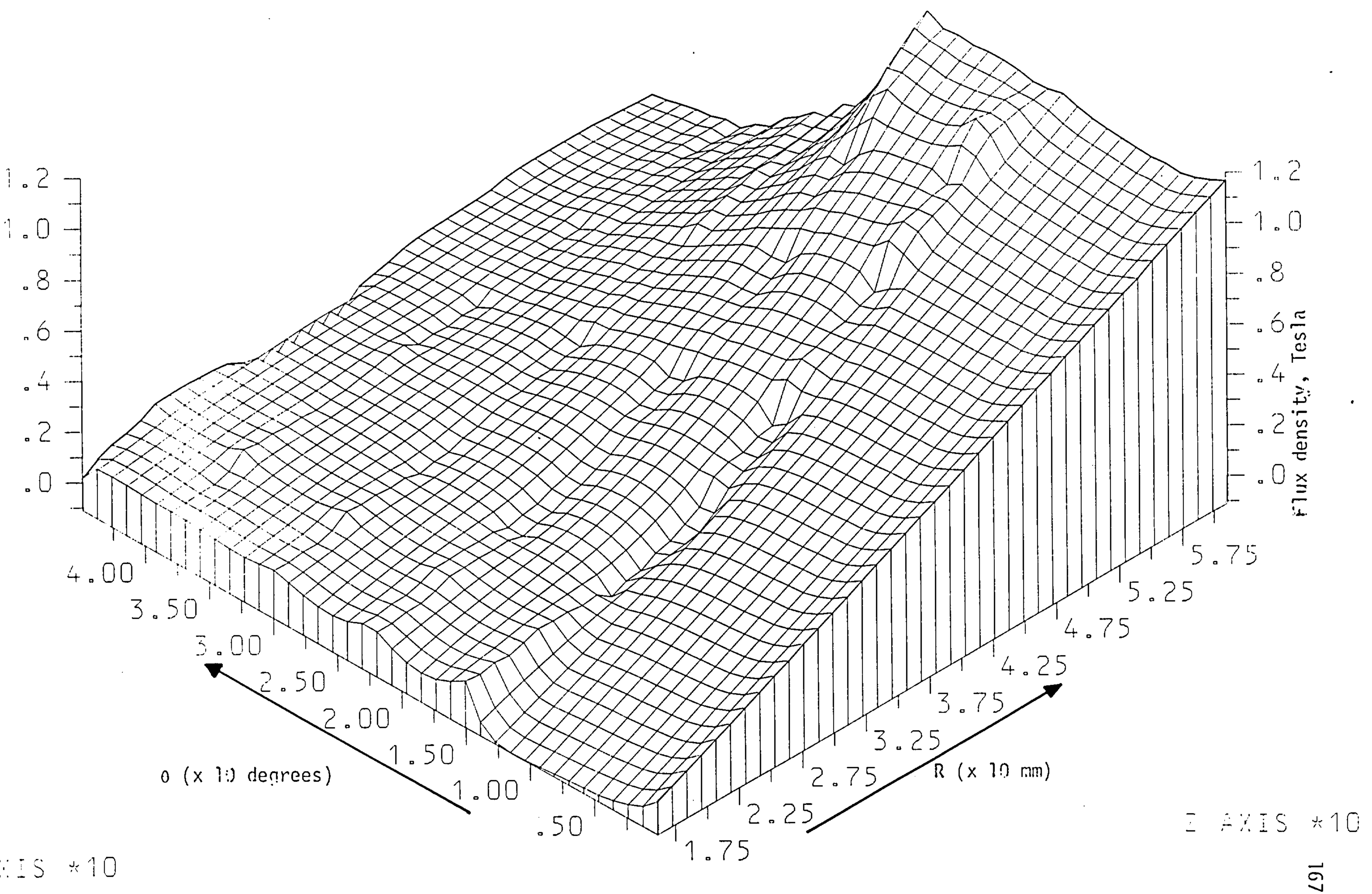

Fig. 6.7 The flux density level (B_{mod}) over the R_0 plane in iron path 1

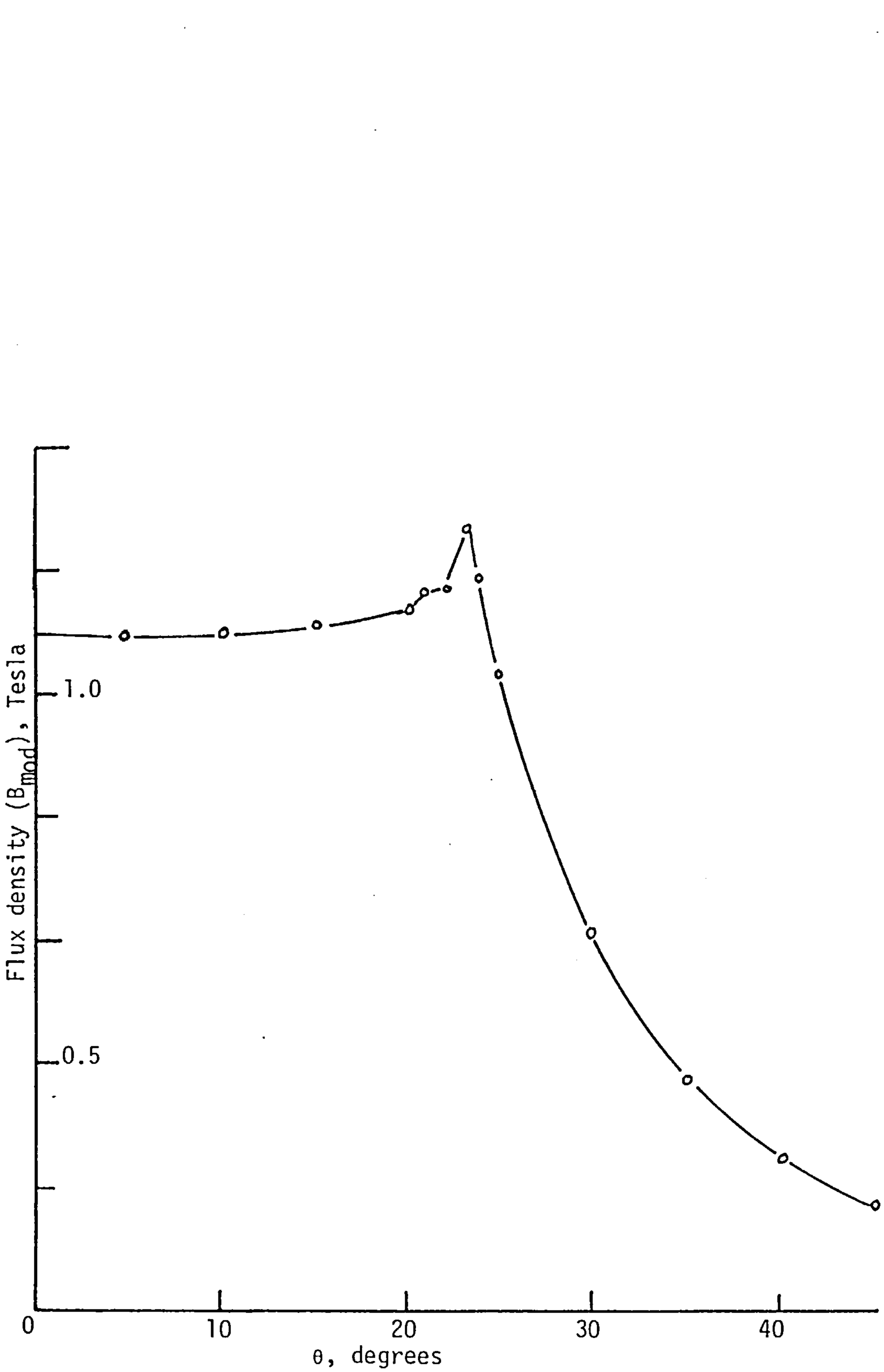

Fig. 6.7(a) The variation of B_{mod} along the edge of iron path 1 (R = 63 mm, Z = 4 mm)

B_{mod} R = 6.20
Z = 0.4

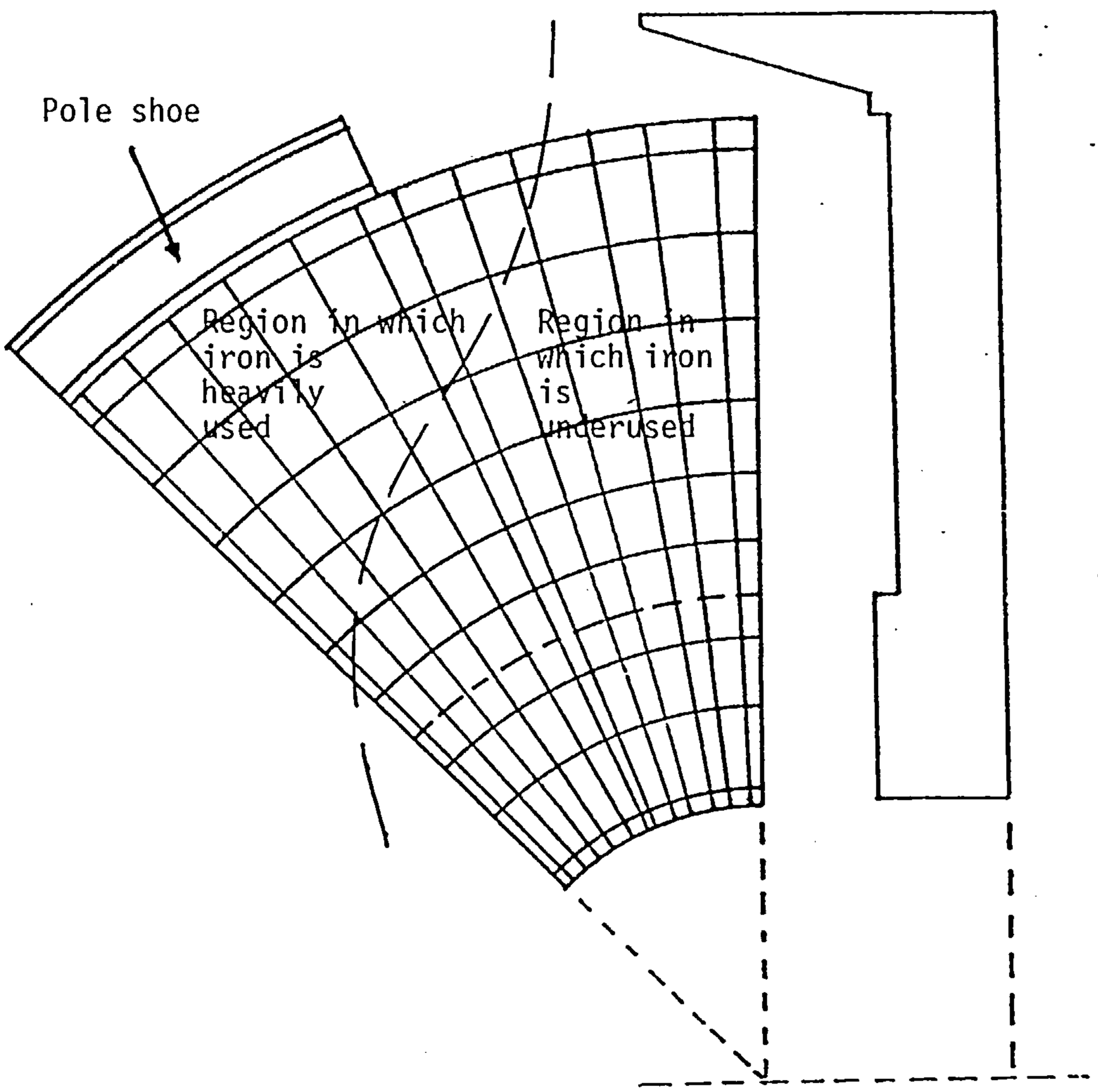

Fig. 6.8 The regions of differential iron usage.

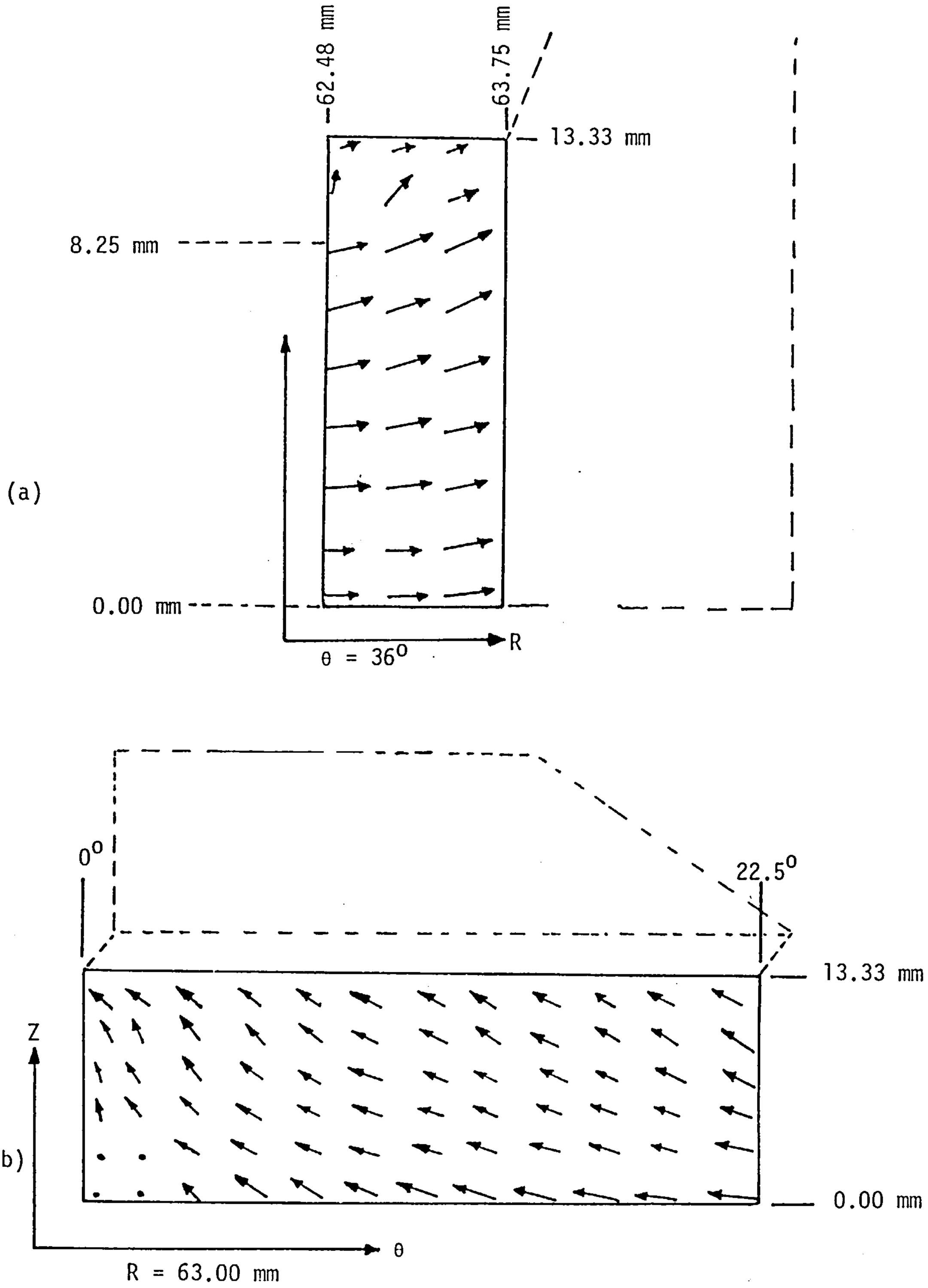

Fig. 6.9 Direction of the flux on the RZ plane and the θZ plane in iron path 2.

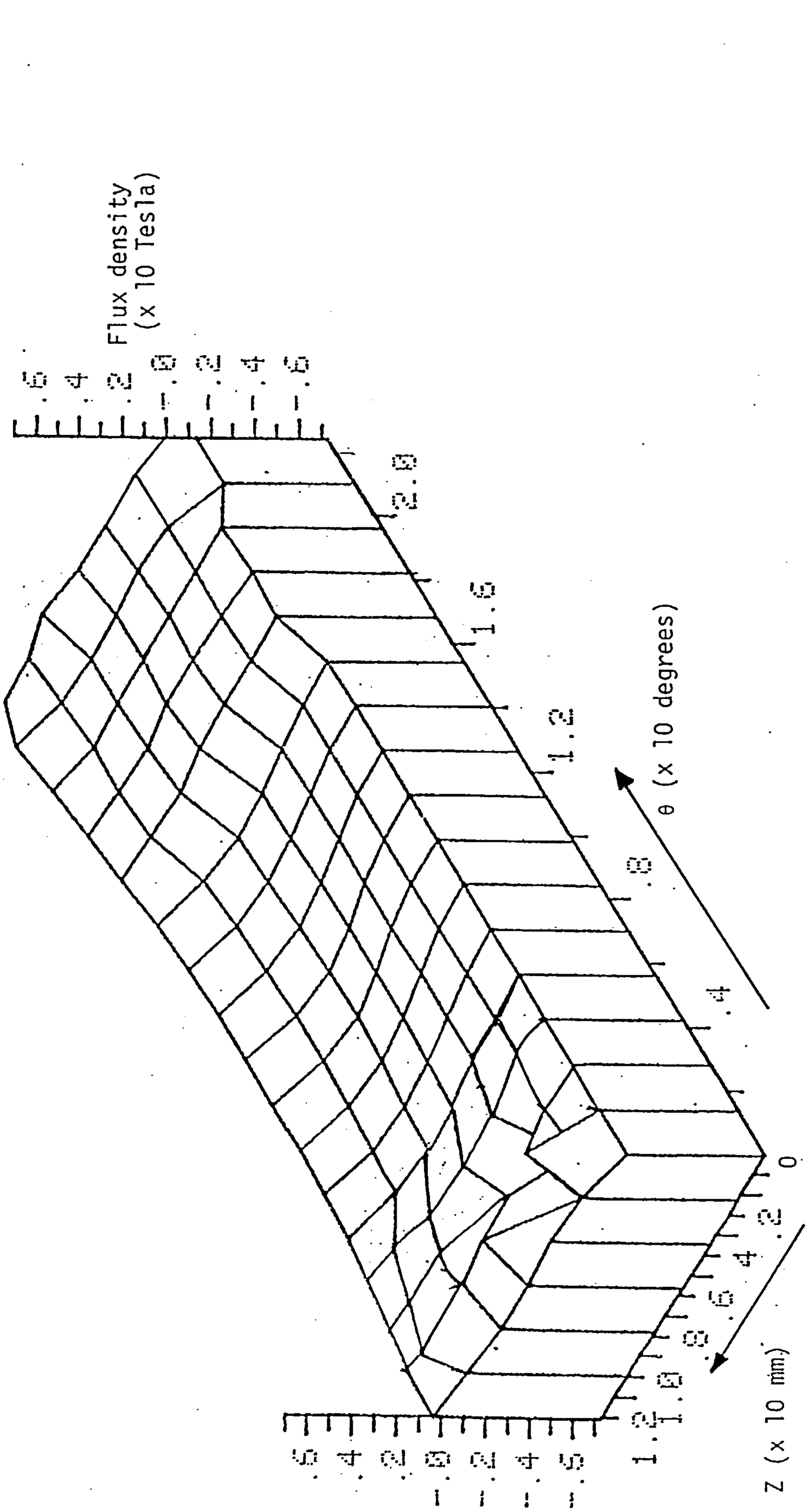

Fig. 6.10(a) The distribution of B_R over the θZ plane in iron path 2

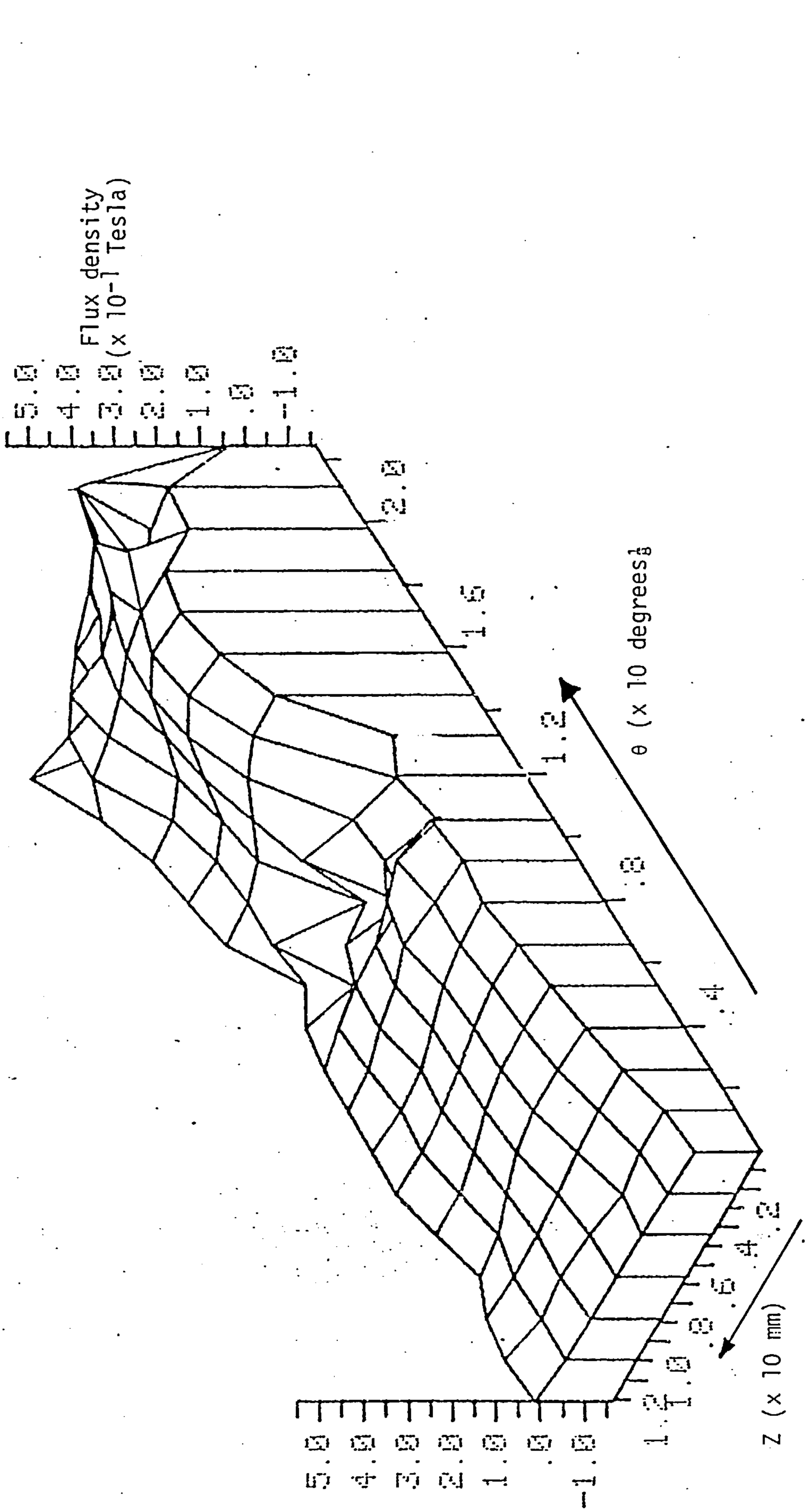

Fig. 6.10(b) The distribution of B_θ over the θz plane in iron path 2

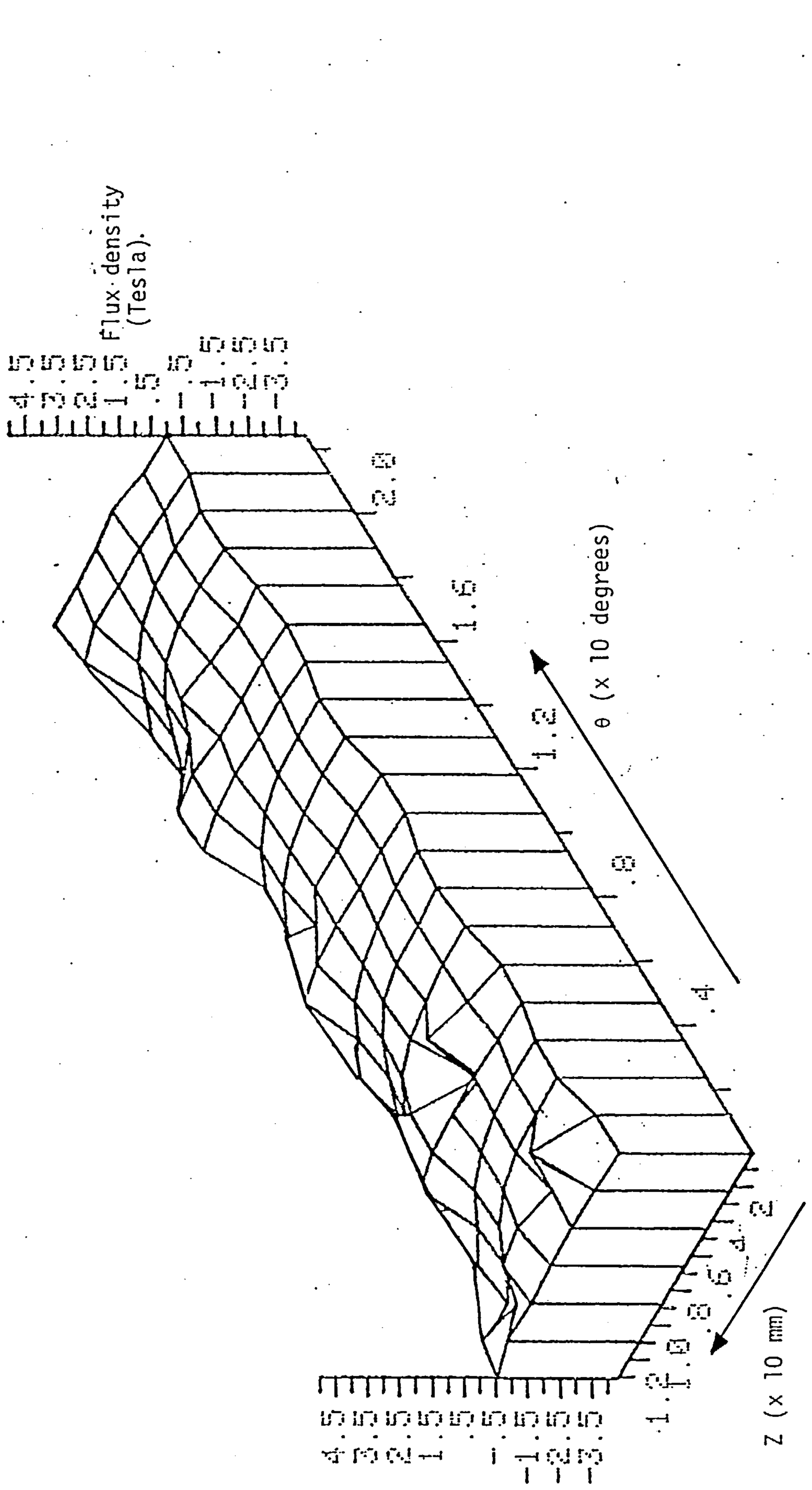

Fig. 6.10(c) The distribution of B_Z over the θZ plane in iron path 2.

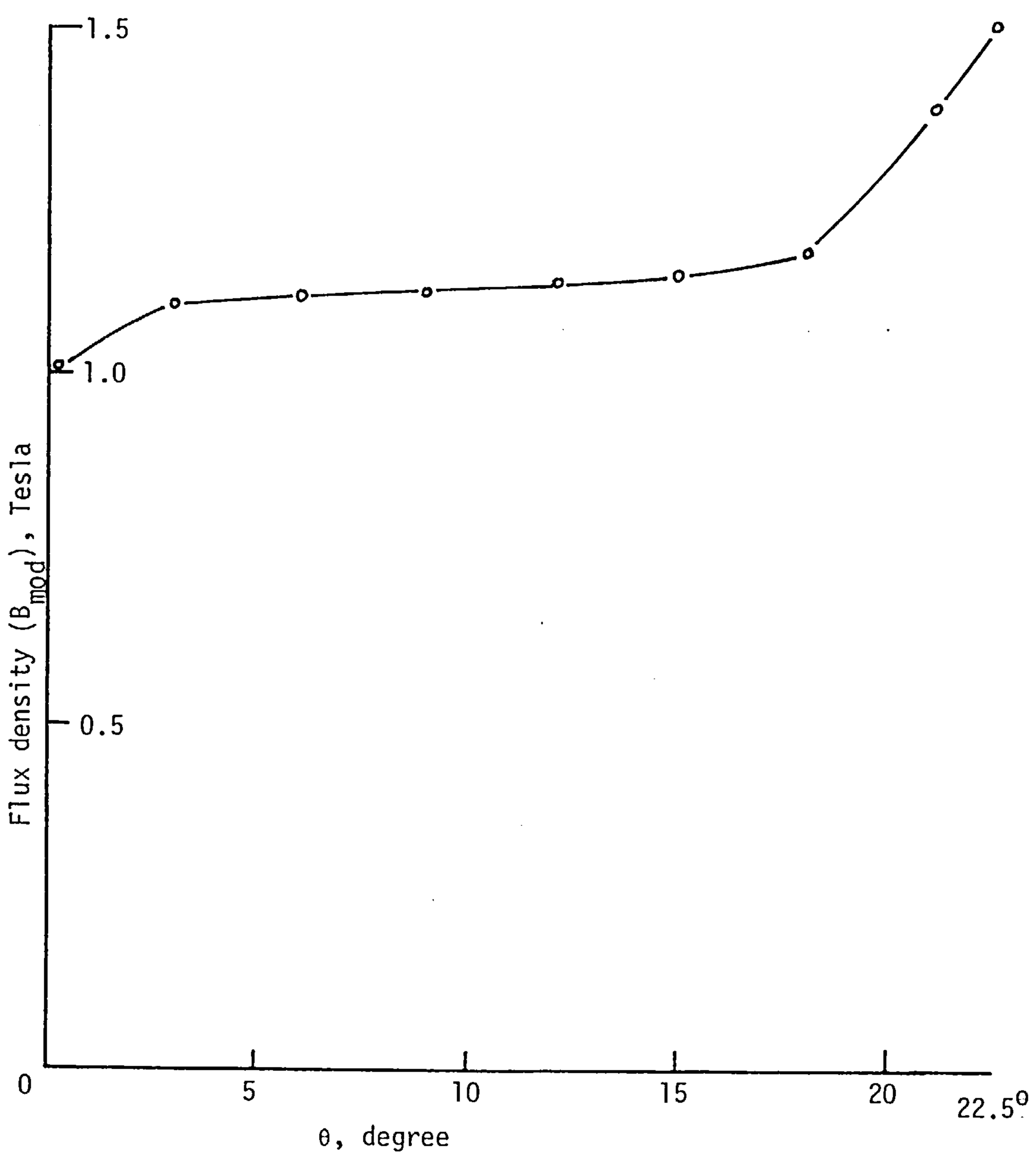

Fig. 6.11 The variation of B_{mod} along the line R = 63 mm, Z = 6.5 mm from 0^o to 22.5^o

B_{mod} at R = 6.30
Z = 0.65

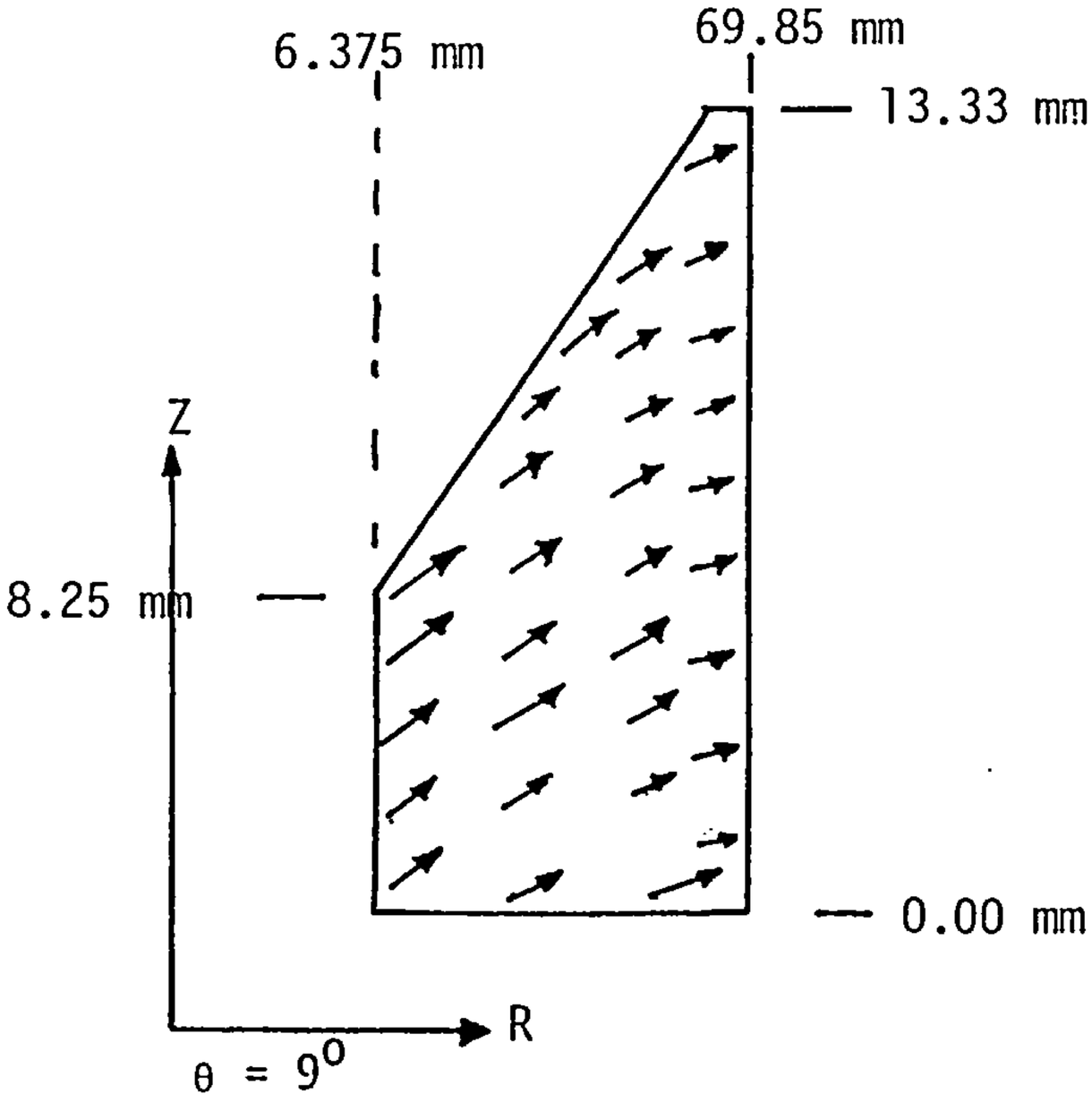

Fig. 6.12 The direction of flux in the RZ plane in iron path 3.

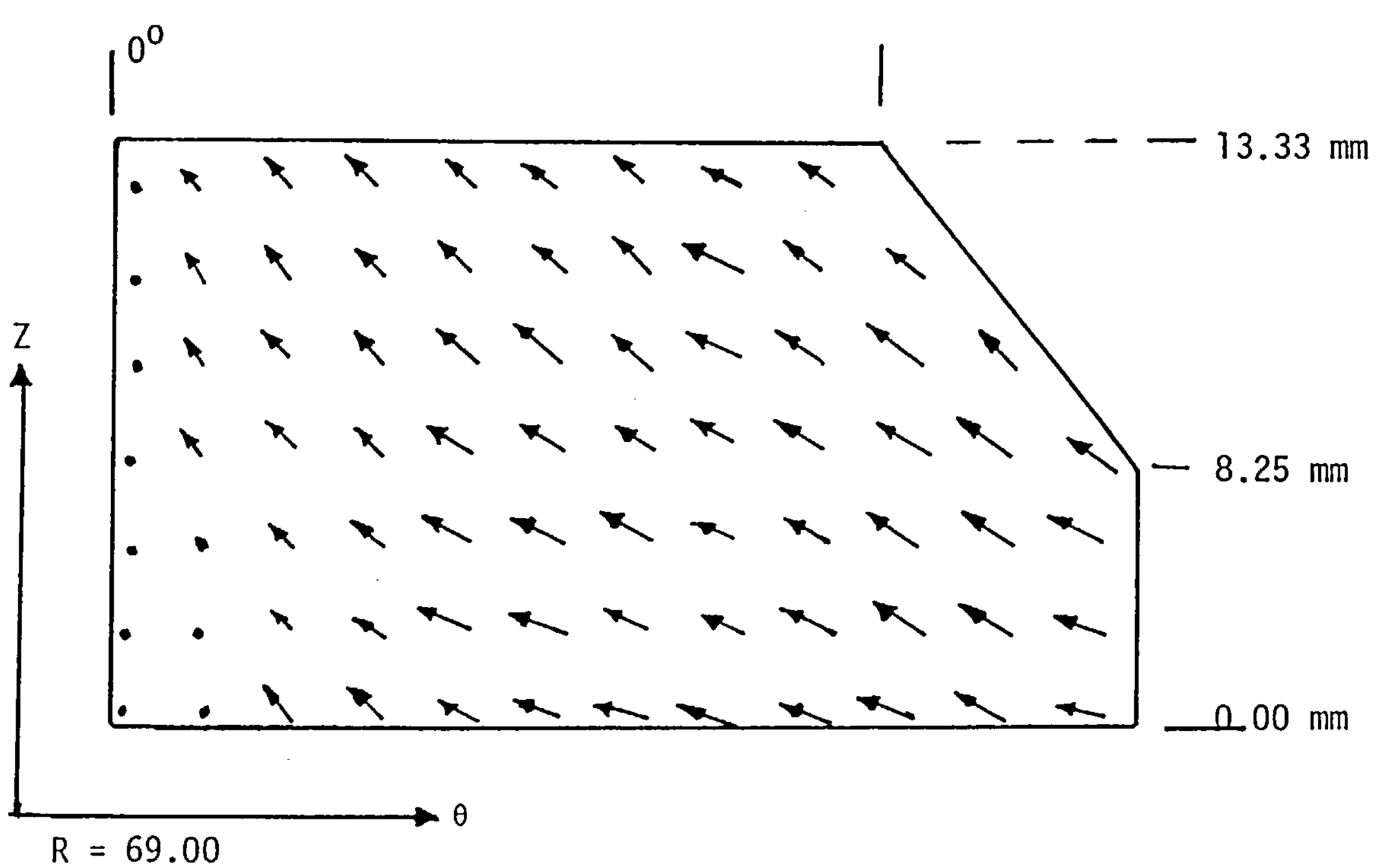

Fig. 6.13 The direction of flux in the θZ plane in iron path 3.

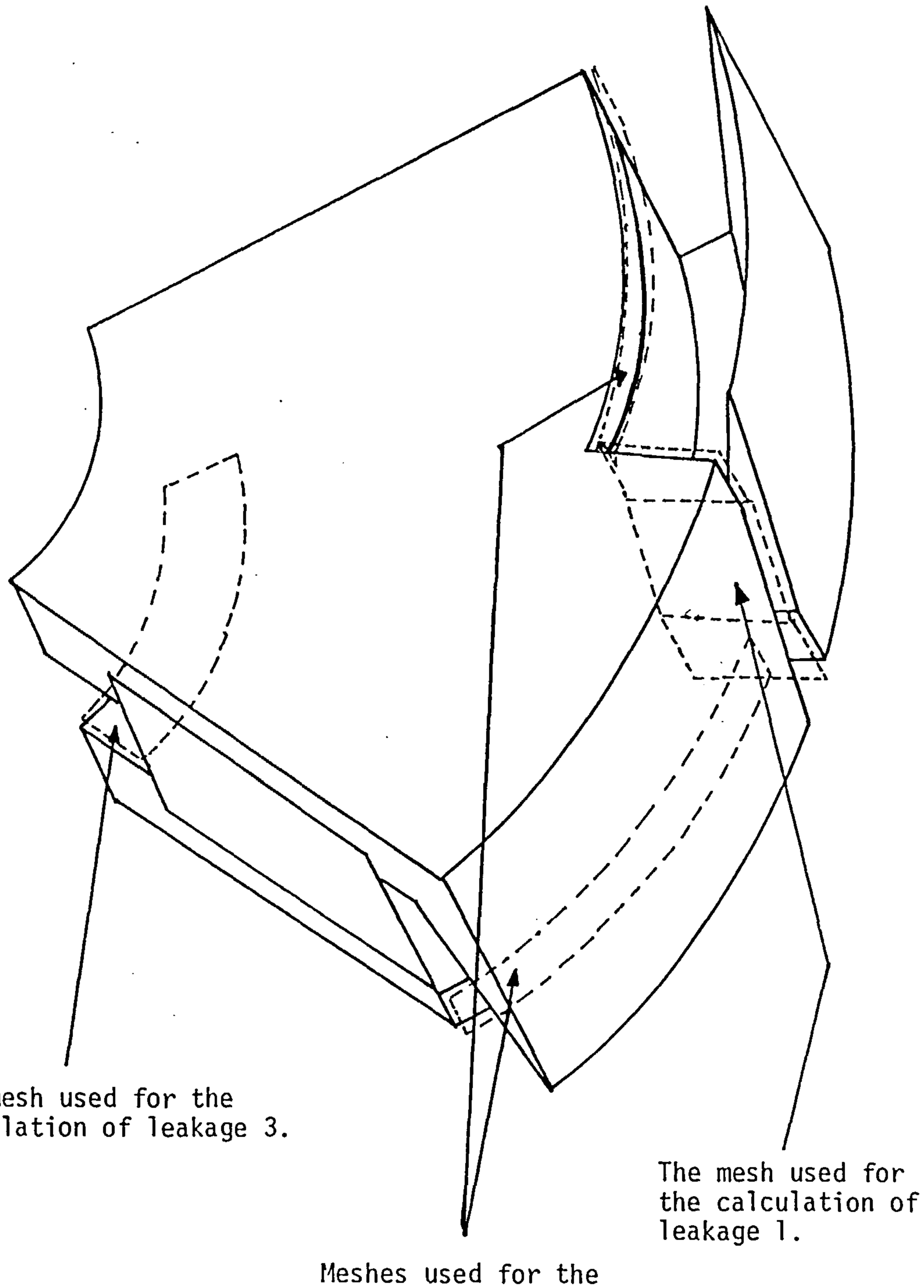

The mesh used for the calculation of leakage 3.

The mesh used for the calculation of leakage 1.

Meshes used for the calculation of leakage 2.

Fig. 6.14 The meshes used for the calculation of the magnitude of the leakage fluxes.

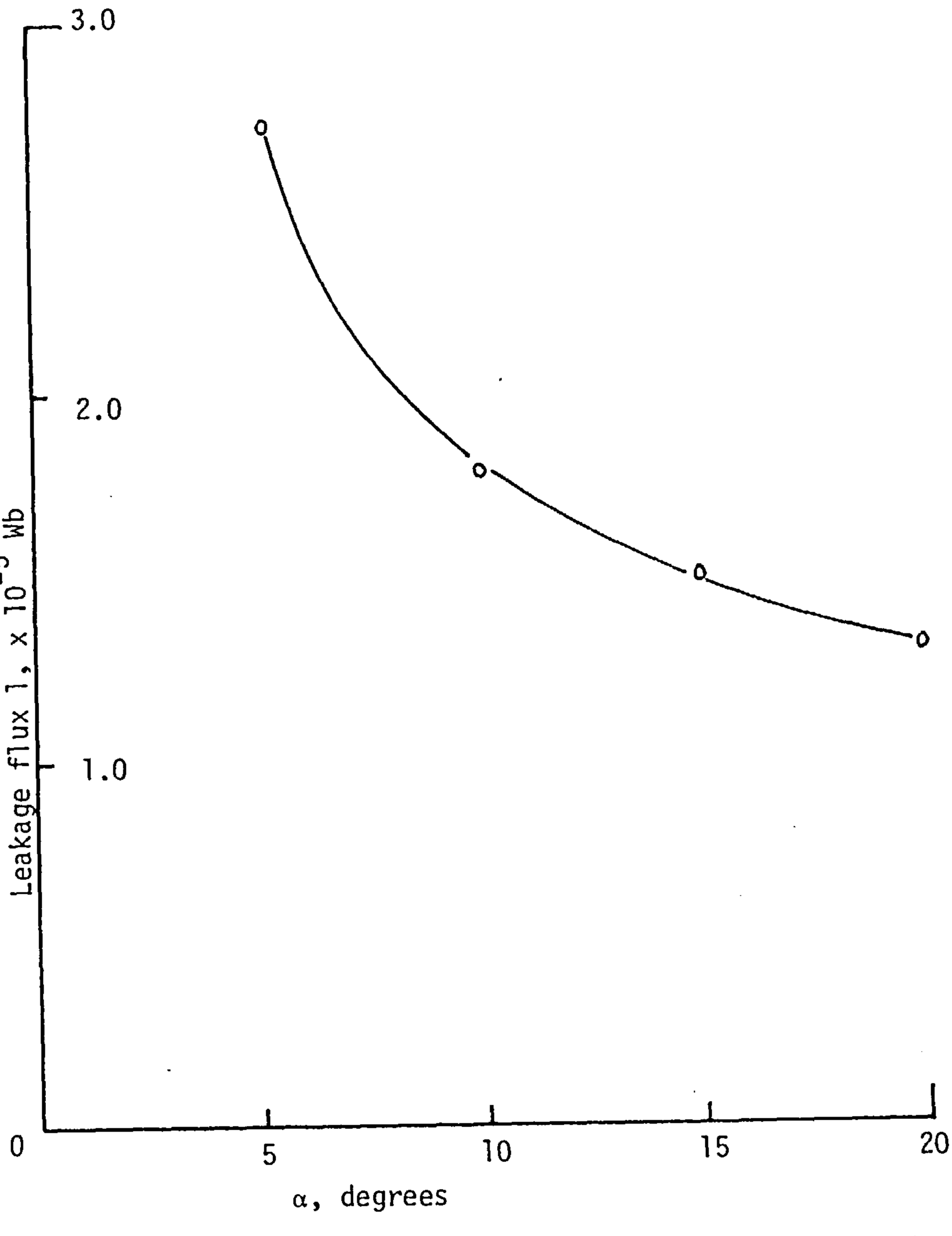

Fig. 6.15 The effect of a change in α on leakage 1.

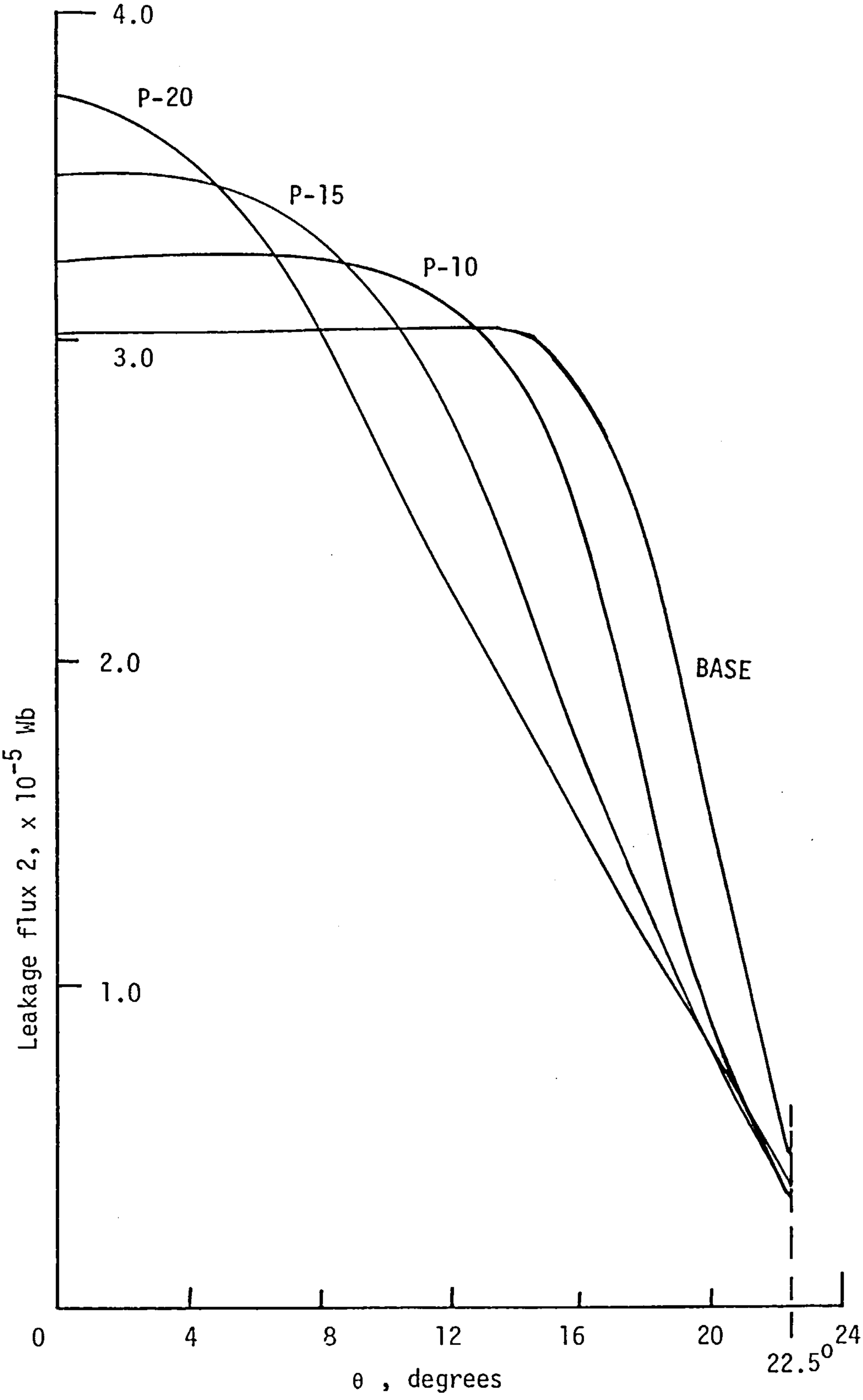

Fig. 6.16 The effect of a change in α on leakage 2.

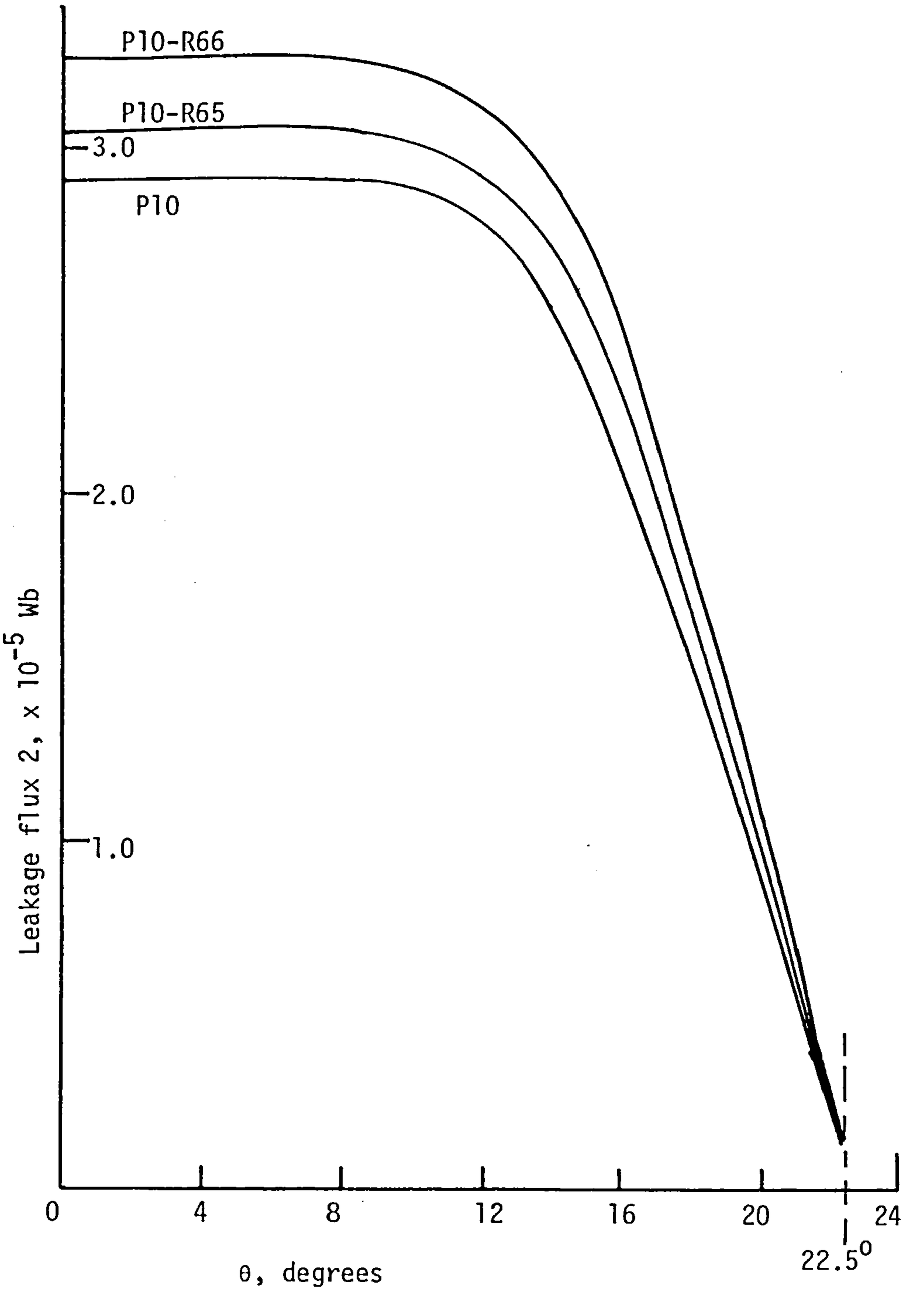

Fig. 6.17 The effect of a change in 'a' on leakage flux 2.

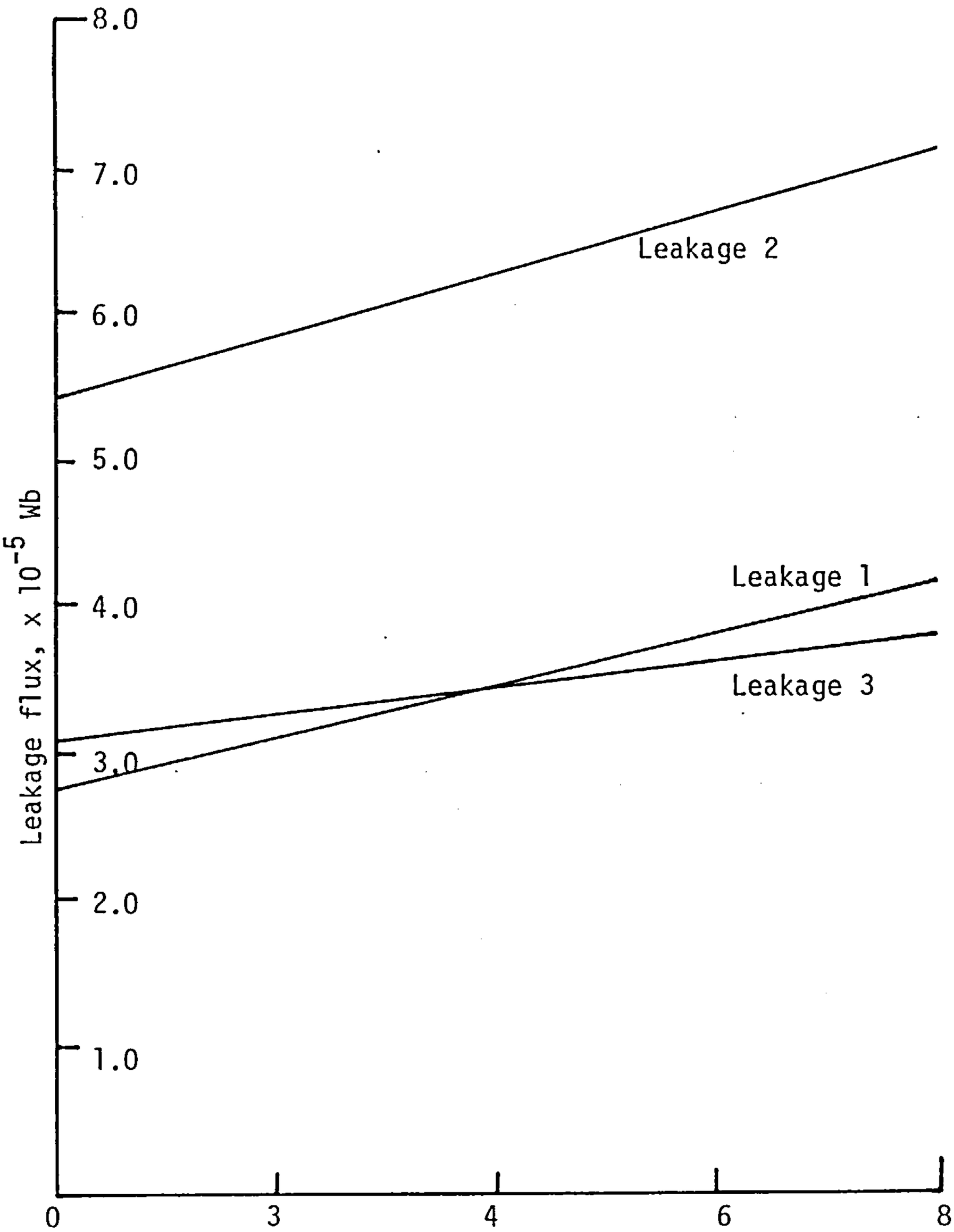

Fig. 6.18 The effect of load on leakage.

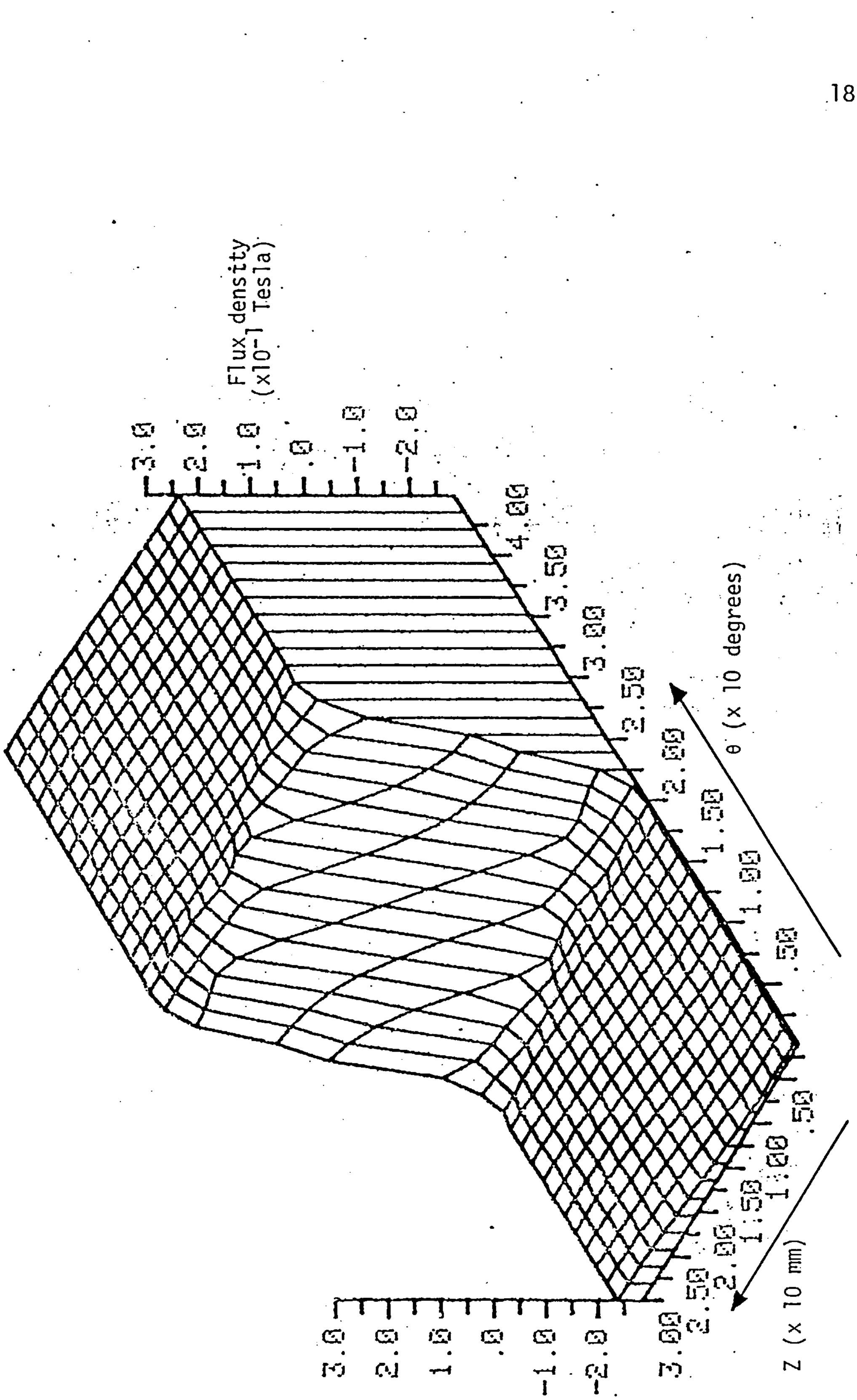

Fig. 6.19 The flux distribution in the air gap for Data-BAEE of generator A.

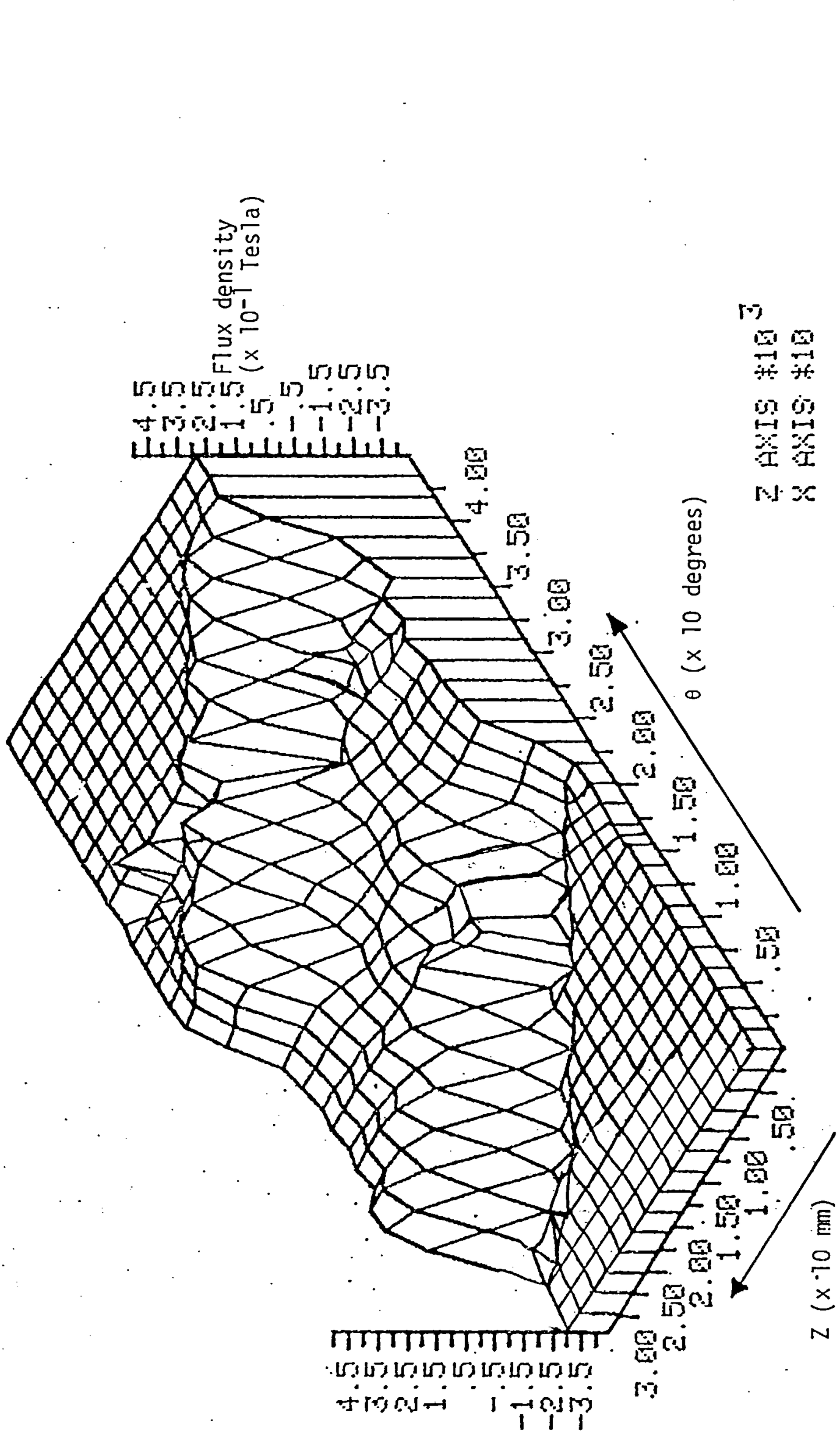

Fig. 6.20 The flux density level in the air gap for dataset P20.

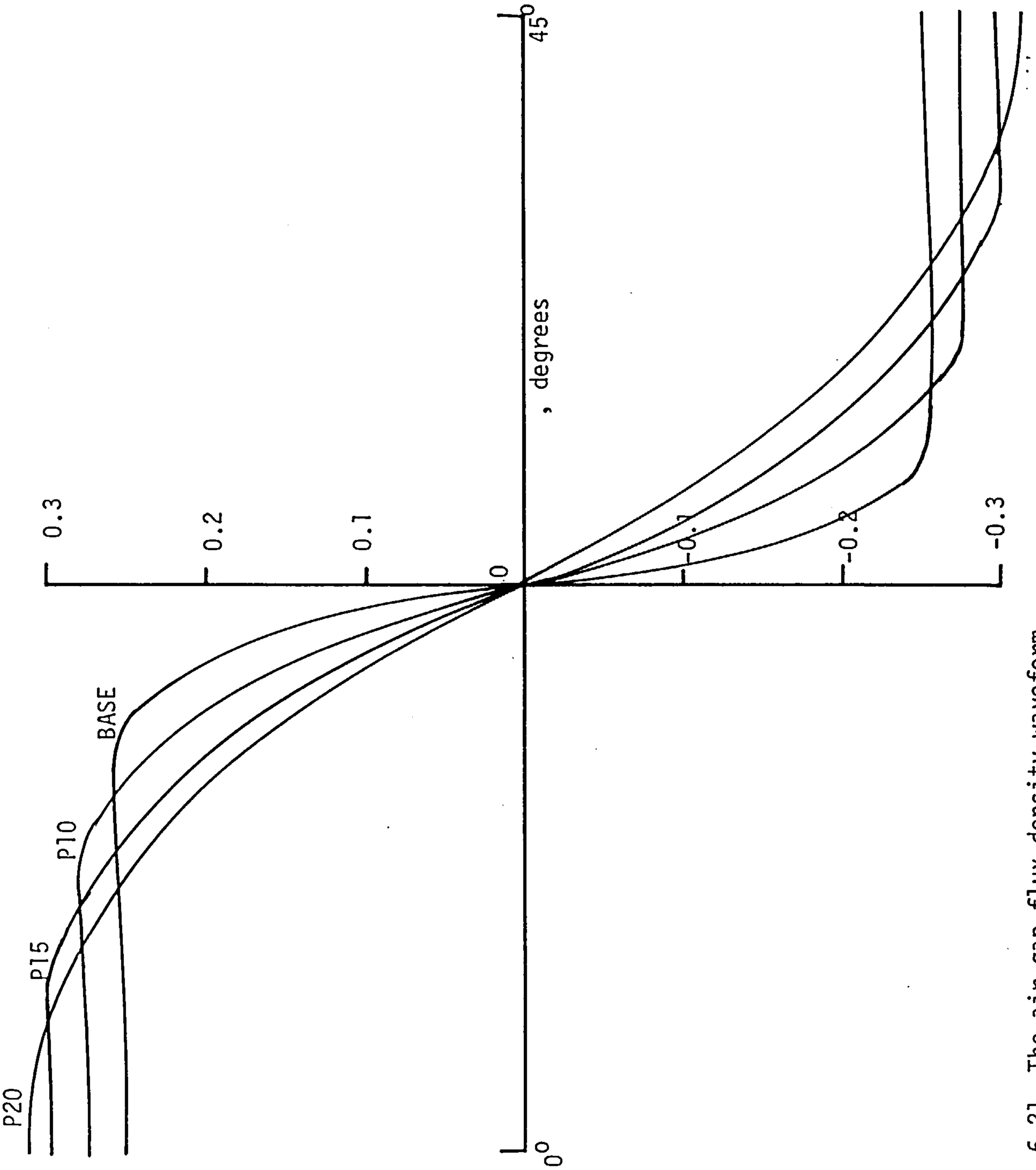

Fig. 6.21 The air-gap flux density waveform.

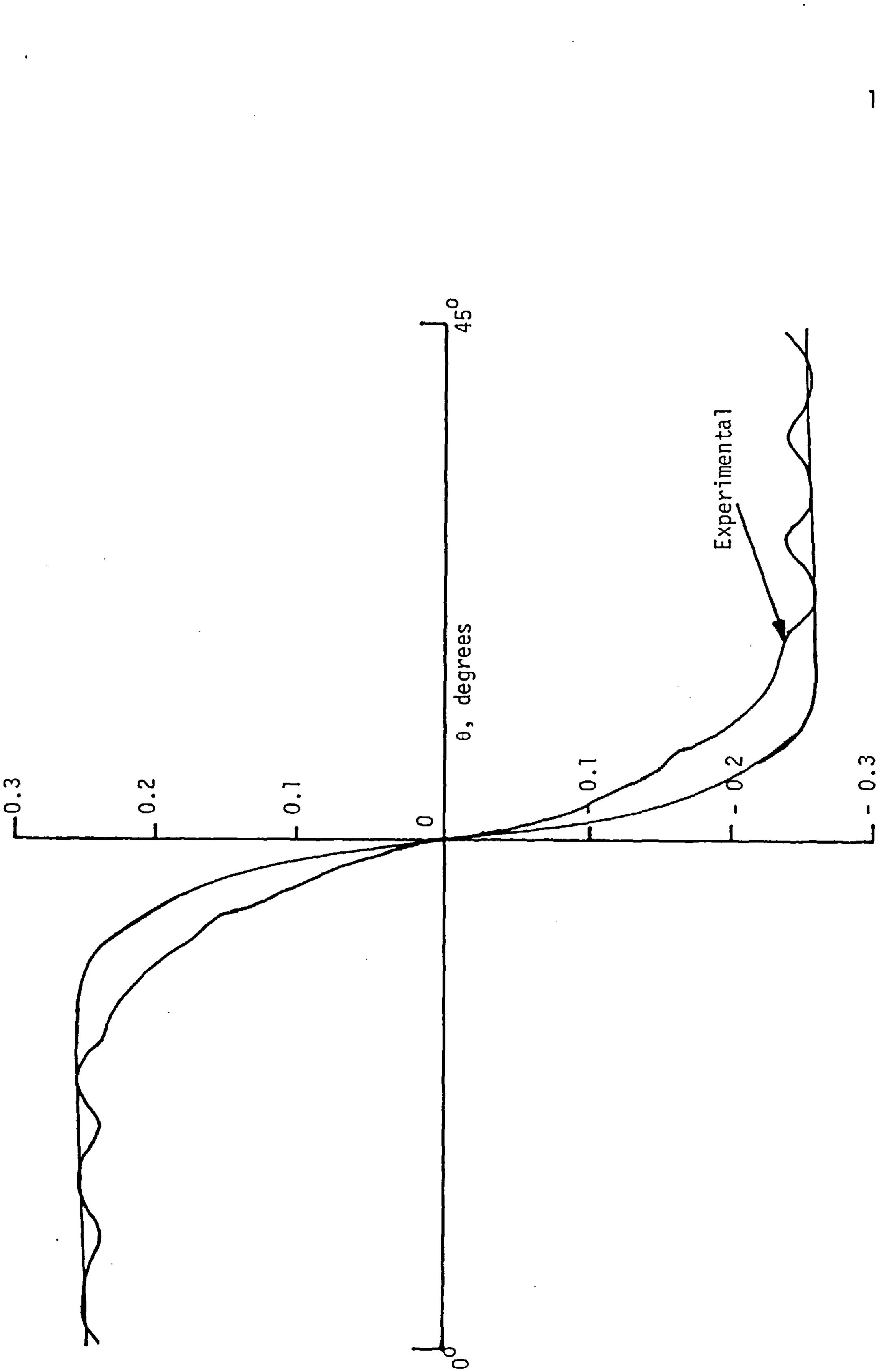

Fig. 6.22 A comparison of the computed air-gap flux waveform and that obtained experimentally.

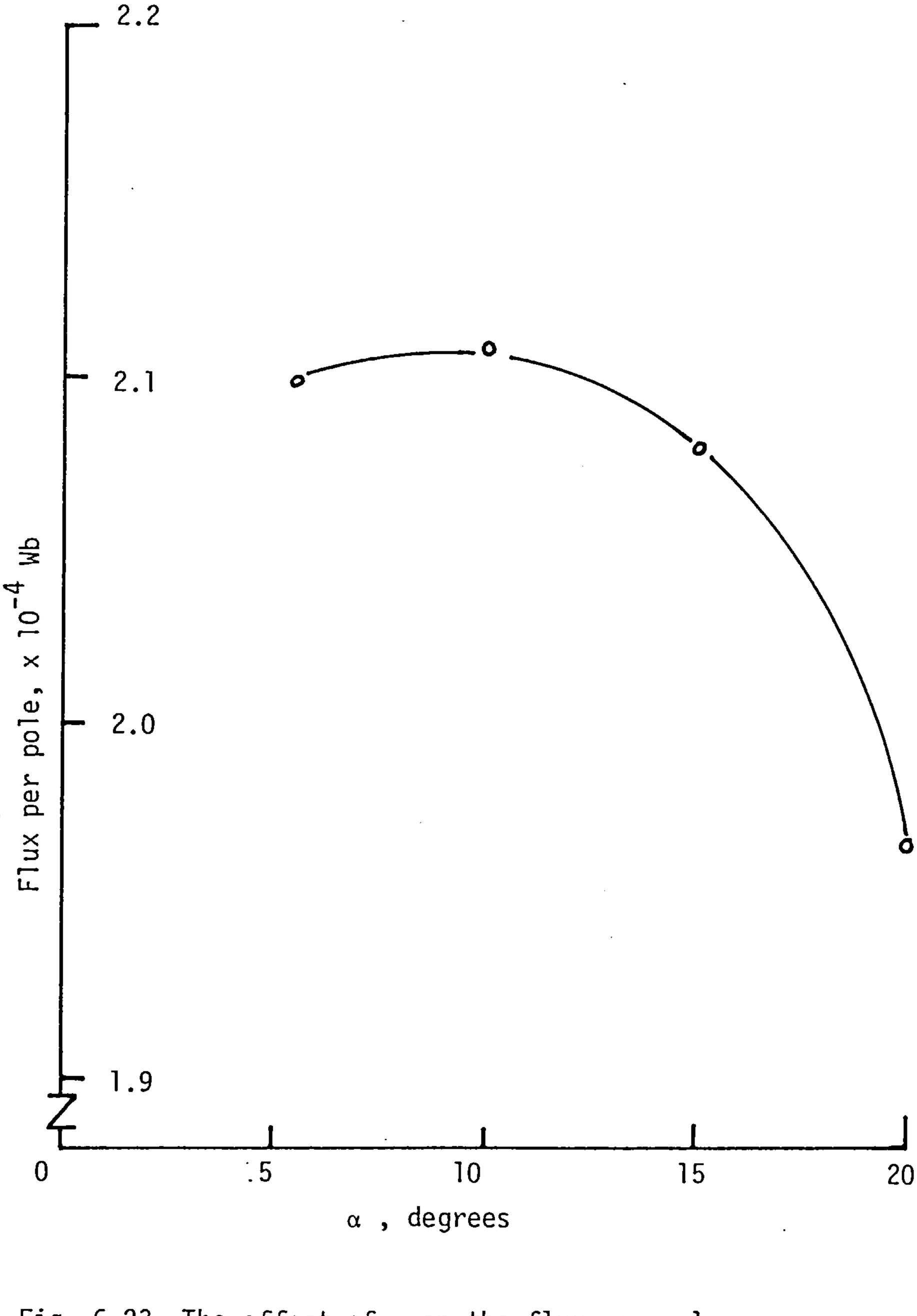

Fig. 6.23 The effect of α on the flux per pole.

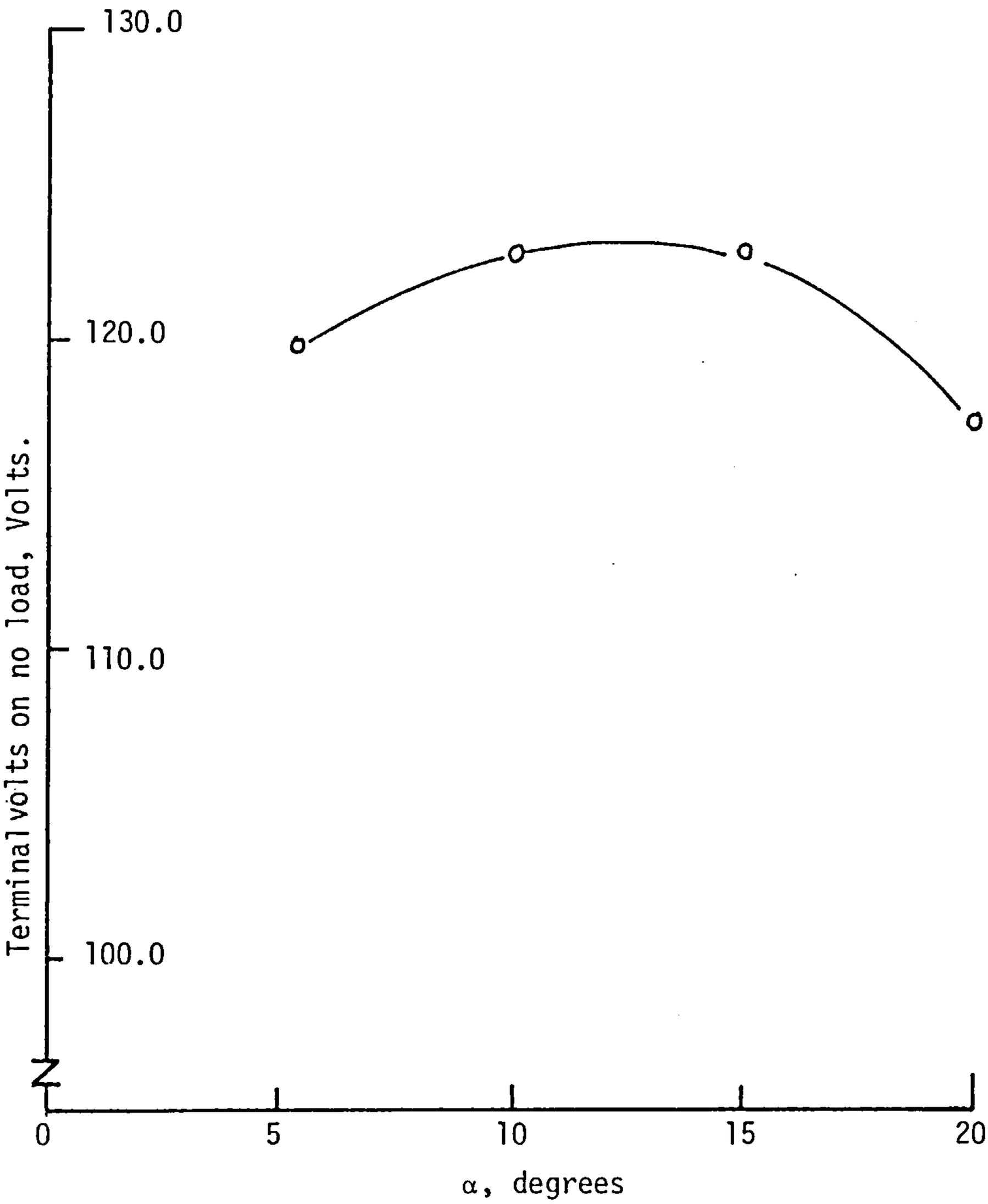

Fig. 6.24 The effect of α on the terminal voltage.

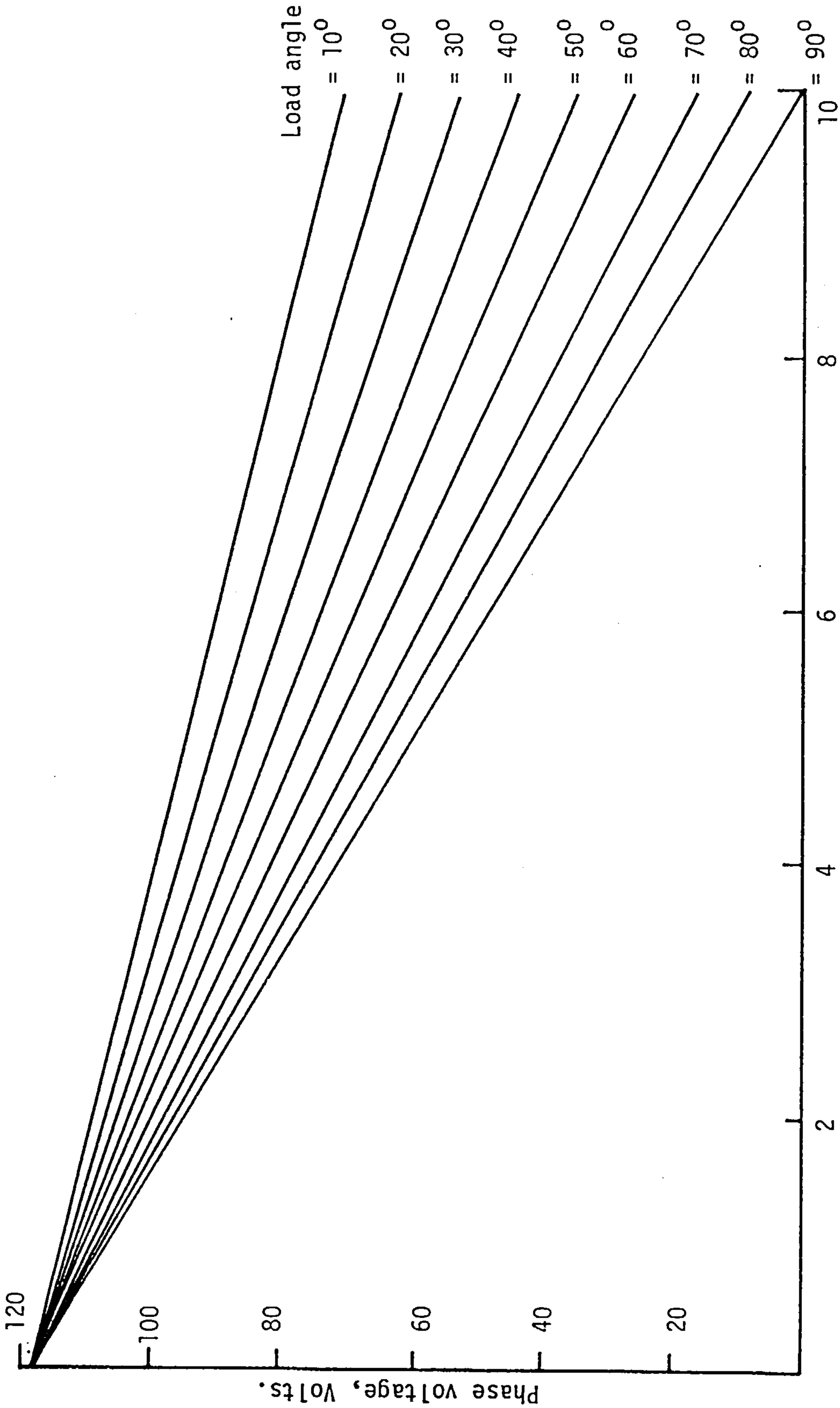

Fig. 6.25 The load characteristics of generator A computed at various load angles.

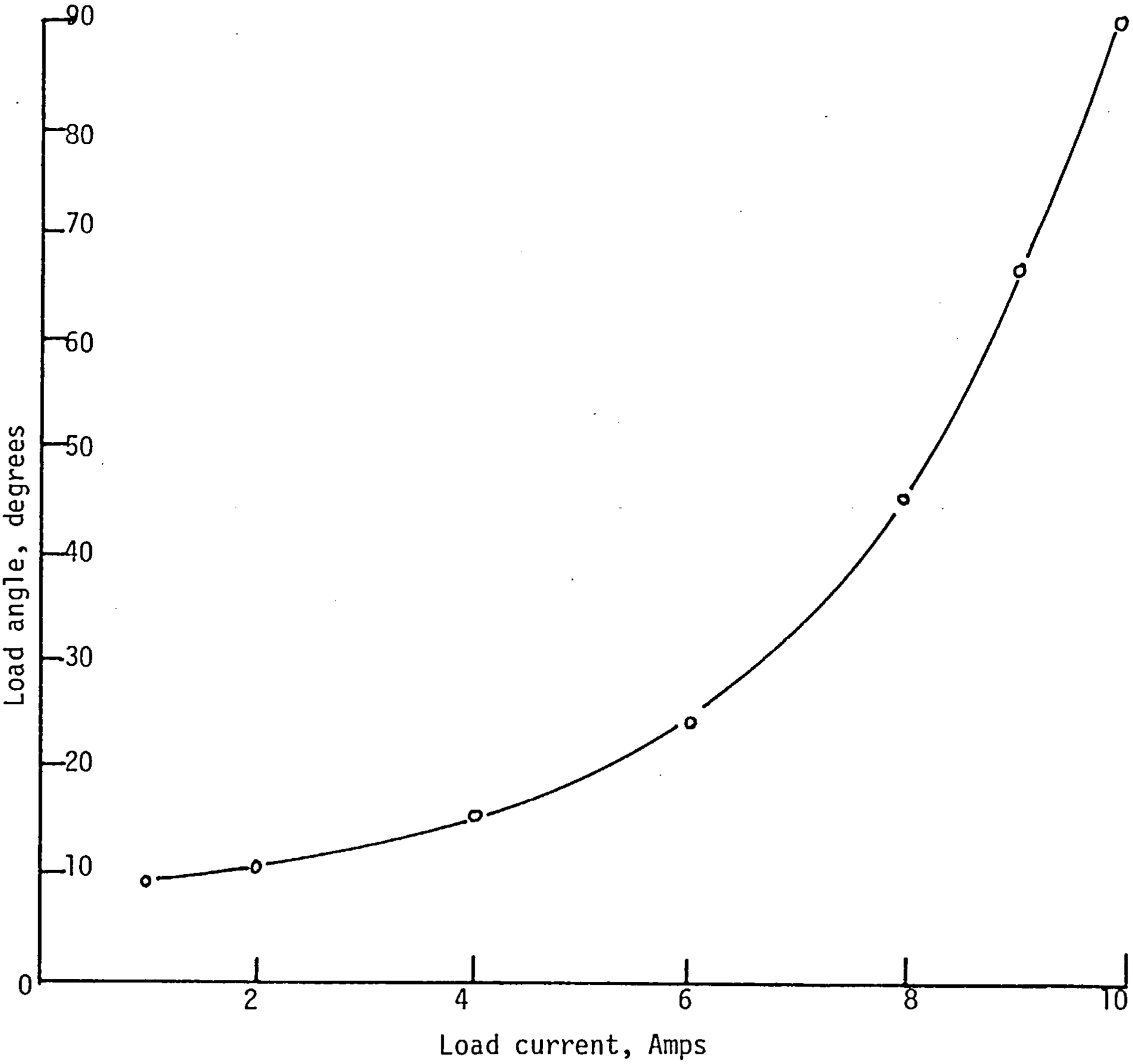

Fig. 6.26 The change in load angle for generator A with load.

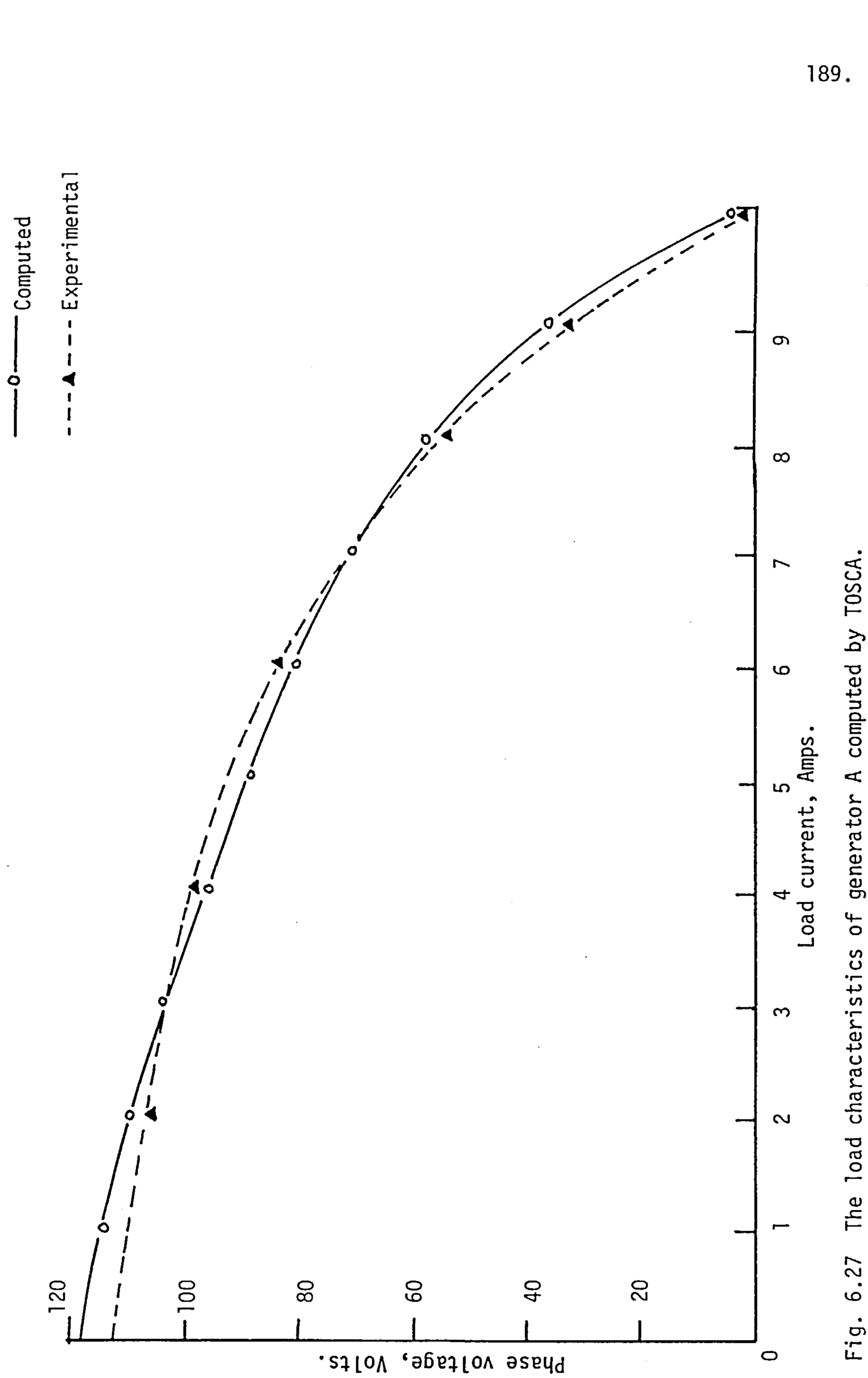

Fig. 6.27 The load characteristics of generator A computed by TOSCA.

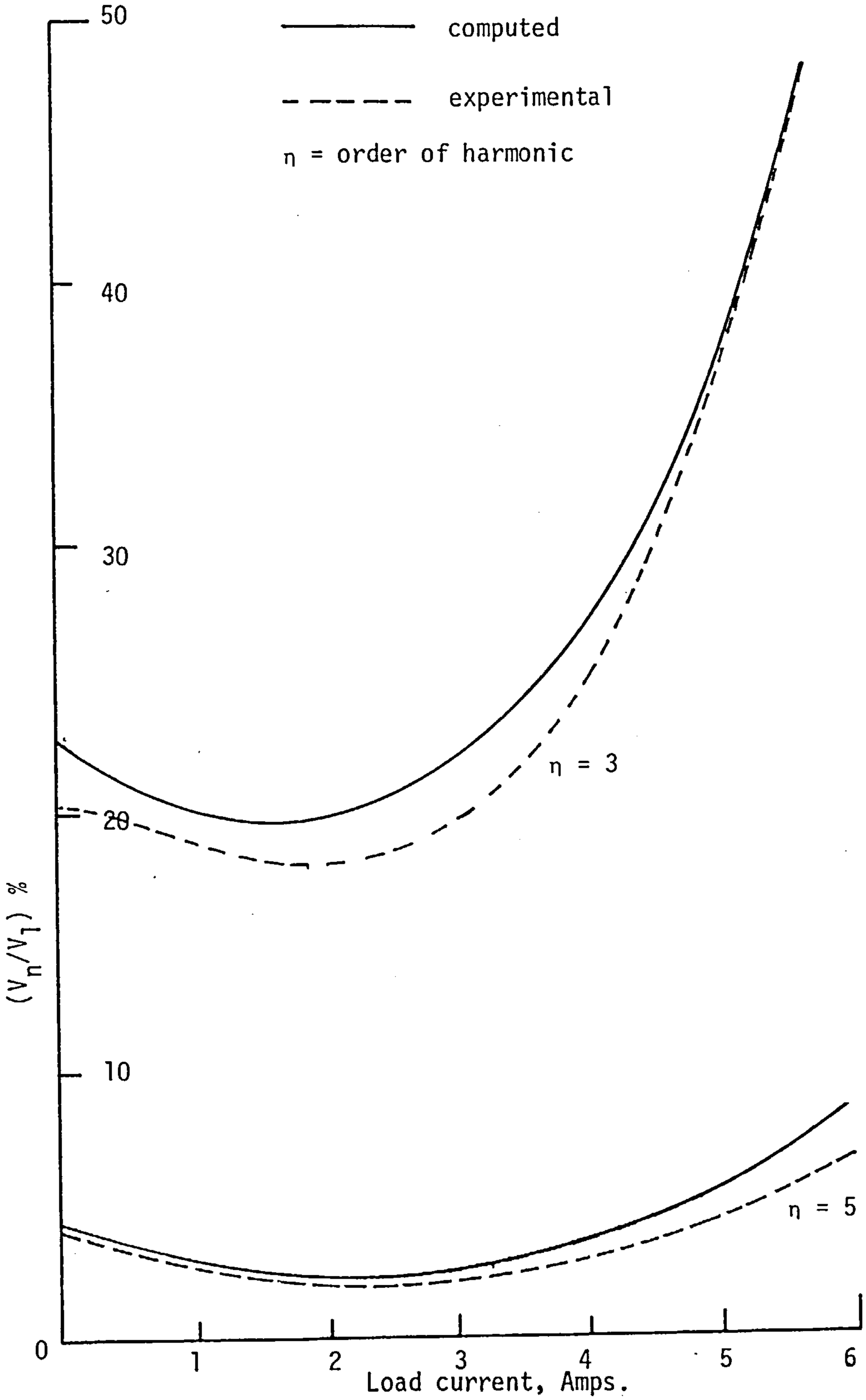

Fig. 6.28 The effect of load on the harmonic content of the air-gap flux waveform - A comparison between computed and experimental results.

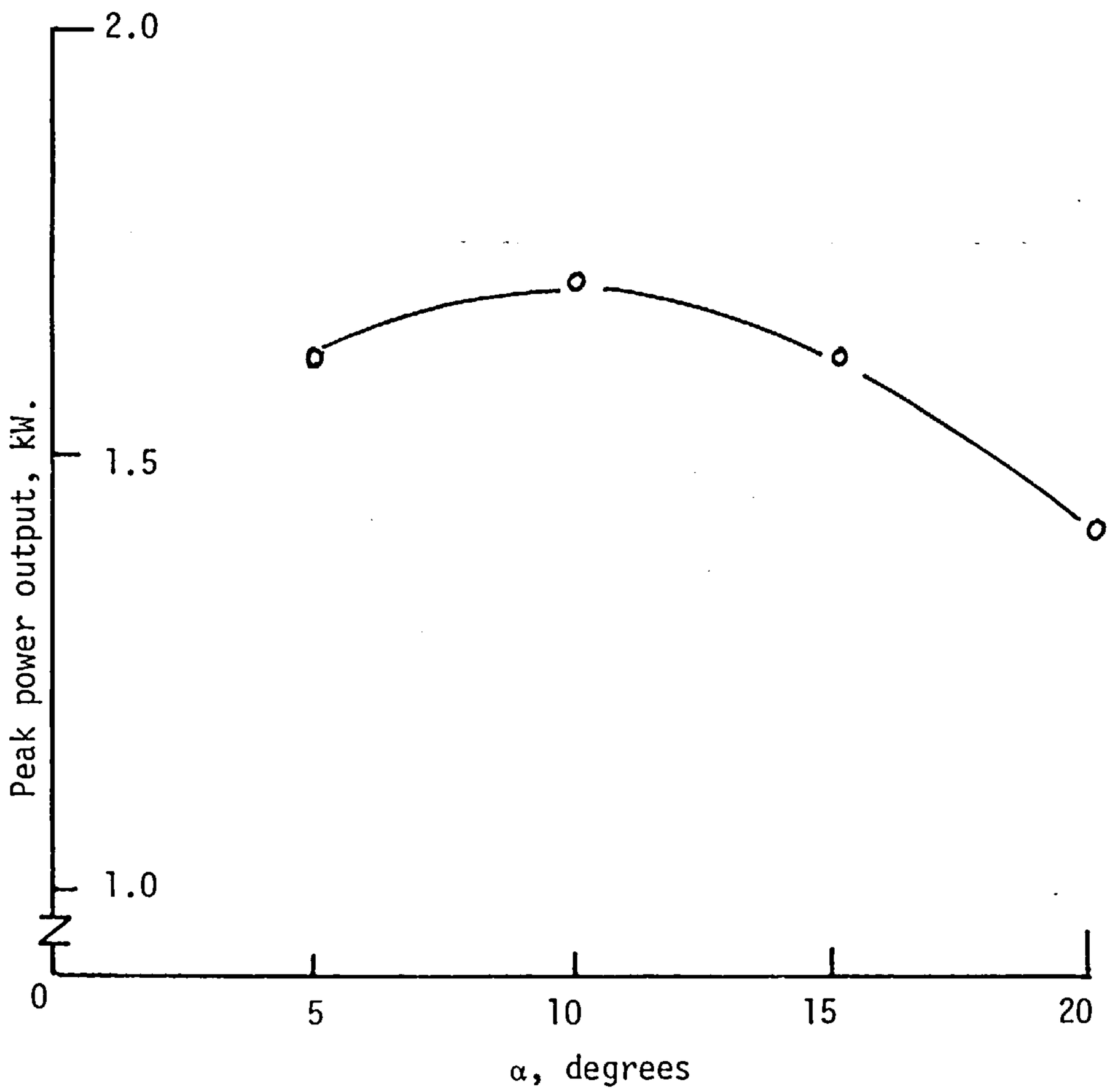

Fig. 6.29 The effect of a change in α on the maximum power output of generator A.

CHAPTER SEVEN

A REVIEW OF THE THREE-DIMENSIONAL FINITE-ELEMENT METHOD OF COMPUTATION AND THE DISCRETE-RELUCTANCE METHOD PROGRAM

CHAPTER SEVEN

A REVIEW OF THE THREE-DIMENSIONAL FINITE-ELEMENT METHOD OF COMPUTATION AND THE DISCRETE-RELUCTANCE METHOD PROGRAM

7.1 INTRODUCTION

The three-dimensional finite-element method of field analysis and the discrete-reluctance method of field analysis are very different. They have both been described in earlier chapters and are used for the analysis of the fields of the multi-stacked imbricated rotor. Each method has its merits and demerits.

The limitations of the discrete-reluctance method of analysis are described in Chapter 4. These limitations lie in the assumptions made in the calculation of the areas and lengths of the flux paths used for the determination of the reluctances. Other limiting factors of the method include the complexity involved in the consideration of harmonics of the air-gap flux waveform and its inability to monitor the effect of changes in the geometry of the flux guide and the pole profile on the flux waveform. In the prediction of the performance of the multi-stacked permanent magnet generator, the inaccuracy, particularly at high loads, is due to the inaccuracies of the assumptions made in the calculation of the reluctances of the flux paths. The program is useful in that it is interactive, inexpensive in CPU time and requires negligible storage. The basic dimensions of the rotor can be changed interactively in the design optimisation of the new rotor. It is, thus, an effective design aid.

The three-dimensional finite-element program has been described in Chapter 5. As in any finite-element method of field analysis, its accuracy relies on the effective discretisation of the space occupied by the geometry of the machine[1,2,3]. The level of accuracy depends

on the number of elements used in the representation of the model. The geometry of the new rotor is highly irregular and demands a large number of elements to represent it accurately. This imposes a high demand on computer storage and requires a considerable amount of computer processing time. The number of nodes used for the representation of the new rotor is about 6,000. Figure 7.1 shows the air-gap flux density at the middle of two adjacent poles computed by TOSCA and the discrete-reluctance method. These two sets of computed results are compared with the measured values. The correlation between the values computed by TOSCA and the measured values is close showing graphically the level of accuracy achieved with the discretisation described in Chapter 5. This accuracy is also seen in Figure 6.27 which shows the favourable comparison between the load characteristic computed using the three-dimensional finite-element method and the experimental results. The computation using the three-dimensional finite-element program for the no-load case (i.e. no current sources) takes 10 minutes of CPU time on an IBM 370/195 system. The computation on-load requires 23 minutes of CPU time. This is due to the need to solve for the right-hand side of Poisson's Equation with the introduction of the current sources. In computing for the load characteristic using TOSCA, many runs are required to account for the changing load angle. This makes it an impractical design tool. This is its major disadvantage. The advantages of this method are: its ability to monitor the effects of changes in the geometry of the flux guide on the field distribution, the ease in the assessment of the magnitude of the leakages in the rotor and the ability to predict the harmonic content of the air-gap flux waveform for a particular geometry. The program TOSCA is thus not used as a design program but is used effectively as a means of computing accurately the leakage fluxes and

the air-gap field. The analysis using the three-dimensional finite-element method program is also used to refine the discrete-reluctance method program by correcting the errors in assumptions and approximations made for the areas and lengths of the flux paths used for the calculation of the reluctances.

7.2 A COMPARISON OF THE RESULTS FROM THE TWO METHODS OF COMPUTATION

The accuracy of the prediction by computation of the air-gap field reflects the value of the computational method. A comparison is done in this section between the air-gap field computed by both methods and the measured flux density. The load characteristics of generator A computed by the two methods of computation are also compared with the experimental results.

The model of generator A is used as the basis of comparison. The axial flux distribution of the radial component of the air-gap flux density, with the rotor stationary, is measured using a Hall-effect probe. This is done at two locations, along the middle of two adjacent poles. Two sets of results are obtained. The first set is for the axial distribution of the flux density along the middle of two poles (North) of two flux guides back to back, and the second is along the middle of two poles (South) with their tips meeting for the same two flux guides back to back. The mid-pole flux density calculated using the discrete-reluctance method is single valued because the axial variations of the air-gap reluctance are ignored. In the three-dimensional finite-element approach the air gap is represented as a mesh and thus takes into consideration changes in flux distribution in all three directions and is shown in Figures 6.19 and 6.20. Figure 7.1 shows the comparison of the results from the two computation methods with the

measured values. The dotted lines AA' and BB' show the lines along which flux density measurements were taken and computed. Figure 7.1(a) shows the results for the north poles while Figure 7.1(b) shows the results for the south poles. The two figures show a very close correlation between the experimental results and those computed using the finite-element method program. The maximum error never exceeded 2%. The correlation between the results computed using the discrete-reluctance method and the experimental results is poor as the discrete-reluctance method computes for the average flux per pole. A proper comparison would be between the line integrals of the two sets of results. This shows a significant inaccuracy of 4.5%

A more important comparison is the load characteristics computed by the two methods with that obtained experimentally. Both methods of computing the load characteristic have been discussed earlier and their results for generator A are shown in Figure 7.2. The dotted line shows the results obtained experimentally. It is clear that the correlation between the characteristic computed using the discrete-reluctance method and the experimental curve is good at low loads but deteriorates at high loads, whilst the comparison for the characteristic computed by the three-dimensional finite-element method is close for the range of operation from open circuit to short circuit. The finite-element method is thus the more accurate computational method for the imbricated rotor. However, the excessive amount of CPU time it requires restricts its use. It is therefore more effiectively used as a means of improving the discrete-reluctance method program.

7.3 COMPARISON OF THE COMPUTED LEAKAGE FLUXES

The accurate assessment of the leakage field is very important. As this comparison is done at no-load, an error made in the calculation of the leakage flux would be magnified on load. The leakage flux comparison is carried out in three main regions: leakage 1 and leakage 2 of the pole region and leakage 3 by the shaft region. If the representation of these leakage paths is correct in the discrete-reluctance method, the leakages computed must compare closely with that computed using the finite-element technique. A comparison with measured values would be highly desirable, but the complicated rotor configuration makes it impossible to obtain direct flux measurements.

The table below shows the comparison of the magnitude of the three leakages computed.

Computed by	Leakage 1	Leakage 2	Leakage 3
	$\times 10^{-5}$ Wb	$\times 10^{-5}$ Wb	$\times 10^{-5}$ Wb
TOSCA	2.729	5.430	3.034
Discrete-Reluctance Method	3.411	7.837	2.060

These results are computed over one pole pitch. The table shows the considerable difference in magnitude computed by the two methods. Assuming TOSCA to be correct, the error in the computation of the leakages by the discrete-reluctance method is +10%, +26% and -32%, for leakages 1, 2 and 3 respectively. The total leakage computed by TOSCA amounts to 11.193×10^{-5} Wb and the result using the discrete-reluctance method is 11.908×10^{-5} Wb. The error in the calculation of total leakage flux is 6%. The accuracy in the computation of the leakages is poor; however, the total leakage computed by the discrete-reluctance method is close to

the result from TOSCA. The inaccuracies can be attributed to the representation of the geometry of the leakage flux paths. The modelling of the iron paths also affects the leakages. The inaccuracies in the representation of these flux paths in the discrete-reluctance method probably account for the high degree of inaccuracy in the leakages computed by it. The improved representation of these flux paths in the light of the analysis of the field using the three-dimensional finite-element program is discussed in the following sections.

7.4 THE CHANGES MADE TO IMPROVE THE DISCRETE RELUCTANCE METHOD PROGRAM

The most important process in the discrete reluctance method program is the calculation of the reluctance. There are three iron paths, three leakage paths and the flux path through the magnet. Areas and path lengths for all of these require accurate determination. The accuracy in the calculation of these flux paths is improved in the light of the analysis performed with the three-dimensional finite-element program.

(i) The flux passing through the magnet is shown by the three-dimensional finite-element program to be very close to uniform. This justifies the assumption made in the discrete-reluctance method that the reluctivity in the magnet is uniform. The area, Sm, and the length, Lm, of this path is thus simply the surface area of the magnet and the thickness respectively.

(ii) In the iron disc attached to the face of the magnet, iron path 1, the flux divides into two components. The majority of the flux is guided out to the poles and emerges as air-gap flux and leakages between the poles, whilst the rest is directed inwards as leakage 3. Iron path 1 is calculated on the assumption that the reluctivity is the same over the whole region. The path length is considered to be equal to the difference between the outer diameter of the disc and its inner diameter

and its cross-sectional area is equal to the outer disc surface. It also assumes that the flux is radial. The results from computation using TOSCA show that the flux is non-radial and that the flux distribution is highly non-linear. However, the variation of the average flux density over the Zθ plane along the R-axis show a trend from which the variation of reluctance can be deduced. The average reluctance of this path can be represented as

$$\left(L_1^I / S_1^I \right) \times \frac{\int_{R_1}^{R_2} \frac{R\ X^2}{R^2+X^2}\, dR}{R_2 - R_1}$$

where R_1 is the inner diameter of the disc and $R_2 = X$ is the outer diameter. $R_2 - R_1 = L_1^I$ and S_1^I is the average of the outer and inner surface area of the disc. Thus

$$R_1^I = \frac{\int_{R_1}^{R_2} \frac{R\ X^2}{R^2 + X^2}\, dR}{S_1^I}$$

This representation is confirmed to be correct by the results from the analysis using the three-dimensional finite-element method where surface integrals were taken at various Zθ planes along the R-axis.

(iii) Iron path 2, described in section 4.4 and shown in Figure 4.2, is bounded by two cylindrical surfaces. This path is relatively short and the flux density is considered to be uniform. In the calculation of the parameters, the path cross-sectional area is assumed to be equal to the average area of the two surfaces of the cylindrical boundaries and the path length is equal to the radial extension which has been labelled as 'a'. The assumption that the field is uniform in this region is validated by the analysis using the finite-element program, though there is a degree of deviation due to the trapezoidal profile of the pole. Therefore, it is multiplied by a factor which is dependent

on the dimension 'a' and the value of r which is the height of the collar. This factor is derived as follows:

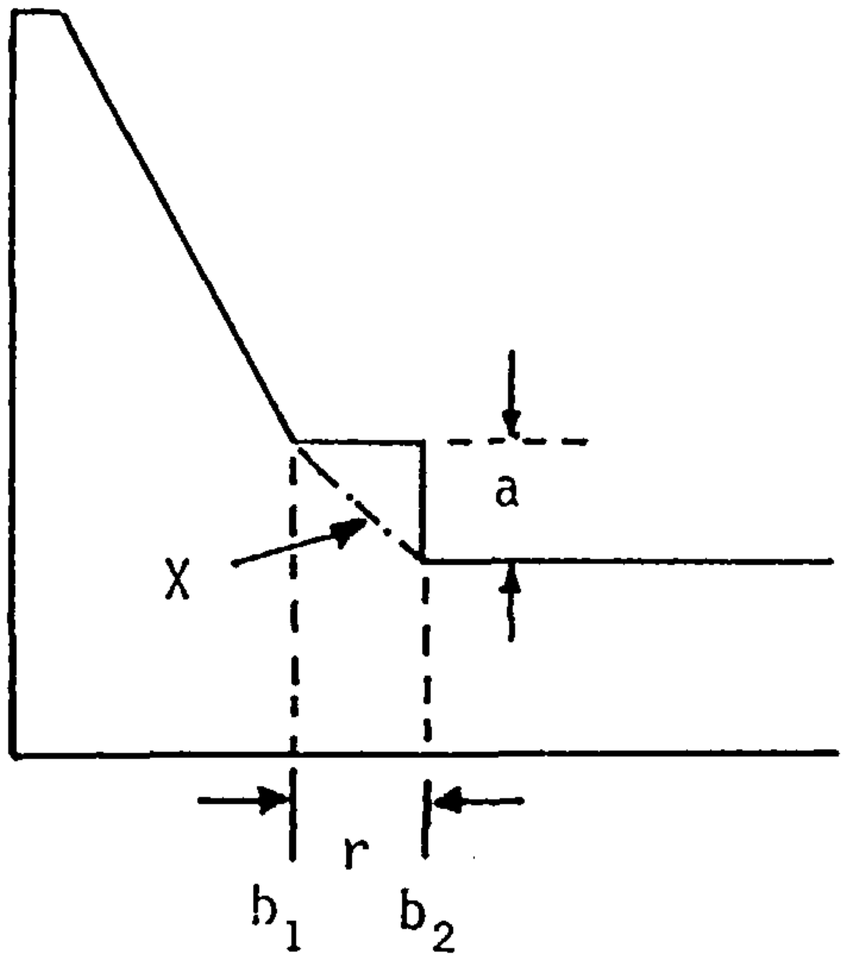

$$X = \sqrt{a^2 + r^2}$$

The average path length between boundary b_1 and b_2 in the figure is

$$= \frac{X + r}{2}$$

$$= \frac{r + r\sqrt{1 + (a/r)^2}}{2}$$

$$= r\left(\frac{1 + \sqrt{1 + (a/r)^2}}{2}\right)$$

Therefore, the factor is

$$\frac{1 + \sqrt{1 + (a/r)^2}}{2}$$

The use of this factor accounts primarily for the divergence of flux due to the increase in surface area of the flux path as it passes from the iron disc into iron path 2 which links the disc with the pole.[4]

(iv) Iron path 3 is the most complicated of the three iron paths. Due to the undercutting of the pole and the tapering of the pole face, the distribution of flux is highly non-uniform over the whole pole structure. Due to this complexity, the region is divided into a finite number of flux paths. This results in an accurate representation of the pole for the calculation of the reluctance of this path.

The calculation of the reluctances of the leakage paths are just as important as the calculation of the reluctances of the iron paths. They form alternative routes by which the magnetic circuit could be completed (See Figure 4.3).

(v) The leakage between the poles is leakage 1 (see Figure 4.3). The area of this path is considered to be the average surface area of the side of the pole. The difficulty in the calculation of the reluctance of this path is the determination of the length of this flux path. The difficulty arises because of the tapering of the poles. From the results obtained from TOSCA, the representation of this path length can be improved. Using the average flux density calculated by the finite-element method program, the mmf drop between the two surfaces is obtained as well as the total leakage flux in that region. These two quantities are related by the equation,

$$\phi = \text{mmf/Reluctance}$$

$$\phi = (\text{mmf})\ \mu_o \frac{S}{L}$$

where A and L are the surface area and length of the flux path. The value of S for leakage path 1, S_1^A, has been determined, thus the length L_1^A can be found from the relationship above. This equivalent length is found to be equal to the volume of the whole flux path divided by the surface area of the side of the pole.

(vi) The underpole leakage (see Figure 4.3) is the leakage between the underside of the pole and the disc of opposite polarity. This is the biggest of the three leakages. The representation of leakage path 2 is difficult. It is assumed to have a surface area equal to the average surface area of the underside of the pole and the opposing disc surface area, see Figure 7.3(a). This surface area is multiplied by a factor equal to 1.7. This factor has been determined experimentally.[4] The inclusion of an empirical factor leads to errors in the computation for designs whose dimensions and geometry is different to that from which the factor was obtained. Using the results from the finite-element

program, the leakage flux and the mmf drop across the leakage path are abtained from which the reluctance of the path is calculated. By improving the representation of the surface area of the path, see Figure 7.3(b), in considering the leakage from the sides of the magnet, the surface area of leakage path 2, S_1^A is calculated with no empirical factor. The length L_2^A is found from the known reluctance. The length of the path L_2^A is found to be a close approximation to the value calculated by dividing the volume of the leakage 2 flux path by the surface area. The dimensions of the path are now all functions of the geometrical parameters of the flux guide.

(vii) The leakage path adjacent to the shaft is the simplest of all the three leakage paths. The surface area of the path is simply the area annular area between the shaft and the inner diameter of the magnet and the length is the clearance between the two flux guides. Thus for a flux guide without the collar adjacent to the shaft, the length is

$$L_3^A = U_{th} - 2\, I_{th}$$

where U_{th} is the thickness of one unit of the multi-stacked machine and I_{th} is the thickness of the iron disc, and the surface area

$$S_3^A = \pi(R_2^2 - R_1^2)$$

where R_2 is the inner radius of the magnet and R_1 is the radius of the shaft.

All the modifications described are incorporated in a new version of the discrete-reluctance method program. The load characteristic of generator A computed by the new version of the program is compared with that computed by the old version in Figure 7.4. The third curve in the same figure, represented by the broken line, is the characteristic obtained experimentally. The comparison shows the improved

correlation between the curve computed by the new version of the discrete-reluctance method program and the experimental curve. This improvement in the prediction of the performance of generator A is shown in Figure 7.5 which is a plot of $(V_{EX} - V_C)$, the difference between the experimental voltage and that computed, against load current.

7.4 CONCLUSIONS

(i) The three-dimensional finite-element method of field analysis is accurate.

(ii) The load characteristic of generator A computed by TOSCA is more accurate than that predicted by the discrete-reluctance method program.

(iii) The inaccuracies in the discrete-reluctance method lie primarily in the reluctance calculations. The representation of these flux paths is improved using the results from TOSCA. The major changes are made in the representation of leakage paths 1, 2 and 3 and iron path 1.

(iv) The improved version of the discrete-reluctance method program gives results which are more accurate than those computed by the old version.

The three-dimensional finite-element program, TOSCA, is a useful method for field analysis. Its accuracy in computation is used to improve the modelling of the flux paths in the discrete-reluctance method. The resultant fast discrete-reluctance method with its improved accuracy is used for the design and optimisation of the multi-stacked permanent magnet generator.

7.5 REFERENCES

1. CHARI, M. V. K., SILVESTER, P., CSENDES, Z. J., KONRAD, A. and PALMO, M. V. A. : 'Three-dimensional magnetostatic field analysis of electrical machinery by the finite-element method', I.E.E.E. Trans. on Power Apparatus and Systems, Vol. PAS-100, No. 8, pp. 4007-4019, Aug. 1981.

2. CHARI, M. V. K., MINNICH, S. H., CSENDES, Z. J., TANDON, S. C. and BERKERLY, J. : 'Load characteristics of synchronous generators by the finite-element method', I.E.E.E. Trans. on Power Apparatus and Systems, Vol. PAS-100, No. 1, pp. 1-13, January 1981.

3. ARMSTRONG, A. G., COLLIE, C. J., SIMKIN, J. and TROWBRIDGE, C. W. 'The solution of three-dimensional magnetostatic problems using scalar potentials', RL-78-088, RAL, Didcot, Oxon., 1978.

4. KURDALI, A. : 'Analysis and performance of a permanent-magnet generator with disc magnets', Ph.D. Thesis, Southampton University, 1979.

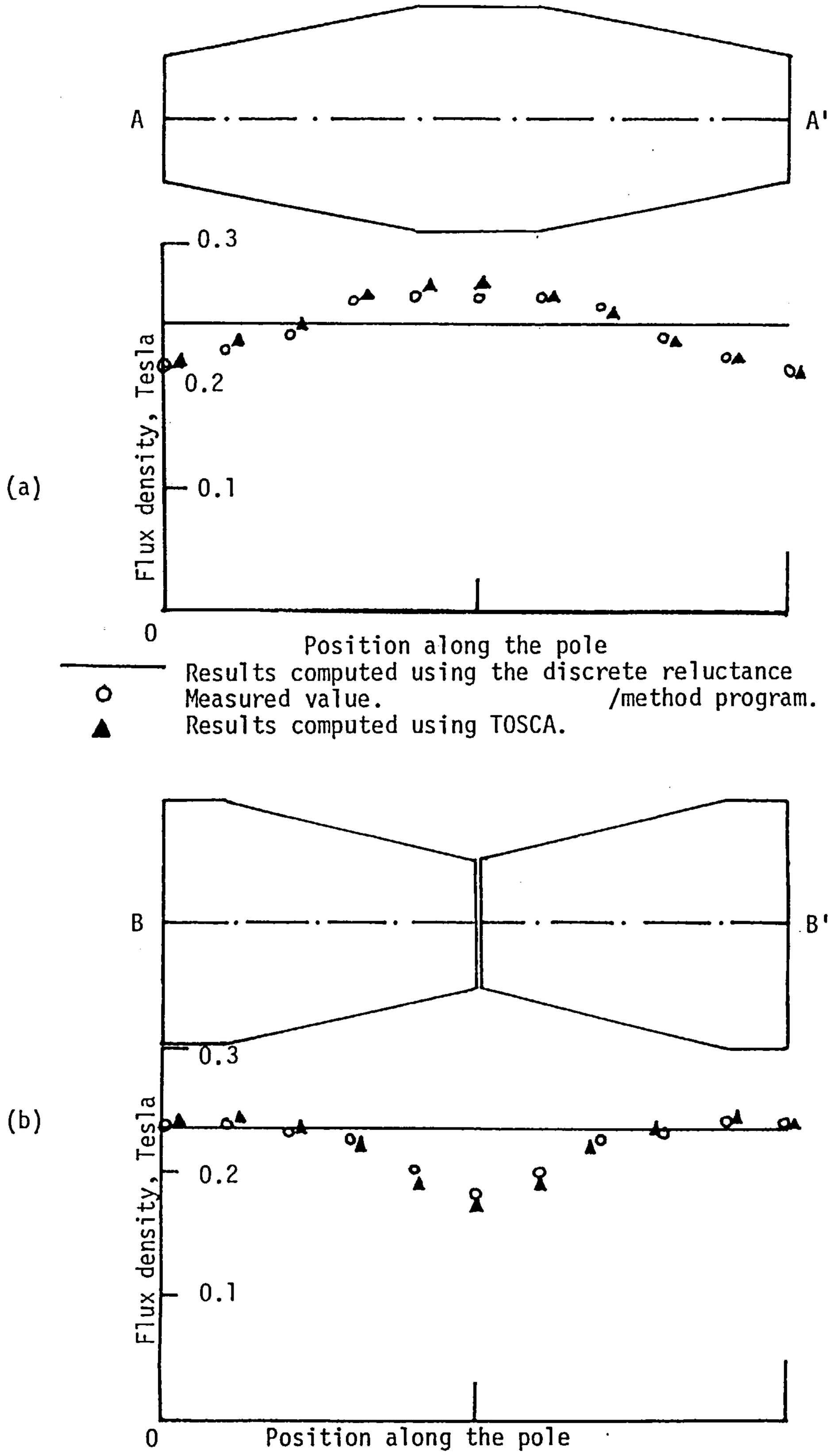

Results computed using the discrete reluctance /method program.

Measured value.

Results computed using TOSCA.

Fig. 7.1 The air-gap flux density at the middle of two adjacent poles.

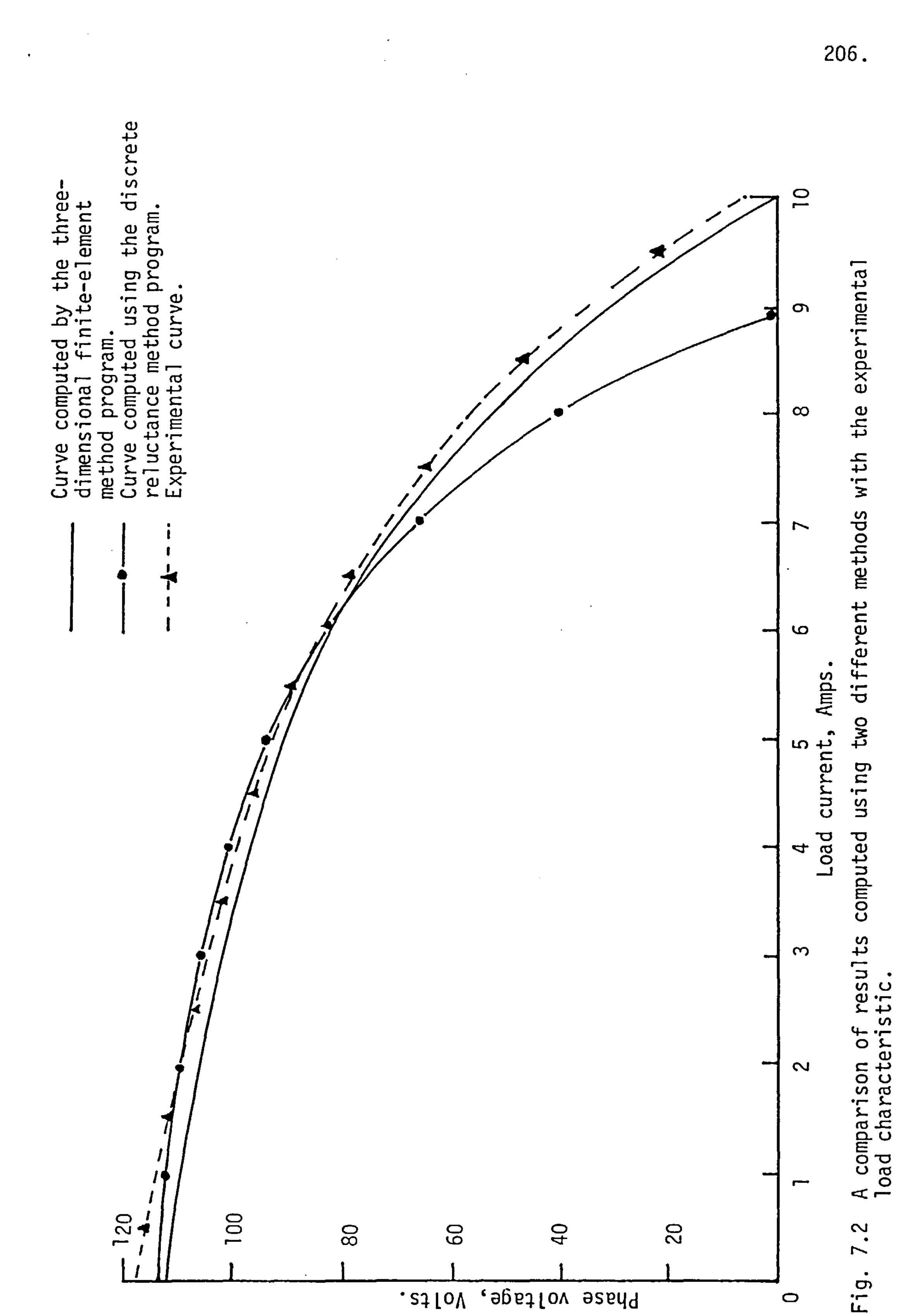

Fig. 7.2 A comparison of results computed using two different methods with the load characteristic.

(a)

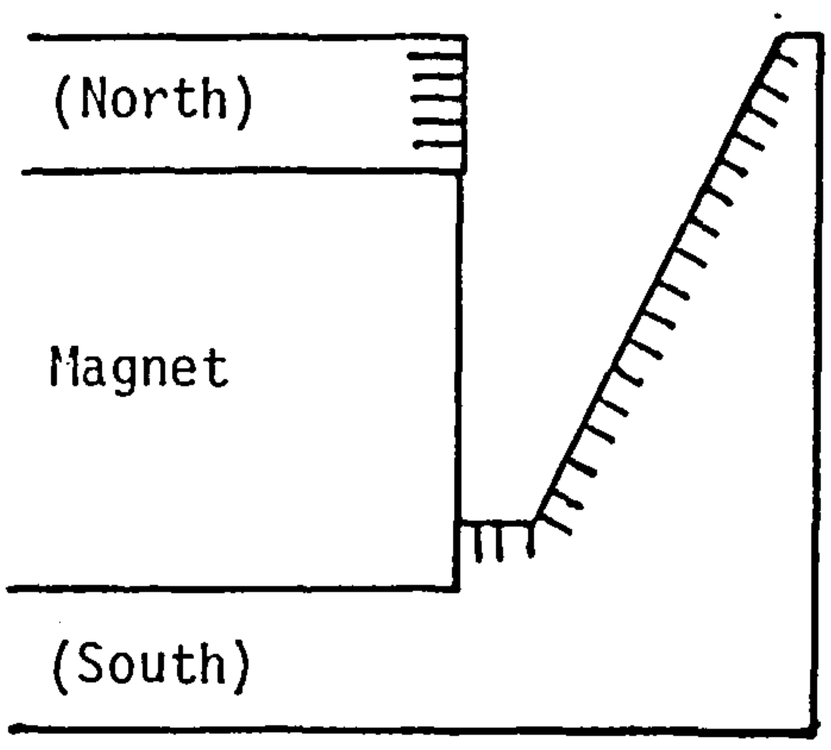

(b)

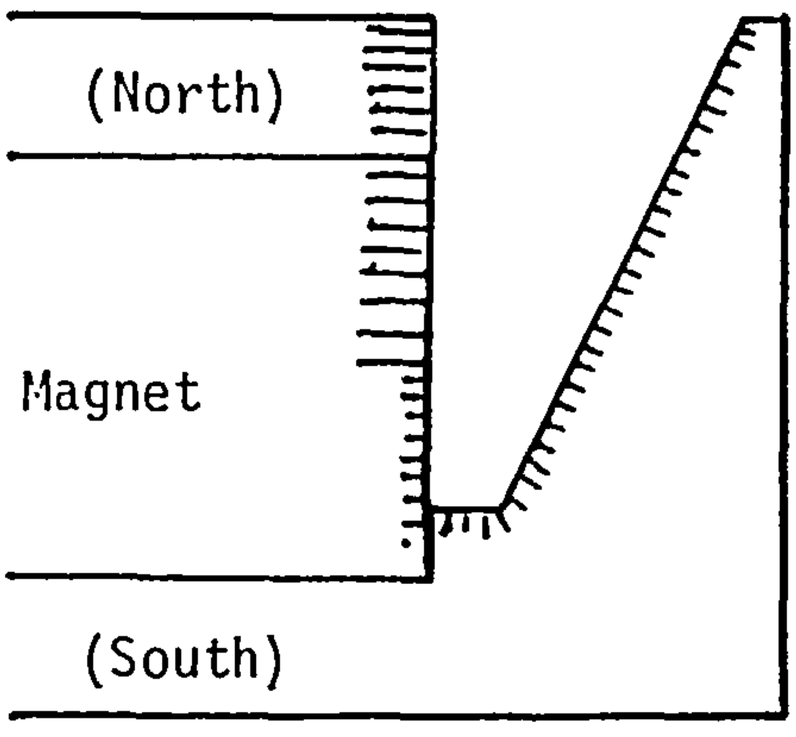

Fig. 7.3 The representation of leakage path 2.

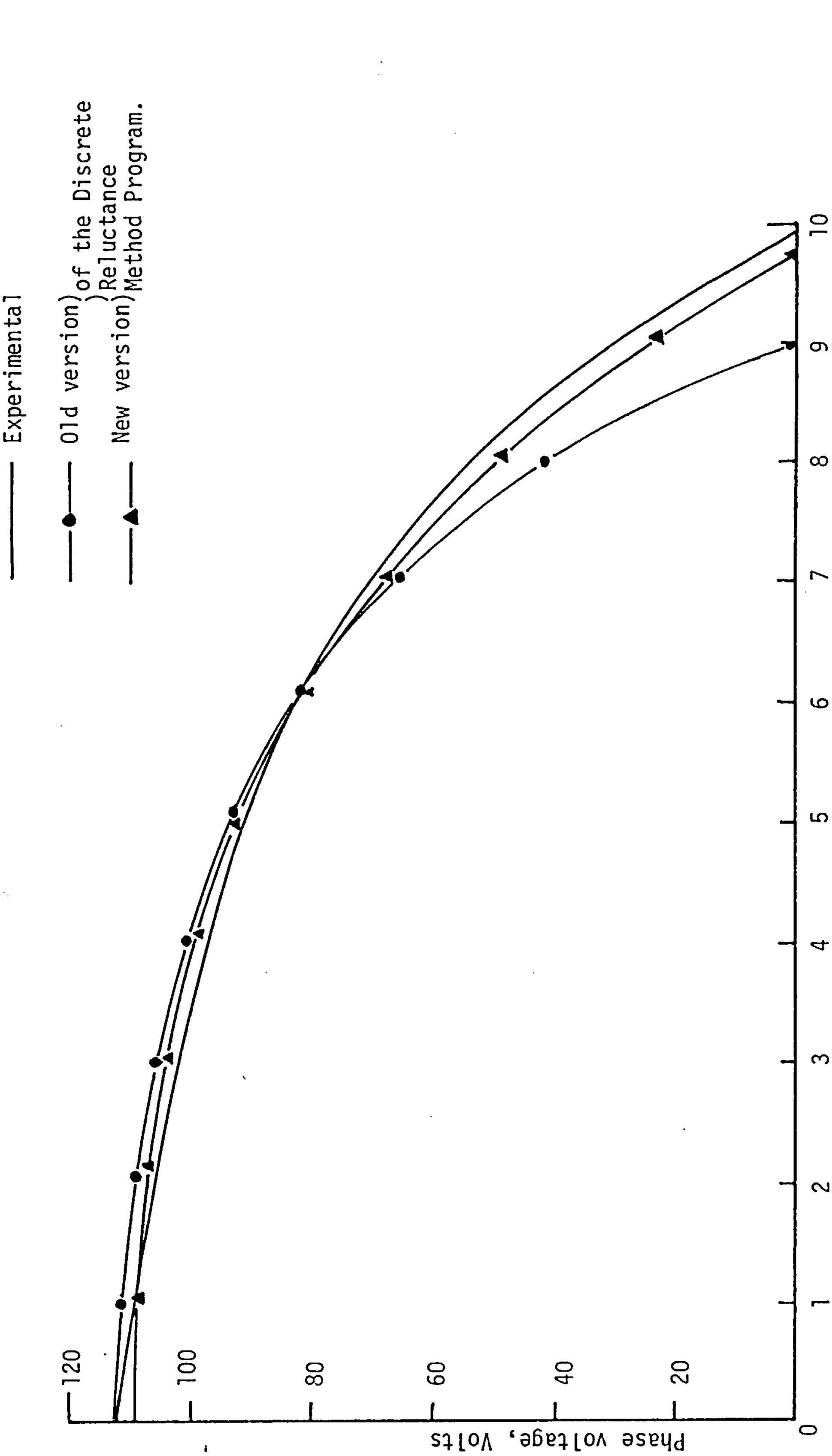

Fig. 7.4 The load characteristic of generator A computed using the improved version of the discrete-reluctance method program.

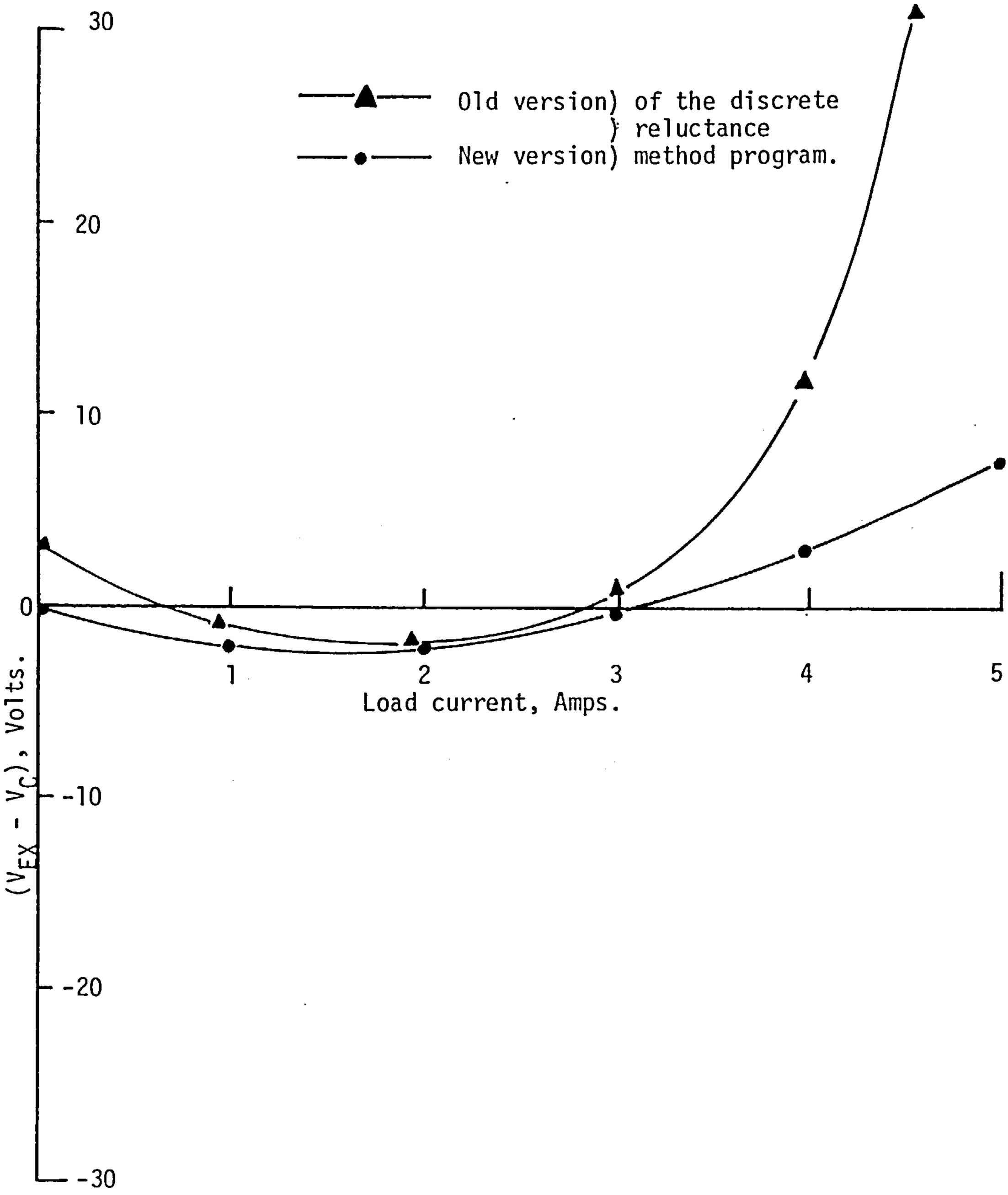

Fig. 7.5 A comparison of the correlation between the results computed using the old and the new version of the discrete reluctance method with the experimental curve.

CHAPTER EIGHT

THE OPTIMAL CONFIGURATION OF THE MULTI-STACKED PERMANENT-MAGNET GENERATOR

CHAPTER EIGHT

THE OPTIMAL CONFIGURATION OF THE MULTI-STACKED PERMANENT-MAGNET GENERATOR

8.1 INTRODUCTION

The shape of the flux guides has been studied and analysed using the discrete-reluctance method and the three-dimensional finite-element method. The flux distribution in this structure has been studied and the leakage fields analysed. The effects of changes in the geometry of the flux guides on the distribution of flux in the rotor and the airgap flux waveform have also been monitored and discussed in Chapter 6. From these studies an optimal configuration can be designed.

In the design of the flux guide practical constraints are imposed to facilitate the economical industrial production of these machines. The design of the flux guide can be separated into two parts. First the design of iron path 1, the piece of iron which is attached to the pole of the disc magnet, and second, the design of the pole piece and its attachment to the iron plate. The flat circular plate which constitutes iron path 1 is not optimal but subject to practical constraints it is the most feasible design. An undulating surface of a remodelled plate based on the results in Chapter 6, shown in Figure 8.1 is more efficient but would demand a matching irregularly shaped magnet and is thus an impractical and uneconomical proposition. The use of a flat plate requires disc magnets with plane parallel faces which are readily available. A change in the geometry of iron path 1 which is beneficial and simple to implement is the elimination of the collar adjacent to the shaft. This collar is non-essential. Its magnetic liability is realised from the computation in Chapter 6 with the data XL3. The removal of this

structure reduces the leakage by the shaft region labelled as leakage 3 and is matched by a comparable percentage increase in the useful flux output per pole.

The pole piece, however, has more scope for improvement.

8.2 IMPROVEMENTS TO THE POLE GEOMETRY

The pole shape involves the parameters 'a', 'aℓ' and the angle α, see Figure 6.1. They all affect the output of useful flux, but the changes in α has a further effect which is more important; it changes the airgap flux waveform. The pole profile can be designed to minimise the harmonic distortion of the flux waveform if the terminal voltage waveform is an important design factor. However, the optimal solution of the airgap field with different criteria may not be a sinusoid and one common requirement is the maximisation of output. Clearly the minimisation of harmonic distortion by increasing α does not result in an airgap flux which gives maximum power output. This is apparent from the results in Chapter 6, see Figures 6.24 and 6.29. The value of α which gives maximum output for generator A is 9.5^{o}. At this value of α the third harmonic component on open circuit is 24% of the fundamental. An increase of to 20^{o} reduces the magnitude of the third harmonic content to 7.5% of α the fundamental but it also reduces the flux per pole. The change in 'a' is not as critical in the shaping of the airgap flux waveform but is an important factor as it affects the leakage of leakage path 1 and 2 and consequently the output of flux per pole. The effect of changes in 'a' has been discussed in Chapter 6 and its optimal value can be computed using the discrete-reluctance method as well.

The shape of the pole depends primarily on the taper which is determined by the angle, α. The amount of taper which is deemed optimal

is dependent on the requirement for the application of the generator. If the output is to be rectified, the shape of the waveform is irrelevant and under such circumstances the optimal value of α would be 8.5^{o}, giving the maximum output flux per pole for the model analysed. If, however, the generator is to be used without rectification, and a high efficiency and power per unit volume is required, the ideal value of α would be 9.5^{o}, giving the maximum output power for that geometry. If an application requires a sinusoidal waveform, the taper has to be increased drastically to shape the waveform.

8.3 THE OPTIMISATION OF AN IDEAL UNIT OF THE NEW ROTOR

The new rotor is an assembly of units which comprise 2 flux guides and a disc magnet. Therefore the search for the optimal configuration of the new rotor can be reduced to the search for an optimal unit of the rotor. The basic shape of the flux guide has already been decided as described in Section 8.1. The shape of the pole face which depends on the value of α, critical to the airgap flux characteristic, is decided as described in Section 8.2. This still leaves many variables to be considered. However, many of these variables would be fixed by the mechanical constraints imposed and constraints due to the dimensions and characteristics of the stator.

Figure 8.2 shows a typical design of a flux guide with all the variables involved. The variables which are fixed are α and the following:

(i) R_1, the inner radius of the flux guide depends on the radius of the shaft used. The size of the shaft depends on the length and diameter of the rotor, as well as the running speed and torque. The choice of shaft is based on the British standard 4999/5000[1], which governs the design of rotating A.C. machines.

(ii) R_2, is the inner radius of the magnet. The clearance between R_1 and R_2 depends on the dimensions of the key which holds the units in place on the shaft. The dimension of the key can be found from the mechanical requirements of the design. The choice of the key and thus the value of R_2 is based on the requirements of B84999/5000!

(iii) R_4 is the outer radius of the rotor. This is fixed by the size of the stator bore and the required airgap clearance or the minimum clearance acceptable.

(iv) The number of units which make up the rotor of variable length is fixed at 4. This number is not arbitrary but is chosen as a result of the analysis of the computation done with machines constructed with 2 units, 3 units and 4 units. A three unit construction for a stator similar to generator A is first considered for a choice of magnet materials. The optimal configuration as regards power per unit volume is found and this is shown in Table 7.1. A four unit system for the same stator is also considered and the results are listed in Table 8.2. It is clear that the output per unit rotor volume is always better for the four unit system than it is for the three unit system but never by a significant margin. It has been found that the loss of output in a two unit case is, however, more significant[2]. It is also noticed that the optimal dimensions of a flux guide of the four unit system is the same as that for the three unit rotor. The choice of 4 units will give an accurate value for the dimension of an ideal single unit.

The variables that remain to be optimised are:

(i) The outer radius of the disc magnet, R_3. This variable determines the surface area of the pole of the disc magnet.

(ii) The length per unit, U_{th}. This dimension, coupled with the magnet thickness, M_{th}, determines the thickness of the iron plate, I_{th}, which is a critical dimension as it is the limiting factor in the passage of flux from the magnet to the poles.

(iii) The magnet thickness, M_{th}.

These are the three major variables which are optimised. The other two variables which are also considered are 's' and 'a', the two dimensions of iron path 2 (see Figure 8.2).

8.3.1 The Method and Criteria of Optimisation

The optimisation is conducted with the stator characteristics fixed but with suitable changes in the armature resistance and reactance as its length changes[3]. The method by which the search for the optimum is done is shown by the flow chart in Figure 8.3. Limits are required to be set for all the variables involved. The length, from the general knowledge that an optimal machine is alsmot square, is optimised between a length equal to half that of its diameter and a length twice its diameter. The magnet thickness is limited by the length per unit and the outer radius of magnet is limited by R_4 (see Figure 8.2), the radius of the rotor. The variable 'a' has the outer radius of the magnet as its lower limit and the radius of the rotor as its outer limit. 's' is limited to half the magnet thickness.

The criteria of choosing the optimum is the maximum power produced per unit length. The following steps outline the optimisation process,

using the discrete-reluctance method program, described by the flow chart in Figure 8.3.

Step 1 : Input the rotor constants, such as the outer diameter of the rotor, shaft diameter, the inner radius of the magnet, the stator data and the number of rotor units. The upper and lower limits of the variables to be optimised are also specified.

Step 2 : Increase the overall axial length of the rotor.

Step 3 : Increase the outer diameter of the magnet.

Step 4 : Increase the magnet thickness.

Step 5 : Adjust the value of armature resistance and reactance accordingly.

Step 6 : Call the load program which is described by the flow chart in Appendix IV, to calculate the load characteristic for a given set of data.

Step 7 : Calculate the maximum power generated per unit length.

Step 8 : Check that the outer diameter of the magnet is less than the maximum.

Step 9 : Check that the magnet thickness is less than the maximum.

Step 10 : Check that the total axial length is within the limits considered.

Step 11 : Search for the optimum design as regards maximum power per unit length.

Step 12 : Fixed the values of the variables optimised, U_{th}, M_{th} and R_3.

Step 13 : Increase 'a'.

Step 14 : Call load program.

Step 15 : Calculate the maximum power per unit length.

Step 16 : Check that 'a' is less than the upper limit.

Step 17 : Search for the optimum value of 'a' from the maxima calculated in Step 15.

Step 18 : Increase 's'.

Step 19 : Call the load program.

Step 20 : Calculate the maximum power generated per unit length.

Step 21 : Check that 's' is within the limits specified.

Step 22 : Search for the optimum of 's' from the maxima calculated in Step 20.

Step 23 : Output optimum dimension for a rotor of fixed diameter and fixed number of units.

The optimal design obtained for a rotor diameter of 139.7 mm which fits a stator size of generator A with $\alpha = 5.366^{o}$ and an airgap of 0.386 mm is shown in Figure 8.4. This design is for use with ceramic-8 magnets.

8.3.2 The Influence of the Rotor Diameter on the Design and Output of the Rotor

The optimisation process described in Section 8.3.1 is done for rotors of different diameters to investigate the influence of the diameter on the design and output of the new rotor. Four rotor diameters are used in the study. They are 139.7 mm, the diameter of the rotor in generator A, 151.8 mm, 19 mm and 242.0 mm. The latter three rotors are labelled X, Y and Z. The stator characteristics of these four generators are shown in Table 8.3. They are all eight pole machines and run at a nominal speed of 1500 rpm. The optimal designs of A, X, Y and Z, for use with ceramic-8 magnets, are tabulated in Table 8.4. It is clear from the results obtained that for each diameter there is an ideal unit length

and its own ideal magnet size. The optimum is essentially a balance between the surface area of the pole of the magnet and the thickness of the iron plate which has to carry the flux. An ideal generator can be formed by 4 or more of these units. The reason for the choice of 4 or more units has been discussed[2], It can be seen that for all the 4 diameters of rotors considered, the choice of 4 units would form machines which are about square.

Figure 8.5 shows the graph relating the ideal length per unit and the diameter of the rotor and Figure 8.6 shows the relationship between the magnet dimensions and the rotor diameter. The plot of the maximum power per unit magnet volume and the plot of the maximum power per unit rotor volume against rotor diameter are shown in Figure 8.7. The peaks of both the graphs in Figure 8.7 are at a rotor diameter of 180 mm. The optimum length per unit, U_{th} = 36.7 mm (from Figure 8.5), magnet thickness, M_{th} = 16.0 mm (from Figure 8.6) and the outer diameter = 164 mm. The theoretical ideal 4 unit machine using ferrite magnets would be 146.8 mm long and it would be capable of generating a maximum output of 4.109 kW (1.100×10^{-3} W/mm^3).

8.4 THE INFLUENCE OF MAGNET CHARACTERISTICS ON THE DESIGN AND OUTPUT OF THE MULTI-STACKED PERMANENT-MAGNET GENERATOR

The different permanent magnet materials that can be used in the new rotor are described in Chapter 2. Their characteristics are shown by the curves in Figure 2.4 and tabulated in Table 2.1. Due to the varying characteristics of these materials, the design, output performance and usage can be expected to be different. The influences of the physical properties have been discussed in Chapter 2. The physical properties considered include the density of the material, the hardness and the

temperature stability. These factors have to be considered carefully in the production and application of the generator. The influence of the temperature stability of the magnet is studied and discussed in more detail in Section 8.4.2.

The permanent magnet, being the source of excitation, determines the output characteristics of these generators. As the dimensions of the flux guide and the magnet are optimised to achieve maximum output, it must mean that the rotor unit is optimised such that the magnet operates at the point where energy product of the permanent magnet, (BH), is at its maximum, at the peak power point. The (BH) characteristic of each material differs from another and the $(BH)_{max}$ point occurs at different values of B and H (see Table 8.5). The difference in values of $(BH)_{max}$ results in the difference in output capability of genertors using the different material and the difference in B-H values results in the difference in design, for example the volumetric ratio between iron and magnet.

8.4.1 A Comparison of the Design and Output of the Multi-Stacked Permanent-Magnet-Generator Using Different Magnet Materials

The four modern magnet materials used for this comparison are ceramic-8, an anisotropic ferrite, HERA, a polymer-bonded rare-earth magnet, H18-B, a form of pure rare-earth and a compound, MnAlC. These magnet materials are abbreviated in the graphs and tables as CE, HE, R2 and MN respectively. For the purpose of this comparison, design optimisation are done for rotors with the four different diameters described in the last section, using the four magnet materials. The results from the computation are shown in the graphs and tables of Figures 8.8 to 8.12.

The Figures 8.8 to 8.12 show the comparison of the primary parameters which determines the design of the rotor. The ideal length per rotor unit for each material of a certain diameter is listed in a Table in Figure 8.8 and shown graphically in the same Figure. Figure 8.9 presents the results of the optimum outer diameter of the disc magnet and the optimum magnet thickness computed for each material at different rotor diameters are shown in the table and graph in Figure 8.10. The differences in the optimum magnet dimensions for the rotors of the same diameter but employing different magnet material are due to the variation in the demagnetisation characteristics of the magnet materials. Rare-earth magnets with high flux density levels have a small outer diamter, thus a smaller surface area, when compared with the outer diameter of the ceramic-8 magnet, due to the low flux density level of ceramic-8 (it is the lowest of the 4 magnets considered). The high coercivity of the rare-earth magnets also enables the use of thinner magnets. These two variables are balanced by the increase in the iron of the flux guide to cope with the high flux density levels. The efficiency in guiding out the flux produced by the magnet is the factor in the efficient exploitation of the potential energy of the magnet material. The change in the ideal length per unit and the change in the optimum diameter of the magnet with a charge in rotor diameter are linear for all the materials. The change in the optimum length per unit vary from 0.123 mm per mm change in rotor diameter for rotor with ceramic-8 magnets to 0.214 mm per mm charge in rotor diameter for rotors with rare-earth magnets. The change in the outer diameter of the magnet is almost equal for all 4 materials at 0.85 mm per mm change in the rotor diameter. The variation in the magnet thickness for rotors with different sizes is non-linear (see Figure 8.10).

The comparisons of the output of the rotors of different sizes employing different magnet materials as regards output power per unit rotor volume and output power per unit magnet volume are shown in Figure 8.11 and Figure 8.12 respectively. They are a measure of the power density that can be achieved with the different types of permanent magnets used in the excitation. It is clear from these tables and graphs that the output per unit rotor volume or even per unit magnet volume is primarily dependent on the choice of magnet material. However the output increases much more slowly than the increase in the maximum energy density in the magnet. A 6:1 increase in maximum energy in the magnet material (between ceramic-8 and H18-B magnets) results in a 3:1 increase in output per unit magnet volume for these forms of machines.

Figures 8.11 and 8.12 also show that there is an optimum diameter for this form of permanent-magnet machine. From Figure 8.11, the optimum diameter for a rotor which uses the rare-earth magnet, H18-B (R_2), is 180 mm and the optimum for rotors using ceramic-8 and MnAlC magnets is at 190 mm. The optimum for rotors using HERA is at a significantly lower value of 165 mm. The optimum rotor diameter as regards maximum power per unit magnet volume is at 190 mm for rotors employing rare-earth magnets (H18-B), Ceramic-8 magnet and MnAlC magnets. The behaviour of rotors using the polymer-bonded rare-earth material, HERA, is different. Its optimum is at a much smaller diameter and out of the range of diameters considered. The two figures, Figure 8.11 and 8.12 also show that the optimum for rotors using the rare-earth material is more critical than the other three materials whose output per unit volumn characteristics are gentler. The performance of rotors using the materials MnAlC and Ceramic-8 do not deviate from the optimum by any appreciable amount over a wide range of diameters.

8.4.2 The Optimisation of Rotors Using Ceramic-8 Magnets of Different Sizes at Constant Voltage

This criteria of optimisation introduces another constraint which has a significant result on the output power generated by the optimal designs for the different rotor diameters. The generated open circuit voltage is kept constant by adjusting the winding characteristics. Consequently the armature resistance and leakage reactance change as well. The open circuit voltage is kept constant at 270 volts per phase in the computation to obtain the optimal design for the rotors of different diameters. The result of the computation is shown in Figure 8.13 which is a plot of the maximum power output per unit rotor volume against rotor diameter. The full line shows the computation at constant open circuit voltage while the dotted line shows the computation with fixed winding characteristics. The new optimum diameter is at 200 mm with a power density of 1.375×10^{-3} W/mm^3. This is better than the maximum power density of 1.235×10^{-3} W/mm^3, when computed with fixed winding characteristics. A comparison of the two curves show that the dominance of the windage losses for small machines results in the poorer output of generators optimised to give a specific open circuit voltage, in this case, a voltage of 270 Volts. For this same reason the output per unit rotor volume increases very rapidly as the rotor diameter increases, till the optimal point is reached. It then falls at a gentle rate to an almost constant level of 0.95×10^{-3} W/mm^3.

8.5 THE INFLUENCE OF TEMPERATURE ON THE OUTPUT OF PERMANENT-MAGNET GENERATORS

In permanent magnet generators there is an additional factor which results in a drop in output, apart from the copper losses, eddy current losses and other forms of stray losses, and mechanical losses due to the bearings. This factor is exclusive to permanent magnet machines and is due to a change in the magnetisation characteristics of the permanent magnets resulting in a reduction in the level of excitation. This demagnetisation process is usually reversible but can be irreversible if there is a large thermal fluctuation in excess of its permitted temperature range.

Reversible demagnetisation in permanent magnets is caused primarily by an increase in temperature[4]. These reversible changes are confined to a specific range of temperature for each material. This has been discussed in Chapter 2. Beyond this range irreversible demagnetisation occurs. It is therefore essential that the new rotor works in an environment where the temperature does not exceed the permitted reversible range. In the case of ceramic-8 magnets, this range of temperature is between $-60^{o}C$ and $300^{o}C$.[4]

Permanent magnet generators, like the multi-stacked permanent-magnet generators being discussed, work at different temperatures, depending on the current loading and the cooling system employed. The source of heat is contributed primarily by the current loading in the stator. The rotor has no excitation coils and therefore no copper losses in rotor, but, eddy currents in the solid poles do contribute to the rise in temperature. An experiment was conducted on generator A to measure the rise in temperature with time. This experiment was done with the generator delivering the maximum power to a resistive load

drawing 5.85 amps per phase from it at room temperature ($17^{o}C$). The temperature of the rotor and the stator coils are measured with thermistors. The result from this experiment is shown in Figure 8.14. The graph of temperature against time shows that the temperature in the machine rises from an ambient temperature of $17^{o}C$ to a thermal equilibrium at $81^{o}C$ after 2.00 hours. The temperature of the rotor is always slightly higher than that of the stator coils. This can be expected as generator A has a completely enclosed frame with no interior or exterior fans. Thus if a fan is incorporated the machine would work at a lower temperature.

At the ambient temperature, the power output from generator A is 1.632 kW. As the temperature rises the output falls due to the reduction in excitation as a result of reversible demagnetisation of the magnets and the increase in copper losses. This drop in output is shown in Figure 8.15. The drop in output at $81^{o}C$ is 290 watts, a drop of 17.8%. This graph is non-linear. This is so because the output varies with the square of the airgap flux density which varies linearly with temperature. The drop in output due to the increase in temperature can be separated into two components; the copper losses and the drop in output due to a reduction in excitation. They can both be calculated using the known temperature coefficients of the magnet and copper. The temperature coefficient of demagnetisation of ceramic-8 = 0.23% per ^{o}C and the temperature coefficient of resistivity of copper = 0.393% per ^{o}C. These two losses and their sum are calculated and compared with the experimental curve in Figure 8.15. At high temperatures the error in the comparison increases. This may be due to the inaccuracy in the declared value of the temperature coefficient of demagnetisation and the non-consideration of eddy-current losses.

A means of overcoming the problem of temperature effects is to use rare-earth magnets which have a low temperature coefficient or Alnicos which are the most temperature resistant of all the materials considered. However, these two types of magnets are expensive compared with ceramic magnets. An alternative is the incorporation of an efficient cooling system.

8.6 CONCLUSIONS

The following conclusions can be drawn from the discussion on the search for an optimal multi-stacked permanent-magnet generator.

(i) The iron disc, iron path 1, can be redesigned to give uniformity in the usage of the iron. The resultant undulating surface would require matching magnet surfaces. This would be difficult to produce. Thus for industrial applications and manufacture, a flat surface despite the disadvantages is desirable.

(ii) The pole geometry can be optimised to give a near sinusoidal flux waveform by choosing α to be 20^{o} but with a reduced magnitude. The optimum as regards maximum power output is at $\alpha = 9.5^{o}$. The value of 'a' and 's' are optimised using the discrete reluctance method program.

(iii) Ideally a rotor should have 3 or more units.

(iv) For each diameter of rotor, there is an ideal unit thickness and its ideal disc magnet size. An ideal rotor of this diameter is formed from 3 or more of this ideal unit.

(v) For each permanent magnet material, there is an optimum rotor diameter. This optimum is 190 mm for ceramic-8 magnets and an ideal 4 unit machine of this rotor diameter can deliver a maximum of 4.109 kW having a power density of 1.100×10^{-3} W/mm^3. The

optimum rotor for the rare-earth magnet, H18-B, is at 180 mm in diameter having a power density of 2.4×10^{-3} W/mm^3.

(vi) Output from these generators depends on the magnet characteristics but it increases much more slowly than the increase in the $(BH)_{max}$ of the magnet. A 6:1 increase in $(BH)_{max}$ results in a 3:1 increase in output per unit magnet volume.

(vii) The optimum diameter of the rotor using rare-earth magnets is more critical than the optimum for ceramic-8 magnets. The output per unit volume characteristics for rotors employing ceramic-8 or MnAlC magnets are gentle and do not deviate from the optimum by an appreciable amount over a wide range of diameters.

(viii) By optimising the rotors of different diameters using ceramic-8 magnets and giving the same open circuit voltage of 270 volts per phase, the optimum diameter is found to be at 200 mm. The power density shows an improvement increasing to 1.375×10^{-3} W/mm^3 of rotor volume.

(ix) A drastic increase in temperature has an adverse effect on the output of permanent magnet generators. In generator A, which uses ceramic-8 magnets, the drop in output for a rise in temperature of 64 degrees is 17.8%.

(x) All the 4 magnet materials considered suitable for use with the new rotor have high H_c. This enables the rotor to withstand strong demagnetisation forces generated by the armature currents. These materials are also highly anisotropic which helps to prevent irreversible demagnetisation by the alignment of the anisotropic forces in the domains.

In the design optimisation of the new rotor, there are many other conditions and constraints which would demand a deviation from the optimum. These constraints are a result of commercial or industrial conveniences. Thus it may be necessary to optimise for a fixed magnet dimension or to optimise a rotor for a standard stator. These would result in a change in the dimension of the flux guide.

Ideally the new rotor will be made up of unit optimised for a particular diameter. The length of the rotor for that particular diameter would increase by the discrete length per unit.

8.7 REFERENCES

1. British Standard 4999/5000.

2. BINNS, K. J. and LOW, T. S. : 'Multistacked permanent magnet generators - the relation between output and magnet characteristics', Proc. of the 2nd International Conf. on Small and Special Electrical Machines, Conf. publication 202, IEE, London, Sept. 1981.

3. LANGSDORF, A. S. : 'Theory of A.C. Machinery', McGraw-Hill Book Company, New York, 1955.

4. McCAIG, M. : 'Permanent Magnets in Theory and Practice', Prentech Press, London, 1977.

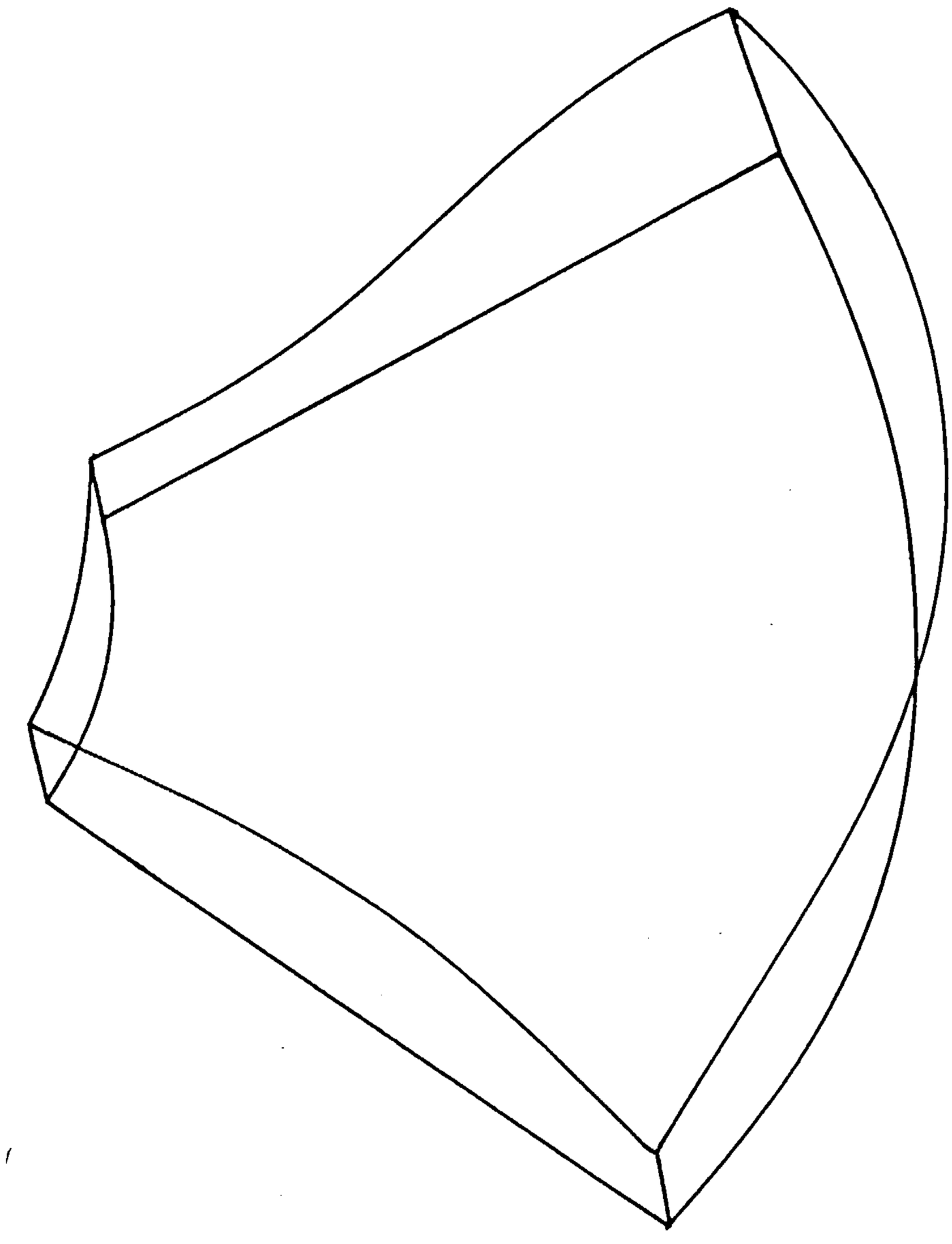

Figure 8.1 A possible geometry of iron path 1 of a new flux guide

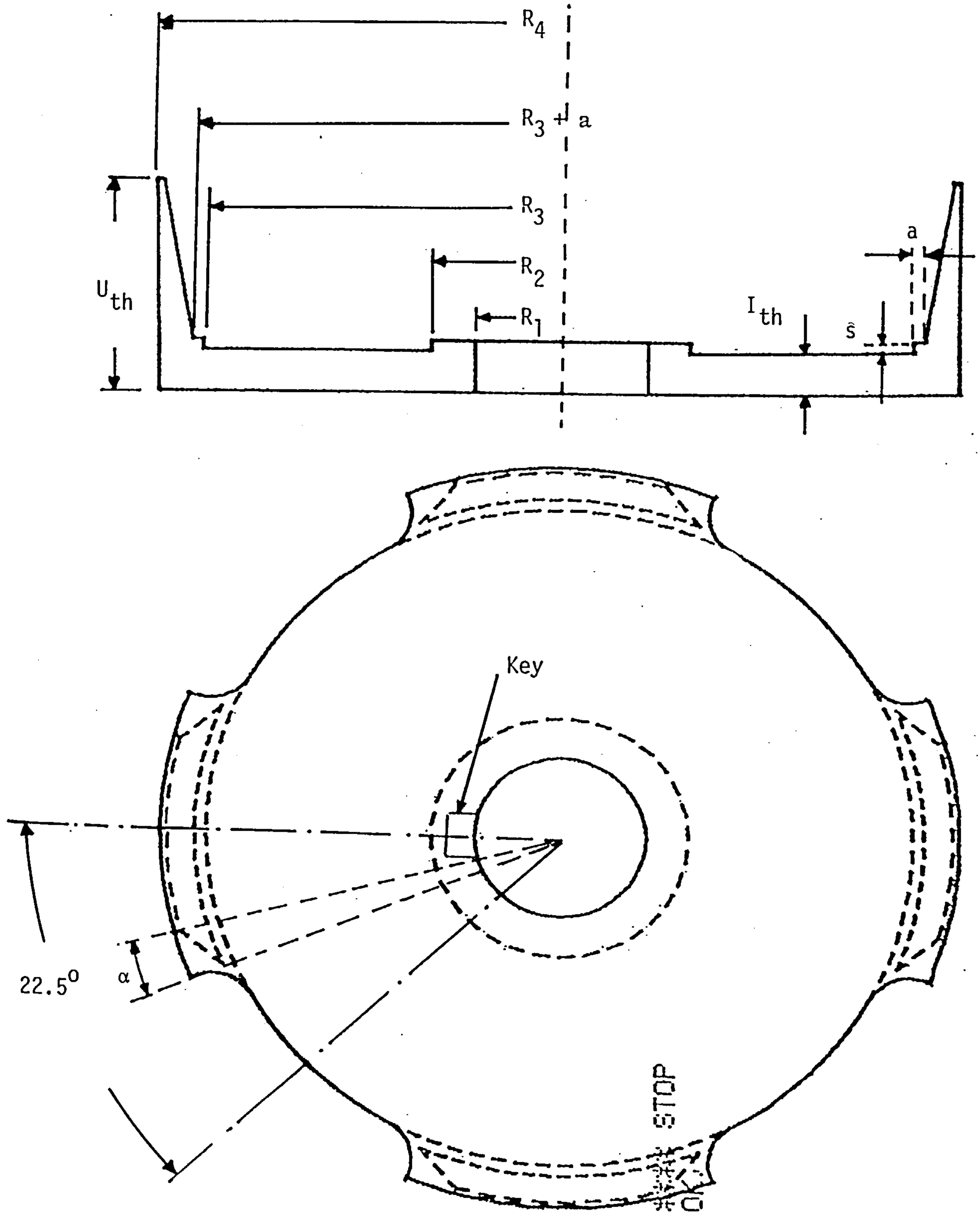

Figure 8.2 A typical flux guide of an eight pole generator with all the variables

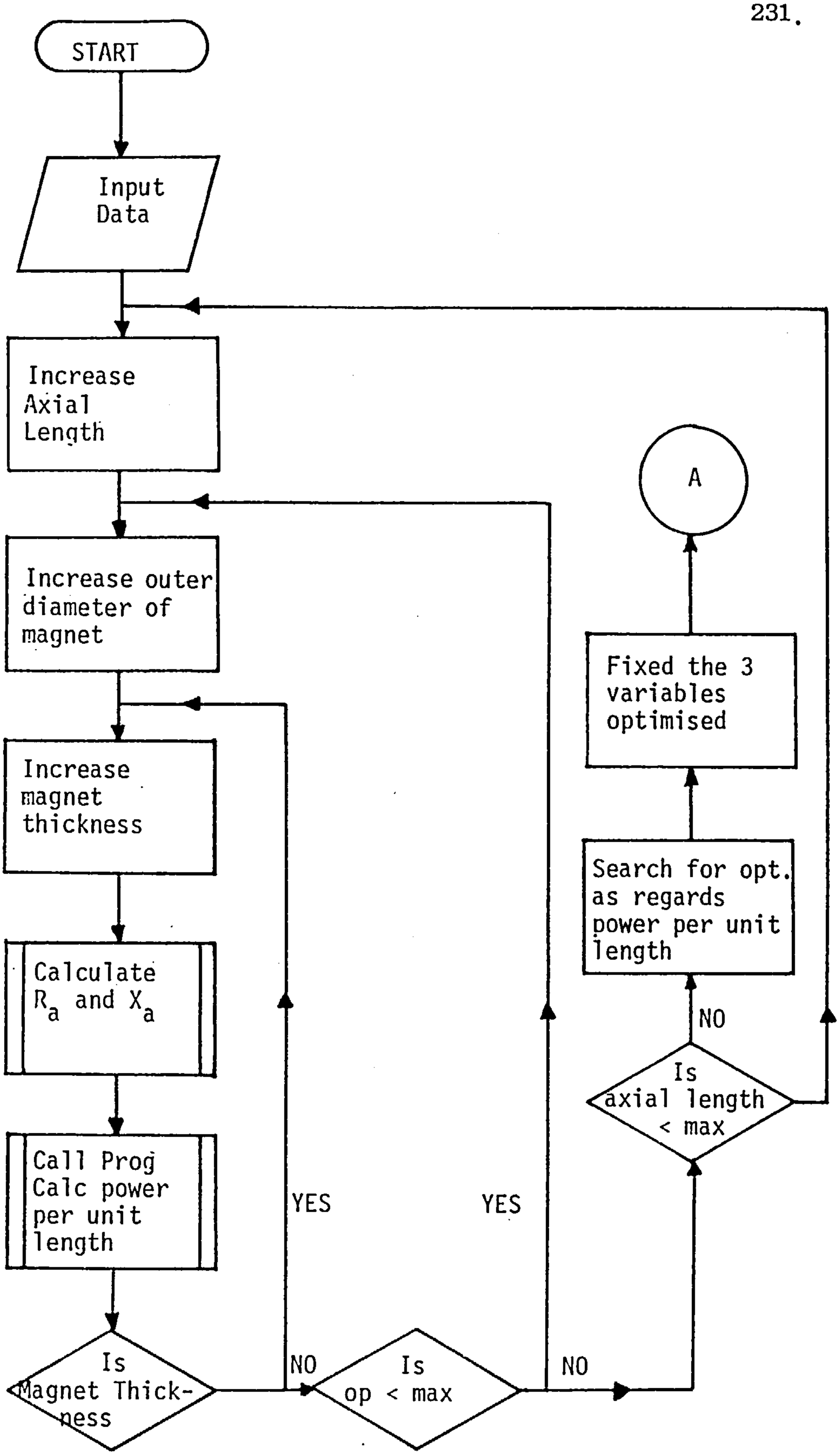

(a)

Figure 8.3 Program flowchart for the optimisation process

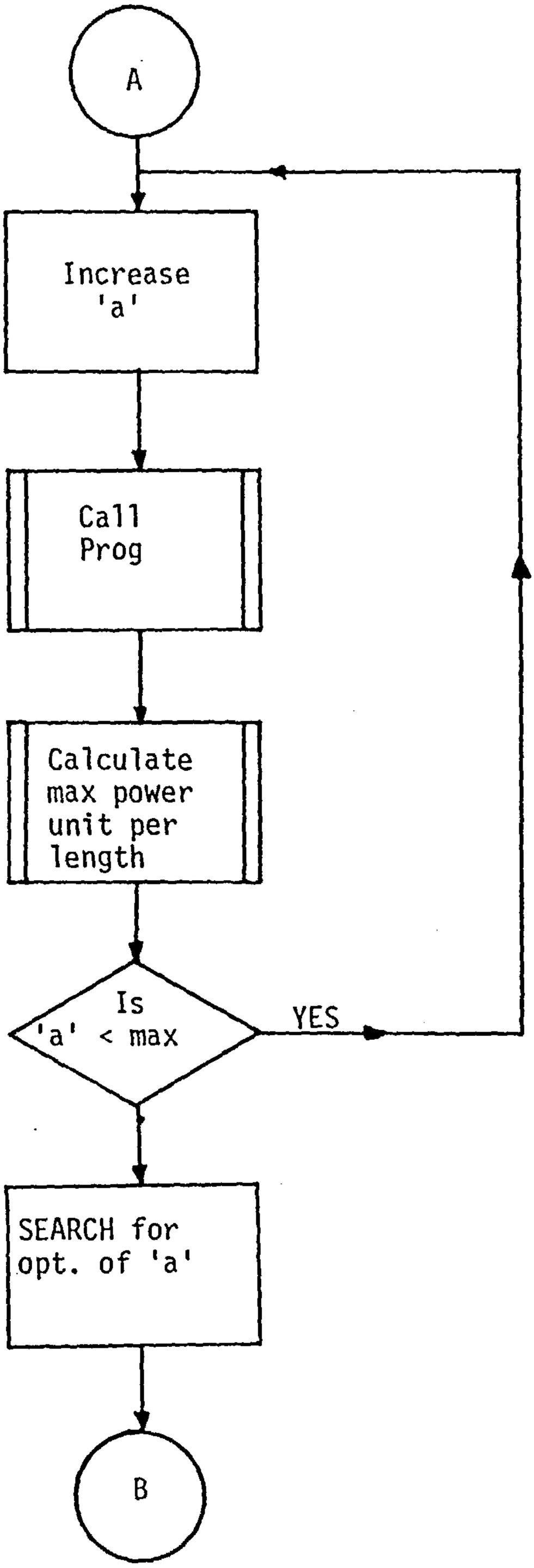
A
Increase 'a'
Call Prog
Calculate max power unit per length
Is 'a' < max
YES
SEARCH for opt. of 'a'
B

(b)

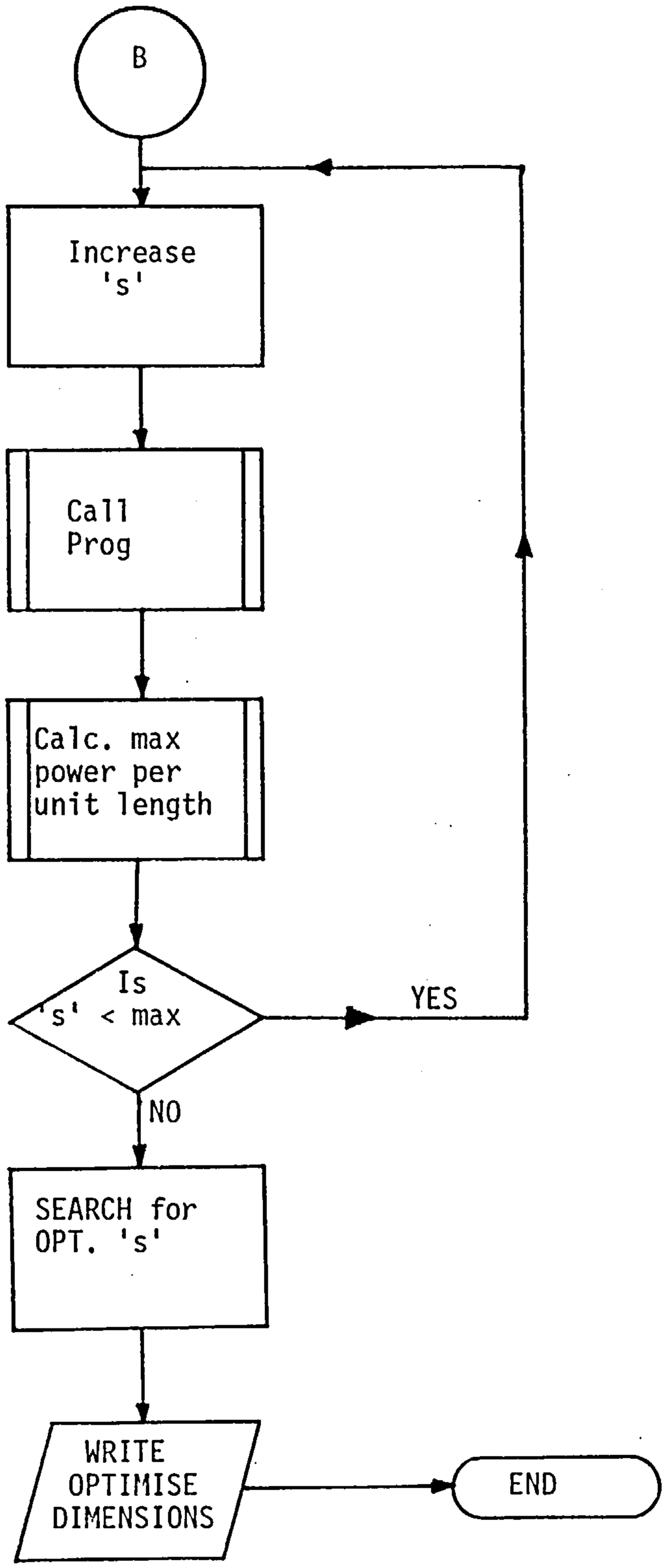
B
Increase 's'
Call Prog
Calc. max power per unit length
Is 's' < max
YES
NO
SEARCH for OPT. 's'
WRITE OPTIMISE DIMENSIONS
END

(c)

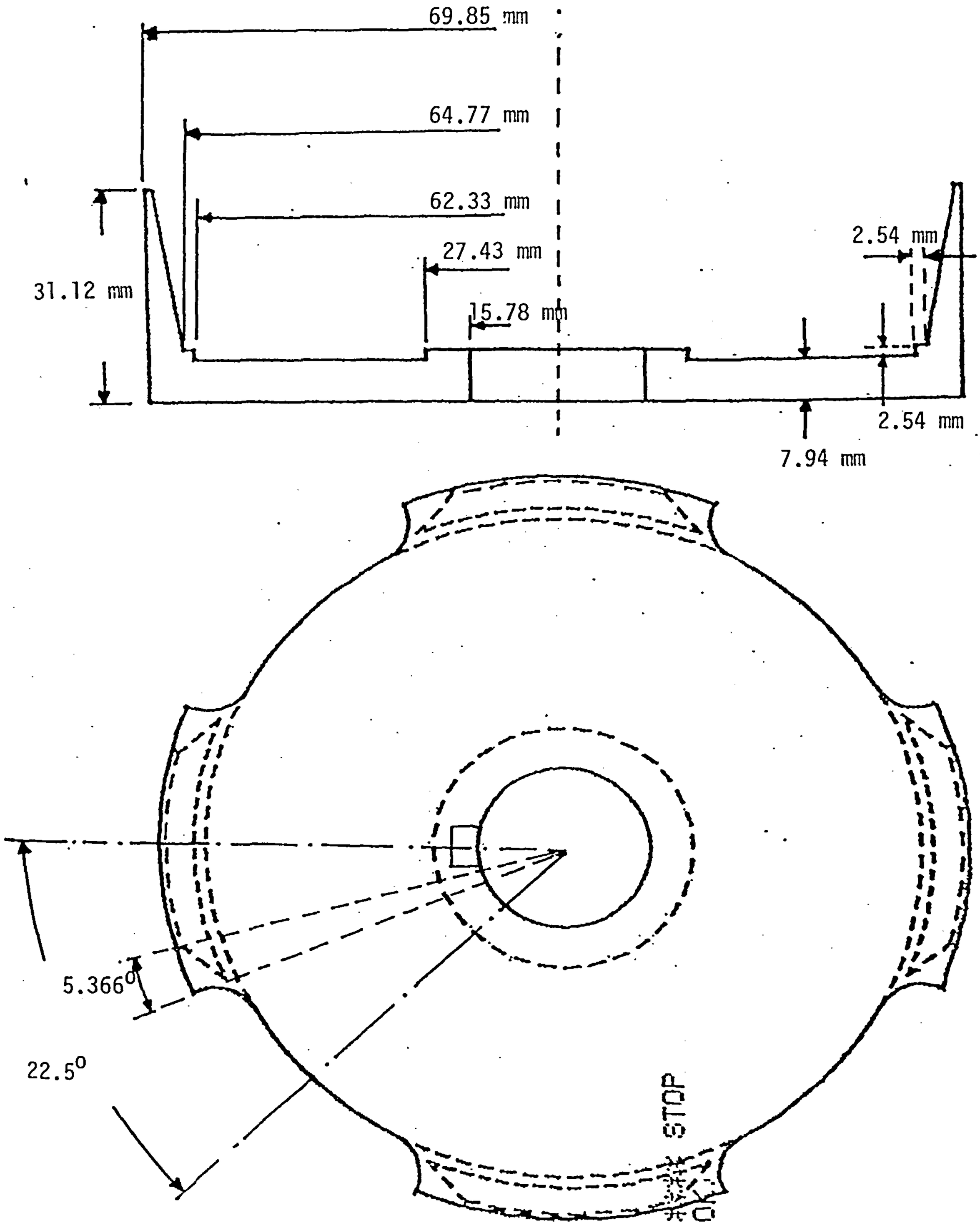

Figure 8.4 The optimal design of a flux guide for generator A

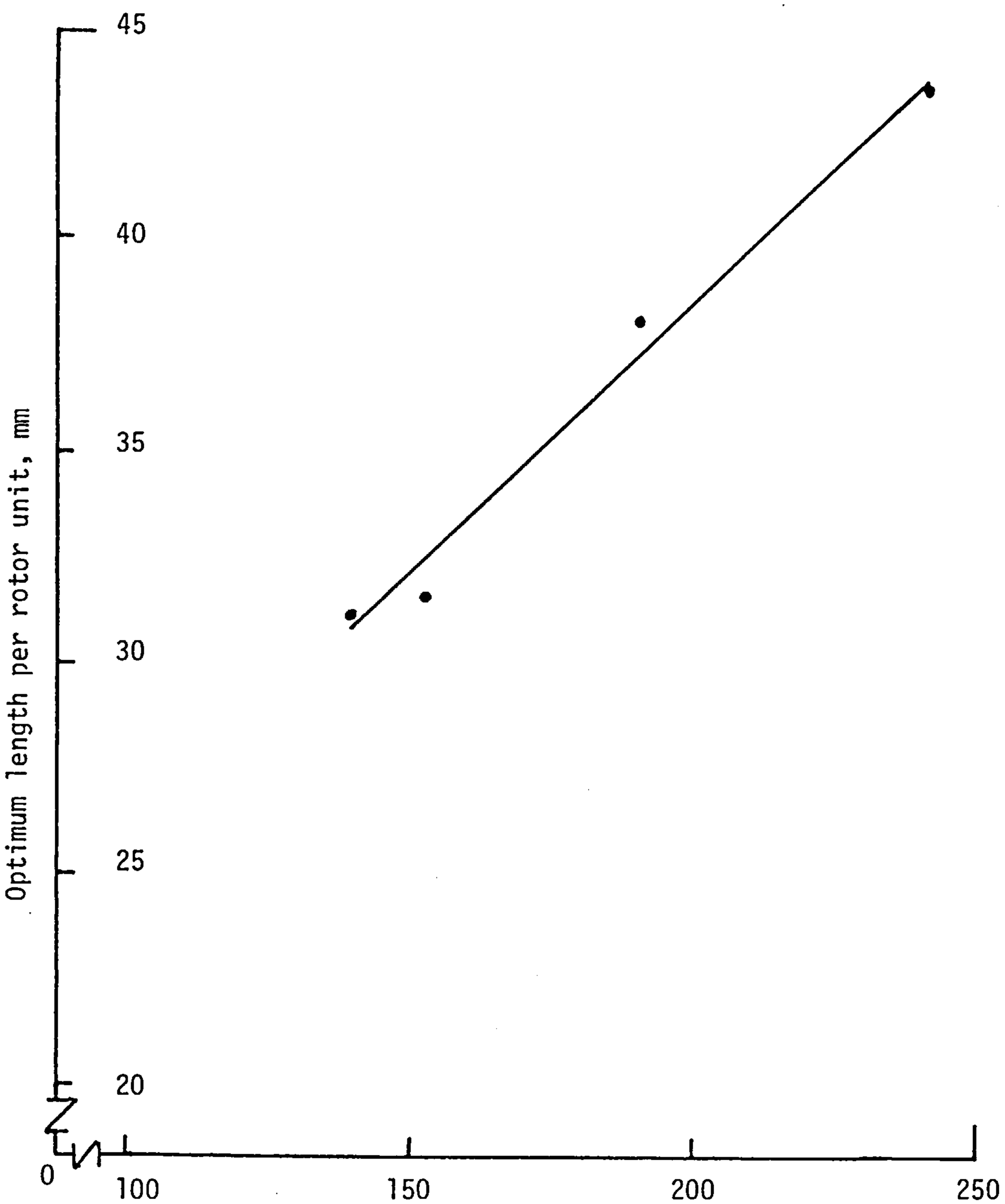

Figure 8.5 The optimum length per rotor unit for rotors of different diameters with ceramic-8 magnets

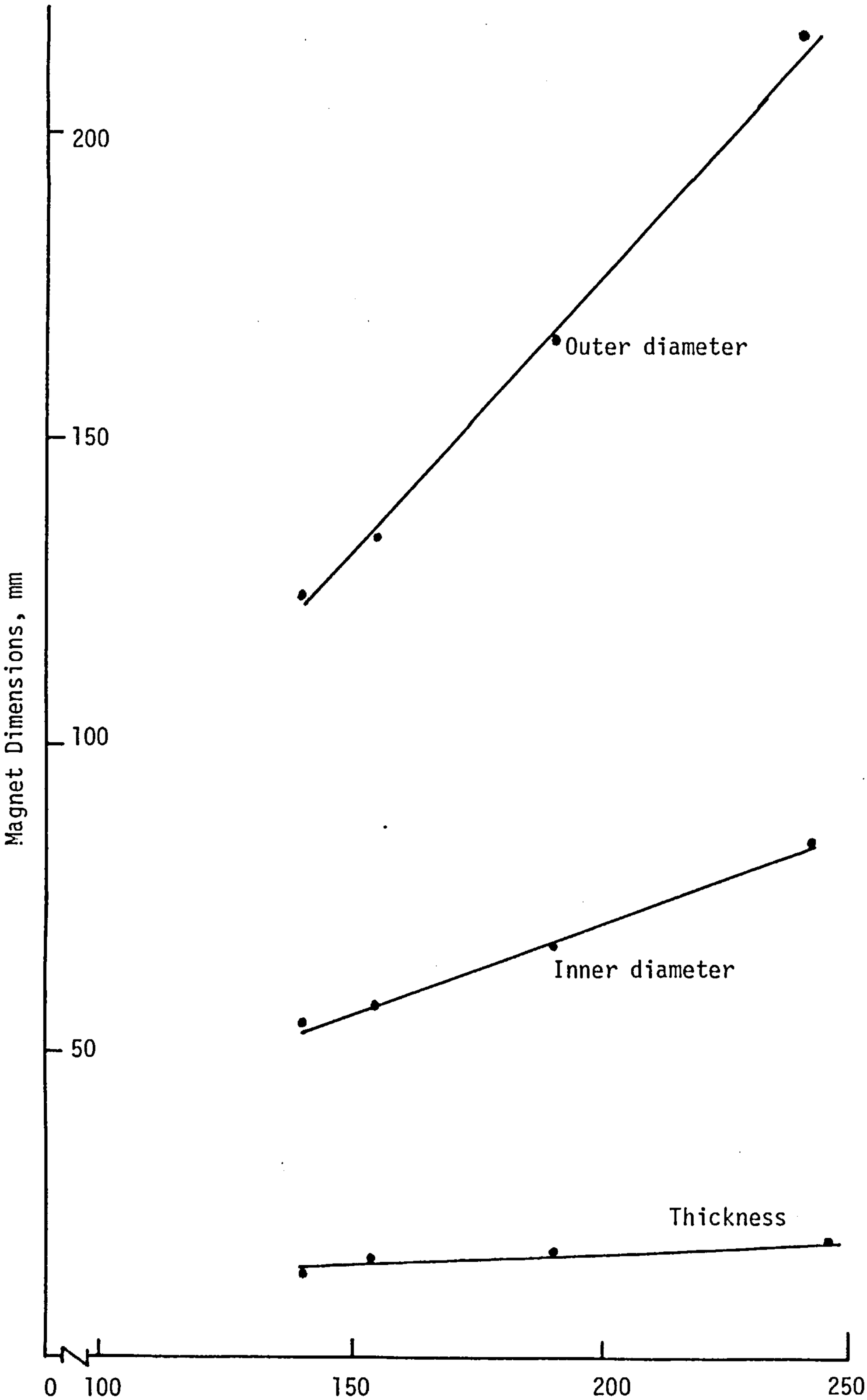

Figure 8.6 The optimum magnet dimensions for rotors of different diameters with ceramic-8 magnets

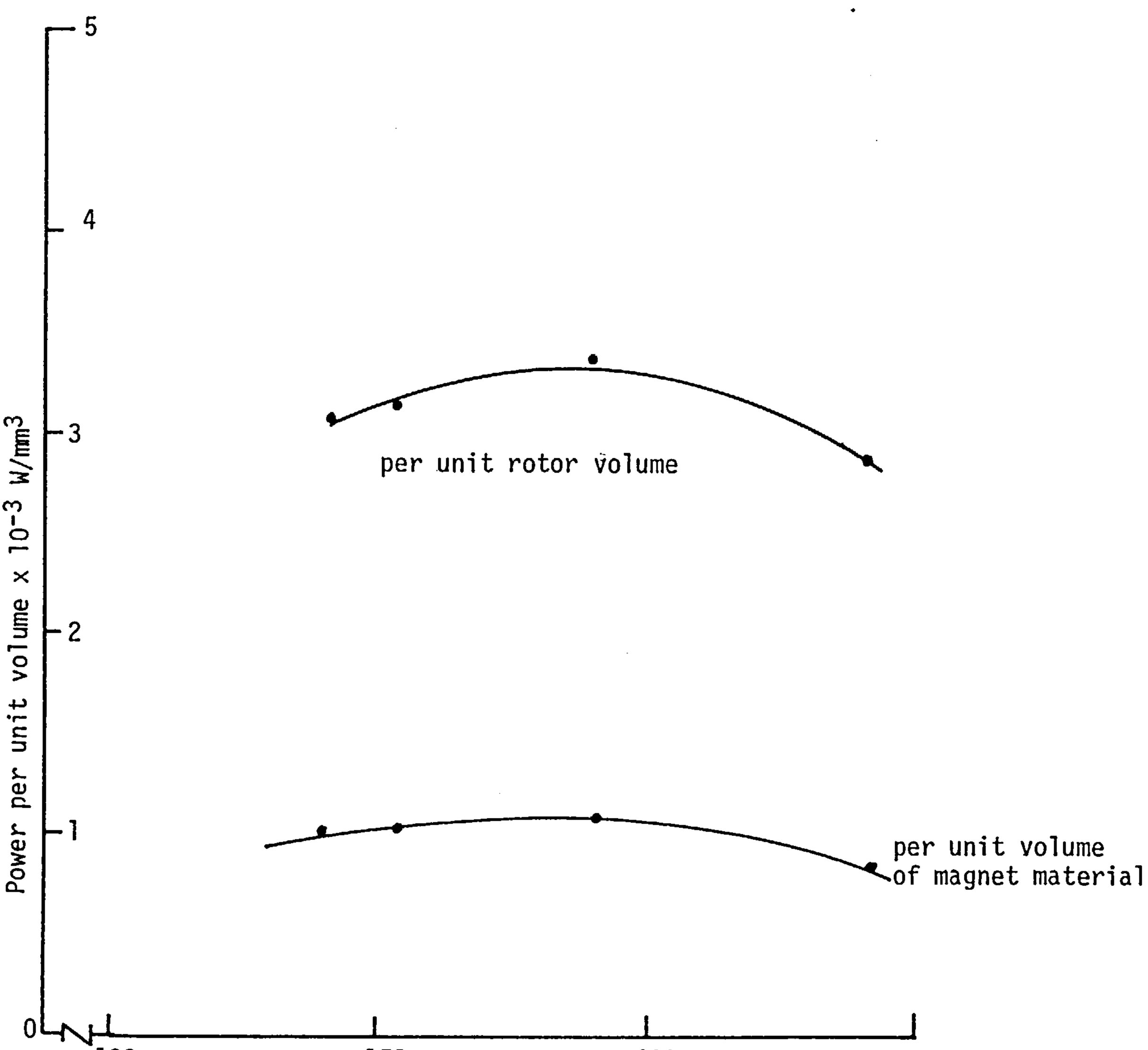

Figure 8.7 The maximum power output per unit volume of rotor and per unit volume of magnet for rotors of different diameter with ceramic-8 magnets

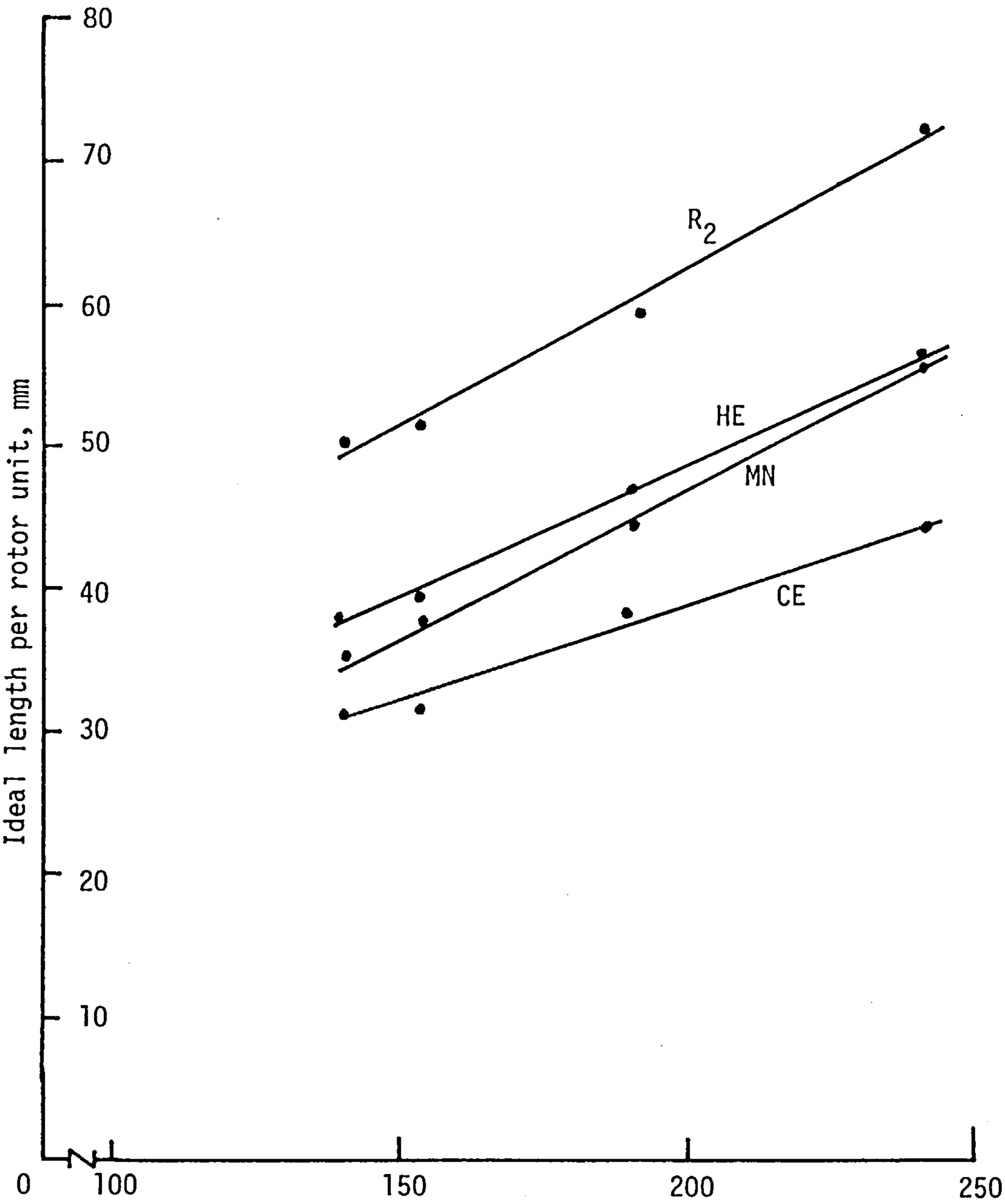

MATERIAL / GENERATOR		EE	HE	MN	R2
Frame	Dia.	Length per unit (mm)			
A	139.7	31.1	38.1	35.6	50.2
X	151.8	31.5	38.6	37.6	51.0
Y	191.2	38.1	46.7	44.7	58.9
Z	242.0	43.7	55.9	55.9	72.1

Figure 8.8 The ideal length per rotor unit, U_{th}, at different diameters for different magnet materials

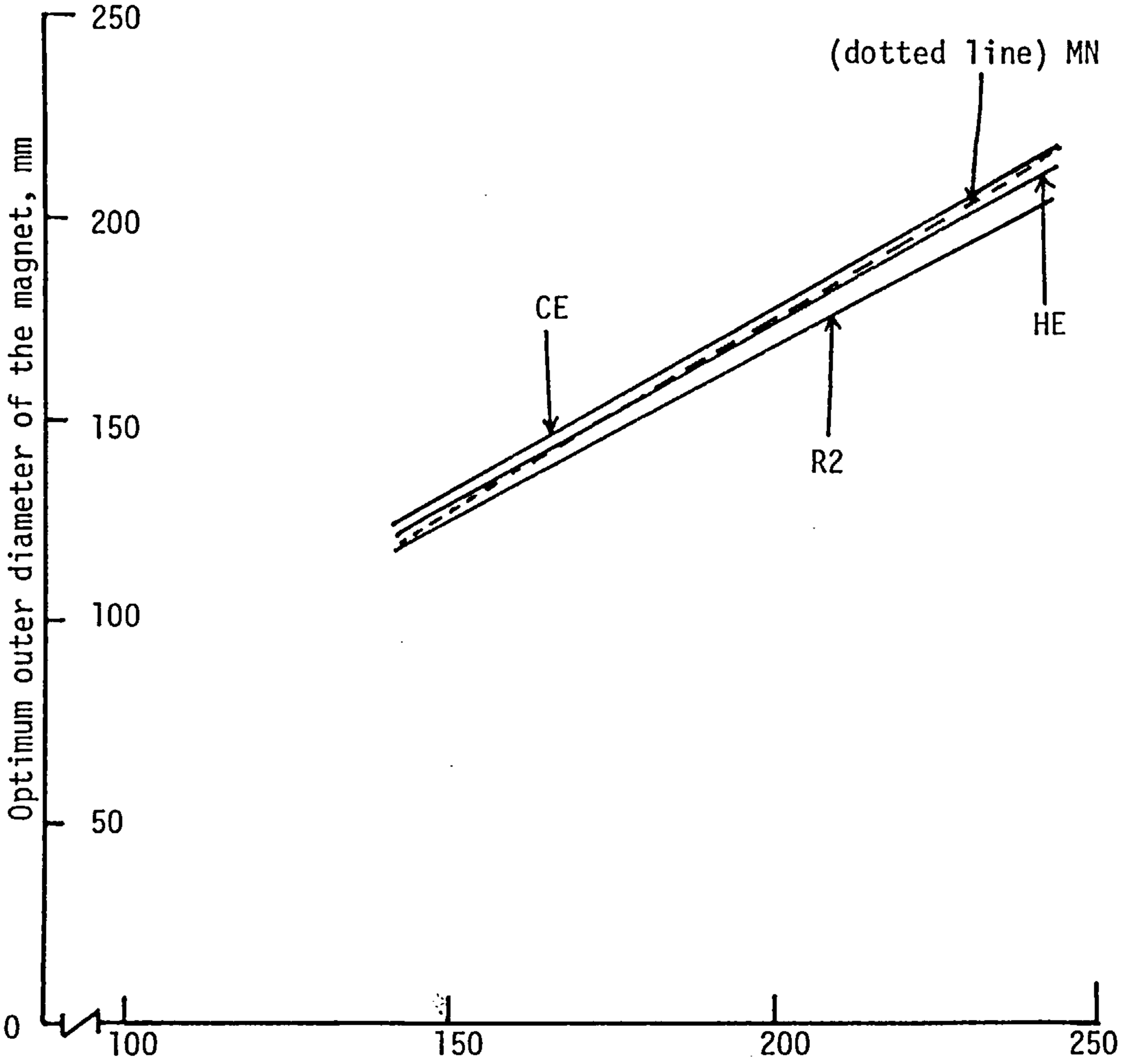

GENERATOR / MATERIAL		CE	HE	MN	R2
Frame	Dia. (mm)	Outer Diameter (mm)			
A	139.7	124.5	119.4	124.5	119.4
X	151.8	134.6	132.1	132.1	129.5
Y	191.2	167.6	165.1	167.6	162.6
Z	242.0	215.9	210.8	213.4	205.7

Figure 8.9 The optimum outer diameter of the disc magnet for rotors of different diameter with different types of magnets

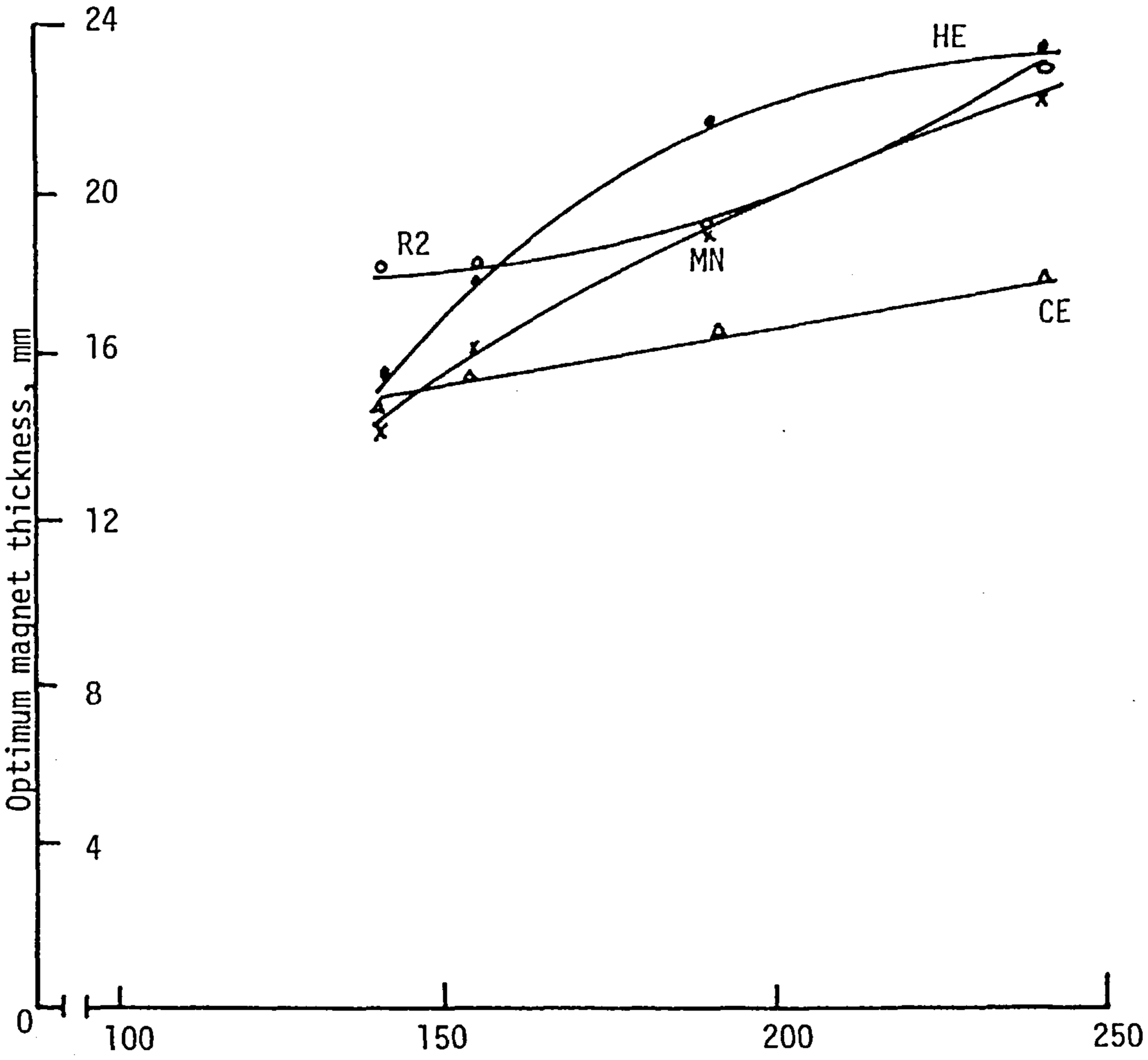

GENERATOR / MATERIAL		CE	HE	MN	R2
Frame	Dia. (mm)	Magnet Thickness (mm)			
A	139.7	14.9	16.5	15.2	17.9
X	151.8	15.5	17.8	17.8	17.9
Y	191.2	16.5	21.6	19.1	19.1
Z	242.0	17.8	22.9	22.9	22.9

Figure 8.10 The optimum magnet thickness for rotors of different rotor diameters with different magnet materials

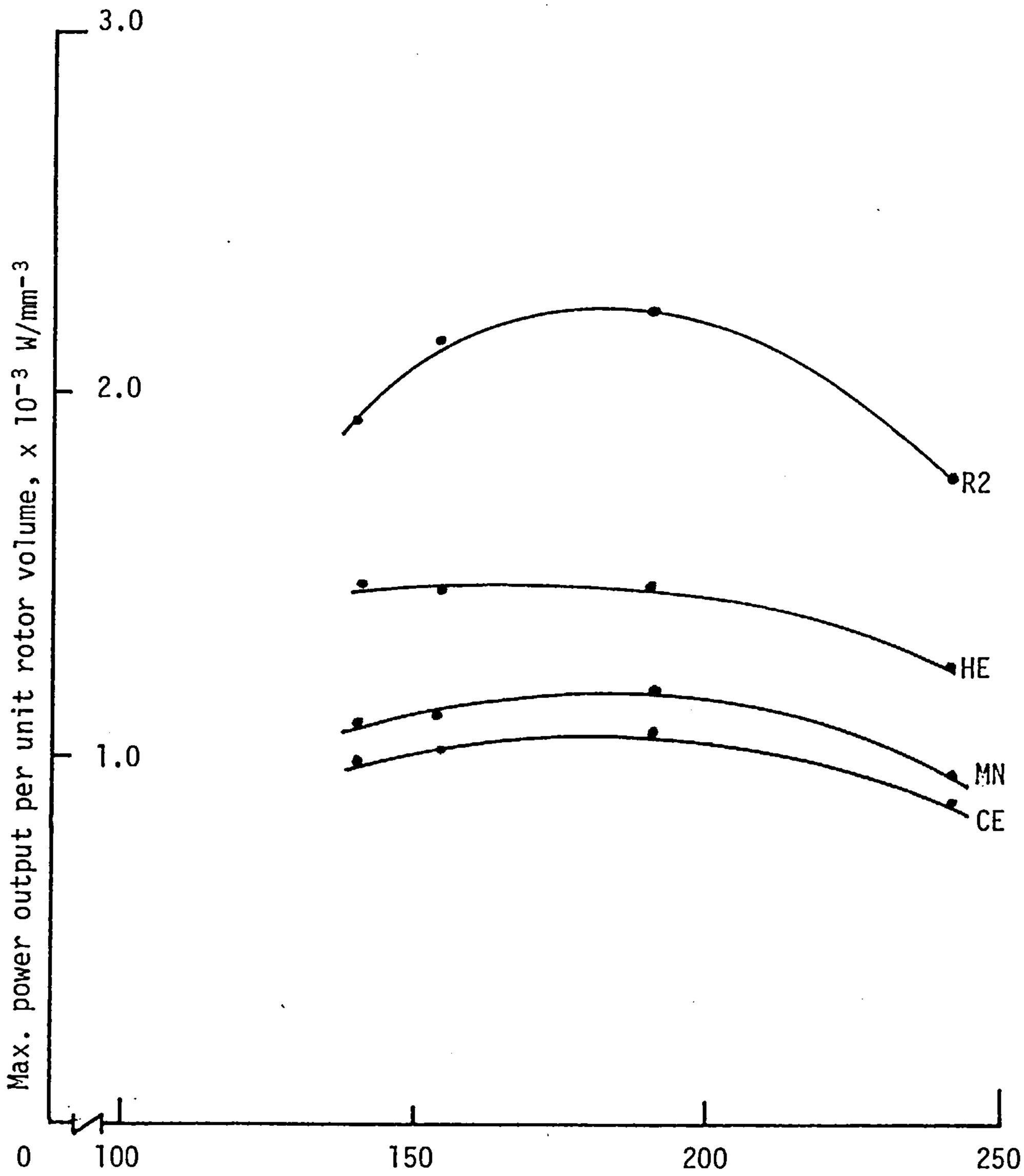

GENERATOR \ MATERIAL		CE	HE	MN	R2
Frame	Rotor Dia. (mm)	Max. Output Power Per Unit Rotor Vol. x 10^{-3} W/mm^3			
A	139.7	0.983	1.460	1.150	1.927
X	151.8	1.001	1.460	1.116	2.189
Y	191.2	1.060	1.477	1.187	2.224
Z	242.0	0.881	1.259	0.975	1.784

Figure 8.11 The maximum output per unit rotor volume for rotors of different diameters with different magnet materials

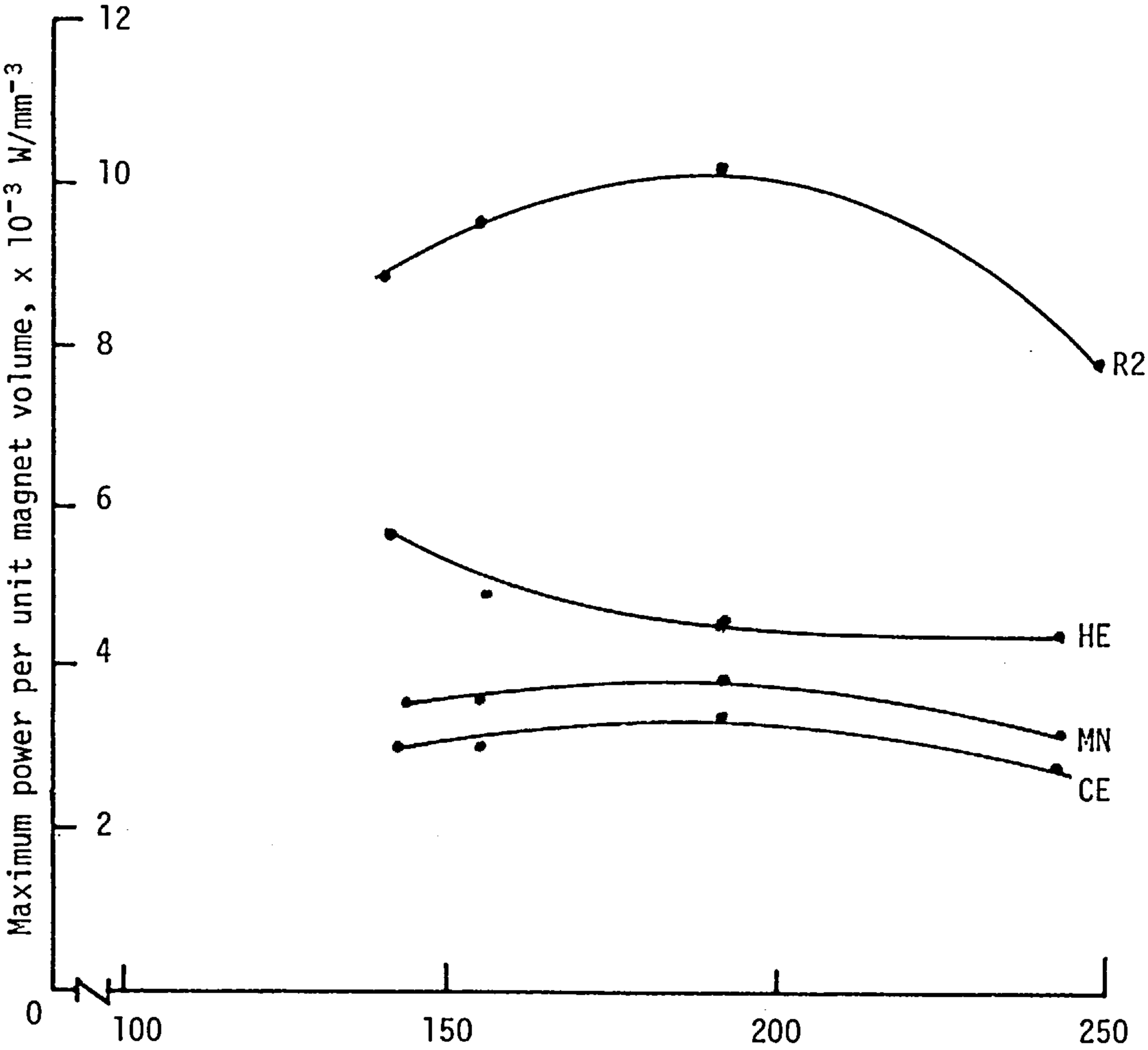

GENERATOR \ MATERIAL		CE	HE	MN	R2
Frame	Rotor Dia. (mm)	Max. Power Output Per Unit Magnet Vol. x 10^{-3} W/mm^3			
A	139.7	3.045	5.628	3.500	8.895
X	151.8	3.100	4.787	3.530	9.659
Y	191.2	3.368	4.550	3.823	10.126
Z	242.0	2.876	4.320	3.250	8.383

Figure 8.12 The maximum output per unit magnet volume for different rotor diameters with different magnet materials

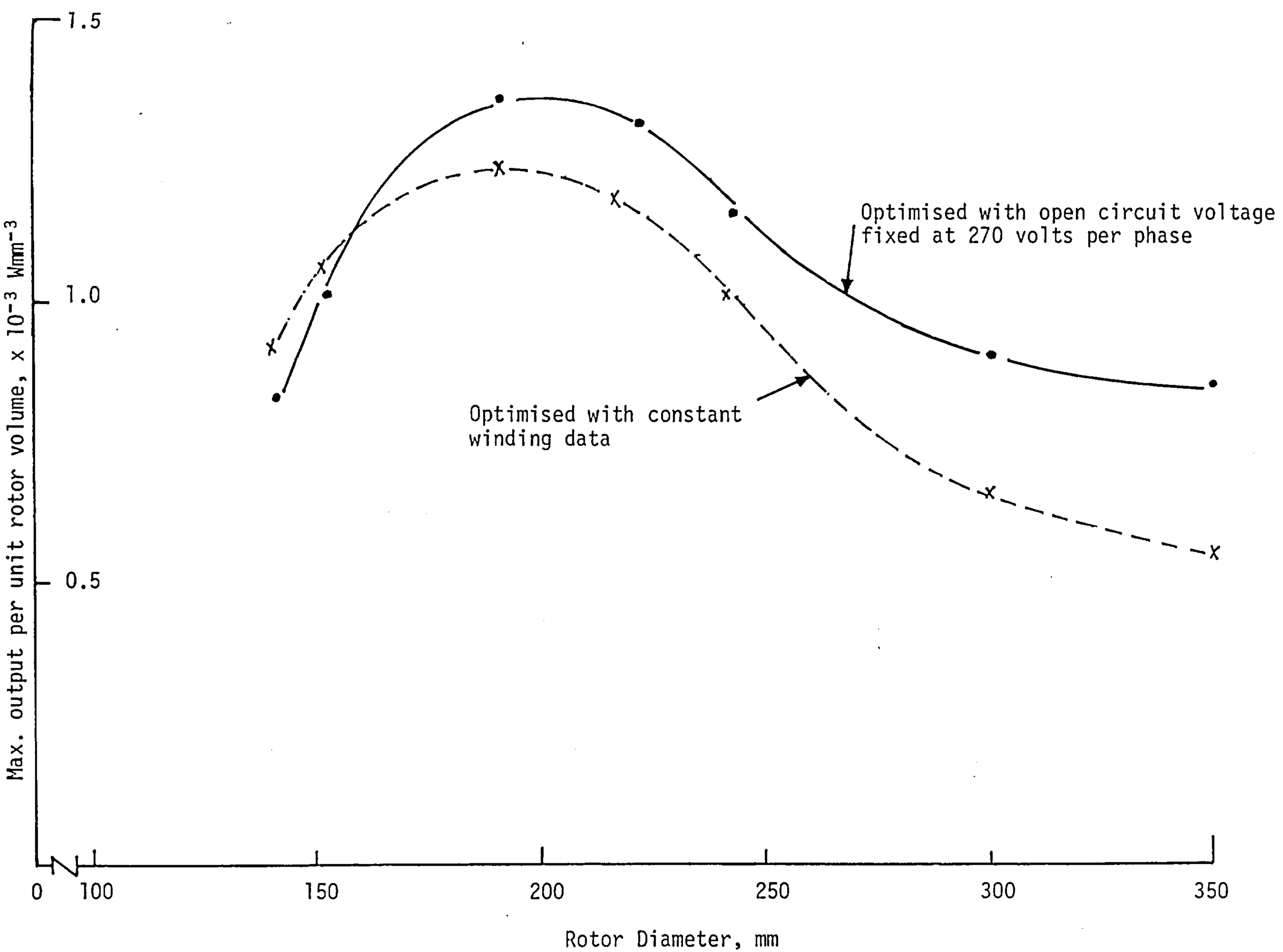

Figure 8.13 Optimisation of rotors of different diameters using ceramic-8 magnets with an open circuit voltage of 270 volts per phase

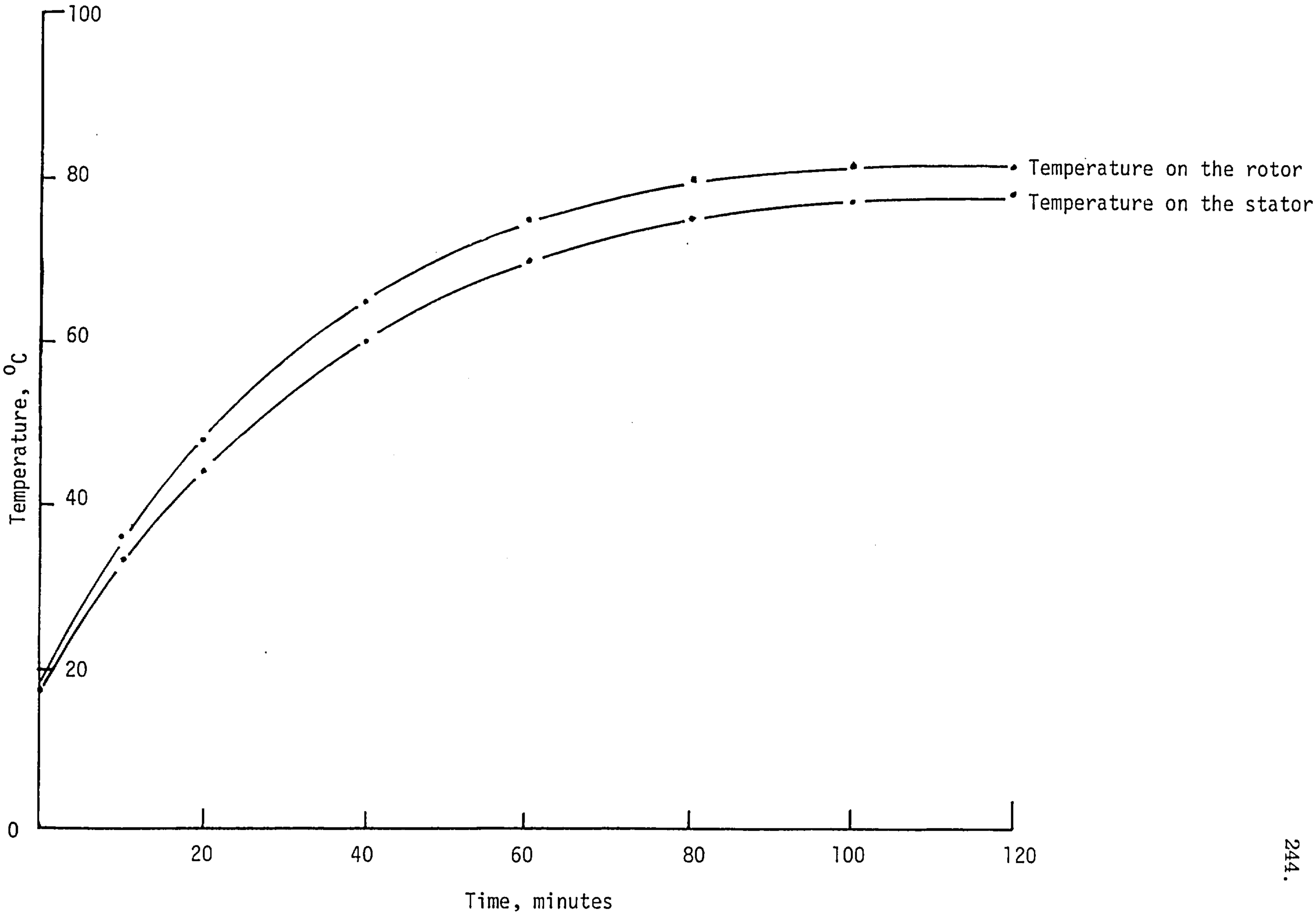

Figure 8.14 The rise in temperature with time for generator A running at peak power

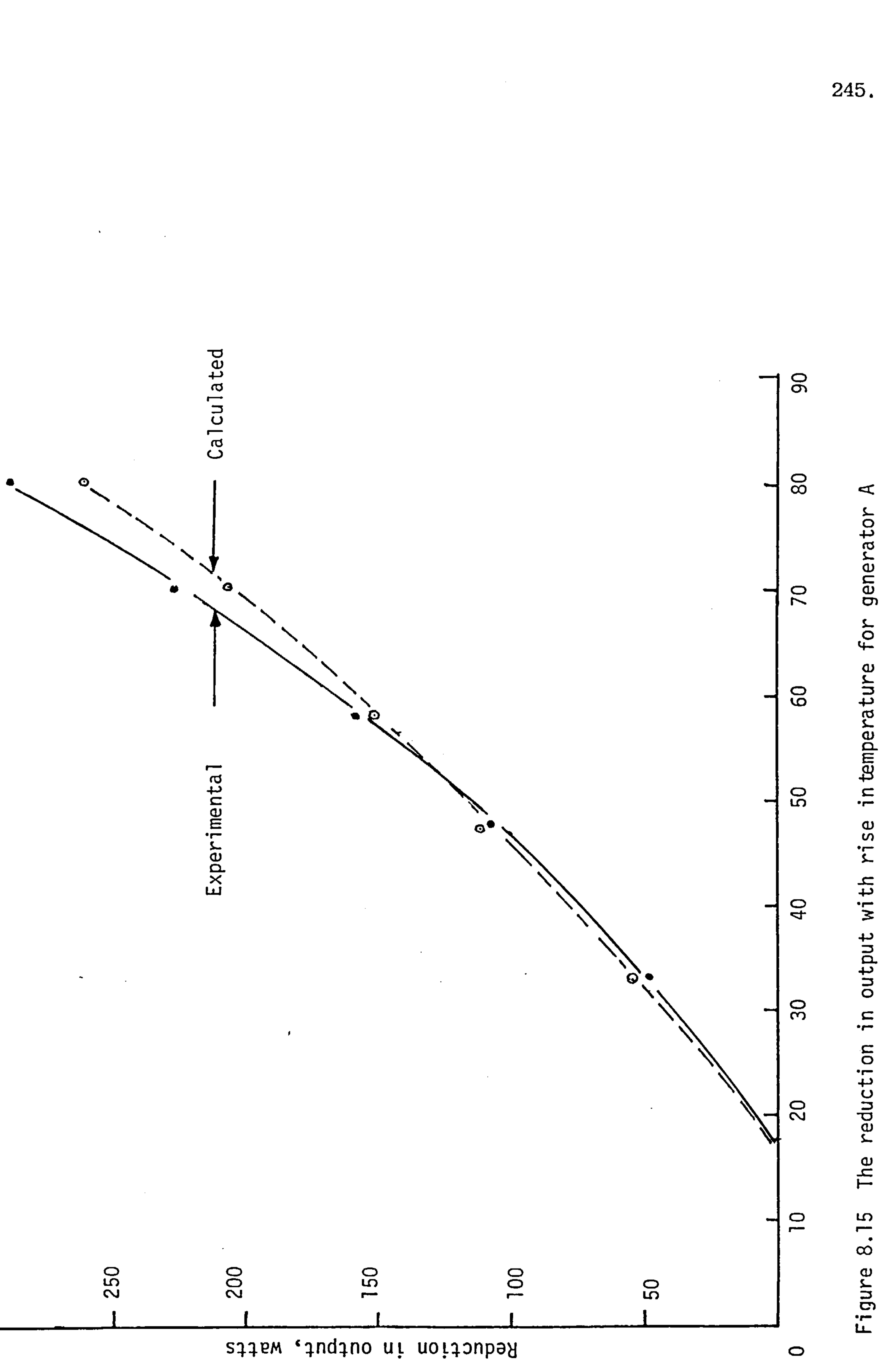
Calculated
Experimental
0
10
20
30
40
50
60
70
80
90
Reduction in output, watts
300
250
200
150
100
50
The reduction in output with rise in temperature for generator A

Figure 8.15 T

Magnet Material	Rotor Length	Length per Unit	Magnet Thickness	Magnet Outer Diameter	Iron Thickness	Max. Power Output P_{max}	P_{max} per unit			o/c Voltage per unit Length
							Rotor Volume	Magnet Volume	Length	
	x 10^{-2} m					kW	x 10^{+6} W/m^3		x 10^{+2} W/m	x 10^{+2} V/m
R1	15.49	5.17	1.78	11.94	1.69	4.73	1.99	8.82	305.09	12.01
R2	14.98	4.99	1.78	11.94	1.61	4.18	1.82	7.80	278.96	11.93
HE	11.43	3.81	1.65	11.94	1.08	2.43	1.39	4.88	212.76	10.71
CE	9.14	3.05	1.40	12.45	0.83	1.33	0.95	2.87	145.18	9.44
AL	15.49	5.17	2.41	11.94	1.37	3.51	1.48	4.83	226.60	9.37
MN	10.67	3.56	1.52	12.45	1.02	1.77	1.08	3.51	165.92	9.86

Rotor Diameter = 1.397×10^{-1} m

Magnet Inner Diameter = 3.810×10^{-2} m

Table 8.1 Output from a 3 unit configuration optimised for output per unit volume

Magnet Material	Rotor Length	Length per Unit	Magnet Thickness	Magnet Outer Diameter	Iron Thickness	Max. Power Output P_{max}	P_{max} per unit			o/c Voltage per unit Length
							Rotor Volume	Magnet Volume	Length	
	x 10^{-2} m					kW	x 10^{+6} W/m^3		x 10^{+2} W/m	x 10^{+2} V/m
R1	20.83	5.17	1.78	11.94	1.69	6.43	2.01	8.99	308.58	12.01
R2	20.32	4.99	1.78	11.94	1.61	5.71	1.83	7.98	280.79	11.93
HE	15.24	3.81	1.65	11.94	1.08	3.28	1.40	4.94	215.26	10.71
CE	12.19	3.05	1.40	12.45	0.83	1.78	0.95	2.89	146.04	9.44
AL	20.83	5.17	2.41	11.94	1.37	4.77	1.49	4.91	228.86	9.37
MN	14.22	3.56	1.52	12.45	1.02	2.39	1.10	3.56	168.03	9.86

Rotor Diameter = 1.397×10^{-1} m

Magnet Inner Diameter = 3.810×10^{-2} m

Table 8.2 Output from a 4 unit configuration optimised for output per unit volume

Stator Frame	Stator Bore Dia.	No. of Slots	Slots per pole per phase	Turns per Coil	Coils per phase	No. of circuits in parallel	Airgap
A	139.7	36	1.5	11	12	1	0.386
X	151.8	36	1.5	10	12	1	0.635
Y	191.2	36	1.5	9	16	2	0.737
Z	242.0	36	1.5	6	16	2	0.900

All units in mm

Table 8.3 The stator characteristics of generators A, X, Y and Z

Rotor	Shaft Dia.	Rotor Dia.	Magnet Inner Dia.	Magnet Outer Dia.	Magnet Thickness	Length per unit	P_{max} per unit length	P_{max} per unit magnet vol.
	(mm)						$\times 10^{-3}$ W/mm	$\times 10^{-3}$ W/mm^3
A	31.7	139.7	54.9	124.5	14.9	31.1	0.983	3.045
X	41.9	151.8	56.9	134.6	15.5	31.5	1.001	3.106
Y	50.8	191.2	60.0	167.6	16.5	38.1	1.060	3.368
Z	76.2	242.0	84.7	215.9	17.8	43.7	0.881	2.876

8 poles, 1500 rpm

Table 8.4 The optimal designs of rotors A, X, Y and Z using ceramic-8 magnets

Material	Abbrev.	$(BH)_{max}$	B at $(BH)_{max}$	H at $(BH)_{max}$
Ceramic-8	CE	27.0	0.189	119
Hera	HE	55.0	0.300	180
MnAlC	MN	47.6	0.40	119
H18-B	R2	143.0	0.42	333

Table 8.5 The $(BH)_{max}$ of some permanent-magnet materials

CHAPTER NINE

AN EXPERIMENTAL INVESTIGATION OF THE BEHAVIOUR OF A POLYMER-BONDED RARE-EARTH MAGNET UNDER EXCITATION IN TWO DIRECTIONS AT RIGHT ANGLES

CHAPTER NINE

AN EXPERIMENTAL INVESTIGATION OF THE BEHAVIOUR OF A POLYMER-BONDED RARE-EARTH MAGNET UNDER EXCITATION IN TWO DIRECTIONS AT RIGHT ANGLES

9.1 INTRODUCTION

In recent years, there has been a significant change in the variety of permanent magnet materials available for industrial use. Some of these magnets are anisotropic and the emergence of rare earth magnet materials with their high stored energy has paved the way for major developments in the application of permanent magnet excitation to electromagnetic devices such as electrical machines. New configurations of machine have emerged[1,2,3,4] and these can involve complex magnetic circuits with flux passing through the magnet not merely in the direction of initial polarisation. Leakage flux in these machines can be important and so an accurate knowledge of the flux distribution within the magnet may be essential for the determination of machine performance.

Some work has already been carried out on the computation of permanent magnet fields using discretisation methods[5-10]. One method involves finite elements and the convergence problem associated with the non-explicit excitation has been overcome by a manipulation of the field equation and a rapidly convergent routine involving under-relaxation[5]. When a two-dimensional model is needed, certain assumptions have been made; a fictitious permeability is used for both directions based on the resultant vector potential gradient or two separate magnetisation equations are used, one relating to the preferred direction of initial polarisation and the other relating to the perpendicular direction where there is zero initial polarisation.

Slomczynska[8] made use of a recoil permeability in the direction perpendicular to the direction of initial polarisation. This method has also been used in a recent paper which makes use of scalar potential and a network model for solution. Reichert[9] discusses a method using vector potential for isotropic media. A model proposed by Zijlstra[10] is based on studies made on a single crystal expressing the magnetic susceptibility in matrix form so that

$$\chi = \begin{vmatrix} \chi_x & 0 \\ 0 & \chi_y \end{vmatrix}$$

where χ_x is the susceptibility parallel to the direction of initial polarisation and χ_y is the susceptibility in a direction perpendicular to the initial polarisation. The non-diagonal elements are assumed zero in an anisotropic material; that is, there is no appreciable mutual interaction between the magnetisation characteristics in the two perpendicular directions.

In reference 3 the authors express the field equation in the form

$$B = \mu' H + M_o$$

where $\mu' = \mu_o (1+\chi)$ and is called the apparent permeability. Where magnetisation in two directions at right angles is involved the relationships become

$$B_p = \mu'_p H_p + M_{op}$$

and

$$B_q = \mu'_q H_q + M_{oq}$$

μ'_p is found from the declared demagnetisation curve in the preferred direction of magnetisation and $M_{op} = B_R$. M_{oq} is zero if there is no initial polarisation in the non-preferred direction. It was felt that there was some uncertainty in the values of μ' in the presence of a significant applied field in the non-preferred direction.

9.2 THE EXPERIMENT

9.2.1 The Experimental Specimen

The shape of the specimen used in the investigation was that of a circular cylinder. This shape was chosen in order to achieve a uniformity of magnetisation in a direction perpendicular to the axis. It is impractical to build and magnetise a specimen of a spherical or toroidal shape. The experimental specimen was built by stacking seven slabs of magnet each 10mm in thickness and 70mm in diameter. The complete specimen is thus 70mm long and 70mm in diameter and is defined as in Figure 9.1 (unless stated otherwise).

The material used was a polymer-bonded rare-earth composite containing samarius cobalt ($Sm\ CO_5$). It is well known that materials of this family of hard materials exhibit anisotropy. The specimen used in the investigation had a straight line demagnetisation curve in the direction parallel to the cylindrical axis and this is shown in Figure 9.2. The typical value of remanence for this material is 0.55 T and the coercivity is 400 KA/m. The magnetisation characteristic in the non-preferred direction (perpendicular to the axis) is, of course, quite different. It has a recoil permeability of 1.1 and a maximum energy product of 55 kJ/m^3.

9.2.2 The Equipment for the Generation of Crossfields

To impose the external crossfields on the cylindrical specimen, a specially designed electromagnet was used. This equipment, shown in Figure 9.3, was designed to give a uniform field between the poles. The test specimen was placed centrally in the central cavity to achieve symmetry in the system. This enables the specimen to be put under the influence of an applied uniform field when the field coils on the top and bottom of the electromagnet assembly are energised. The magnetisation

characteristic under the imposed vertical field is shown in Figure 9.4.

9.2.3 Experimental Procedure and Results

The two basic quantities which were studied are the radial flux density, B_R, and the axial flux density, B_A. These quantities were investigated with the magnet under the influence of applied fields, first perpendicular and then parallel to its direction of initial polarisation.

9.2.4 The Effects of External Fields Perpendicular to its Initial Polarisation

The permanent magnet was subjected to external fields perpendicular to its initial polarisation using the electromagnet assembly. The magnet was held in a paxolyene cylinder and placed in the specially designed electromagnet assembly and a field strength of up to 180 KA/m was achieved. To monitor the influence of these fields on the flux distribution in the permanent magnet, measurements of field quantities were taken at regular intervals from 0 KA/m to 180 KA/m. The measurements taken were:

(a) The radial flux density, B_R, was measured on the surface of the magnet along aa', bb', cc', ..., and mm' at intervals of 10mm, from end to end (See Figure 9.1). B_R was measured with a Hall effect probe and a gaussmeter. This measurement was facilitated by grooves in the paxolyene cylinder holding the magnet allowing the probe to slide in and out.

(b) Measurements were taken of, ΔB_E, the change in the flux density levels at the ends of the cylinder. These changes of axial flux densities at the ends were obtained with search coils placed at the ends of the magnet parallel to the end faces. The changes in flux induce an emf in the coils and this is integrated to give the change in the flux density level.

(c) Another quantity measured was the change in axial flux inside the permanent magnet specimen, $\Delta\phi_A$. This would yield information about the change in axial flux density, ΔB_A. For this measurement, search coils were again used. These coils had to be inserted into the magnet and this was done by cutting the magnet into two at a point 20mm from the front end, with slits of 3 mm deep and 0.5mm in width being cut into the face of the larger piece. The coils were then dropped into these grooves (see Figure 9.5a). The coils are labelled SC_{III}, SC_{IV}, SC_V and SC_{VI}. The change in flux associated with each coil was measured with a galvonometer at carious distances from the centre along Ao, Bo, Co, etc. (see Figure 9.5b). These readings were taken with the magnet under different transverse field strengths.

The field distribution along the surface of the magnet obtained from the measurements taken when no external field was imposed, is shown in Figure 9.6. Figure 9.6 shows the radial flux density and indicates the amount of leakage through the sides of the magnet. Using this graph and invoking the condition of continuity in flux, the axial flux densities B_A, over various planes along its length, were calculated. For example, the axial flux density, B_A, for the plane through point 'x' in Figure 9.7, is obtained from all the flux passing through that plane, which is the sum of the flux emerging from the end and the leakage from the sides, divided by the cross-sectional area. The total flux passing through a plane at point x is given by

$$\phi_A = B_E (\pi r^2) + \int_0^x B_R (2\pi r) \, d\ell$$

Therefore, the axial flux density, B_A, for that plane is given by

$$B_A = B_E + 2\pi r \int_0^x \frac{B_R}{\pi r^2} \, d\ell$$

Figure 9.8 shows the distribution of B_{A_i}, the axial flux density levels in the permanent magnet specimen when no external field was applied. The information on the effects of the crossfields applied perpendicularly to its initial polarisation were extracted by processing the experimental results. By simple mathematical operations, the following quantities were obtained:

(a) ΔB_R, the difference between B_R measured at points along the lines aa', bb', etc. when the magnet was under the influence of the external field.

(b) $\int_0^{2\pi r} \Delta B_R \, d\ell$: the integration of B_R round the circumference.

(c) $\Delta\phi_{SN(\text{for SN-1 to 7})}$ for each slab. This can be obtained by averaging the $\int_0^{2\pi r} \Delta B_R \, d\ell$ on the boundaries of each slab and multiplying it by the thickness of the slabs.

(d) The change in axial flux density, ΔB_A, which is given by $\frac{\Delta\phi_{SN}}{\pi r^2}$. This value is the change in axial flux density level of each slab. (The ΔB_E which is the) ΔB_A at the two ends of the permanent magnet specimen ΔB_E was measured. These two values are assumed to be correct since they were measured directly.

Therefore, the sum of ΔB_E at each end equals $\sum_1^7 \Delta B_A$ + Error. This gives a corrected value for ΔB_A for each slab, which is $\Delta B_A + \frac{\text{Error}}{7}$.

(e) $\sum\Delta B_A$, the summation of the change in axial flux density level of each slab. As flux is continuous, the summation gives the contribution to the change in axial flux density of each slab and gives $\sum\Delta B_{A_{BN(\text{for BN = 0-7})}}$, the total change in flux density level in planes which form the boundaries of the seven slabs. The average of $\sum\Delta B_{A_{BN}}$ of the two boundaries of a slab gives the total change in flux passing through that slab and thus the change in flux density level, $\sum\Delta B_{A_{SN(N = 1-7)}}$.

The effect of the transverse external crossfield on the axial field of the permanent magnet specimen can be shown by plotting the ratio $\frac{\sum\Delta B_{A_{SN}}}{B_{EX}}$ against B_{A_i} (the axial flux density level) in that slab. This is shown in Figure 9.9.

To verify the results obtained from surface measurements of the field quantities, search coils were placed inside the magnet. The search coils inside the magnet give a direct measurement of the change in axial flux density level in that plane. The symmetry in the transverse plane allows readings along the line, A and I, B and H, etc. to be averaged to reduce error (see Figure 9.5b). Figure 9.10 shows the variation of B_A, in the plane where the search coils are placed, for various angular displacements (e.g. $\frac{A+I}{2} = 90^o$, $\frac{E+E}{2} = 0^o$) against distance from centre. The mean error for the ΔB_A in this plane between the values measured by the search coils and that derived from surface measurements is 8 per cent.

9.2.5 The Effect of an External Field Parallel to its Direction of Initial Polarisation

The same electromagnet assembly was used to impose a field parallel to the magnet's direction of initial polarisation. The magnet was held

in a box and placed in the cavity as shown in Figure 9.11. The top and bottom coils were energised with a pulse from a magnetic charger. A coil on the side was used as a search coil. As the number of turns in the coil is large (184 turns), it is sufficiently sensitive to give an accurate reading. Measurements were taken, with the aid of a storage oscilloscope, for applied fields at regular intervals between 0 KA/m to 180 KA/m. The results obtained show that the change in field intensity in the axial direction has negligible effect on the field of the transverse direction.

9.3 ANALYSIS AND DISCUSSION OF RESULTS

The demagnetisation characteristics of permanent magnet materials can be classified into two groups. The first are those whose demagnetisation characteristics are linear over the second quadrant of the B-H plane. Such a characteristic is typified by polymer-bonded rare-earth materials, rare-earth magnets, and by the normal working range of ferrites. The other group has a non-linear mode of operation over the second quadrant of the B-H plane and is possessed by metallic AlNiCo magnets. The polymer-bonded rare-earth magnet used for this investigation has a straight line demagnetisation curve shown in Figure 9.2. This demagnetisation characteristic applies strictly to the field of the magnet in the direction of initial polarisation. The relationship in this direction can be represented by

$$B = \mu_{rec}\, \mu_o\, H + M$$

where $M = B_r$, and μ_{rec}, μ_o are constants. B_r for the permanent magnet material used is 0.55 T and μ_{rec} is 1.1. Therefore, the magnet characteristic in the axial direction is

$$B_A = 1.1\, \mu_o\, H_A + 0.55 \qquad (9.1)$$

Results from the experiments performed show that this axial field is significantly affected by an external crossfield perpendicular to it. The effect of this transverse field is described by the graph in Figure 9.9. It is a plot of the ratio $\frac{\sum \Delta B_{A_{SN}}}{B_{EX}}$ against B_{A_i}. This graph relates the change in the axial flux density with the imposed field and the flux level in the magnet itself. Due to the symmetry of the magnet and the uniformity of the crossfield, the change over half the length of the magnet would be identical with the other half. The relationship between $\frac{\sum \Delta B_{A_{SN}}}{B_{EX}}$ can be approximated by a linear equation. The result is the equation:

$$\sum \Delta B_{A_{SN}} = \left(4.2|1-2.04 \left(\frac{B_{A_i}}{B_R} - 0.51 \right)|10^{-2} \right) B_{EX} \qquad (9.2)$$

The relationship between B_{EX} and H_{EX} is simply the magnetisation characteristics of the electromagnet used to provide the field described in Figure 9.4. This graph can be represented by the equation:

$$B_{EX} = \mu_o H_{EX} \qquad (9.3)$$

where $H_{EX} = NI/\ell$

where ℓ = the airgap between the poles.

Substituting for B_{EX} in equation 9.2 gives

$$\sum \Delta B_{A_{SN}} = (0.09 - 0.09 \frac{B_{A_i}}{B_r}) \mu_o H_{EX} \qquad (9.4)$$

The behaviour of the cylindrical specimen of magnet in the axial direction under the influence of an external field perpendicular to it is therefore the summation of equations 9.1 and 9.4. The former is the contribution from its polarisation and the latter due to the interaction of the external transverse field.

Thus,

$$B_A = 1.1\ \mu_o H_A + 0.55 + \left|\left(0.09 - 0.09 \frac{B_{A_i}}{B_r}\right) \mu_o H_{EX}\right| \qquad (9.5)$$

The characteristic of the magnet in the transverse direction, which is its non-preferred dirction of magnetisation, can be extracted from the experimental data. The values of B_R measured without an imposed field along aa' (see Figure 9.1) are subtracted from the values of B_R obtained under the different applied fields. This gives the magnetisation characteristic of the electromagnet, with the magnet in the cavity instead of air, at various points along aa'. The average is represented by the curve in Figure 9.12. This is the characteristic of the magnet in the transverse direction. It is linear and can be represented to a good approximation by the linear equation

$$B_T = 1.22\ \mu_o H_T \qquad (9.6)$$

As discussed earlier (section 9.2.5), the experiments with applied fields in the axial direction (parallel to its direction of magnetisation) show that their interaction with the field of the magnet in the transverse direction to be negligible. The characteristic of the magnet in the transverse direction in the presence of external crossfields is therefore similar to equation 9.6.

Equations 9.5 and 9.6 are in polar coordinates. They are equally applicable in Cartesian coordinates where the axial direction is the x-axis and the transverse direction is the y-axis. Equations 9.5 and 9.6 can thus be rewritten as:

$$B_x = 1.1\ \mu_o H_x + 0.55 + \left|\left(0.09 - 0.09 \frac{B_{x_i}}{B_r}\right) \mu_o H_y\right| \qquad (9.7)$$

$$B_y = 1.22\ \mu_o H_y \qquad (9.8)$$

These two equations describe the behaviour of the polymer-bonded rare-earth magnet under external crossfields in two directions at right

angles. A two-dimensional model can be formulated in the form of a matrix, with x the preferred axis of magnetisation.

$$\begin{vmatrix} B_x \\ B_y \end{vmatrix} = \begin{vmatrix} 1.1\ \mu_o & (0.09 - 0.09 \frac{B_{X_i}}{B_r})\ \mu_o \\ 0 & 1.22\ \mu_o \end{vmatrix} \begin{vmatrix} H_x \\ H_y \end{vmatrix} + \begin{vmatrix} 0.55 \\ 0 \end{vmatrix}$$

This model takes into account the interactions of external crossfields which is significant for a transverse crossfield. This effect is dependent on the strength of the imposed field as well as the flux level in the magnet. The change in axial flux density level varies proportionally with the strength of the applied field and inversely with the flux level in the magnet. In both cases, the changes are limited by the saturation of the magnet.

The increase in flux level in the direction of initial polarisation, when a field is applied perpendicularly to it, is due to the highly anisotropic nature of the polymer-bonded rare-earth magnet. It uses the applied field to align the remaining domains in the presferred direction, thus enhancing the field strength in that direction.

A field applied parallel to its polarisation has negligible effect on the transverse field. This is also due to the high anisotropy field possessed by this type of magnet.

9.4 THE USE OF THE PERMEABILITY TENSOR FOR THE REPRESENTATION OF THE PERMANENT MAGNET IN FIELD COMPUTATION

The permeability tensor has been incorporated into a two-dimentional finite-element field analysis program. This program makes use of certain basic assumptions to simplify the solution procedure. These assumptions are:

i. The B-H curve of the iron circuit is assumed to be single-valued This is a reasonable assumption for quasi-static fields.

ii. The demagnetisation curve is that of a stabilised magnet, that is the recoil loop is single-valued. This assumption holds for polymer-bonded rare-earth magnets as they have a linear demagnetisation curve.

iii. The field outside the region of interest is insignificant.

iv. A two-dimensional cross-section may be taken, on the assumption that the field variation in one direction is negligible.

As the permeability of the permanent magnet is to be represented by a matrix, the field equations and the functional to be minimised are modified accordingly (see Appendix V).

The program with the new method of magnet representation is used for the solution of the simple problem described in Figure 9.13. It consists of an electromagnet with an airgap at the centre of which a cylindrical permanent magnet is placed. The polarisation of the permanent magnet is placed perpendicular to the field of the electromagnet. The geometry of the iron circuit is designed to work the iron below its saturation point. This geometry is represented by discretisation into 1148 elements. The field imposed on the permanent magnet is obtained using discrete currents in current nodes shown in Figure 9.13. The effect on the axial field of the permanent magnet is monitored for imposed fields of 0.15 T, 0.3 T and 0.45 T. These results are shown in Figure 9.14. They are compared with the results for axial flux density when no external crossfield is applied. This curve is shown by the dotted line in Figure 9.14. If no interaction between the external crossfield and the field in the preferred direction of magnetisation is assumed, the curve would remain unchanged when subjected to externally applied fields perpendicular to its direction of magnetisation. The effects of the interaction term on the field of the permanent magnet

when it is subjected to an external cross-field is, therefore, demonstrated in Figure 9.14.

9.5 CONCLUSION

Experiments have been performed to determine the behaviour of an anisotropic, polymer-bonded rare-earth magnet in the presence of external crossfields. Results were obtained with crossfields applied perpendicular and parallel to its direction of polarisation and their effects on the fields of the magnet in the preferred and non-preferred direction of magnetisation have been analysed. The effect of a cross-field perpendicular to the polarisation of the magnet is significant whilst a field parallel to it has negligible effect on the field in the non-preferred direction. From the experimental data equations for the magnets under the influence of external fields were obtained. A model of the behaviour of the magnetisation in two dimensions is presented as a matrix. A general matrix proposed for the representation of anisotropic permanent magnets would be of the form

$$\begin{vmatrix} B_x \\ B_y \end{vmatrix} = \begin{vmatrix} \mu_x & (K_1 + K_2 \frac{B_{X_i}}{B_r}) \\ 0 & \mu_y \end{vmatrix} \begin{vmatrix} H_x \\ H_y \end{vmatrix} + \begin{vmatrix} M_x \\ 0 \end{vmatrix}$$

In the case of polymer-bonded rare-earth magnets, experiment has indicated values of K_1 and K_2 of 0.09 μ_o and -0.09 μ_o respectively.

9.6 REFERENCES

1. BINNS, K. J. and KURDALI, A. : 'Permanent magnet a.c. generator', Proc. IEE, Vol. 126, No. 7, p. 690, July 1979.

2. BINNS, K. J. : 'High output stabilised permanent magnet machine', British Patent 1437348, November 1976.

3. BINNS, K. J., BARNARD, W. R. and JABBAR, M. A. : 'Hybrid permanent magnet synchronous motors', Proc. IEE, Vol. 125, No. 3, pp. 203-208, March 1978.

4. BINNS, K. J. and JABBAR, M. A. ; 'High-field self-starting permanent-magnet synchronous motor', Proc. IEE, Vol. 128, Pt. B, No. 3, May 1981.

5. BINNS, K. J., JABBAR, M. A. and BARNARD, W. R. : 'Computation of the magnetic field of permanent magnets in iron cores', Proc. IEE, 1975, 122(12), pp. 1377-1381.

6. HARROLD, W. J. : 'Calcualtion of equipotentials and flux lines in axially symmetrical permanent magnet assemblies by computer', IEEE Trans, Vol. Mag. 8, p. 23, 1972.

7. KAMMINGA, W. : 'Finite element solutions for devices with permanent magnets', J. Physics, D, Appl. Phys., Vol. 8, 1975, p. 841.

8. SLOMCZYNSKA, J. : 'Non-linear analysis of the magnetic flux distribution in the magnetised magnet stabilised in air', IEEE Trans, Vol. Mag. 10, No. 4, 1974, p. 113.

9. REICHERT, K. : 'The calculation of magnetic circuits with permanent magnet by digital computers', IEEE Trans, Vol. Mag. 6, 1970, p. 283.

10. ZIJLSTRA, H. : 'Permanent magnets in magnetic field calculations', Proc. Compumag, 76, pp. 164.

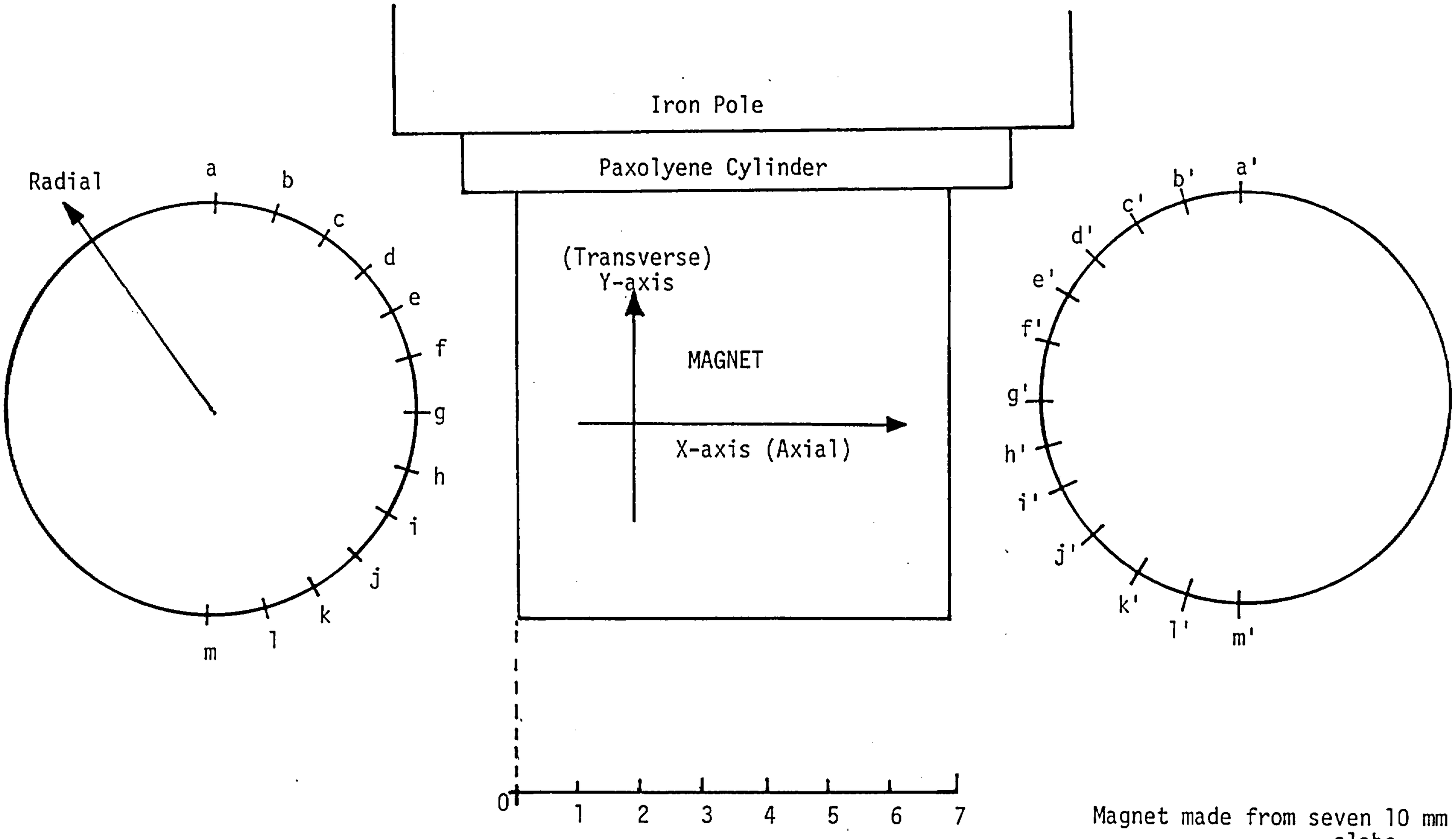

Magnet made from seven 10 mm slabs.

Figure 9.1 Labelling of the magnet

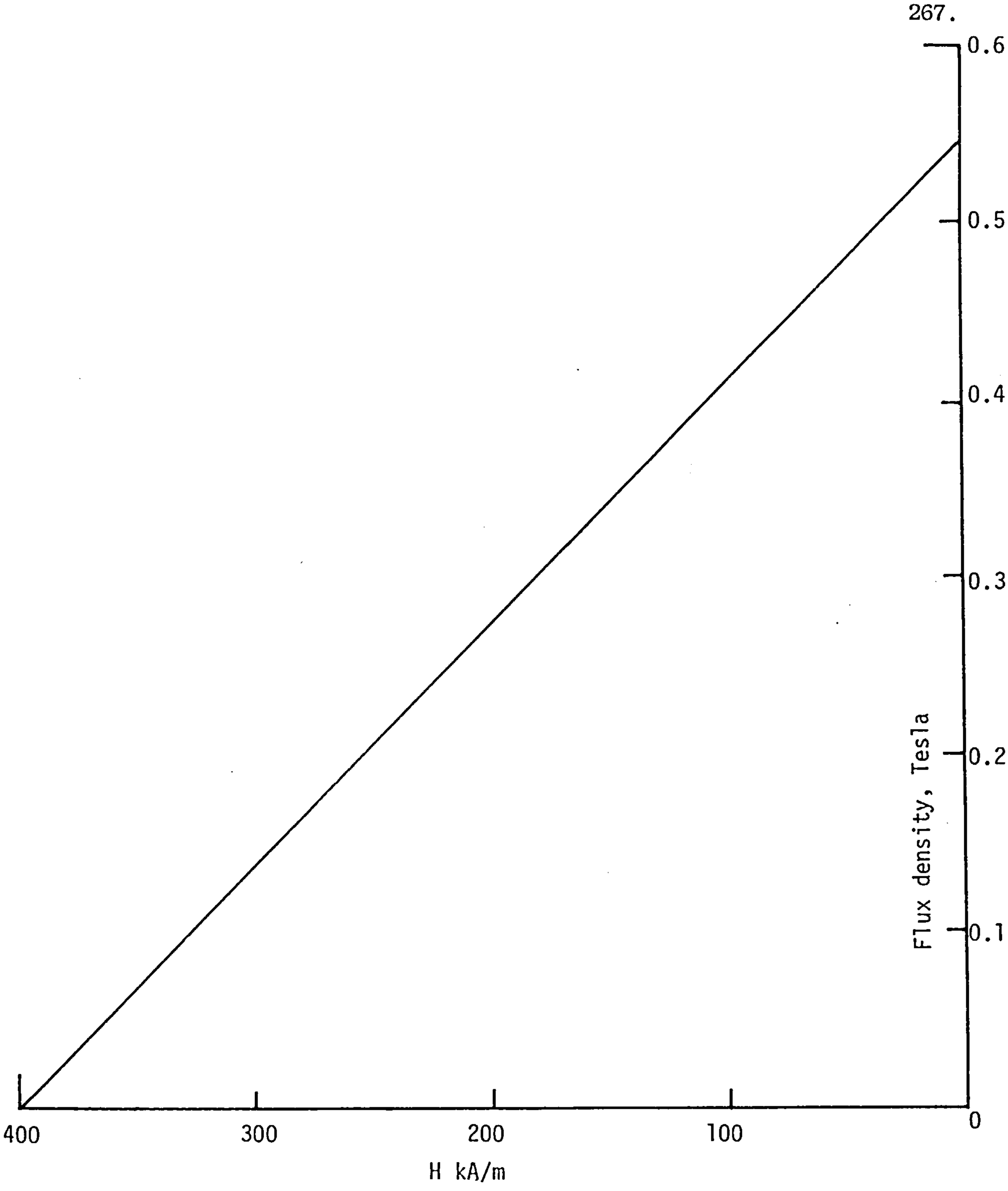

Figure 9.2 The demagnetisation characteristic of the polymer-bonded rare-earth magnet used in the investigation.

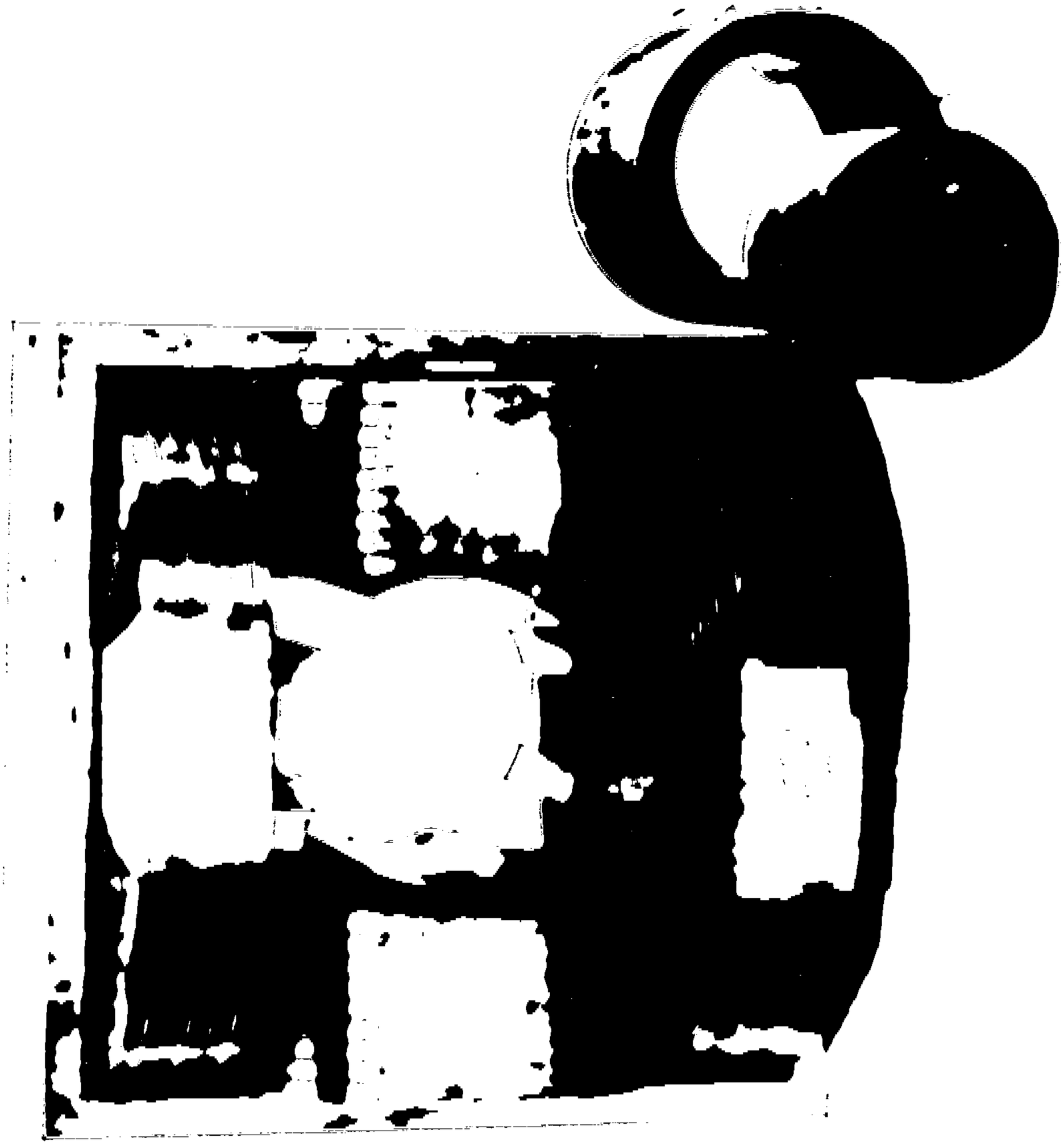

Fig.9.3 The Electromagnet Assembly Used In The Experiment.

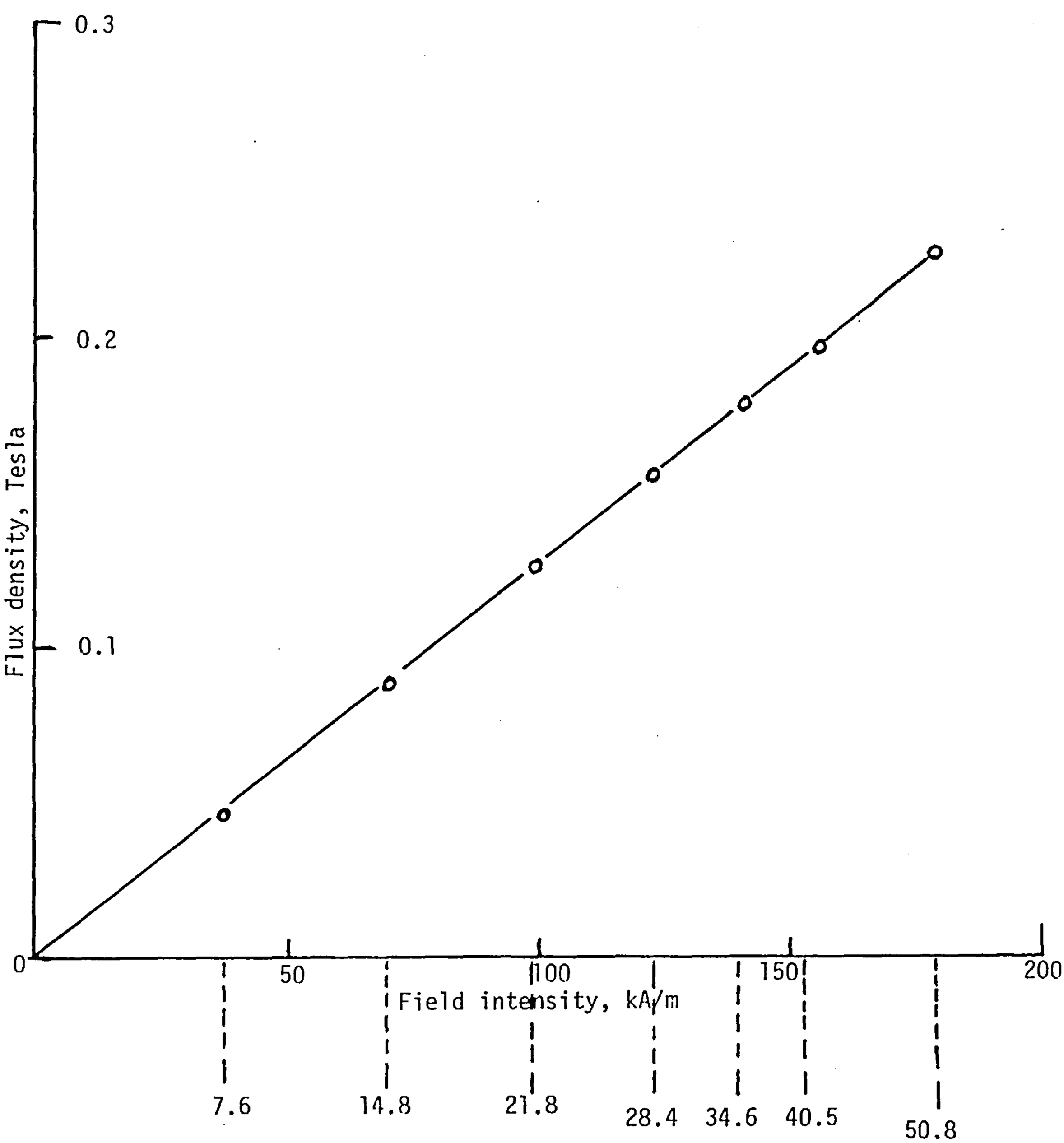

Figure 9.4 The magnetisation characteristic of the electromagnet used for applying the crossfields.

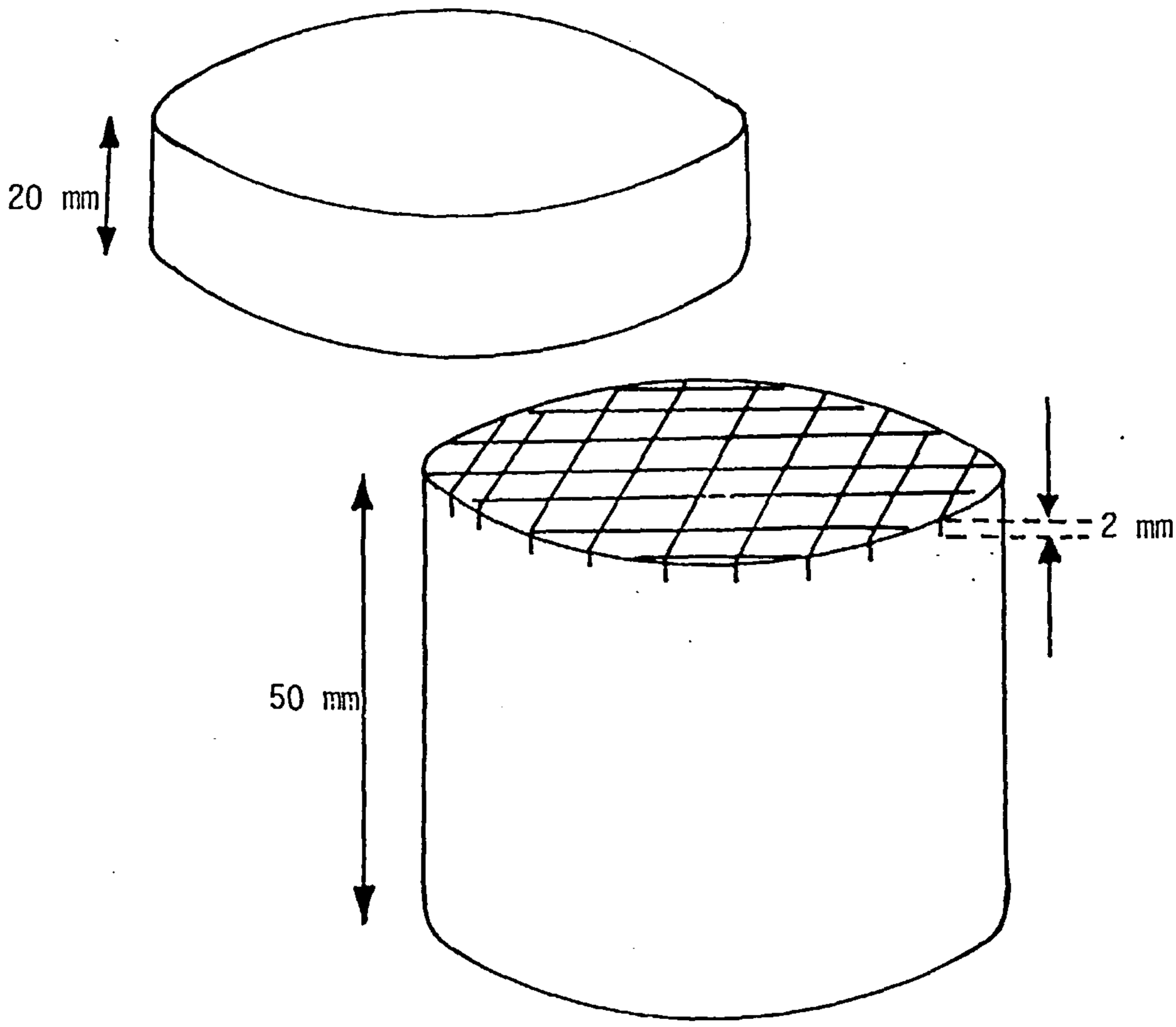

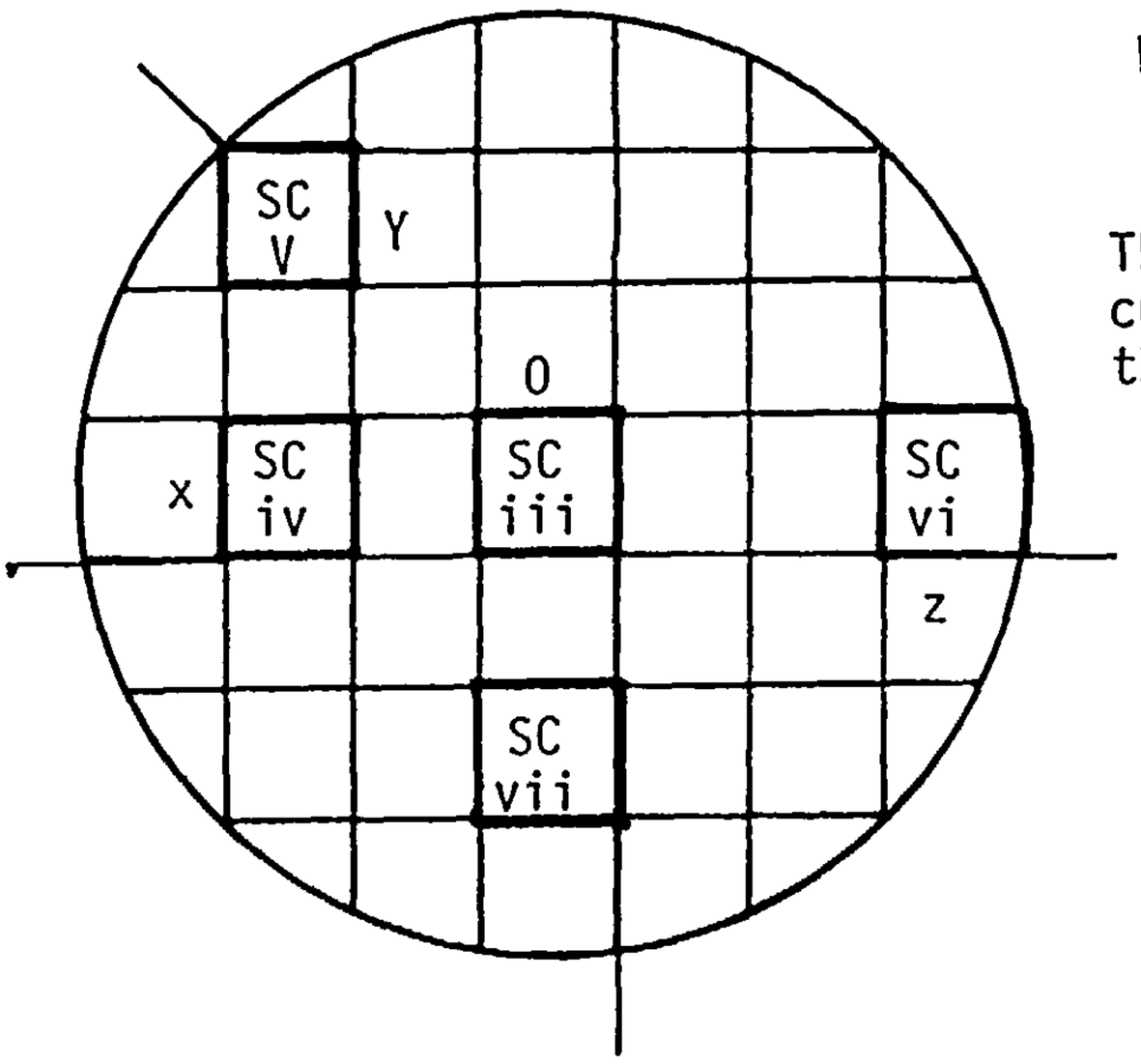

Width of grooves is 0.5 mm

The pattern of grooves cut into the face of the magnet.

Figure 9.5a Position of search coils inside the magnet.

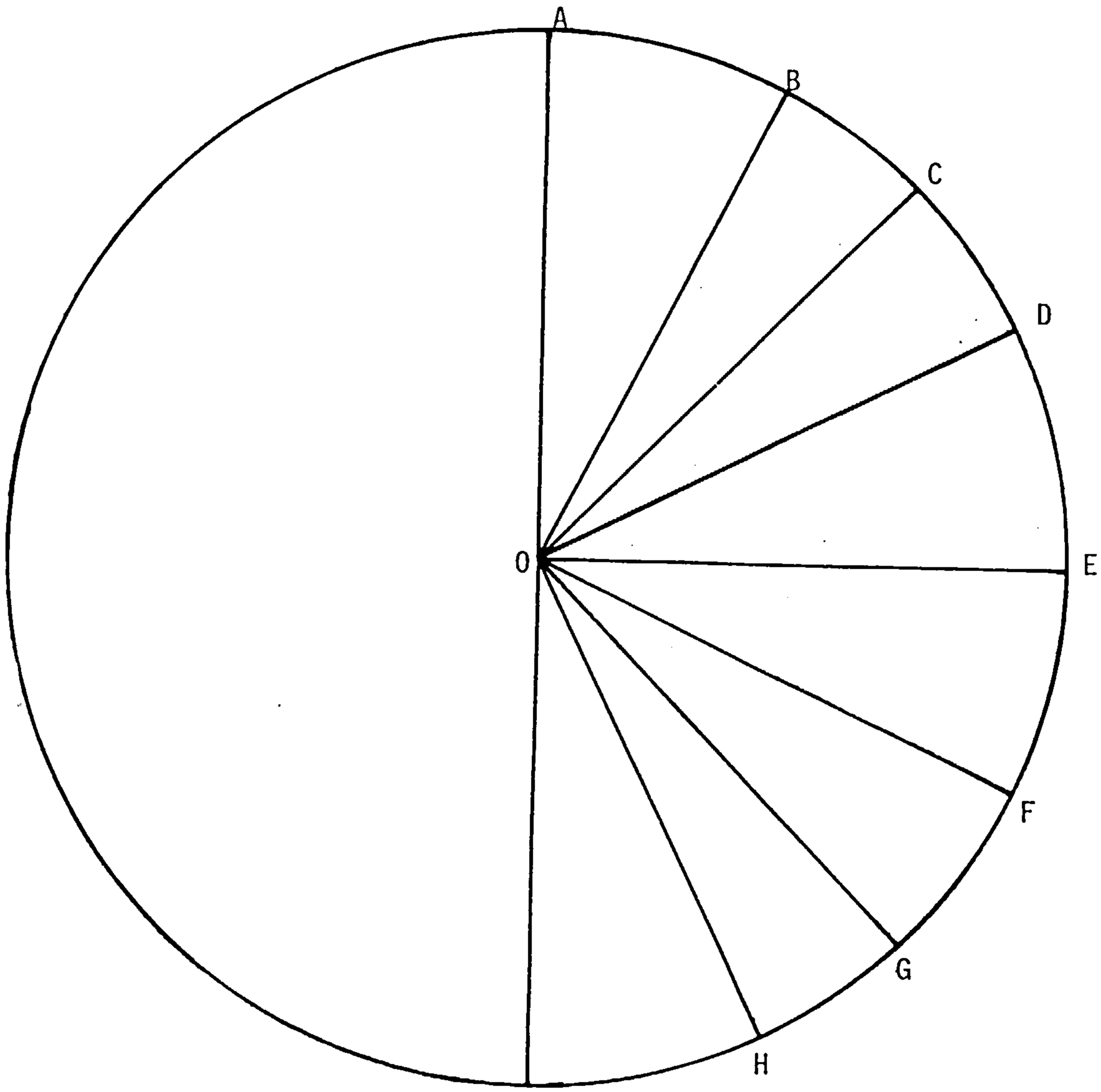

Figure 9.5b The radial lines along which changes in axial flux were monitored by the search coils.

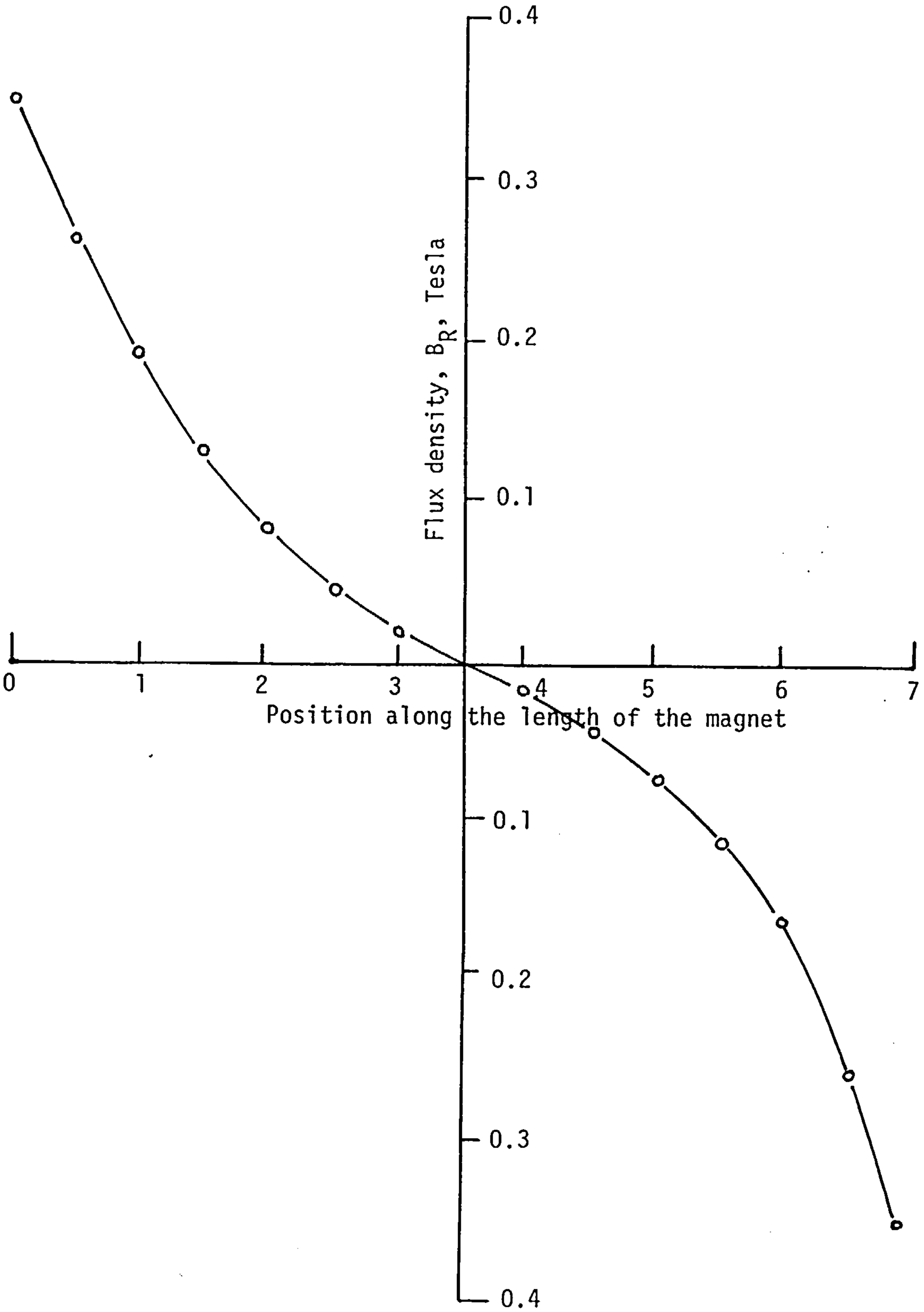

Figure 9.6 Variation of the radial flux density in the axial direction.

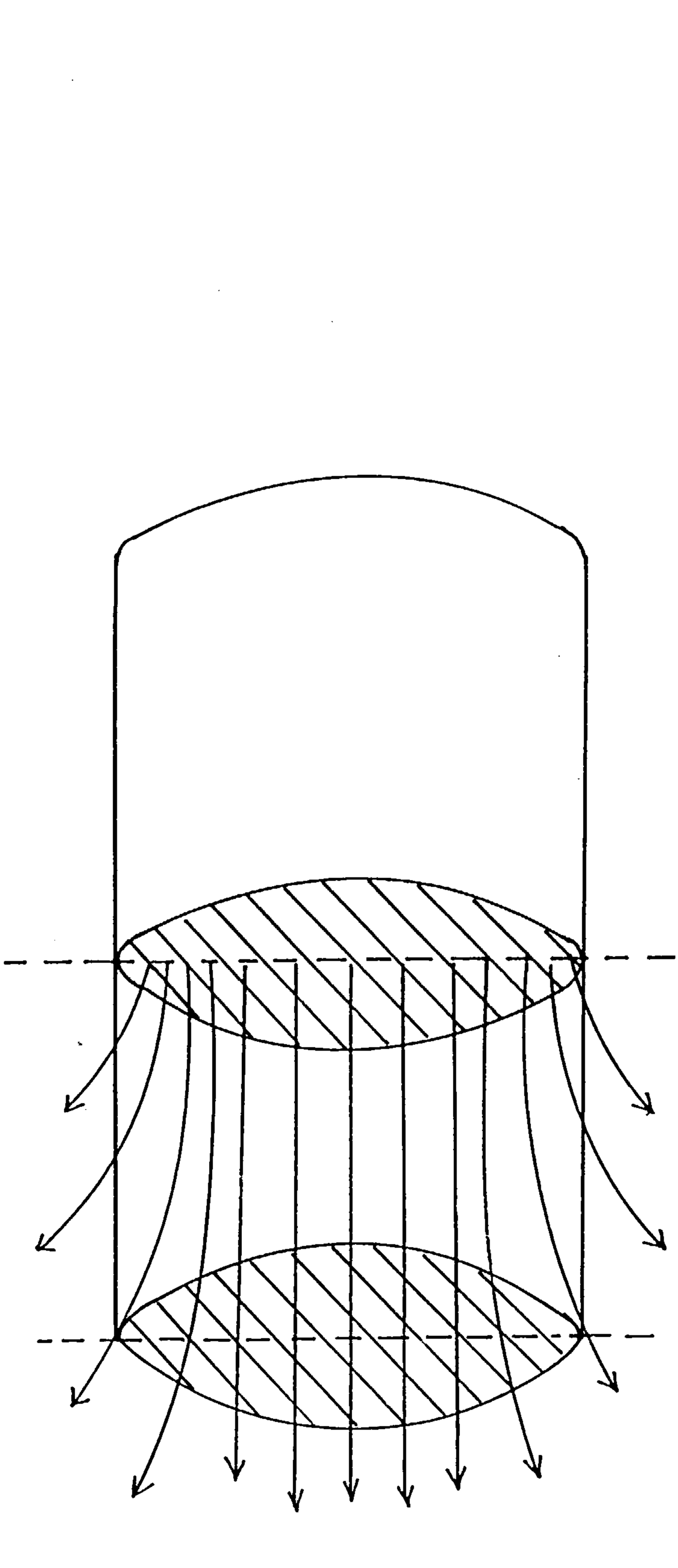

Figure 9.7 The model used for the calculation of axial flux density in the magnet.

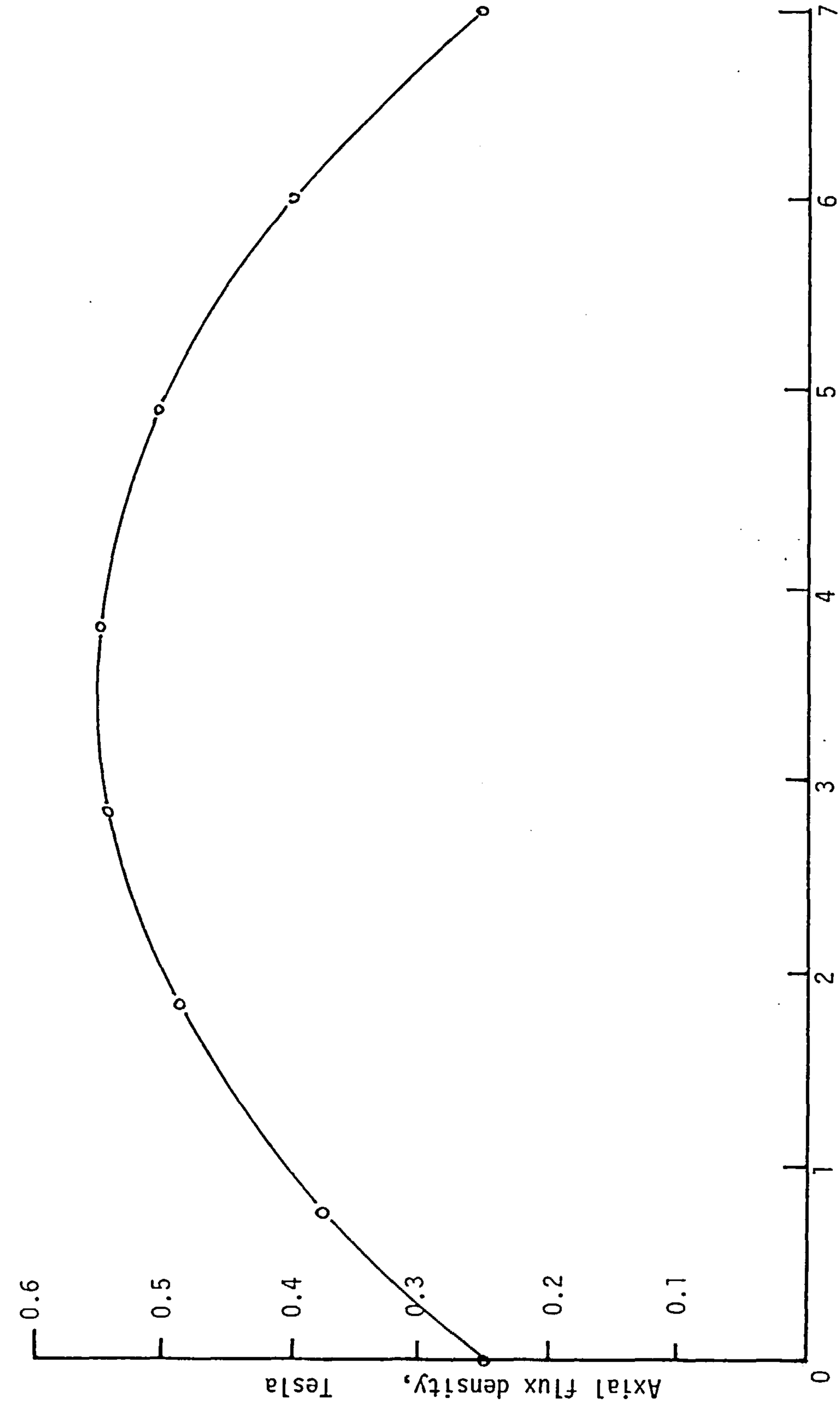

Figure 9.8 The axial flux density distribution in the magnet

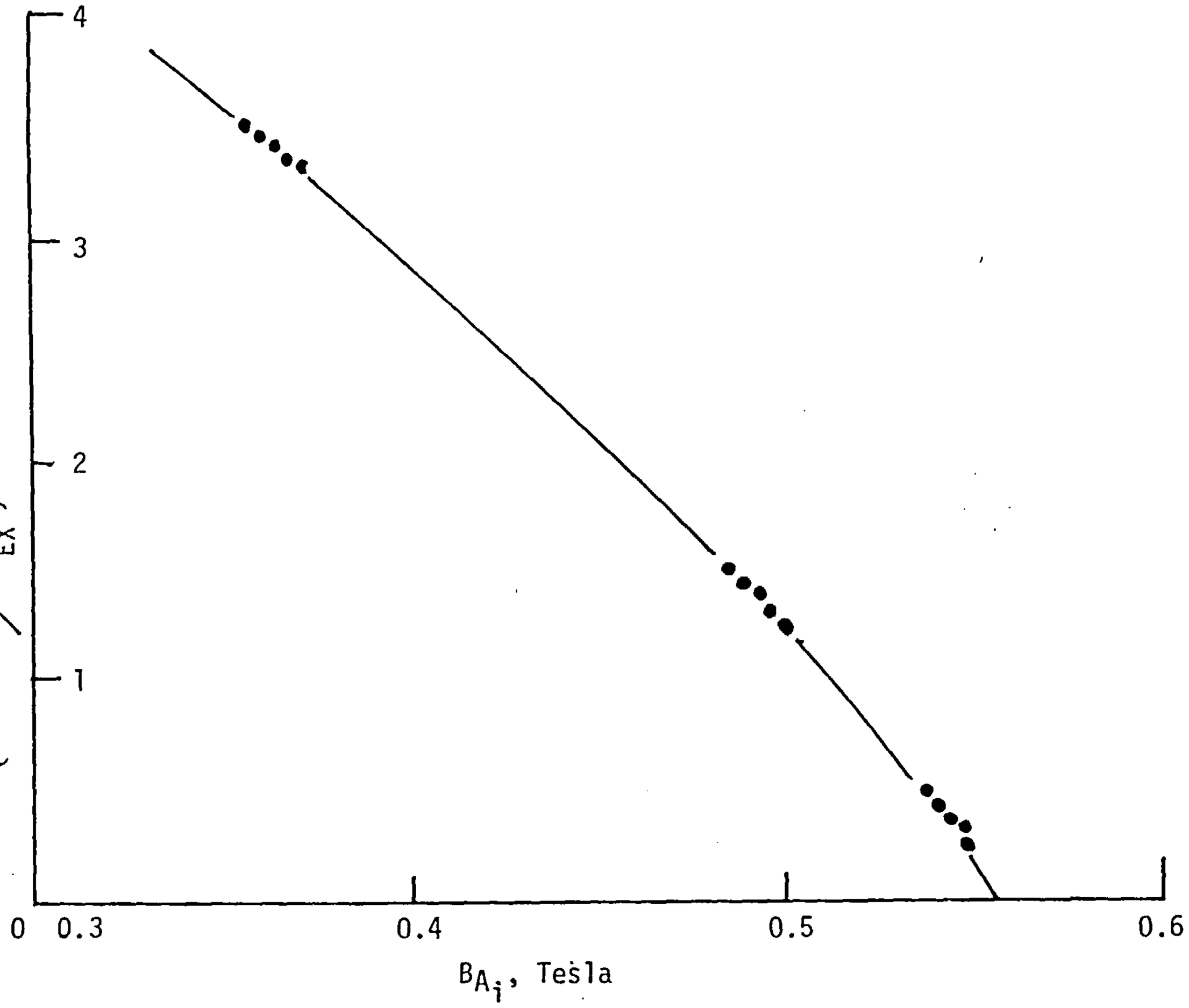

Figure 9.9 The relationship of the interaction of an external applied field with the flux level in the magnet due to its own polarisation.

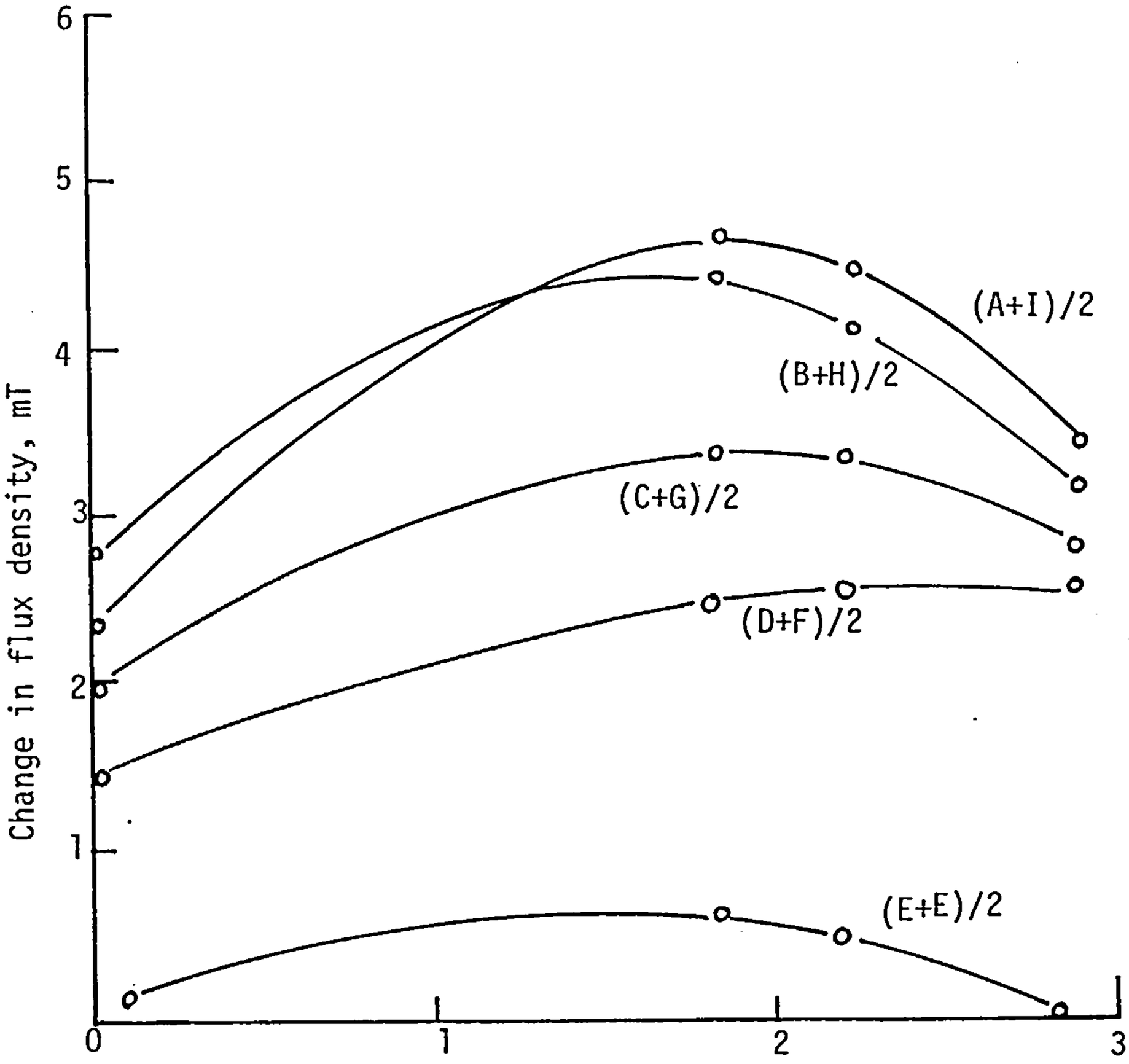

Figure 9.10 The variation of the change in flux density due to an imposed field of 180 kA/m, across the face of the plane 20 mm from the front end.

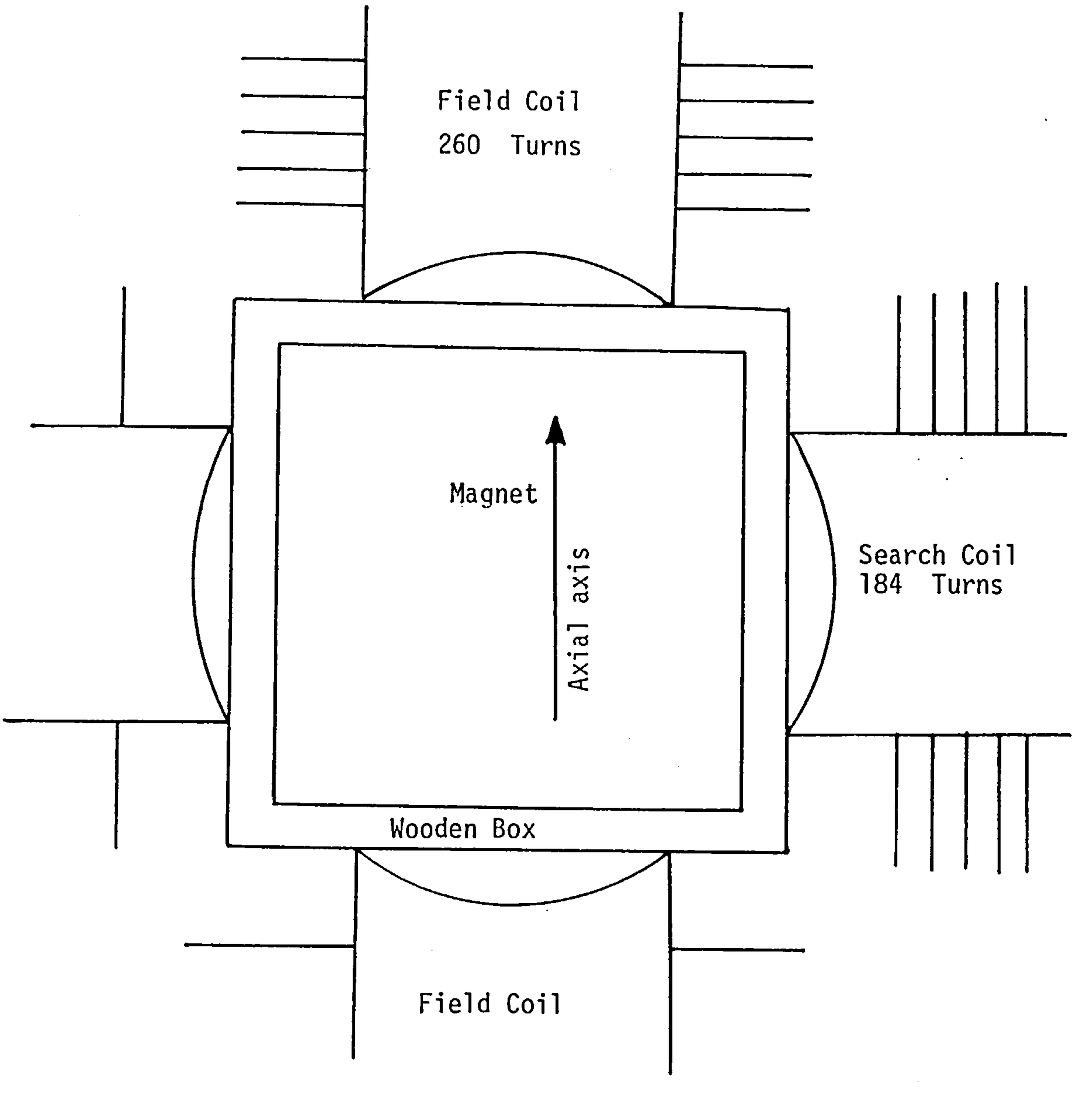

Figure 9.11 Position of the magnet in the electromagnet assembly in the experiment with the external field parallel to its preferred direction of magnetisation.

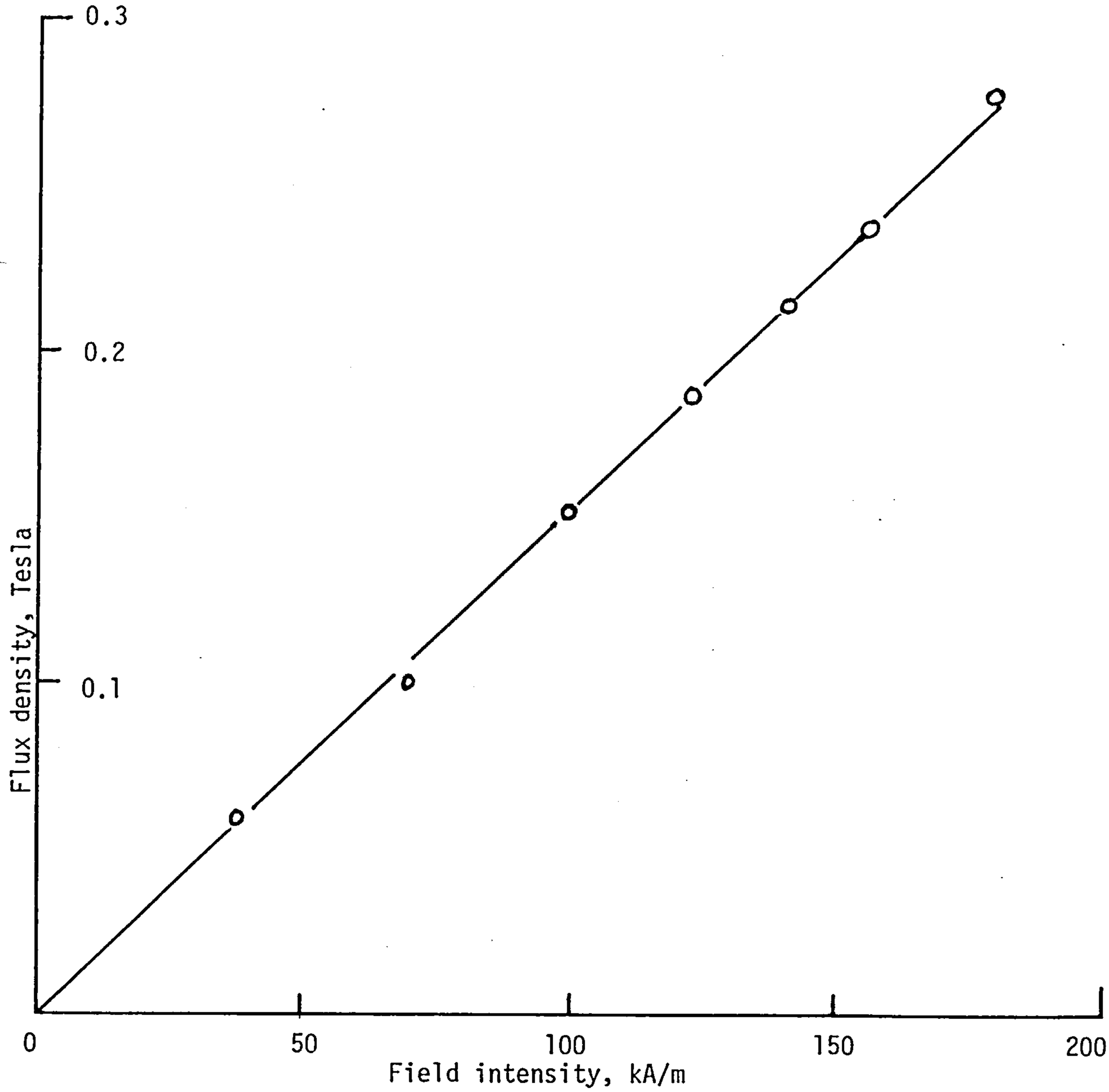

Figure 9.12 The magnetisation characteristics of the magnet specimen in the transverse direction.

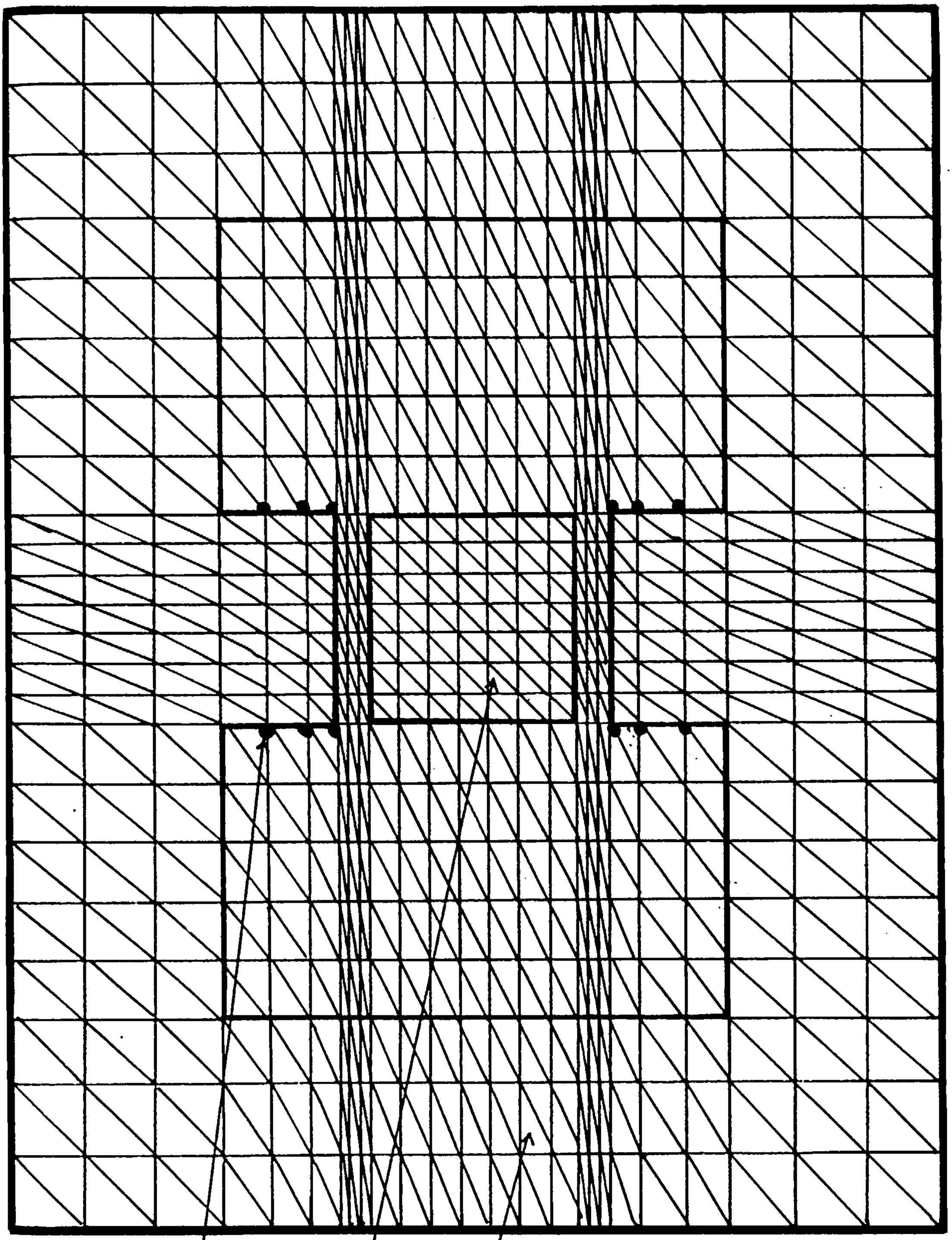

Figure 9.13 The discretisation of the model used for computation.

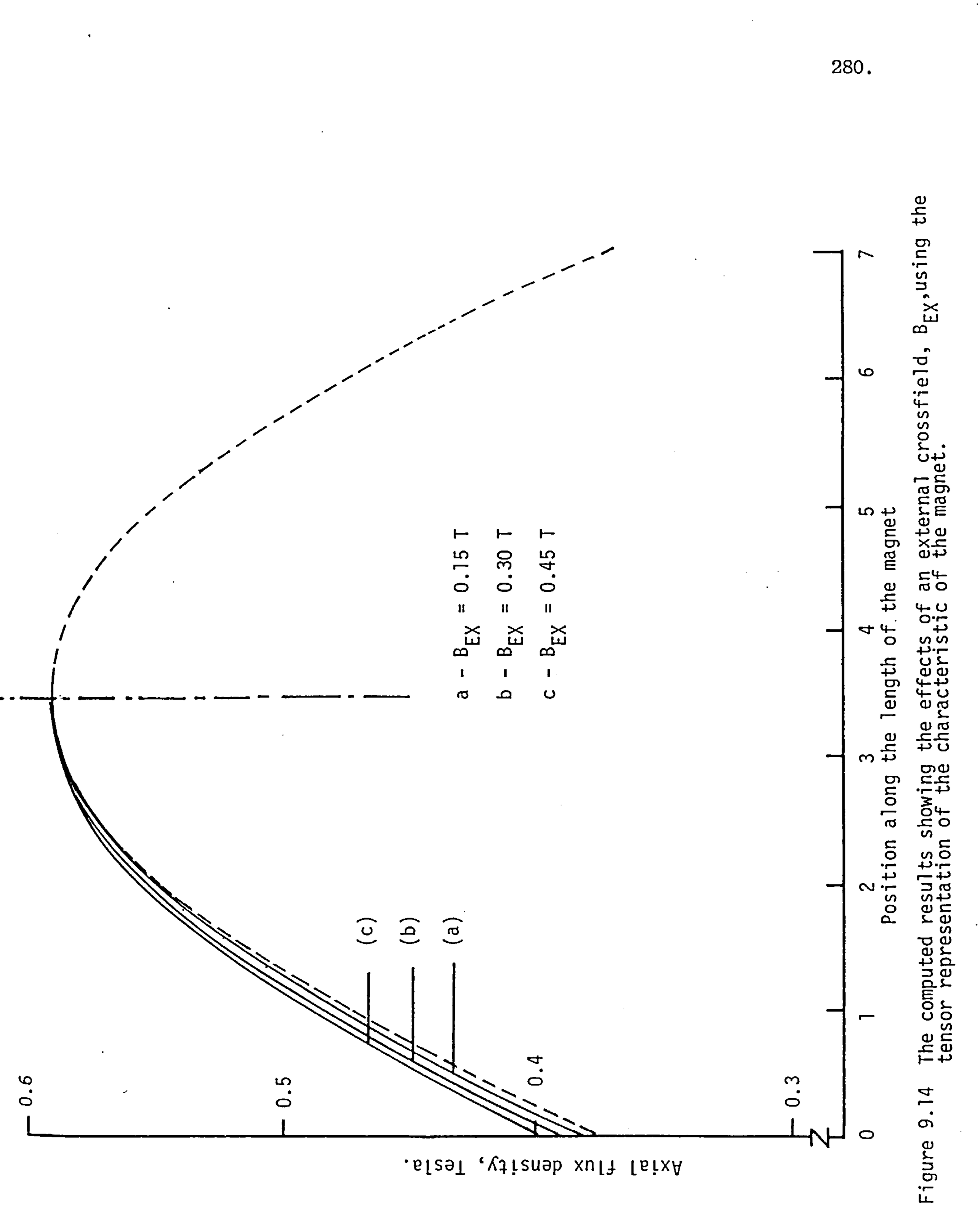

Figure 9.14 The computed results showing the effects of an external crossfield, B_{EX}, using the tensor representation of the characteristic of the magnet.

CHAPTER 10

CONCLUSIONS

10.1 INTRODUCTION

This thesis is concerned with the design of an optimal multi-stacked permanent-magnet generator. In the search for the optimal configuration of the new imbricated rotor, two computational methods are used for the analysis of the field. These two methods of computation are the discrete reluctance method and the finite-element method. The results from these two methods of computation are validated experimentally and used to design the optimal configuration for the new rotor. In this chapter the conclusions from the preceding chapters are summarised and suggestions made for future research. However, before considering these conclusions it is useful to review work discussed in the previous chapters.

A discrete-reluctance method for the analysis of three-dimensional fields is used to design several permanent-magnet generators (listed in Appendix I). These prototypes are used in the experiments to ascertain the accuracy of the discrete-reluctance program in predicting the characteristics of these multi-stacked generators. A comparison between the computed and experimental results shows the limitations of the discrete-reluctance method as regards the accuracy of the discrete-reluctance method program in predicting the performance of the multi-stacked permanent-magnet generator. This method is also unable to cope with the detailed analysis of the fields and their response to changes in the geometry of the flux guide. This calls for a more accurate form of field analysis to check the assumptions made in the discrete-reluctance method. The method employed for this purpose is a three-dimensional finite-element-method (TOSCA). The results using this method of analysis is used to improve the discrete-reluctance method program.

The information from the analysis of the field of the imbricated rotor using both methods are used to design and optimise an ideal configuration for the flux guide employed by this rotor. The variations in the design parameters of the configuration with different magnet materials and for different sizes are also studied.

An experimental analysis of the behaviour of a hard magnetic material, a polymer-bonded rare-earth magnet, is performed to study its behaviour when subjected to intense crossfields. The experimental results are used to model the material in the form of a permeability tensor for use in a finite-element scheme used for the calculation of permanent-magnet fields.

10.2 SUMMARY OF CONCLUSIONS

10.2.1 Experimental Results

The experiments conducted on the prototypes built show that the multi-stacked permanent magnet generators considered have the following characteristics.

i) The regulation at high loads is poor. When the generator is delivering maximum power the regulation is about 30%.

ii) The efficiency over a wide range of operation is in excess of 80%. In generator A, the maximum efficiency is 87%. This is good for the frame size considered, in comparison with machines with wound rotor.

iii) Capacitors have a significant effect on the output of these generators if used correctly. It is a method by which the magnitude of the output and the regulation can be controlled. When parallel capacitors are used on the output terminals of generator A, the increase in maximum output achieved if the capacitors are 8 μF, 20 μF and 30 μF, are 11%, 35% and 54% respectively. The regulation

is also improved. Series capacitors were found to be more effective for generators C and F which are both low voltage, high current generators.

iv) A variable speed experiment on generator A on open circuit show that 'iron loss', which predominates on open circuit, is very low at 50 Hz. At 200 Hz, the error in prediction by the discrete reluctance method program is 6%.

v) All the prototypes built use ceramic-8 magnets for excitation. They are therefore very sensitive to temperature as ceramic-8 has a very high temperature coefficient of demagnetisation. Experiments with generator A, which is totally encased and without a fan, show that a dynamic equilibrium is reached at a temperature of $90^{o}C$ (the ambient is $17^{o}C$) after running the generator for 2 hours. The drop in output which results is due to the increase in copper loss and the reduction in the level of excitation due to reduction in the level of magnetisation of the magent. The reduction in output of generator A at $90^{o}C$ is 20%. To overcome the problem of temperature an efficient cooling system can be incorporated to work the magnet at an acceptable temperature.

vi) The harmonic analysis on the airgap flux waveforms obtained experimentally shows a high level of harmonic distortion. The 3rd, 5th, 7th and 9th harmonic are all measurable. The third harmonic is most prominent being 21% of the fundamental, on open circuit, and increasing to 50% when the generator is delivering maximum power. The power spectral analysis show that the third harmonic power dissipated by the generator, as a percentage of the fundamental power, increases exponentially with load.

10.2.2 The Discrete-Reluctance Method Program

The load characteristics of the prototypes computed using the discrete-reluctance method program are compared with the experimental results. The following conclusions can be drawn from the comparison.

i) The accuracy of prediction differs between machines.

ii) In the region between open circuit and the peak power point the correlation is close. On further loading the correlation between the computed values and those from experiments deteriorates.

iii) The prediction of the maximum output is never more than 7% in error when compared to the experimental results for the range of generators which were built.

The inaccuracy of this method of computation can be attributed to several factors:

i) Limitations due to factors independent of the computational method. This class of factors encompasses the accuracy of the B-H characteristics of the iron and the magnet used. It also includes values of armature resistance and reactance, both which have been shown (in Chapter 4) to be critical in the accurate computation of the output characteristic of the machine.

ii) Limitations due to factors related to the program and the computational method. This class of factors includes the accuracy of the calculation of the reluctance of the flux paths in the model. It also includes the inability of the program to cope with harmonics efficiently. The omission of the harmonics in the computation thus introduces an inherent error. The leakage by the shaft is also not considered. The effects of eddy-currents is also ignored.

Despite these limitations this program is cheap and fast in computer terms and thus an efficient design aid. With the aid of a 3-dimensional finite-element field analysis program this program can be improved.

10.2.3 The Three-Dimensional Finite-Element Analysis of the Multi-Stacked Rotor

The method used is one which uses scalar potentials for the solution of magnetostatic fields (see Chapter 5). The model used is one pole pitch and is described in Section 5.5. The stator is represented as a smooth surface and the slotting is compensated for by extending the airgap which employs a coefficient commonly known as Carter's coefficient. 5896 nodes are used to represent the model. The no-load computation takes 12 minutes of computer processing time and the load case requires 23 minutes. From the analysis of the field in the rotor using this method, with changes in the geometry of the flux guide, the following conclusions are drawn.

i) The limiting factor in the passage of flux from the surface of the magnet to the poles is the surface area of the boundary between the iron disc and the pole.

ii) The pole profile is the predominant factor which determines the distribution of flux in the pole and thus the airgap, in particular the taper of the pole.

iii) The three leakages on open circuit were computed to be 7%, 12.95% and 7% of the useful flux respectively. They all increase with load. The total leakage at short circuit over a pole pitch is 1.7×10^{-4} Wb. This works the magnet at a flux density level of 0.12T which is above the knee on the demagnetisation characteristic of ceramic-8 and thus works on the major loop.

iv) These three leakages can be reduced by changing the pole profile by altering the taper and the value of 'a'.

vi) There is an optimum taper as regards maximum flux output and maximum power output.

vii) The taper has a pronounced effect on the airgap flux waveform. If the taper in generator A is increased to $\alpha = 20^{o}$ the third harmonic content on open circuit is reduced to just 7% of the fundamental.

viii) The collar adjacent to the shaft is a redundant feature in the prototypes built.

ix) The output characteristic of generator A computed by the three-dimensional finite-element program compared closely with the experimental load characteristic.

x) This program also predicts the harmonic content of the airgap field and its variation with load. The computed results compares closely with the experimental results.

10.2.4 Improvement to the Discrete-Reluctance Method Program

The results from the field analysis using the 3-dimensional finite-element program is used to improve the discrete-reluctance method program. The improvement is effected by assessing the assumptions made in the calculation of the reluctances of the 3 iron paths and the three leakage paths. Improvements were made to the representation of the areas and lengths of iron path 1 (the iron disc), iron path 2, leakage 1 (interpolar leakage), leakage 2 (the underpole leakage) and leakage 3 (the leakage in the region by the shaft). The load characteristic of generator A using the discrete-reluctance method programs with the new representation shows a close correlation with the experimental curve.

10.2.5 An Optimal Configuration of the Multi-Stacked Permanent-Magnet Rotor

An optimal configuration is proposed with the aid of the analysis from the two methods of computation. This optimal geometry has a pole shape derived from the analysis using the finite-element program, optimised for maximum power output and minimum harmonic distortion. The other dimensions of the flux guide and the dimensions of the magnet are optimised using the improved discrete-reluctance method program. The influence of magnet material and rotor diameter are assessed. It is concluded that for each magnet material at a fixed rotor diameter, there is an ideal single unit. An ideal rotor can then be formed from 3 or more of these units. There is, however, an optimum diameter as regards maximum power per unit volume. This varies for each material and is between 180 mm to 200 mm for the 4 materials (ceramic-8, rare-earth H18-B, MnAlC and polymer-bonded rare-earth) considered.

10.2.6 The Tensor Representation of Anisotropic Permanent Magnets

The study of an anisotropic polymer-bonded rare-earth magnet in the presence of external crossfields shows that the effect of a field perpendicular to its axis of magnetisation is significant whilst a field parallel to it has negligible effect on the field in the preferred direction. From the experimental data a model of the behaviour of the magnetisation in two dimensions is presented as a matrix. A general matrix proposed for the representation of anisotropic magnets would be of the form,

$$\begin{vmatrix} B_x \\ B_y \end{vmatrix} = \begin{vmatrix} \mu_x & (K_1 + K_2 \frac{B_{x_i}}{B_r}) \\ 0 & \mu_y \end{vmatrix} \begin{vmatrix} H_x \\ H_y \end{vmatrix} + \begin{vmatrix} M_x \\ 0 \end{vmatrix}.$$

In the case of HERA, the polymer-bonded rare-earth magnet studied, K_1 and K_2 has values of 0.09 μ_o and -0.09 μ_o respectively.

10.3 GENERAL REMARKS

The multi-stacked imbricated rotor has been studied in detail and its field analysed using the discrete-reluctance method program and the three-dimensional finite-element program. Both programs have their limitations. In considering their merits, the purpose and application of the two contrasting techniques of analysis should be identified. The finite-element program, TOSCA, is a sophisticated and an inherently accurate form of analysis. Any inaccuracies are due to the quasi-static nature of the solution and the discretisation. This program is capable of monitoring the effects of changes in the geometry of the flux guide on the flux distribution. It is also capable of predicting the airgap flux waveform and its harmonic content. This program, however, is expensive in CPU time. The discrete reluctance method is cheap and fast in computer terms. The time taken by the discrete-reluctance method program is one tenth that taken by TOSCA. It is also an interactive program. Therefore, the program TOSCA is used as a tool to refine the discrete-reluctance method program, by analysing the field in the imbricated rotor in detail, while the optimisation of designs is left to the discrete-reluctance method program.

The optimal configuration of a flux guide for the rotor is obtained with the help of the field analysis from both methods. The permanent-magnet generator with this new rotor is an efficient, robust and versatile machine. It has great potential as aircraft generators, vehicle alternators, welding generators and as a generating unit in an isolated environment.

The power density can be increased significantly with the use of rare-earth magnets and this will extend its range of applications.

The research into the behaviour of anisotropic permanent magnets compliments the research into permanent-magnet machines. A more accurate representation of the magnet would improve the accuracy in the field analysis of problems involving permanent magnets.

10.4 SUGGESTIONS FOR FURTHER WORK

Subjects for further research and development on the multi-stacked permanent-magnet generator are suggested below.

i) The application of permanent magnet materials, apart from ferrites, needs to be studied in detail and prototypes built to assess their merits experimentally in comparison with existing prototypes which use ceramic-8 magnets. This would compliment the computational studies that have been conducted on the use of different magnet materials. The materials used should be studied in relation to the application. However, there are some materials which show little promise.

ii) A feasibility study on the viability of a 100-200 kW machine of this configuration. The behaviour of permanent-magnet machines with changes in size has not been well investigated. The well-known principles which are applicable for electromagnetic machines may not apply for permanent magnet machines. A parameter of interest would be how the power density varies with scale, and the efficiency in working the magnet.

iii) The bulk of future work would be mainly concerned with the transient aspects and the control of the regulation of these generators. A full transient analysis of the performance of a machine based on

field solution methods will be very complicated and time consuming, although a limited study of some particular aspects of transient behaviour is possible[1,2]. The alternative approach is a 2-axis representation of the machine as has been used by Lawrenson[3] for reluctance machines, and others[4,5,6] for synchronous machines. This method is also based on operational impedances of the machine and can be used either to calculate mean values by solving complex algebraic equations[5], or to compute a full transient solution by solving differential equations of both electromagnetic and mechanical in origin. This method is simpler and the accuracy of the solution depends on how accurately the machine is modelled. There is, however, the problem of non-linearity, and the airgap field is far from sinusoid. The modelling of the permanent-magnet generator with equivalent circuits[7] is another possibility.

The dynamic response of the generator is important especially in cases when a heavy load is switched on suddenly, or when a heavy demand is placed on the generator at a fixed or variable frequency.

iv) In many applications, the output from the generator has to be regulated. This is a difficult process in permanent magnet generators as the exciting field cannot be easily controlled. Thus an external regulating device in the form of a chopper, for example, is required. This is an area which work is required to match the multi-stacked permanent-magnet generator with a cheap and efficient regulator.

v) Research into the use of this configuration as a motor, making use of the rotor's efficiency in energy conversion is a distinct possibility.

vi) Investigations into the application of the multi-stacked generator in alternative energy schemes, and high speed air and spacecraft energy systems should be seriously considered.

10.5 REFERENCES

1. HANNALLA, A. Y. and MACDONALD, D. C. : 'Numerical analysis of transient field problems in electrical machines', Proc. IEE, Vol. 123, pp 893-898, 1976.

2. HANNALLA, A. Y. : 'Transient analysis of solid rotor turbo alternators allowing for saturation and eddy currents', Ph.D. thesis, University of London, 1975.

3. LAWRENSON, P. J., MATHUR, R. M. and STEPHENSON, J. M. : 'Transient performance of reluctance machines', Proc. IEE, Vol. 118, pp 777-783, 1971.

4. DE JONG, H. C. : 'Starting performance of synchronous motors with laminated salient poles', Trans. IEEE, Vol. 87, pp 1083-1098, 1976.

5. ADKIN, B. : 'The general theory of electrical machines', Chapman and Hall, London, 1964.

6. FRANTHOME, B. A., VADHER, V. and WEDMAN, L. : 'The application of design and analysis in small machines for aircraft', Second International Conf. on Small and Special Electrical Machines, IEE, London, Sept. 1981.

7. ADBULAZIZ, M. and JUFFER, M. : 'Steady state and transient analysis of a permanent magnet synchronous generator with claw-shaped rotor', Second International Conf. on Small and Special Electrical Machines, IEE, London, Sept. 1981.

Machine	Rotor diameter (mm)	Rotor length (mm)	Radial air gap (mm)	Number of Magnets	Number of poles	Rotor speed (rpm)	Machine output (kW)
A	140	121	0.386	4	8	1,500	1.72
B	152	146	0.635	5	8	1,500	2.81
C	216	109	0.584	4	6	3,000	9.00
D	196	249	0.737	7	4	1,500	7.10
E	215	184	0.635	5	16	350	4.00
F	121	95	0.380	4	8	3,000	3.00

Permanent magnets used in these machines are Ceramic-8.

Specification of Prototypes

APPENDIX I

APPENDIX II

The computer used for the analysis of the voltage wave-forms produced by the permanent magnet generator is the data analysis computer, a PDP 11/45, in the Institute of Sound and Vibration Research, University of Southampton. The programs are constructed by calling a sequence of available routines.

Program A

```
/KILL(1,2,3,4,5,6,7,8,9)
/ACQUIR(1000,1024,1,1)
/NORM(1,2,1)
/DISPLY(2,0)
/CONV(2,3,4,200,*)
/DISPLY(3,0)
/FFTA(3,4,-1)
/MOPH(4,5,-1)
/DISPLY(5,0)
/PEAK(5,6,4)
/SCREEN(6)
END
```

Program B

```
/KILL(1,2,3,4,5,6,7,8,9)
/ACQUIR(1000,1024,2,1)
/NORM(2,3,1)
/DISPLY(3,0)
/CONV(3,4,0,513,*)
/PSD(4,5)
/DISPLY(5,0)
/PEAK(5,6,4)
/SCREEN(6)
```

APPENDIX III

DERIVATION OF EQUATIONS FOR FLUX IN PATHS AND FLUX DENSITIES

The equations for the flux quantities are based on the model in Figure 3.1. The basic equations which are going to be used are listed below:-

If the reluctance of the stator is not included, the set of equations is:

$$\left(\int H d\ell\right)_q^M - \left(\int H d\ell\right)_q^I - I_q = 0 \quad \text{for each branch q.} \tag{A3.1}$$

Flux ϕ is a function of the form:

$$\phi = f(H_m, R_1^I, R_2^I, R_3^I, \text{geometry}) \tag{A3.2}$$

Magnet representation is achieved using u' - the apparent permeability.

$$H_m = -H = (B_r - B)\nu' \tag{A3.3}$$

where ν' is the apparent reluctivity.

By putting $\left(\int H d\ell\right)_q^M = H_m L_m$, and $\nu' = \nu_m$, into A3.1 and A3.3 and solving them the following equation results:

$$L_m \left(B_r - \frac{\phi}{S_m}\right) \nu_m = \left(\int H d\ell\right)_q^I + M_q^G = \phi/\Lambda_3 \tag{A3.4}$$

where $M_q^G = \left(\int H d\ell\right)_q^G + I_q$ (A3.5)

The total flux passing through iron path 3 to the air-gap is:

ϕ_3^I

$$\text{if} \quad R_3^I = \frac{1}{\sum_{j=1}^{j=N} \frac{1}{r_{3j}^I \nu_{3J}^I}} \tag{A3.6}$$

$$\left(\int H d\ell\right)_3^I = \phi_3^I R_3^I \tag{A3.7}$$

The flux crossing the air gap in the q^{th} path is:

$$\phi_q^G = \left(\int Hd\ell \right)_q^G u_o \frac{S_q^G}{L_q^G} = (M_q^G - K_q I) u_o \frac{S_q^G}{L_q^G} \qquad \text{(A3.8)}$$

$$\left.\begin{aligned} S^G &= S_1^G + S_2^G + S_3^G + \ldots + S_n^G \\ \text{if} \quad C &= \frac{u_o}{L_g} (K_1 S_1^G + K_2 S_2^G + \ldots + K_n S_n^G \end{aligned}\right\} \qquad \text{(A3.9)}$$

By substituting (A3.9) in to the air-gap flux formula, we arrive at:

$$\phi G = M_q^G \Lambda_g - CI \qquad \text{(A3.10)}$$

where $\Lambda_g = u_o S^G / L_g$ (permeance).

Iron paths 1 and 2 are considered to have one element each which means that each path has a single reluctance. The flux crossing path 1 is equal to the flux ϕ_1^I and that crossing path 2 is ϕ_2^I (Figure 3.1).

It is possible to write the integral of Hdℓ along each path as

$$\left(\int Hd\ell \right)_1^I = \phi_1^I R_1^I$$

$$\left(\int Hd\ell \right)_2^I = \phi_2^I R_2^I$$

or as the function of the reluctivity of the material of each path

$$\left(\int Hd\ell \right)_1^I = \phi_1^I r_1^I \nu_1^I \qquad \text{(A3.11)}$$

$$\left(\int Hd\ell \right)_2^I = \phi_2^I r_2^I \nu_2^I \qquad \text{(A3.12)}$$

where

$$r_1^I = L_1^I / S_1^I$$

$$r_2^I = L_2^I / S_2^I$$

Figure 3.1 shows that the driving force across leakage path 1 is equal to that across the air gap added to the stator current (or M_q^G).

ϕ_1^A is the flux in leakage path 1 and Λ_1 is the permeance of the path, hence the following equation:

$$\phi_1^A = M_q^G \Lambda_1 \qquad \text{(A3.13)}$$

It is found in a similar way that the flux in a branch of leakage path 2 is:

$$\phi_2^A / 2 = \left[M_q^G + \left(\int Hd\ell \right)_3^I + \left(\int Hd\ell \right)_2^I / 2 \right] \Lambda_2 / 2 \qquad \text{(A3.14)}$$

By substituting (A3.13), (A3.10)into (3.7) and putting

$$\phi_3^I = \phi G + \phi_1^A$$

the following equation results :

$$\left(\int Hd\ell \right)_3^I = \left(M_q^G (\Lambda_1 + \Lambda_g) - CI \right) R_3^I \qquad \text{(A3.15)}$$

By substituting $\left(\int Hd\ell \right)_3^I$ from equation (A3.15) in (A3.14), the following results:

$$\phi_2^A / 2 = \left[M_q^G (1 + (\Lambda_1 + \Lambda_2) R_3^I) - CI R_3^I + \left(\int Hd\ell \right)_2^I / 2 \right] \Lambda_2 / 2 \qquad \text{(A3.16)}$$

It is shown from Figure 3.1 that

$$\phi = \phi G + \phi_1^A + \phi_1^A + \phi_3 \qquad \text{(A3.17)}$$

Substituting the values of ϕG, ϕ_1^A and ϕ_2^A from equations (A3.10), (A3.13) and (A3.16) in equation (A3.17) gives the equation:

$$\phi - \phi_3 = M_q^G \left[\Lambda_g + \Lambda_1 + \Lambda_2 (1 + (\Lambda_g + \Lambda_1) R_3^I) \right] + \left(\int Hd\ell \right)_2^I \Lambda_2/2 - CI \ (1 + \Lambda_2 R_3^I) \qquad \text{(A3.18)}$$

It is shown from Figure 3.1 that

$$\phi_2^I = \phi G + \phi_1^A + \phi_2^A / 2 \qquad \text{(A3.19)}$$

and

$$\phi_1^I = \phi - \phi_3 \qquad \text{(A3.19)'}$$

Substituting ϕ_1^I from (A3.19)' in (A3.11) gives

$$\left(\int Hd\ell \right)_1^I = (\phi - \phi_3) \, r_1^I \, \nu_1^I \qquad \text{(A3.11)}$$

Solving (A3.19), (A3.10), (A3.13) and A3.16) for ϕ_2^I gives

$$\phi_2^I = M_q^G \left[\Lambda_g + \Lambda_1 + \frac{\Lambda_2}{2} \left(1 + (\Lambda_g + \Lambda_1) R_3^I \right) \right] + \left(\int Hd\ell \right)_2^I \Lambda_2/4 - CI \left(1 + R_3^I \, \Lambda_2/2 \right) \qquad \text{(A3.20)}$$

Solving equations (A3.12), (A3.18) and (A3.20) for M_q^G

$$M_q^G = \frac{(\phi - \phi_3) \left(1 - r_2 \, \nu_2 \, \frac{\Lambda_2}{4} \right) + CI \left(1 + \Lambda_2 \, R_3 + \nu_2 \, r_2 \, \frac{\Lambda_2}{4} \right)}{\Lambda_g + \Lambda_1 + \Lambda_2 \left[1 + (\Lambda_g + \Lambda_1) R_3^I \right] + \nu_2^I \, r_2^I \, (\Lambda_g + \Lambda_1) \, \Lambda_2 \, / \, 4} \qquad \text{(A3.21)}$$

Substituting the value of M_q^G from (A3.21) in (A3.18) and solving for $\left(\int Hd\ell \right)_2^I$ gives the following equation

$$\left(\int Hd\ell \right)_2^I = \left[\frac{(\phi - \phi_3) \left[\Lambda_g + \Lambda_1 + \Lambda_2/2 \left(1 + (\Lambda_g + \Lambda_1) R_3^I \right) \right] - \Lambda_2 CI/2}{\Lambda_g + \Lambda_1 + \Lambda_2 \left[1 + (\Lambda_g + \Lambda_1) R_3^I \right] + \nu_2^I \, r_2^I \, (\Lambda_g + \Lambda_1) \, \Lambda_2/4} \right] r_2^I \, \nu_2^I \qquad \text{(A3.22)}$$

The values of $\left(\int Hd\ell \right)_1^I$, $\left(\int Hd\ell \right)_2^I$, $\left(\int Hd\ell \right)_3^I$, and M_q^G are substituted from equations (A3.11) , (A3.22), (A3.7) and (A3.21) in equation (A3.4), solving for ϕ gives the following equation:

$$\phi = \frac{A_1 \left(f + SIG + A_5 \, R_3^I + A_2 \, \nu_2^I \right) \nu_m - CI \left(1 - A_3 \, \nu_2^I \right)}{f \nu_m r_m + SIG_1 (1 + A_3 \nu_2^I) R_3^I + 1 + A_4 \nu_2^I + (SIG + A_5 R_3^I + A_2 \nu_2^I)(\nu_m r_m + r_1^I \nu_1^I)} \qquad \text{(A3.23)}$$

where f is a function given by the following equation

$$f = \Lambda_3 \left[SIG_1 (1 + A_3 \, \nu_2^I) \, R_3^I + 1 + A_4 \, \nu_2^I + (SIG + A_5 \, R_3^I + A_2 \nu_2^I) \, \nu_1^I \, r_1^I \right]$$

and the constants SIG, SIG_1, A_1, A_2, A_3, A_4, A_5, r_m are:-

$$
\left.
\begin{aligned}
SIG &= \Lambda_g + \Lambda_1 + \Lambda_2 \\
SIG_1 &= \Lambda_g + \Lambda_1 \\
A_1 &= L_m B_r \\
A_2 &= SIG_1 \, r_2^I \, \Lambda_2 / 4 \\
A_3 &= r_2^I \, \Lambda_2 / 4 \\
A_4 &= (SIG_1 + \Lambda_2 / 4) \, r_2^I \\
A_5 &= \Lambda_2 \, SIG_1 \\
r_m &= L_m / S_m
\end{aligned}
\right\} \qquad \text{(A3.24)}
$$

From (A3.21) and (A3.24)

$$
M_q^G = \frac{(\phi-\phi_3)\,(1 - A_3\,\nu_2^I) + CI\,(1 + R_3^I\,\Lambda_2 + A_3\,\nu_2^I)}{SIG + A_5\,R_3^I + A_2\,\nu_2^I} \qquad \text{(A3.25)}
$$

where the value of ϕ_3 is substituted from equation (A3.4).

To get the flux density distribution in the air gap, it is enough to find the value of ϕ from (A3.23), substitute it in (A3.25) and find the values for the flux in the air-gap paths from equation (A3.8).

It is important to mention that equation (A3.23) cannot be solved explicitly, because the values of ν_m, ν_1^I, ν_2^I, and R_3^I depend on the value of ϕ itself. The solution is obtained by giving ϕ an initial value, finding the values of the different reluctivities and substituting in (A3.23) for calculating ϕ. These steps are repeated many times until a stable value of ϕ is obtained. To get the numerical solution the problem must be formulated in a suitable way for solving by a digital computer.

APPENDIX IV

DETAILS OF THE PROGRAM FLOW CHART

The program flow chart is presented in Figure A4.1. It outlines the main steps of execution which are described below.

Step 1 : Read machine parameters such as rotor dimensions, air gap, iron and magnet B/H curves, rotor synchronous speed. Write some of the machine data to check.

Step 2 : Check data units of length and transfer to meters if necessary.

Step 3 : Calculate the circuit parameters such as iron paths, leakage paths and air-gap paths. Calculate the flux formula constants from equations (A3.24).

Step 4 : Set the armature reaction pattern.

Step 5 : Set the initial values like the current increment, the internal power factor angle increment, the maximum stator phase current and the initial value of the flux ϕ. Set the value of IND to zero (IND is an index used to determine whether the initial value of ϕ is suitable or not).

Step 6 : Give the under-relaxation factor (ω) the starting value of ω_o. Set NOS to zero (NOS is an index used to check whether the flux ϕ converges to a single value after a number of solutions).

Step 7 : Set ITR to zero (ITR is an index representing the number of iterations with one value of ω).

Step 8 : Test the values of NOS.

Step 9 : Call subroutine FXCALC.

This is the subroutine that contains the instructions to iteratively calculate the flux ϕ; in it equation (A3.23) is executed sixteen times, every time updating the values of the various reluctances. This subroutine is going to be explained separately. Figure A4.2 shows the flowchart describing it, and in it are the following instructions.

Step 9.1 : Compare NA with zero.

Step 9.2 : Set NM to zero.

Step 9.3 : Calculate B_m the magnet flux density. Evaluate ν_m the magnet material apparent reluctivity (linear interpolation is used to find ν_m from the B/H curve). Set NI and j to zero.

Step 9.4 : Calculate H^I_{3j} dividing $\left(\int H \, d\ell \right)^I_3$ by L^I_{3j} (equation (A3.15)). Evaluate ν^I_{3j} and H^I_{3j} (by linear interpolation).

Step 9.5 : Compare j with 15.

Step 9.6 : Calculate R^I_3 (from equation (A3.6)).

Step 9.7 : Calculate B^1_1 where

$$B^I_1 = \phi / S^I_1$$

Evaluate ν^I_1 from B^I_1 and the iron B/H curve (linear interpolation).

Step 9.8 : Calculate B^I_2 where

$$B^I_2 = \phi / S^I_2$$

Evaluate ν^I_2 from B^I_2 and the iron B/H curve (linear interpolation).

Step 9.9 : Calculate ϕ from the equation (A3.23). Calculate M^G_q from equation (A3.25) and ϕ^I_2 from equation (A3.12) and (A3.22). Increase NI by one.

Step 9.10 : Compare NI to 4

Step 9.11 : Increase NM by 1

Step 9.12 : Compare NM to 4

Step 9.13 : Calculate the initial values for all element material reluctivities.

This step is executed only once at the beginning of the program.

Step 10 : Increase ITR by one.

Step 11 : Calculate the difference between two successive values of ϕ as percentage of the present value, compare it with 0.01.

Step 12 : Compare ITR with 7.

Step 13 : Reduce the value of (ω) and increase NOS by one.

Step 14 : Increase (ω) and recalculate ϕ.

Step 15 : Find the flux density waveform in the air-gap region (equation (A3.8)) where M_q^G is calculated from (A3.25). Calculate the terminal voltage (v) and the load power factor (PF).

Step 16 : Compare stator current to zero.

Step 17 : Write the value of no load voltage.

Step 18 : Set the initial values of ψ to zero and the current to the current increment. Put $v_o = v/10$.

Step 19 : Reduce ψ by the value of the angle increment.

Step 20 : Calculate C from equation (A3.9).

Step 21 : Compare IND with zero.

Step 22 : Compare PF to the desired value of the power factor (PF_θ).

Step 23 : Set IND to 1 (this is to indicate that the initial value of ψ is correct).

Step 24 : Compare the power factor with (PF_θ).

Step 25 : Find the value of the terminal voltage (V_θ) at the desired power factor (PF_θ) from the calculated values of (v) in step 15 by linear interpolation. Find the value of ψ related to the same voltage (ψ_θ).

Step 26 : Write the values of the terminal voltage and current at the power factor (PF_θ).

Step 27 : Compare V_θ to V_o and I to I_{max}.

Step 28 : Increase the current by the amount of the current increment.

Set the value of ψ to ψ_θ - INC where INC is the angle increment.

Step 29 : Increase ψ by the amount of the single increment.

STOP

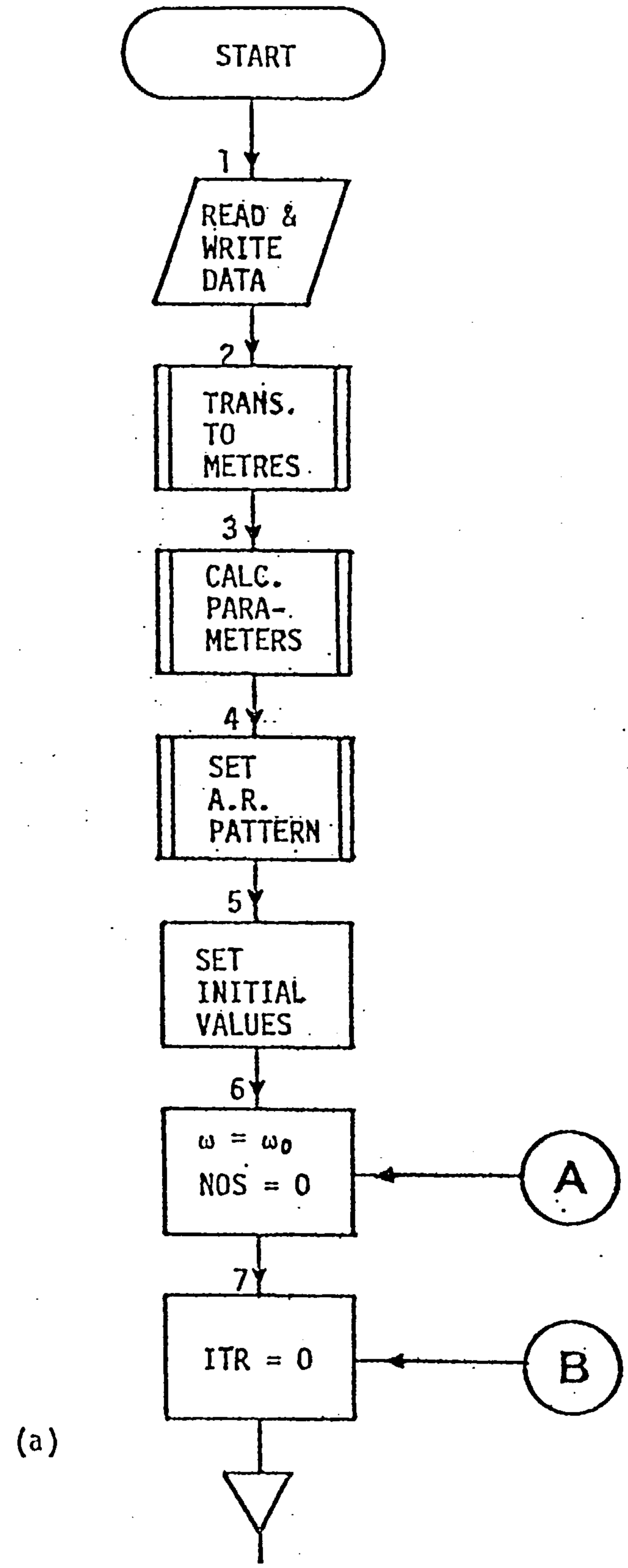

(a)

Fig.A4.1 Program flowchart.

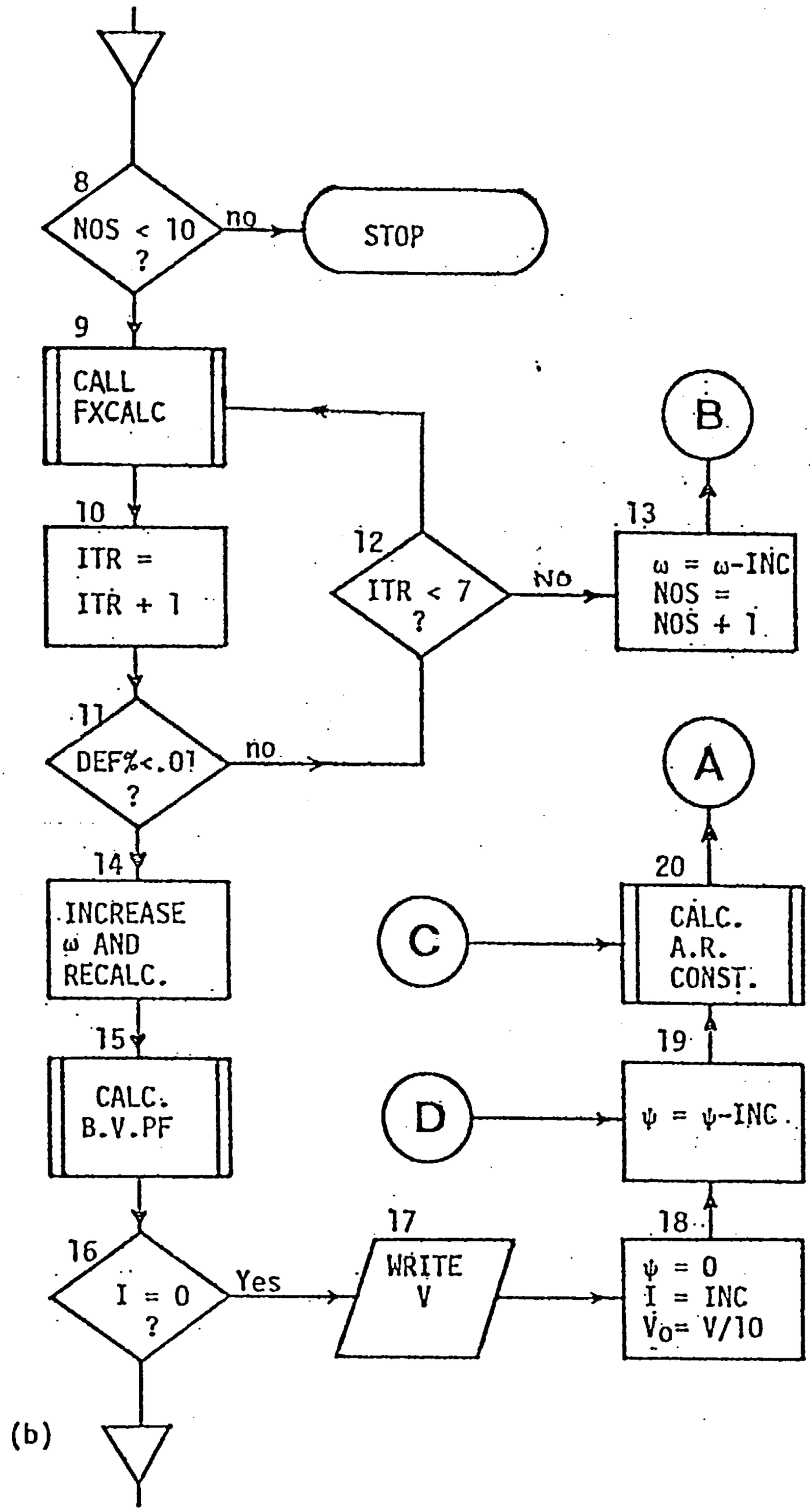
8
NOS < 10 ?
no
STOP
9
CALL FXCALC
10
ITR = ITR + 1
11
DEF%<.01 ?
no
12
ITR < 7 ?
NO
13
ω = ω-INC
NOS = NOS + 1
B
A
C
D
14
INCREASE ω AND RECALC.
15
CALC. B.V.PF
16
I = 0 ?
Yes
17
WRITE V
18
ψ = 0
I = INC
V_0= V/10
19
ψ = ψ-INC.
20
CALC. A.R. CONST.
(b)

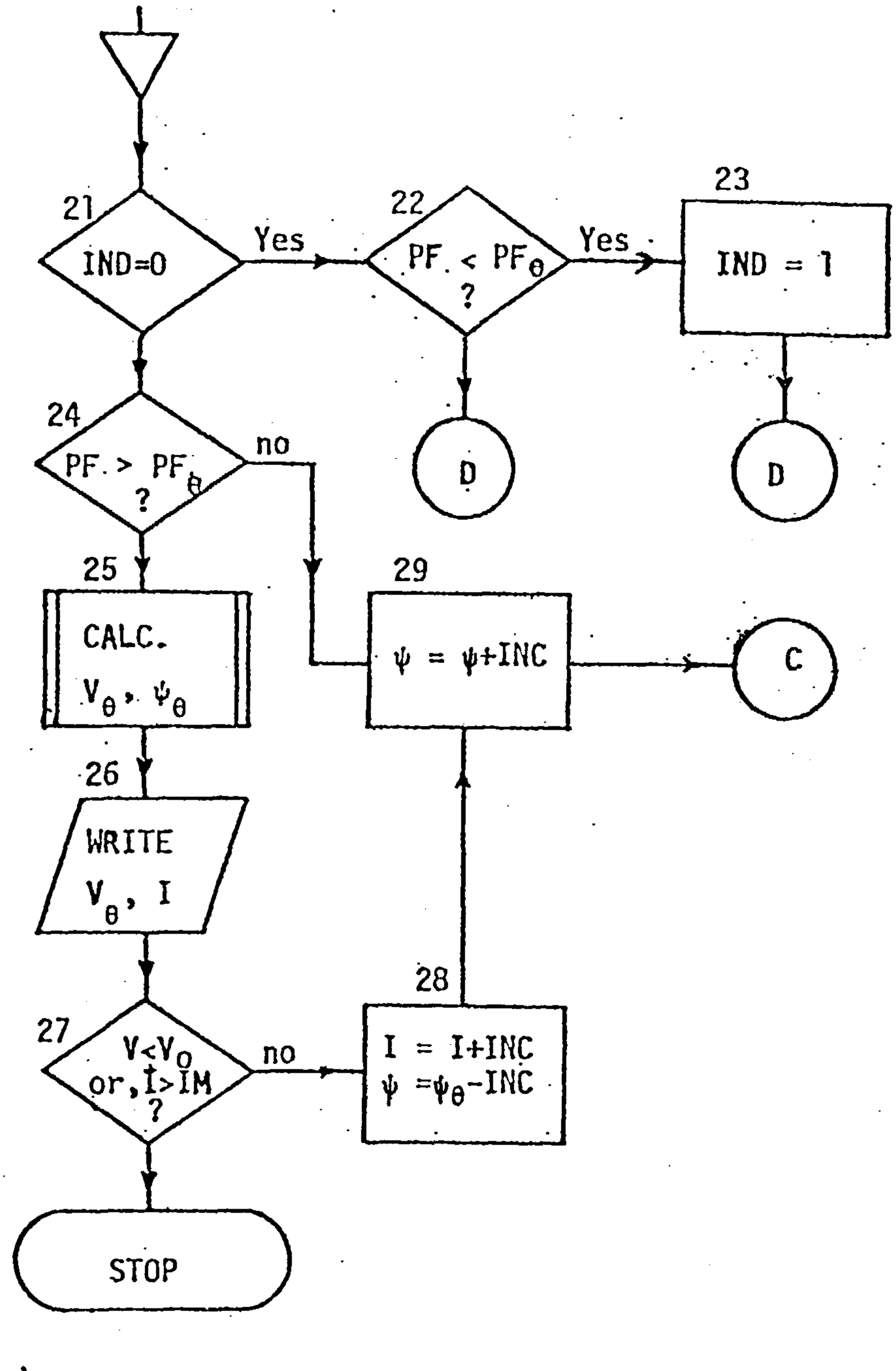
21
IND=0
Yes
22
PF < PFθ ?
Yes
23
IND = 1
D
D
24
PF > PFθ ?
no
25
CALC. Vθ, ψθ
29
ψ = ψ+INC
C
26
WRITE Vθ, I
28
I = I+INC
ψ =ψθ-INC
27
V<Vo or, I>IM ?
no
STOP

(c)

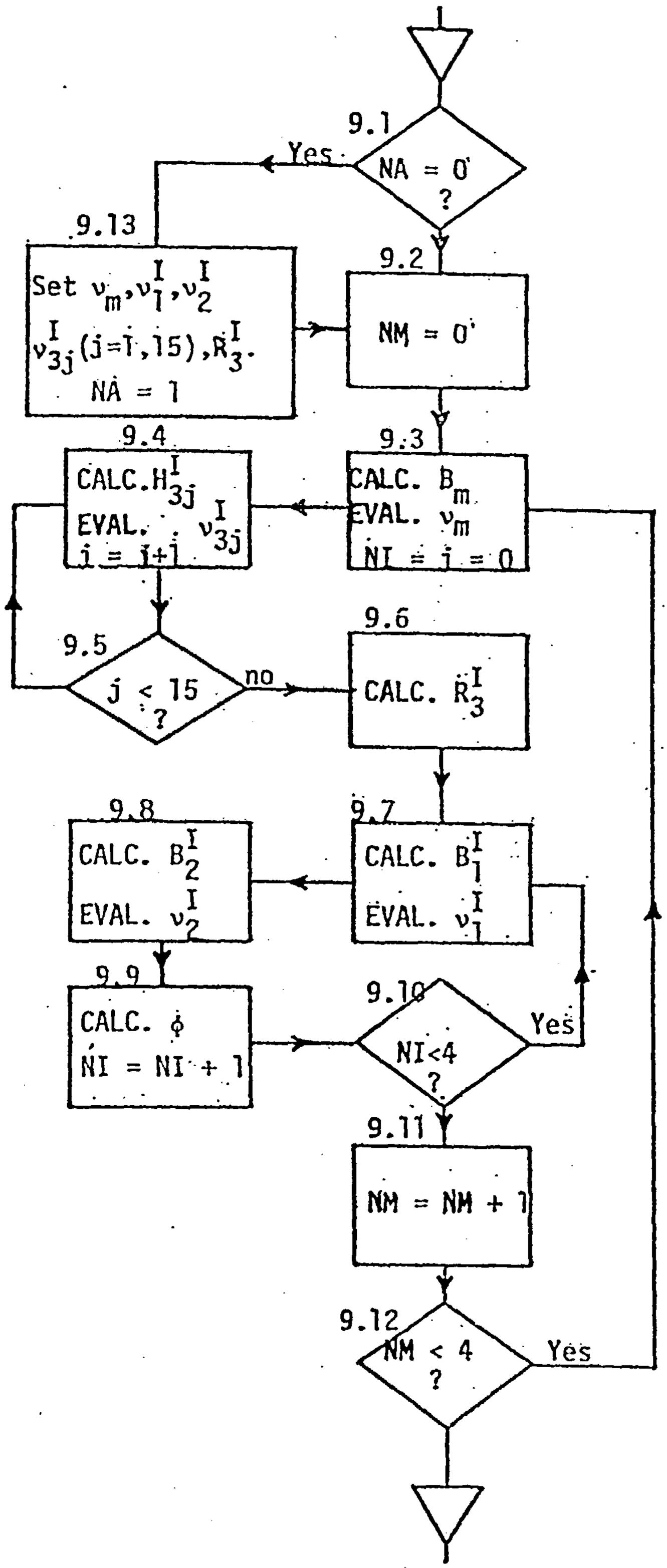

Fig. A4.2 Flowchart of subroutine FXCALC.

APPENDIX V

The representation of an anisotropic permanent magnet by a permeability tensor is derived as follows.

$$B = \mu_o H + M$$

$$= \mu_o H + M'(H) + M_o$$

$$= \mu_o H + \mu_o \mu' H + M_o$$

$$= \mu_o H + \mu_o \mu' H + M_o$$

Thus $B = \mu_o H (1 + \mu') + M_o$

$$= \mu_o \mu_r H + M_o = \mu H + M_o$$

where $\mu = \begin{vmatrix} a & b \\ c & d \end{vmatrix}$

Therefore, $\mu H = B - M_o$ or $H = \mu^{-1} B - \mu^{-1} M_o$.

Taking the curl of both sides,

$$\nabla \times H = +J = \nabla\times(\mu^{-1}B) - \nabla\times(\mu^{-1} M_o)$$

or $\nabla\times(\mu^{-1} B) = J + \nabla\times(\mu^{-1} M_o)$

$$= J + Jm$$

where $Jm = \nabla\times(\mu^{-1} M_o)$

or $\iint Jm\, ds = \iint_R \nabla\times(\mu^{-1} M_o)\, ds$.

Using Stoke's Theorem $Im = \oint (\mu^{-1} M_o)\, d\ell$

This integral can be evaluated as follows:

$$Im = \oint (\mu^{-1} M_o)\, d\ell$$

$$\mu^{-1} M_o = \begin{vmatrix} d' & -b' \\ -c' & a' \end{vmatrix} \begin{vmatrix} M_{ox} \\ M_{oy} \end{vmatrix} = \begin{vmatrix} d'M_{ox} - b'M_{oy} \\ -c'M_{ox} + a'M_{oy} \end{vmatrix}$$

where $a = \mu' x$

$b = \oint (x, \ell, H_y)$

$c = \oint (x, \ell, H_x)$

$d = \mu' y$

$a' = a/_{(ad-bc)}$

$b' = b/_{(ad-bc)}$

$c' = c/_{(ad-bc)}$

$d' = d/_{(ad-bc)}$

Therefore, $\oint (\mu^{-1} M_o)\, d\ell = |dx'\ dy'| \begin{vmatrix} d' M_{ox} - b' M_{oy} \\ -c' M_{ox} - a' M_{oy} \end{vmatrix}$

$= |(d' M_{ox} - b' M_{oy})\, dx' + (c' M_{ox} + a' M_{oy})\, dy'|$

where

$dx' = dx \cos\theta + dy \sin\theta,$

and $dy' = dx \sin\theta + dy \cos\theta$

dx' and dy' are in local coordinate axes in parallel to M_{ox} and M_{oy} respectively. These two coordinate systems are separated by an angle θ and the transformation tensor is,

$$\top = \begin{vmatrix} \cos\theta & \sin\theta \\ -\sin\theta & \cos\theta \end{vmatrix}$$

and $$\begin{vmatrix} x' \\ y' \end{vmatrix} = \left|\top\right| \begin{vmatrix} x \\ y \end{vmatrix}$$

The left hand side of equation (ii), denoted by L.H.S., is given by

$\Delta \times (\mu^{-1} B)$

$$= \Delta x \begin{vmatrix} a & b \\ c & d \end{vmatrix}^{-1} \begin{vmatrix} B_x \\ B_y \end{vmatrix}$$

$$= \frac{1}{\Delta x\ (ad-bc)} \begin{vmatrix} d & -b \\ -c & a \end{vmatrix} \begin{vmatrix} B_x \\ B_y \end{vmatrix}$$

$$= \nabla x \frac{1}{(ad-bc)} \begin{vmatrix} dB_x & -bB_y \\ -cB_x & aB_y \end{vmatrix}$$

$$\begin{vmatrix} i & j & k \\ \frac{\partial}{\partial x} & \frac{\partial}{\partial y} & \frac{\partial}{\partial z} \\ \frac{dB_x - bB_y}{ad-bc} & \frac{-cB_x + aB_y}{ad-bc} & 0 \end{vmatrix}$$

$$= i\frac{\partial}{\partial z}\left(\frac{-cB_x+aB_y}{ad-bc}\right) - j\frac{\partial}{\partial z}\left(\frac{dB_x-bB_y}{ad-bc}\right) + k\left|\frac{\partial}{\partial x}\left(\frac{-cB_x+aB_y}{ad-bc}\right) - \frac{\partial}{\partial y}\left(\frac{dB_x-dB_y}{ad-bc}\right)\right|$$

Since the field is uniform in the z-direction, the z-derivatives of B_x and B_y vanishes. Therefore,

$$\nabla x(\mu^{-1} B) = k\left|\frac{\partial}{\partial x}\left(\frac{-cB_x+aB_y}{ad-bc}\right) - \frac{\partial}{\partial y}\left(\frac{dB_x-bB_y}{ad-bc}\right)\right|$$

But $B = \nabla \times A$,

and in the two-dimensional case, $A = A_z$.

Thus $B_x = \frac{\partial A}{\partial y}$,

and $B_y = \frac{\partial A}{\partial x}$.

Therefore, L.H.S. $= \frac{\partial}{\partial x}\left(\frac{-c\frac{\partial A}{\partial y} - a\frac{\partial A}{\partial x}}{ad - bc}\right) - \frac{\partial}{\partial y}\left(\frac{d\frac{\partial A}{\partial y} + b\frac{\partial A}{\partial x}}{ad - bc}\right)$

$$= -\frac{\partial}{\partial}\left(c'\frac{\partial A}{\partial y} + a'\frac{\partial A}{\partial x}\right) - \frac{\partial}{\partial y}\left(d'\frac{\partial A}{\partial y} + b'\frac{\partial A}{\partial x}\right)$$

$$= -\frac{\partial}{\partial X}\left(a'\frac{\partial A}{\partial x} + c'\frac{\partial A}{\partial y}\right) - \frac{\partial}{\partial y}\left(b'\frac{\partial A}{\partial x} + d'\frac{\partial A}{\partial y.}\right)$$

Therefore, the partial differential equation representing the field terms of the vector potential is

$$\frac{\partial}{\partial x}\left(a\frac{\partial A}{\partial x} + c\frac{\partial A}{\partial y}\right) + \frac{\partial}{\partial y}\left(b'\frac{\partial A}{\partial x} + d'\frac{\partial A}{\partial y}\right) = -(J + Jm)$$

The functional to be minimised is,

$$F = \int \left\{ \left[\left(a'\frac{\partial A}{\partial x} + c'\frac{\partial A}{\partial y}\right)\frac{\partial A}{\partial x} + \left(b'\frac{\partial A}{\partial x} + d'\frac{\partial A}{\partial y}\right)\frac{\partial A}{\partial y} \right] - 2(J + Jm)\, A \right\} dR$$

The minimisation with respect to Am gives

$$\frac{\partial F}{\partial A_m} = 0, \text{ for } m = 1, 2, \ldots, n$$

Thus,

$$\frac{1}{2} \frac{\partial}{\partial A_m} \int_R \{ (a' \frac{\partial A}{\partial x} + c' \frac{\partial A}{\partial y} \frac{\partial A}{\partial x} + (b' \frac{\partial A}{\partial x} + d' \frac{\partial A}{\partial y} \frac{\partial A}{\partial y}\} \, dR = \frac{\partial}{\partial A_m} \int (J+Jm)A \, dR$$

Therefore, L.H.S.

$$= \frac{1}{2} \frac{\partial}{\partial A_m} \int_R \Big| (a' \sum b_k A_k/2\Delta + c' \sum c_k A_k/2\Delta) (\sum b_k A_k/2\Delta)$$

$$+ (b' \sum d_k A_k/2\Delta + d' \sum c_k A_k/2\Delta) (\sum c_k A_k/2\Delta) \Big| \, dR$$

where $A(x,y) = \frac{1}{2\Delta} (a_k + b_k x + c_k y)$,

and Δ = area

Therefore, L.H.S.

$$= \frac{1}{8\Delta^2} \int_R \frac{\partial}{\partial A_m} \Big| a'(\sum b_k A_k)^2 + c'(\sum c_k A_k) (\sum b_k A_k)$$

$$+ b'(\sum b_k A_k) (\sum c_k A_k) + d' (\sum c_k A_k) \Big| \, dR$$

$$= \frac{1}{8\Delta^2} \int_R 2 a' (\sum b_k A_k) \frac{\partial}{\partial A_m} (\sum b_k A_k) + (b' + c')$$

$$\Big| (\sum c_k A_k) \frac{\partial}{\partial A_m} (\sum b_k A_k) + (\sum b_k A_k) \frac{\partial}{\partial A_m} (\sum c_k A_k) \Big|$$

$$+ 2d (\sum c_k A_k) \frac{\partial}{\partial A_m} (\sum c_k A_k) \, dR$$

Unless m = k, the differentiation with respect to Am will produce a zero. Therefore, the L.H.S.

$$= \frac{1}{8\Delta^2} \int_R 2 a' \sum_m \sum_k b_m b_k A_m + 2d' \sum_m \sum_k c_m c_k A_m + (b' + c')$$

$$(\sum_m \sum_k b_m c_k A_m + \sum_m \sum_k b_k c_m A_m) \, dR$$

The integration is now trivial as every term is constant, hence the L.H.S.

$$= \frac{1}{8\Delta^2} \left\{ \sum_m \sum_k \left(2a'b_m b_k + 2d'c_m c_k + cb'+c') (b_k c_m + b_m c_k) \right) A_m \right\}$$

In a triangular element with three nodes, m = k = 3. Thus the equation above can be expressed in a 3x3 matrix.

The right hand side denoted by R.H.S. is given by

$$\frac{\partial}{\partial A_m} \int_R (J+Jm)\ A\ dR$$

$$= \int_R (J+Jm) \frac{\partial A}{\partial A_m}\ dR$$

If $A = \frac{1}{3} \left(\sum_{k=1}^{3} A_k \right)$, then the equation above becomes

$$R.H.S. = \sum_{k=1}^{3} \frac{1}{3} \int_R (J+Jm)\ dR$$

$$= \sum_{k=1}^{3} (J+Jm)\ \Delta/3$$

= nodal currents.

BIBLIOGRAPHY

The literature referred to in this thesis is listed below in alphabetical order.

1. Ahamed, S. V. and Erdelyi, E. A. : 'Flux distribution in d.c. machines on-load and over-loads', I.E.E.E. Trans., Vol. PAS-85, No. 9, pp. 960-967, 1966.

2. Anderson, O. W. : 'Iterative solution of finite element equations in magnetic field problems', Paper C72 425-7, I.E.E.E. (PES) Summer meeting, San Francisco, Calif., 1972.

3. Armor, A. F. and Chari, M. V. K. : 'Heat flow in the stator of large turbine generators by method of three-dimensional finite elements - Parts I and II', I.E.E.E. Trans., Vol. PAS-85, No. 5, pp. 1648-1668, 1976.

4. Armstrong, A. G., Collie, C. J., Simkin, J. and Trowbridge, C. W. : 'The solution of three-dimensional magnetostatic problems using scalar potentials', RL-78-088, Rutherford Laboratories, 1978.

5. Bailey, L. J. and Richter, E. : 'Development report on a high-speed permanent magnet generator of 200 kVA rating', Proc. of the 2nd International Workshop on rare-earth cobalt magnets and their applications, Dayton, Ohio, U.S.A., 1976.

6. Bell, D. A., 'Permanent magnets versus electromagnets', Proc. IEE, Vol. 112, No. 9, pp. 1707-1712, 1965.

7. Binns, K. J. : 'High-output stabilised permanent magnet machine', U.K. Patent, 1,437,348, 1976.

8. Binns, K. J. and Kurdali, A. : 'Permanent-magnet a.c. generator', Proc. I.E.E., Vol. 126, No. 7, pp. 690-696, 1979.

9. Binns, K. J. and Lawrenson, P. J. : 'Analysis and Computation of electric and magnetic field problems', Pergamon, Oxford, 1963.

10. Binns, K. J. and Lloyd, M. R. : 'A method of evaluating the starting characteristics of solid salient pole synchronous motors', Proc. I.E.E., E.P.A., Vol. 1, No. 4, 1978.

11. Binns, K. J., Jabbar, M. A. and Barnard, W. R. : 'Computation of the magnetic field of permanent magnets in iron cores', Proc. I.E.E., Vol. 122, No. 12, pp. 1377-1381, 1975.

Note: This bibliography does not include the references in chapter 10.

12. Binns, K. J., Barnard, W. R. and Jabbar, M. A. : 'Hybrid permanent magnet synchronous motors', Proc. I.E.E., Vol. 125, No. 3, pp. 203-208, March 1978.

13. Binns, K. J. and Jabbar, M. A. : 'High-field self-starting permanent-magnet synchronous motor', Proc. I.E.E., Vol. 128, pt. B, No. 3, May 1981.

14. Binns, K. J. and Low, T. S. : 'Multistacked permanent magnet generators - the relation between output and magnet characteristics', 2nd International Conference on Small and Special Machines, I.E.E., London, Conf. publication 202, pp. 138-141, September 1981.

15. Brainard, M. W. : 'Synchronous machines with rotating permanent magnet fields - Pt. 1', Trans. A.I.E.E., Vol. 71, pp. 670-676, 1952.

16. British Standard 4999 and 5000.

17. Bolton, H. R. and Niwdemou, U. C. : 'Operation of self-excited generators for windmill operation', Proc.I.E.E. , Vol. 126, No. 9, p. 815, 1979.

18. Borger, W. U. : 'Rare-earth magnets and 400 Hz aircraft power systems - an overview', Proc. of the 3rd Int. Workshop on Rare-Earth Magnets and their Applications, San Diego, Calif., U.S.A., pp. 67-72, 1978.

19. Carpenter, C. J. : 'Comparison of alternative formulations of three-dimensional magnetic-field and eddy current problems at power frequencies, Proc. I.E.E., Vol. 124, No. 11, 1977.

20. Carter, F. W. : 'Note on air-gap and interpolar induction', Journal of the I.E.E., Vol. 29, p. 925, 1900.

21. Carter, F. W. : 'The magnetic field of the dynamo-electric machine', Journal of the I.E.E., Vol. 64, p. 1115, 1926.

22. Chalmers, B. J. : 'Electromagnetic problems of A.C. Machines', Chapman and Hall, 1965.

23. Chari, M. V. K., Silvester, P. J., Csendes, Z. J., Konrad, A. and Palmo, M. A. : 'Three-dimensional magnetostatic field analysis of electrical machinery by the finite element method', I.E.E.E. Trans., Vol. PAS-180, No. 8, pp. 4007-4019, 1981.

24. Chari, M. V. K., Minnich, S. H., Csendes, Z. J., Tandon, S. C. and Berkery, J. : 'Load characteristics of synchronous generators by the finite-element method', I.E.E.E. Trans., Vol. PAS-100, No. 1, pp.1-13, 1981.

25. Erdelyi, E. A. and Fuchs, E. F. : 'Non-linear magnetic field analysis of d.c. machines, Pt. I, II, III', I.E.E.E. Trans. Vol. PAS-89, No. 7, pp. 1546-1572, 1970.

26. Gratzmuller, J. L. : 'Permanent-magnet rotor for an electric machine', U.S. Patent 3,513,341, September 1970.

27. Gratzmuller, J. L. : 'Improvements in and relating to permanent magnet rotors', U.K. patent 1,171, 858.

28. Harahan, H. R. and Toffolo, D. S. : 'Permanent magnet generators - Part I: Theory', Trans. A.I.E.E., Vol. 76, pp. 1098-1103, 1957.

29. Harrold, W. J. : 'Calculation of equipotentials and flux lines in axially symmetrical permanent magnet assemblies by computer', I.E.E.E. Trans., Vol. MAG-8, p. 23, 1972.

30. Hague, B. : 'The principles of electromagnetism', Dover publications, New York, 1962.

31. I.S.V.R., Southampton University: 'Descriptions of programs available in the PDP 11/75 - Sections 1, 2, 3, 4', Data Analysis Centre, I.S.V.R., Southampton.

32. Jabbar, M. A. : 'Analysis of the performance of a permanent-magnet a.c. machine', Ph.D. Thesis, Southampton University, 1977.

33. Kamminga, W. : 'Finite element solutions for devices with permanent magnets', J. Physics, D, Appl. Physics, Vol. 8, p. 841, 1975.

34. Karmaker, H. C. and Robertson, S. D. T. : 'An integral equation formulation for electromagnetic field analysis in electrical apparatus', I.E.E.E. Trans., Vol. PAS-98, No. 2, pp. 465-470, 1979.

35. Ketha, V. and Sario, E. : 'On the construction of a generator magnetised by barium ferriteemagnets', State Inst. Res. Rep. II (Finland), No. 24, pp. 1-24, 1968.

36. Knudson, L. I. : 'Design considerations for the optimisation of $SmCo_5$ permanent magnet alternators', Proc. of the 2nd Int. Workshop on Rare-Earth Magnets and their Applications, pp. 251-258, Dayton, Ohio, U.S.A., 1976.

37. Kumazawa, Y. : 'Improvements on or relating to permanent magnet rotors for alternating-current generators', U.K. Patent 1,204,844.

38. Kurdali, A. : 'Analysis and performance of a permanent-magnet generator with disc magnets', Ph.D. Thesis, Southampton University, 1979.

39. Langsdorf, A. S. : 'Theory of alternating current machinery', McGraw-Hill Book Company, New York, Y.Y., U.S.A., 1955.

40. Liebmann, G. : 'Solution of partial differential equation with a resistance network analogue, British Journal of Applied Physics, Vol. 1, pp. 92-103, 1950.

41. McCaig, M. : 'Present and future technological applications of permanent magnets', I.E.E.E. Trans., Vol. MAG-4, pp. 221-228, 1968.

42. McCaig, M. : 'Permanent magents in theory and practice', Pentech Press, London, 1977.

43. Millner, A. R. : 'A high speed high frequency permanent magnet generator', Proc. of the 3rd Int. Workshop on Rare-Earth Cobalt Magnets and their Applications, San Diego, Calif., USA, 1978.

44. Mole, C. J. : 'Permanent magnet generators', Electrical Times, Dec. 1956, pp.893-898, 1956.

45. Parker, R. J. : 'Rare-earth permanent magnets and large machines', Proc. 3rd Int. Workshop on Rare-Earth Cobalt Magnets and their Applications.

46. Peterson, A. D. : 'The influence of magnet material selection on the configuration and performance of radial magnet permanent-magnet rotor', Proc. 3rd Int. Workshop on Rare-Earth Cobalt Magnets and their Applications, San Diego, Calif., USA, 1978.

47. Peterson, A. D. : 'Performance and producibility comparisons of the radial vs. transverse magnet $SmCo_5$ permanent-magnet generator configurations', Proc. 3rd Int. Workshop on Rare-Earth Cobalt Magnets and their Applications, San Diego, Calif., USA, 1978.

48. Reichert, K. : 'The calculation of magnetic circuits with permanent magnets by digital computers', I.E.E.E. Trans., Vol. MAG-6, p. 283, 1970.

49. Richter, E. : 'Rare-earth Cobalt permanent magnet for electric machines of medium to large power rating', Goldschmidt, 2/79. p. 50, 1979.

50. Sarma, M. S. : 'Computer-aided analysis of three-dimensional electromagnetic field problems as applied to the design of electrical machines', IE(I) Journal-El, Vol. 54, 1974.

51. Sarma, M. S. : 'Application of digital computers to three-dimensional field determination', I.E.E.E. Trans. on Computers, Vol. C-20, pp. 914-917, 1971.

52. Saunders, R. M. and Weekly, R. H. : 'Design of permanent-magnet alternators', Trans. A.I.E.E., Vol. 70, pp. 1578-1581, 1951.

53. Siemens : 'Permanent-magnet generators for medium-high frequencies', Siemens Review XLIII (1976), No. 6.

54. Siemens : 'An electric machine having permanent magnets mounted in the rotor between its pole segments', U.K. Patent 1,777,247.

55. Silvester, P. and Chari, M. V. K. : 'Finite element solution of saturable magnetic field problems', I.E.E.E. Trans., Vol. PAS-89, No. 7, pp. 1642-1651, 1970.

56. Silvester,P., Cabayan, H. S. and Browne, B. T. : 'Efficient techniques for finite element analysis of electric machines', I.E.E.E. Trans., Vol. PAS-92, pp. 1274-1281, 1973.

57. Silvester, P. and Chari, M. V. K. : 'Finite element analysis of magnetically saturated a.c. machines', Trans. I.E.E., Vol. PAS-90, pp. 2362-2376, 1971

58. Simkin, J. and Trowbridge, C. W. : 'Magnetic field computed using an integral equation derived from Green's Theorem', RL-76-041, RAL, OXON, 1976.

59. Simkin, J. and Trowbridge, C. W. : 'On the use of total scalar potential in the numerical solution of field problems in electromagnets', Int. Journal for numerical methods in Engineering, Vol. 14, pp. 423-440, 1979.

60. Simkin, J. : 'TOSCA User Guide', CAG/80-B, RAL, Oxon, 1981.

61. Simkin, J. and Trowbridge, C. W. : 'Solution of three-dimensional non-linear electromagnetic fields using scalar potential', I.E.E. Proc., Vol. 127, pt. B, No. 6, November 1980.

62. Slomczynska, J. : 'Non-linear analysis of the magnetic flux distribution in the magnetised magnet stabilised in air', I.E.E.E. Trans., Vol. MAG-10, No. 4, P. 113, 1974.

63. Spreadbury, F. G. : 'Permanent magnets', Chapter IV - Magnetic Leakage, Pitman and Sons, London, 1949.

64. Stevenson, A. R. : 'Fundamental theory of flux plotting', Gen. Electric. Review, Vol. 29, pp. 797-804, 1926.

65. Strausse, F. : 'Sunchronous machines with rotating permanent magnet fields, Part II - Magnetic and electrical design considerations', Trans. A.I.E.E., Vol. 71, Part III,

66. Trowbridge, C. W., Armstrong, A. G., Collie, C. J. Diserens, N.J., Newman, M. J. and Simkin, J. : 'GFUN-3D User Guide', RL-76-029/A, RAL, Oxon, 1976.

67. Trowbridge, C. W., Armstrong, A. G., Collie, C. J., Diserens, N.J. Newman, M. J. and Simkin, J. : 'New development in the magnet design program GFUN', RL-75-066, RAL, Oxon, 1975.

68. Walsh, J. : 'Finite difference and finite elements of approximation', Proc. Royal Society of London, Vol. 323, pp. 155-165, 1971.

69. Zaky, S. G. and Robertson, S. D. T. : 'Integral equation formulation for the solution of magnetic field problems - Parts I and II', I.E.E.E. Trans., Vol. PAS-92, pp. 808-823, 1973.

70. Zienkiewicz, O. C. and Cheung, Y. K. : 'Finite elements in the solution of field problems', The Engineer, Vol. 220, pp. 507-510, 1965.

71. Zijlstra, H. : 'Permanent magnets in magnetic field calculations', Proc. Compumag '76, p. 164, 1976.